Mass-ejection phenomena in chemically rich outflows : a study of Cepheus E

André Schutzer

To cite this version:

André Schutzer. Mass-ejection phenomena in chemically rich outflows : a study of Cepheus E. Physics [physics]. Université Grenoble Alpes [2020-..], 2022. English. NNT : 2022GRALY070 . tel-04028517

HAL Id: tel-04028517
https://theses.hal.science/tel-04028517

Submitted on 14 Mar 2023

THÈSE

Pour obtenir le grade de

DOCTEUR DE L’UNIVERSITÉ GRENOBLE ALPES

École doctorale : PHYS - Physique
Spécialité : Astrophysique et Milieux Dilués
Unité de recherche : Institut de Planetologie et dAstrophysique de Grenoble

Phénomènes d'éjection de masse dans les flots chimiquement riches: une étude de Cepheus E

Mass-ejection phenomena in chemically rich outflows: a study of Cepheus E

Présentée par :

André SCHUTZER

Direction de thèse :

Bertrand LE FLOCH DIRECTEUR DE RECHERCHE, Université Grenoble Alpes	Directeur de thèse

Rapporteurs :

KRISTENSEN LARS EGSTRØM
Professeur associé, Københavns Universitet
FABRICE HERPIN
Astronome, UNIVERSITE DE BORDEAUX

Thèse soutenue publiquement le **14 décembre 2022**, devant le jury composé de :

CATHERINE DOUGADOS Directeur de recherche, CNRS DELEGATION ALPES	Présidente
JONATHAN FERREIRA Professeur des Universités, UNIVERSITE GRENOBLE ALPES	Examinateur
KRISTENSEN LARS EGSTRØM Professeur associé, Københavns Universitet	Rapporteur
FABRICE HERPIN Astronome, UNIVERSITE DE BORDEAUX	Rapporteur
RAFAEL BACHILLER Astronome, National Astronomical Observatory	Examinateur
TIMEA CSENGERI Chargé de recherche, CNRS DELEGATION AQUITAINE	Examinatrice

Résumé

Les premiers stades de la formation des étoiles s'accompagnent de puissantes éjections de masse sous forme de jets hypersoniques et d'écoulements bipolaires, qui interagissent avec leur enveloppe parentale par le biais de chocs. Ainsi, ces chocs injectent de la masse et de l'énergie, modifiant les propriétés du matériau protostellaire qui alimente l'étoile naissante. De plus en plus de preuves montrent qu'ils modifient fortement la complexité moléculaire du gaz protostellaire, alors qu'ils peuvent servir à sonder la composition chimique du gaz moléculaire et de la poussière pendant la phase pré-stellaire. Ainsi, l'objectif principal de cette thèse était de contraindre les processus physiques et chimiques générés dans et par la région d'éjection protostellaire. Pour ce faire, j'ai réalisé une étude approfondie de la composition chimique des chocs d'éjection associés au système protostellaire Cep E. Cet objet est un système binaire de classe 0 isolé, de masse intermédiaire, possédant une géométrie 3D bien caractérisée et un flot bipolaire brillant.

Mon travail était basé sur l'analyse et la modélisation d'un large jeu de données obtenu avec l'interféromètre IRAM/NOEMA, dans le cadre du Grand Programme SOLIS, avec une résolution angulaire de $0.5''$ à 1.3 mm et $2''$ à 3 mm, respectivement. J'ai également analysé les données du projet W14AF avec une résolution angulaire de $1.5''$ à 1.3 mm et $2.5''$ à 3mm. Dans un premier temps, une recherche systématique de molécules dans le jet a été effectuée et grâce à la haute qualité des données spectrales, j'ai pu détecter 15 transitions moléculaires de SiO, SO, HCN, HCO^+, CS, H_2CO et CH_3OH (pour la première fois) dans le jet de Cep E. La présence de matières organiques dans les jets n'est pas seulement rare mais reste déroutante, en effet elle soulève plusieurs questions sur l'interaction des chocs avec l'enveloppe protostellaire ainsi que sur le mécanisme à l'origine de ces chocs, à savoir le jet protostellaire lui-même, et les phénomènes de perte de masse.

Par conséquent, mon premier travail de A. Schutzer et al. (2022) a été consacré à la construction d'un scénario cinétique pour le jet de Cep E, avec les données de résolution angulaire les plus élevées. J'ai identifié deux composants dans le jet : un interne, étroit et collimaté ; et une couche de gaz externe plus large. Le jet montre des preuves de la variabilité de l'éjection de masse, tracée par les nombreux chocs internes détectés (18) le long des lobes à grande vitesse. En outre, une échelle de temps dynamique de 55 ans entre les éjections ultérieures à proximité de la protoétoile avec une variabilité de vitesse qui pourrait permettre des collisions de nœuds. De même, nous avons observé qu'une partie du matériau de l'enveloppe est entraînée par le jet à grande vitesse et écartée.

Après avoir caractérisé la cinétique du jet Cep E, nous nous sommes attaqués à l'origine de la riche chimie de cette région. Le lobe nord est plus riche que le sud. Nous avons proposé que cette différenciation chimique soit due au fait que la matière entraînée (gaz et poussière) est entraînée par le jet, puis la matière gelée sur les manteaux de poussière (CH_3OH), est libérée en raison des chocs internes dans le jet à plus distants par rapport à la protoétoile, en plus du fait que le jet frappe les parois de la cavité riches en produits chimiques.

Enfin, en collaboration avec le Dr P. Rivera-Ortiz, nous avons utilisé le code chimio-HD WALKYMIA pour modéliser la formation et reproduire les propriétés de l'émission de CO dans Cep E flot. La comparaison entre le modèle et de les observations nous a permis de reproduire avec un accord très satisfaisant : la morphologie et les propriétés de l'écoulement (masse et taille), le taux de perte de masse et l'historique 3D des événements de perte de masse qui a façonné le système Cep E. De plus, nous avons pu contraindre les conditions du processus d'éjection et déterminer l'interaction du jet avec l'enveloppe parentale.

Abstract

The earliest stages of star formation are accompanied by powerful mass ejections in the form of hypersonic jets and bipolar outflows, which interact with their parental envelope through shocks. Thereby, these shocks inject mass and energy, modifying the properties of the protostellar material which feeds the nascent star. There is mounting evidence that they strongly alter the molecular complexity of the protostellar gas, while they can serve to probe the chemical composition of the molecular gas and dust during the pre-stellar phase. Thus, the main goal of this thesis was to constrain the physical and chemical processes originated in and by the protostellar outflow region. To do so, I carried out a comprehensive study of the chemical composition of the outflow shocks associated to the protostellar system Cep E. This object is an isolated, intermediate-mass, Class 0 binary system, with a well characterized 3D geometry and a bright bipolar outflow.

My work was based on the analysis and modelling of a large dataset obtained with the IRAM/NOEMA interferometer, as part of the Large Program SOLIS, with an angular resolution of 0.5″ at 1.3 mm and 2″ at 3 mm, respectively. I also analyzed data from the W14AF project with an angular resolution of 1.5″ at 1.3 mm and 2.5″ at 3mm. Initially, a systematic search for molecules in the jet was performed and thanks to the high-quality of the spectral data, I was able to detect 15 molecular transitions of SiO, SO, HCN, HCO^+, CS, H_2CO and CH_3OH (for the first time) in the jet of Cep E. The presence of organics in jets is not just rare but still puzzling, indeed it raises several questions on the shock interaction with the protostellar envelope and also on the mechanism at the origin of these shocks, namely the protostellar jet itself, and the mass-loss phenomena.

Therefore, my first work de A. Schutzer et al. (2022) was dedicated to building a kinematic scenario for the jet of Cep E, with the highest angular resolution data. I identified two components in the jet: an internal, narrow and collimated one; and an external broader gas layer. The jet shows evidence for mass-ejection variability, traced by the many internal shocks detected (18) along the high-velocity lobes. Also, a dynamical timescale of 55 years between subsequent ejections close to the protostar with velocity variability that could permit knot collisions. Likewise, we observed that part of the material from the envelope is being entrained by the high velocity jet and dragged away.

After having characterized the kinematics of the Cep E jet, we tackled the origin of the rich chemistry in this region. The northern lobe is richer than the southern. We proposed this chemical differentiation is due to entrained material (gas and dust) being dragged away by the jet, and then the material frozen onto the dust mantles (CH_3OH), is released due to the internal shocks in the jet at further distances with respect to the protostar, additionally to the fact that the jet is hitting the chemically rich cavity walls at certain positions.

Finally, in collaboration with Dr. P. Rivera-Ortiz, we have used the WALKYMIA chemo-Hydro Dynamical code to model the formation and reproduce the properties of the CO emission in the Cep E outflow. The comparison between the model and PdBI observations of the CO emission at arcsec scale have allowed us to reproduce with very satisfying agreement: the outflow morphology and properties (mass and size), the mass-loss rate and the 3D history of the mass loss events that shaped the Cep E system. Moreover, we could constrain the ejection process conditions and determine the jet interaction with the parental envelope.

Resumo

Os estágios iniciais da formação estelar são acompanhados por poderosas ejeções de massa na forma de jatos hipersônicos e ejeções bipolares, que interagem com seu envelope parental por meio de choques. Assim, há diversas evidências de que eles alteram fortemente a complexidade molecular do gás protoestelar, enquanto podem servir para investigar a composição química do gás molecular e da poeira durante a fase pré-estelar. O principal objetivo desta tese foi restringir os processos físicos e químicos originados na e pela região de ejeção protoestelar. Para tanto, venho realizando um estudo abrangente da composição química dos choques de escoamento associados ao sistema protoestelar Cepheus E. Este objeto é composto por um sistema binário isolado, de massa intermediária, Classe 0, com geometria 3D bem caracterizada e uma ejeção bipolar luminosa.

Meu trabalho baseou-se na análise e modelagem de um grande conjunto de dados obtido com o observatório IRAM/NOEMA, como parte do Large Program SOLIS, com resolução angular de $0,5''$ na banda de emissão de 1,3 mm e $2''$ na de 3 mm, respectivamente. Também analisei dados do projeto W14AF com resolução angular de $1,5''$ em 1,3 mm e $2,5''$ em 3mm. Inicialmente, realizei uma busca sistemática de moléculas no jato e graças à alta qualidade dos dados espectrais, consegui detectar 18 transições moleculares de CO, SiO, SO, HCN, HCO^+, CS, H_2CO e CH_3OH (pela primeira vez) no jato de Cep E. A presença de orgânicos em jatos não é apenas rara e bastante intrigante, na verdade levanta várias questões sobre a interação do choque com o envelope protoestelar e também sobre o mecanismo na origem destes choques, como o próprio jato protoestelar, e os fenômenos de perda de massa.

Portanto, meu primeiro trabalho de A. Schutzer et al. (2022) foi dedicado a construir um cenário cinemático para o jato de Cep E, com os dados de maior resolução angular. Identifiquei duas componentes no jato: uma interna, estreita e colimada; e uma camada de gás externa mais larga. O jato mostra evidências de variabilidade de ejeção de massa, rastreada pelos muitos choques internos detectados (18). Além disso, uma escala de tempo de 55 anos entre ejeções subsequentes perto da protoestrela com variabilidade de velocidade que poderia permitir colisões de choques. Da mesma forma, observamos que parte do material do envelope está sendo arrastado pelo jato de alta velocidade e arrastado.

Depois de caracterizar a cinemática do jato de Cep E, conseguimos abordar a origem da rica química nesta região. O jato na parte norte é mais rico que o sul. Propomos que esta diferenciação química é devido ao material (gás e poeira) sendo arrastado pelo jato, e então o as moléculas congeladas nos grãos de poeira (CH_3OH), acabam sendo liberadas devido aos choques internos no jato.

Finalmente, em colaboração com o Dr. P. Rivera-Ortiz, usamos o código WALKYMIA chemo-HD para modelar a formação e reproduzir as propriedades da emissão de CO no jato e cavidades de Cep E. A comparação entre o modelo e as observações nos permitiram reproduzir de forma muito satisfatória: a morfologia e propriedades (massa e tamanho), a taxa de perda de massa e o histórico 3D dos eventos de perda de massa que moldou o sistema Cep E. Além disso, pudemos restringir as condições do processo de ejeção e determinar a interação do jato com o envelope parental.

Acknowledgments

I strongly believe that the real outcome of a Ph.D. is not the manuscript itself but the person responsible for producing it. As a consequence, this person, in this case myself, was not alone during this trajectory. A trajectory that has not began just when I started this Ph.D. but long ago. Therefore, I would like to thank everyone that has crossed my path but, in particular, those that have been walking with me along this, I can not thank you more for being with me: my wife Tai, my mother Tina, my father Herbert, my brother Luiz, my sister Mari and my whole family. Muito obrigado, eu amo vocês! Speaking about my scientific path, my first experience in science, more specifically, in radioastronomy began with one the brightest researchers in Brazil, without her support, I would probably not be writing this manuscript now, therefore, I thank you Zulema, for being a mentor during my many years studying at IAG-USP.

Furthermore, in this last three years, I got to know brilliant scientists, some incredible people, and more importantly, I was really lucky to work with someone that is both, my supervisor B. Lefloch. During these years, I have faced several situations from tough confinements in France, missing family and my home country, to periods of being lost during my thesis, and thanks to his support, I made through these periods. Therefore, I have to thank you for not being just a real scientist and supervisor, but also for being so understanding, and also for treating us, Ph.D. students, as humans and not numbers. It was an honor to work and share several conversations with you, thank you very much!

I was really lucky to join an European project, ACO, where I got to discover and learn scientific fields different from astrophysics but, more importantly, I have met incredible people from completely different cultural backgrounds. Some of them, I can gladly now call not just colleagues but friends. I want to thank all the ESRs for sharing several frustrations and incredible moments during these last years, in particular: Ross, Marcus, Lorenzo, Simón, Stefano, Aurèle, Layal, Seyma and all the others involved in ACO.

My home institution in France, IPAG, was really helpful offering bureaucratic, scientific and psychological support. I want to thank you all the IPAG staff (from informatics to administration) and colleagues, in particular: Pedro, Marie, Jolantha, Joan, Marta, Mathilde, Cécile and others. I have to thank particularly Pedro for being so collaborative and real friend, making the environment in the team lighter: gracias, tío. Inside the Interstellar team, I really appreciated the support from our team leader N. Ponthieu and the rest of our international-friendly group.

I can not forget my long-term friends that even living far abroad but, in a way or another, managed to be connected and not forgotten, I thank you for your loyalty and friendship: Oliver, Pereira, Mirabella, Bruno, G. Barros, M. Vicentin and all my other real friends. It would not be fair, if I also did not thank my young and most loyal friend, my dog: Bounes. I sincerely appreciate all your valuable comments and suggestions, which helped me in improving the quality of the manuscript: R. Rezende, G. Barros and T. Nony.
Finally, I would like to acknowledge and thanks everyone that believes that only through science we will, as humankind, evolve to a better, sustainable and fair society.

Contents

List of Figures

List of Tables

Part I

Introduction

Chapter 1

Introduction

In this chapter, I will situate where we stand in terms of composition of interstellar material, what is known about the early stages of star formation. Furthermore, during these stages, we will focus and describe particularly the outflow features of protostellar regions, its interaction with the ambient material and the impact on the change of physical conditions and chemical composition in these regions. Finally, I will present the main open questions regarding protostellar outflow formation and implications to discuss, therefore, the goals of this PhD thesis.

1.1 Interstellar matter in the Milky Way

We are, above all, inhabitants of a Galaxy, the Milky Way. The Milky Way (MW) is a vast and complex system with billions of stars, dust and gas, linked by electromagnetic radiation, magnetic field and a field of cosmic rays. The MW has a total mass of $\sim 10^{11}\, M_{\odot}$, mainly composed of stars and dark matter, around $\sim 50\%$ each (Draine, 2011). Only a small fraction of the mass is made of gas and dust ($< 1\%$), which constitutes the Interstellar Medium (ISM).

The InterStellar Medium (ISM) is composed mainly by mixed gas and dust. The gas represents $\sim 99\%$ of the fraction of mass of the ISM, and it is constituted basically by Hydrogen (H) - the most abundant element in the universe - representing a fraction of 70% of the total ISM mass, the second most abundant element in the interstellar environment is Helium (He) consisting of 28% mass. Interstellar gas also contains some traces of heavier elements, also in atomic or molecular form, such as carbon (C), nitrogen (N), oxygen (O), sulfur (S), magnesium (Mg), iron (Fe), silicon (Si) or argon (Ar), constitute about 2% of the mass of the gas. The ISM also contain molecular species like H_2 where is located 10% of the reservoir of Hydrogen in the Galaxy.

1.1.1 Structures and composition of interstellar medium

The ISM plays a key role in the history and evolution of our galaxy, of our universe, because it is the place where stars and planets will form. The gas and dust in the ISM constantly receives cosmic and electromagnetic radiation covering all wavelengths (see Figure 1.1). These radiations are produced by the stars, envelopes, nebulae and supernovas which are associated with certain stages of stellar evolution, and by other extremely varied physical

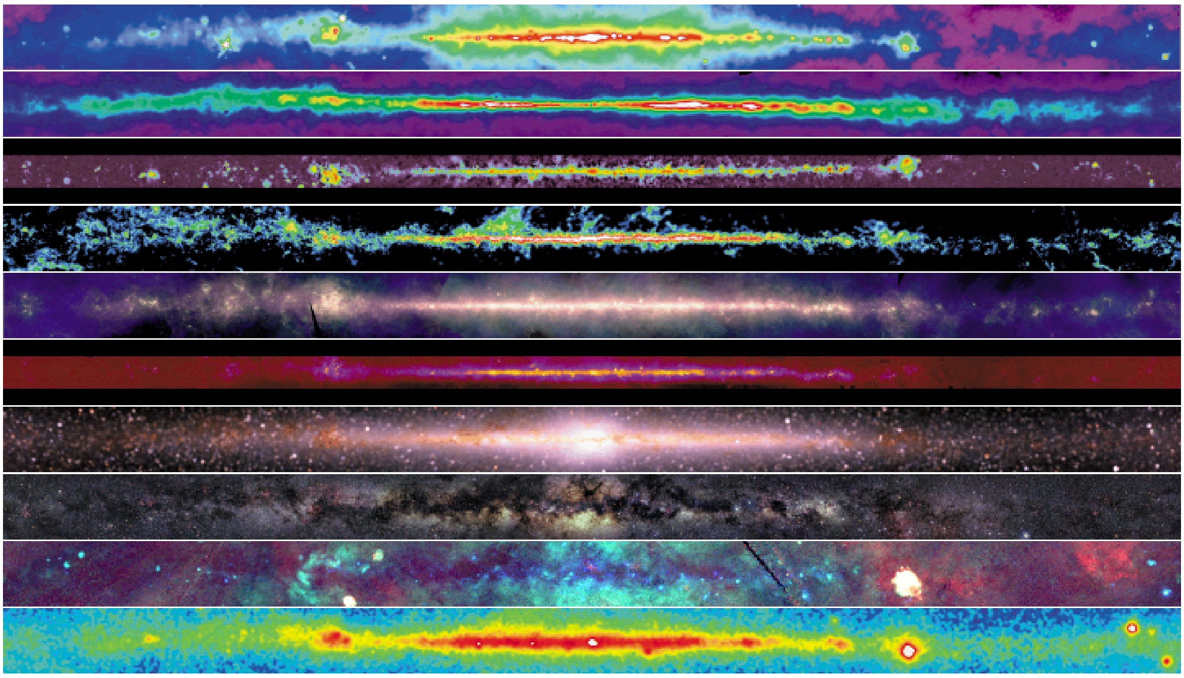

Figure 1.1: Images of the galactic plane at different wavelengths in ascending frequency order: continuum Radio (408 MHz); atomic Hydrogen (1.4 GHz); continuum Radio (2.4–2.7GHz); Carbon monoxide CO (115 GHz); Infrared (3–25×10^3 GHz); Middle Infrared (3×10^4 GHz); Near-Infrared (9–24×10^4 GHz); Optical (4.6×10^5 GHz); Ultraviolet; X-rays (6–36 × 10^7 GHz); Gamma-rays ($> 2.4 \times 10^{13}$ GHz). Image taken from NASA/Goddard Space Flight Center document.

processes. These interactions between the ISM and its environment are at the core of star formation processes.

The physical conditions in which interstellar matter is encountered cover a very wide range of densities n(H)$\simeq 10^{-3}$-10^6 cm^{-3} and temperatures $T = 10$–10^6 K (Draine, 2011). It is possible to classify the ISM into different phases depending on the the state of interstellar matter (ionized, neutral and molecular), density and temperature. Six major different phases are identified:

- **Hot Ionized Medium (HIM)**, the hottest phase with temperatures $T \geq 10^5$ K and diffuse (n(H)= 10^{-3}–10^{-2} cm^{-3}) gas. These extreme conditions are caused due to shock waves of supernovae explosions. This medium is essentially composed of ionized hydrogen (H II) and occupies about half the volume of gas filling the galactic disk.

- **Warm Ionized Medium (WIM)**, constituted of ionized hydrogen (H II). The ionization in this medium is essentially produced by radiation from massive O,B-type stars. This phase occupies about 10% of the volume of the galactic disk and is characterized by temperatures of the order of $T = 10^4$ K and various densities between n(H) = 0.3–10^4cm^{-3}, varying from region to region.

- **Warm Neutral Medium (WNM)**, composed of neutral atomic hydrogen HI. This phase reaches high temperatures around $T \sim 5000$ K and a density n(H)≈ 0.6 cm^{-3}.

This phase occupies around 4% of the galactic disk and contains around 60% of the atomic hydrogen H I of the Milky Way (Heiles & Troland, 2003).

- **Cold Neutral Medium (CNM)**, is composed of neutral atomic hydrogen HI. It is much denser (n(H) $\approx$ 20–50 cm^{-3}), cold (T$\approx 10^2$ K) and occupies only a small part of the galactic volume (a few %). This phase contains about 40% of all hydrogen in atomic H I form (Heiles & Troland, 2003).
- **Diffuse Molecular Cloud**, it is similar to CNM, but with sufficiently higher densities (n(H) $\sim 10^2$ cm^{-3}) to form a self-shielding layer of molecular hydrogen H_2. This layer allows higher H_2 abundances in the inner regions.
- **Dense Molecular Cloud (DMC)**, are structures of the interstellar medium with a typical size of 1 to 10 pc and temperatures T $\sim$ 10–30 K. They consist mainly of molecular hydrogen (H_2, $\sim$ 63% of the mass) and helium (He, 36%). The remaining 1% is made up of dust, aggregates of silicate grains and carbonaceous materials covered with ice, and varying in size from nm to μm. Finally, there are many molecules, in the gas phase or in the ice of the grains, including carbon monoxide (CO), the most abundant after H_2. Molecular clouds are the main sites for star formation, the most studied ones are the clouds closest to the Sun, an area more conducive to the formation of low-mass stars than to that of massive stars. Indeed, the vast majority of massive star formation sites are located in the major arms of our Galaxy (Urquhart et al., 2014).

1.1.2 Molecular composition: dust and gas

Nowadays, up to 270 molecular species have been identified in the interstellar medium (Guélin & Cernicharo, 2022). This number grows almost everyday thanks to the high sensitivity and the broad spectral bands of the telescopes in operation, particularly the radio telescopes and interferometers. There are simple (2-3 atoms) molecules, such as carbon monoxide CO and water H_2O. And also "complex" molecules such like methanol CH_3OH, acetic acid CH_3COOH and even dihydroxyacetone $(CH_2OH)_2CO$ were detected. Excluding Polycyclic Aromatic Hydrocarbons (PAHs), the largest molecular species contain up to $\sim$ 19 atoms. Molecules of this size are aromatic cycles such as Benzene C_6H_6 (Cernicharo et al., 2001), Benzonitrile (c-C_6H_5CN) and Cyanonaphtalenes c-$C_{10}H_7CN$ (McGuire et al., 2021), Indene c-C_9H_8 (Cernicharo et al., 2021). Another indication of complexity comes from the detection of molecular species with heteroatoms such as formamide NH_2CHO (Kahane et al., 2013; López-Sepulcre et al., 2015) or the recently detected $NH_2CH_2CH_2OH$ (Rivilla et al., 2021).

The majority of the molecules detected in the ISM are organics, among them the complex organic molecules (COMs), which are defined as molecules of 6 atoms or more and including at least one heavy element other than carbon (Herbst & van Dishoeck, 2009). COMs represent almost 30% of the molecules detected in space. Among them methanol is definitely one the most abundant. It is also one of thew COMs for which the formation pathway, which consists of successive hydrogenations of CO on dust grains is rather well understood thanks to laboratory experiments (Watanabe & Kouchi, 2002; Watanabe et al., 2004).

The molecular richness of ISM is strongly linked to the physical conditions to which matter is exposed (such as pressure, temperature, cosmic and electromagnetic radiation).

For example, diffuse clouds are characterized by their low gas density and an average temperature of $\sim 100\,\mathrm{K}$, and are exposed to the Galactic UV radiation field. In these regions, the chemical reactions are dominated by ionized species (Porras et al., 2014), most of the reactions are with neutral species and electrons, which makes their abundances quite low. As for the most complex molecules, such as nitriles, aldehydes, alcohols, acids or hydrocarbons, these are detected in the cores of dense molecular clouds (Ohishi & Kaifu, 1998; Winnewisser & Kramer, 1999). These dense molecular clouds, which are also the sites of star formation, present a significant agglomeration of interstellar dust. They make it possible to protect the internal regions from the energetic radiation of the ISM, which shields the molecules formed from being destroyed by this radiation, therefore, playing an important role in the chemically enrichment of the environment.

Chemical reactions in the gas phase are numerous and take place in the different phases of the ISM. We note that if a lot of reactions have been listed in the chemical databases such as KIDA[1] (Wakelam et al., 2012), only a small fraction of these reactions has actually been characterized experimentally, in a regime of conditions which could be applied to the interstellar medium. In practice, the majority of these reactions is badly known and their properties (reaction rate, etc.) are essentially estimated or "guessed", as only $< 20\%$ of them (at most) have been tested in laboratories. The different physical conditions in the gas determine the types of reactions taking place: the processes related to radiation and cosmic-rays are dominant in a diffuse medium, while they are of a different nature inside dense clouds. Cosmic-rays are fundamental for dust heating in the cores of pre-stellar condensations (at 6–7 K) and for non-thermal desorption processes of dust grains in these environments. The physical conditions of star formation sites are relatively sparse (yet the densest in the ISM!) and cold, which makes collisions between two particles rare. However, the size and timescale of the evolution of these structures are sufficient to allow a rich and complex chemistry to take place (Tielens, 2005; Draine, 2011).

As previously mentioned, another important component of the ISM are the dust grains. Interstellar dust is in the form of extremely small grains, whose typical size is of the order of a fraction of a micron, but whose size distribution actually ranges from nm to mm for the biggest ones. These interstellar grains are formed in the atmosphere of evolved stars as well as in novae and supernovae (Draine, 2011). There are several populations of dust grains according to their composition, based either on silicates (Si) or on amorphous carbon. In addition, the size of the dust grains are connect to the absorption and scattering of light in wavelengths ranging from UV to visible. After absorbing a photon, the dust can re-emits the light in the infrared and sub-millimeter range, which creates a reddening effect of interstellar light. This phenomenon is known as interstellar extinction.

Dust grains play a very active role in interstellar chemistry and act in particular as catalysts for chemical reactions. Thus, they play a fundamental role in efficiently forming H_2 (Pantaleone et al., 2021), the most abundant molecule in the Universe. The grains provide a surface on which the adsorbed H atoms can meet and react, and they absorb the energy released in the formation, which prevents the formation in the gas phase of a stable molecule. Very few molecules have been detected directly in the grain surface, many of them, including COMs are known to be formed in these surfaces where they eventually form a thick ice mantle covering grains. These ice are essentially made of water H_2O, carbon monoxide CO, carbon dioxide CO_2, ammonia NH_3, methanol CH_3OH (see Boogert et al.,

---

[1] https://kida.astrochem-tools.org/

2015). They are released through gas-grain and grain-grain collisions, since they can not be formed under gas phase conditions (for instance CH_3OH, Boogert et al., 2015). Therefore, dust grains play a major role in the chemical enrichment of the ISM.

1.2 Star formation

It is well established that stars are formed by the fragmentation and collapse of gas clumps in molecular clouds of the Galaxy. The first step in star formation is the fragmentation of a molecular cloud into stable substructures denser than their surroundings. This fragmentation process is directly linked to the balance between different forces, the main one being gravity, which tends to concentrate matter. The other forces that oppose gravity and therefore provide support against gravitational collapse are: the thermal pressure force caused by gas agitation at the molecular level; turbulence, described as the effect of random (non-thermal) movements of gas at "small" scale, which corresponds to the hierarchical (cascading) distribution of energy and compression movements (such as shocks, collapse, etc.); the magnetic field and; finally, the centrifugal "force" related to the conservation of the angular momentum of the (rotating) cloud.

There is no single model of star formation, several models and scenarios have been proposed depending on the physical condition in the cloud. For instance, an outer perturbation (e.g. shock wave) drives the compression and propagation of the external gas layers inside the inner region, where they will eventually trigger the gravitational collapse of the inner region, in an "outside-in" motion. Conversely, an accumulation of matter in the central region of a dense, quiescent core, as a result of ambipolar diffusion, will lead to the formation of a wave of gravitational collapse propagating from the inner region to the outer envelope ("inside-out" collapse; Shu & Adams, 1987).

1.2.1 Low-mass stars

Observationally, the main stages of the evolutionary star formation process can be distinguished, and classified, according to the shape of the Spectral Energy Distribution (SED) of the source (Lada, 1987). The evolutionary sequence of the formation of low-mass stars ($M \lesssim 2\,M_\odot$) is summarized in Figure 1.2: it includes the pre-stellar core phase and the different protostellar stages (class 0, I, II and III) until nuclear fusion in the core forms He and the protostar(s) reaches the main sequence. Significant changes in the shape of SEDs are observed during the pre- and protostellar phases. They are related to the amount of dust and its properties and well as its spatial distribution in the object's envelope.

Pre-stellar core

The birth of a star takes place in dense cores, referred to as prestellar cores, within the molecular clouds of the Milky Way. These cores are gas condensations in which the thermal pressure, turbulence and magnetic field counterbalance the gravitational collapse, so that it may take up to one million years for the onset of gravitational collapse, unless some outer perturbation (shock wave) accelerates (triggers) the process. The physical and chemical properties of these cores are described in detail in the review by Bergin & Tafalla (2007).

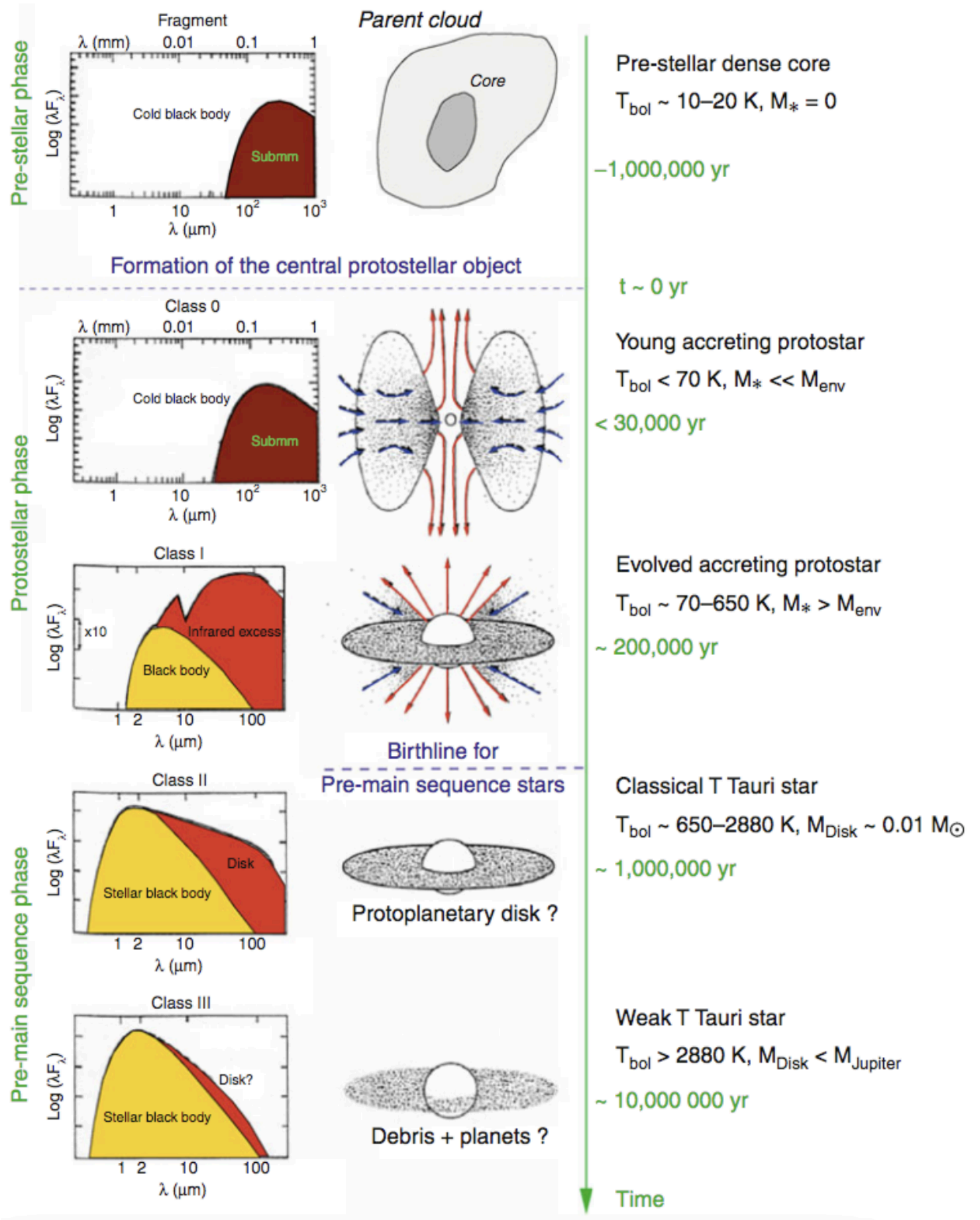

Figure 1.2: Evolutionary sequence for the formation of low-mass stars. On the left of the figure is schematized the structure of the heart, on the right its spectral energy distribution (SED). Image from André (2002).

Ward-Thompson et al. (1994) performed a systematic study of the 800 μm continuum emission of a sample of 21 prestellar (or "starless") cores with the *James Clerk Maxwell*

Telescope (JCMT). Their results showed that the density profile of these objects does not follow a simple power law, but is composed of a plateau in the inner regions (3000–6000 au) and a density profile $\propto r^{-2}$ (approximately) in the outer regions, which implies hydrostatic equilibrium. Finally, it appears that the SEDs of the pre-stellar cores obtained from observations in the infrared and in the (sub)millimeter are well reproduced by the emission of a black body with a temperature of 10–20 K (Myers & Benson, 1983; Beichman et al., 1986; Bergin et al., 2002). The low temperatures derived have a strong implication on the chemical composition of these objects. One of the first indications of these chemical "changes" was reported by Caselli et al. (1999), who found evidence of significant CO depletion in the gas phase (Caselli et al., 1999; Bacmann et al., 2002). Depletion of other molecular species such as CS, H_2CO, C_3H_2 and CCS were also reported later on (Bergin et al., 2001; Lai et al., 2003; Young et al., 2004). The chemical complexity of pre-stellar cores turned out to be greater than expected, with the detection of COMs such as $HCOOCH_3$ and CH_3OCH_3 by several teams in the same objects where CO and other simply species were known to be depleted in the gas phase (Bacmann et al., 2012; Cernicharo, 2012; Vastel et al., 2014).

Observational studies have shown significant enrichment in deuterated species in the gas phase (e.g. Lis et al., 2002; Bacmann et al., 2003; Parise et al., 2004). In particular, Bacmann et al. (2003) reported the presence of doubly deuterated formaldehyde D_2CO; later on Roueff et al. (2005) reported the detection of the single, doubly and triply deuterated forms of ammonia NH_3: NH_2D, ND_2, ND_3. This work allowed to establish a close correlation between the degree of CO depletion and the enrichment in deuterated isotopologues. Ceccarelli et al. (2007) later on proposed the concept of "super-deuteration" in pre-stellar cores. Soon after, molecular deuteration in prestellar cores has subsequently been the subject of numerous observational and theoretical studies which extended from prestellar cores to the more advanced evolutionary phases of star formation, to become "The Ariadne's thread from the prestellar phase to meteorites and comets in our Solar system" (Ceccarelli et al., 2014).

Class 0

At the same time the pre-stellar envelope gravitationally collapses, the accretion phase begins in the center of the core. The mass accretion on the central source is accompanied by phenomena of material ejection under the form of winds and high-speed molecular jets. The protostar now enters into the Class 0 stage, a phase which will last a few tens of thousands of years (André, 2002). During this phase, the mass of the central embedded object remains low compared to that of the envelope ($M_{env} \gg M_{star}$). Observationally, the class 0 phase is characterized by: a) the detection of a centimeter source and a molecular bipolar outflow (Bachiller, 1996); b) a flow of entrained molecular gas, which can reach speeds of several tens of km/s, associated with a fast jet, observed in the (sub)millimeter range if molecular, or observed in the optical range if ionized; c) a continuous dust extended emission and concentrated in the center, signature of a circumstellar envelope; d) a strong ratio between the sub-millimeter flux and the bolometric flux indicating that the flux of the object is dominated by the emission of the envelope.

In this phase, the physical and chemical structure of the envelope is affected by the presence of an internal heating source, the protostar. Like in pre-stellar cores, one observes super-deuteration in the envelope of Class 0 solar-type protostars. This super-deuteration is found both in the cold, outer regions of the envelope, where significant CO depletion has been observed, and in a central, dense and compact region around the protostar. The molecular deuteration observed in the cold outer envelope is somewhat a legacy of the pre-stellar core phase. In the central protostellar region, the temperature rises gradually beyond 100 K, reaching values so high that the icy mantles of dust grains evaporate and release in the gas phase the molecular material stored at the surface of the grains, water H_2O, organics and COMs. This is the definition of a hot corino, i.e. a hot, dense region, with a rich content in COMs. Note that the detection and the determination of the properties of the H_2O emission around "hot corinos" was one of the main goals of the *Herschel* space mission (Pilbratt et al., 2010). It turned out that only the rare isotopologues of H_2O, such as $H_2^{18}O$ were tracing the emission from hot corinos, when the line profiles of the main isotopologue H_2O were actually dominated by the emission from the outflowing gas and the associated shocks.

These dense and compact "molecular rich" protostellar regions were first detected towards high-mass star-forming regions, and called "hot cores". The similarity of the names hot cores/hot corinos precisely reflect the similarity of the observed chemical enrichment in the gas phase, and the physical processes responsible for this enrichment in both kinds of objects. Super-deuteration is also observed around massive protostars too, though at a much lower degree (Ceccarelli et al., 2007). These observational constraints have naturally raised questions on the nature of the differences and similarities in the molecular composition and abundances, beyond the initial chemical conditions, on the influence of the mass and the local physical conditions in the observed gas composition, and the involved processes. A first answer to these questions through a "systematic" (unbiased) observational approach was brought by the IRAM 30m Large Program ASAI (Lefloch et al., 2018).

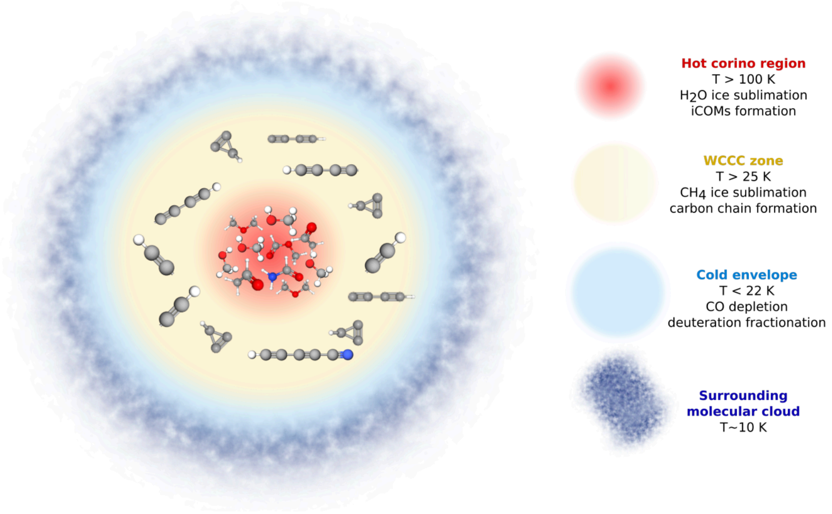

Figure 1.3: Scheme representing the typical structure of Class 0/I protostellar envelope. For simplicity the outflow and disk are not represented. The different region sizes can vary from one protostar to another and are not scaled. Image taken from Mathilde Bouvier Ph.D. thesis, IPAG, 2022.

This first example of a hot corino was provided by Class 0 protostar IRAS 16293-2422 (Cazaux et al., 2003), which then became a prototypical object for these studies. The physical structure of the envelope of IRAS 16293-2422 was modeled by Ceccarelli et al.

(2000). This work has in particular highlighted the overabundance of several molecules such as H_2O, H_2CO and CH_3OH. This overabundance is explained by the sublimation of the ice mantle of the grains when the temperature of the dust exceeds the sublimation temperature of the water ice $T_{dust} > 100\,K$ (Ceccarelli et al., 2007). The water molecules as well as the different molecules stuck on the grains are then released in the gas phase, which causes the observed increase in abundance. Cazaux et al. (2003) detected many COMs in the envelope of IRAS 16293-2422: HCOOH, CH_3CHO, $HCOOCH_3$, CH_3CN, C_2H_5 CN and CH_3CCH.

The first indication of significant chemical diversity in the envelopes of low-mass protostars, with the detection of objects exhibiting a rich content of carbon chains and various chemically related species in the absence of COMs rich was provided by Sakai et al. (2008). The prototype for this class of objects is the low-mass protostar L1527 in the Taurus region. Contrary to IRAS 16293-2422, the molecular lines of $HCOOCH_3$ are not detected and the lines of methanol are much less intense. This kind of sources has been named Warm-Carbon-Chain-Chemistry (WCCC) objects. Sakai et al. (2009) proposed that the composition of the ice mantles would in fact be different from that hot corinos, and dominated, instead of COMs, by CH_4. This last main component of the grain mantles evaporates in the "warm" regions ($T \sim 30\,K$) of the envelope, favoring the formation of carbon chains in the gas phase, and the increase in the abundances thus observed. The properties of both hot corinos and WCCCs are displayed in the scheme in Figure 1.3. Recent observations of WCCC protostars with ALMA, NOEMA and IRAM-30m revealed that some sources (e.g. L483) could display signatures of both classes of chemistry (WCCC: Sakai et al., 2009, COMs Oya et al. (2017); Jacobsen et al. (2019)) in the envelope. Similar results were obtained in a sample of a few protostars in the Perseus molecular cloud by Higuchi et al. (2018).

Class I

Class I sources were first identified thanks to the IRAS point source catalog (Lada, 1987). The SED of a Class I is made of Black Body at high temperatures plus an infrared excess due to the emission of the accretion disk and the protostellar envelope. As the envelope collapses onto the central object, the mass of the central star increases and becomes greater than the mass of the surrounding envelope. The bolometric temperature is $> 70\,K$ and the SED has a spectral slope $\alpha_{IR} > 0$ in the infrared in this phase. The accretion process is accompanied by mass-loss phenomena in the form of low-velocity outflows and sometimes molecular jets which contribute to emptying the reservoir of matter from the protostellar envelope, while the mass of the central object gradually increases. The lifetime of this phase is estimated at 10^5 years.

Bontemps et al. (1996) showed that the activity of Class 0 and Class I sources was significantly different, more precisely that the outflows of Class 0 sources are much more powerful than those of their Class I counterparts. Based on a sample of 36 outflows from Class I sources and 9 outflows from Class 0 sources, the authors also showed that the outflow momentum flux is closely correlated with the brightness of the central source for Class I sources. Class 0 sources are a factor of 10 above the observed correlation. Nevertheless, the momentum flux is well correlated with the envelope mass in both cases, which the authors interpret as an indication of a gradual decrease in momentum flux with time during the accretion phase, reflecting a decrease of the mass accretion rate.

The physical properties of Class I sources have been systematically studied, but their chemical properties have been investigated in a much less systematically way than those of Class 0 sources, which are younger and brighter, and display a richer molecular emission spectrum at millimeter wavelengths. The Class I protostar SVS13A in the Perseus cloud NGC1333 has been the subject of a systematic study of its chemical composition within the framework of the Large ASAI Program (Lefloch et al., 2018), and the first results obtained on the deuteration of formaldehyde H_2CO in the envelope made it possible to establish a link between the different stages of the star formation sequence, from prestellar and Class 0 sources, to Class I, and Class II sources (Bianchi et al., 2017). Molecular deuteration appears somewhat a more complex process in SVS13A. On the one hand,the CH_3CN deuteration rate is of the same order as the values measured in younger prestellar cores and Class 0 protostars; on the other hand, the CH_3OH deuteration rate appears to decrease with respect to the values measured in sources at an earlier evolutionary stage (PSC, Class 0).

Class II

When the protostellar envelope is finally dissipated (thanks to outflow and/or wind) the star together with the disc becomes visible in the near IR. The object becomes a classical TTauri. The accretion disk dominates the SED in infrared with an $-2 \leq \alpha_{IR} \leq 0$. The disk accretion rates on the star ($\dot{M}_{acc} \sim 10^{-8}\, M_{\odot}\, \mathrm{yr}^{-1}$) are calculated from the excess UV created by the shocks of the magnetospheric accretion columns on the central star. The lifetime of this phase is the dissipation time of the accretion disk, it is estimated at some 10^6 years.

The study of the chemical composition of protoplanetary disks is comparatively much more difficult than in protostellar envelopes. Their size is much smaller (typically a few seconds of arc) and the risk of confusion with the surrounding material (residual envelope and molecular cloud) often have to be taken into account, which makes studies with single dish telescopes and interferometers difficult. The work of Dutrey et al. (1997) revealed for the first time the presence of organic molecules, such as H_2CO, in the disks of the TTauri stars DM Tau and GG Tau. The authors also identified the signatures of CN, HCN, HNC, CS, HCO^+, N_2H^+, H_2CO and CCH. Recent studies with the ALMA interferometer have finally unveiled the presence of COMs in the disc of Class II sources: CH_3CN (Öberg et al., 2015), CH_3OH (Walsh et al., 2016) and HCOOH (Favre et al., 2018). Detection of COMs remains difficult and often rely on "stacking" techniques (averaging signal of various lines). About 25 species detected, most of them composed of 2-3 atoms, but the presence of HCOOH (and CH_3OH) show that organic chemistry is at work in discs.

Class III

Class III is the last stage of star formation, known as "weak TTauri stars" (wTTs) because their SEDs are essentially composed of a black body of several thousand Kelvins to which is added a weak infrared excess ($\alpha < -2$) due to the emission of the debris disk, their spectra no longer have emission lines. These objects have practically no accretion disk and if present, they are optically thin. The number of Class II and III objects are comparable, which implies that their lifetimes are also comparable and estimated at 10^7 years. Finally, when the temperature becomes high enough to initiate hydrogen fusion reactions, the star joins the main sequence.

1.2.2 High-mass stars

Unlike the case for low-mass stars, there is no observational evolutionary sequence that is firmly established for high-mass star formation. One of the main differences between high-mass and low-mass stars is that the radiation field of a massive star ($M \geq 8\,M_{\odot}$) plays a more important role during its whole life and already in its formation phase. Massive protostars evolve very rapidly within their parent clouds, making it difficult to observe the early stages of these objects because they are heavily buried in very dense molecular clouds. Observationally, we see that massive objects are systematically detected in clusters (McCaughrean et al., 1994; Hillenbrand & Hartmann, 1998; Testi et al., 1999; Megeath et al., 2005). All these constraints indicate that the environment of massive protostars plays a key role in their formation. For very detailed information regarding high-mass star formation, see the reviews by Zinnecker & Yorke (2007); Motte et al. (2018).

At least four models have been proposed to explain high-mass star formation: a) Stellar coalescence (Bonnell et al., 1998), in this model cloud collapse would only result in low mass stars, while massive stars are formed through the fusion of these objects; b) Competitive accretion (Bonnell et al., 2001), this model suggests a higher material accretion rate compared to low-mass star formation regions (for a factor of hundred), this value can be reached in a dense protostellar cluster where several objects share the same material reservoir; c) Monolithic collapse and accretion disk (Tan & McKee, 2003), this model follows the low mass star formations but with a particular geometry; d) Hierarchical global collapse (Motte et al., 2018), this new model suggests that massive pre-stellar cores could actually be low-mass pre-stellar cores inside clusters or Massive Dense Cores (MDC). On a small scale, the low-mass prestellar cores will become low-mass protostars. On a large scale, the global collapse of the parent molecular cloud generates a flow of gas that will feed the MDCs and therefore the protostar.

The evolutionary scheme proposed by Motte et al. (2018) for the formation of high-mass stars is displayed in Figure 1.4. It is an empirical scenario qualitatively reminding the global hierarchical collapse and clump-fed accretion scenarios (Vázquez-Semadeni et al., 2009; Longmore et al., 2009):

1. High-mass stars form in molecular complexes hosting massive clouds and often O-B clusters. Parsec-scale massive clumps/clouds called ridges and hubs are often the sites for high-mass star formation. Their infall velocity and density structure suggest ridges/hubs undergo a global but controlled collapse;

2. At first, IR-quiet Massive Dense Cores (MDCs) are 0.1 pc massive cloud fragments, which host low-mass prestellar cores. They represent the starless MDC phase lasting for about one free-fall time ($\sim 10^5$ yr);

3. The global collapse of ridges/hubs generates gas flow streams, which simultaneously increase the mass of MDCs and, on 0.02 pc scales, that of their hosted protostar. Typically, in $\sim 10^5$ yr, two high-mass protostars form in 0.1 pc MDCs;

4. When inflowing gas streams are efficient to reach and feed the low-mass protostellar cores, the latter become IR-quiet high-mass protostars. They have 0.02 pc sizes, but still only harbor low-mass, $< 8\,M_{\odot}$, stellar embryos. Their accretion rates are strong, they drive outflows and power hot cores;

5. When stellar embryos reach $> 8\,M_{\odot}$, their luminosity sharply increases and high-mass protostars become IR-bright. Their hot cores grow in size and they soon develop HCHII (Hypercompact H II) regions quenched by infalling gas or localized toward photo-evaporating disks;

6. Stellar embryos have increasing UV fields that develop H II regions, which along with other processes, including outflows and winds, slow and later on eventually stop gas accretion toward the newborn star. This terminates the main accretion phase.

The study of the chemistry of massive protostars came from the detection of regions rich in COMs: the Hot Molecular Cores (HMC), also known as hot cores (Walmsley, 1989). These hot cores are located in the very hot parts of the massive protostars envelope. A rich chemical diversity within regions of massive star formation is observed, the prototype of this region is Orion KL and SgrB2 (Johansson et al., 1984; Turner, 1989; Tercero et al., 2011; Crockett et al., 2014). Several studies have reported a dichotomy between the spatial distribution of O-bearing and N-bearing COMs where the latter come from regions where the gas is warmer (Favre et al., 2011; Crockett et al., 2014), but also differences between chemically related species (Favre et al., 2017).

1.2.3 Intermediate-mass stars

Intermediate-mass (IM) stars play an important in the ecology of the Galaxy as they are among the main sources of the Galactic Far Ultraviolet field, which regulates the phases of the ISM and the Galactic star formation processes. The formation of IM stars ($2\,M_{\odot} \leq M_{star} \leq 8\,M_{\odot}$) has been less studied than the low- and high-mass counterparts. Studying them is important because they make the link between low-mass and high-mass stars (di Francesco, 1997; Mannings & Sargent, 1997, 2000), and thus bring constraints on the physical and chemical processes at work in the formation of stars. During their formation, they inject a large amount of energy into the interstellar medium via molecular jets, which modifies the physical conditions, enhances the chemistry and causes the dissipation of the parental envelope (Fuente et al., 2005).

The formation path of IM stars is generally similar to that of solar-type protostars, i.e. they go through Class 0 and Class I phases, which are the precursors of Herbig Ae/Be stars. Although some IM protostars (Serpens-FIRS 1, IC1396N, CB3) are observed in star clusters around massive stars (Testi & Sargent, 1998; Neri et al., 2007; Fuente et al., 2007), others are isolated objects, as observed for low-mass stars (Testi et al., 1999).

The first systematic study of the physical structure of IM protostellar envelopes was carried out by Crimier et al. (2010). The authors investigated a sample of 6 sources chosen to span the luminosity range 30–1000 $L_{\odot}$: OMC2-FIR4, CB3-mm, Cep E-mm, IC1396N-BIMA 2, NGC7129-FIRS2 and Serpens FIRS 1, and they modelled the SED between 1300 μm and 24 μm. The density profiles of these sources were fitted by a power law $\rho \propto n^{-\alpha}$ for which the authors obtained an average spectral index $\alpha \approx 1.6$ and the temperature profiles were calculated in a self-consistent way. Crimier et al. (2010) concluded from their study that the physical properties of the envelopes of intermediate-mass protostars vary without apparent discontinuity between low-mass and massive sources.

If several studies have been dedicated to the emission of specific molecular transitions in the envelope of IM protostellar envelopes, only few systematic studies have been per-

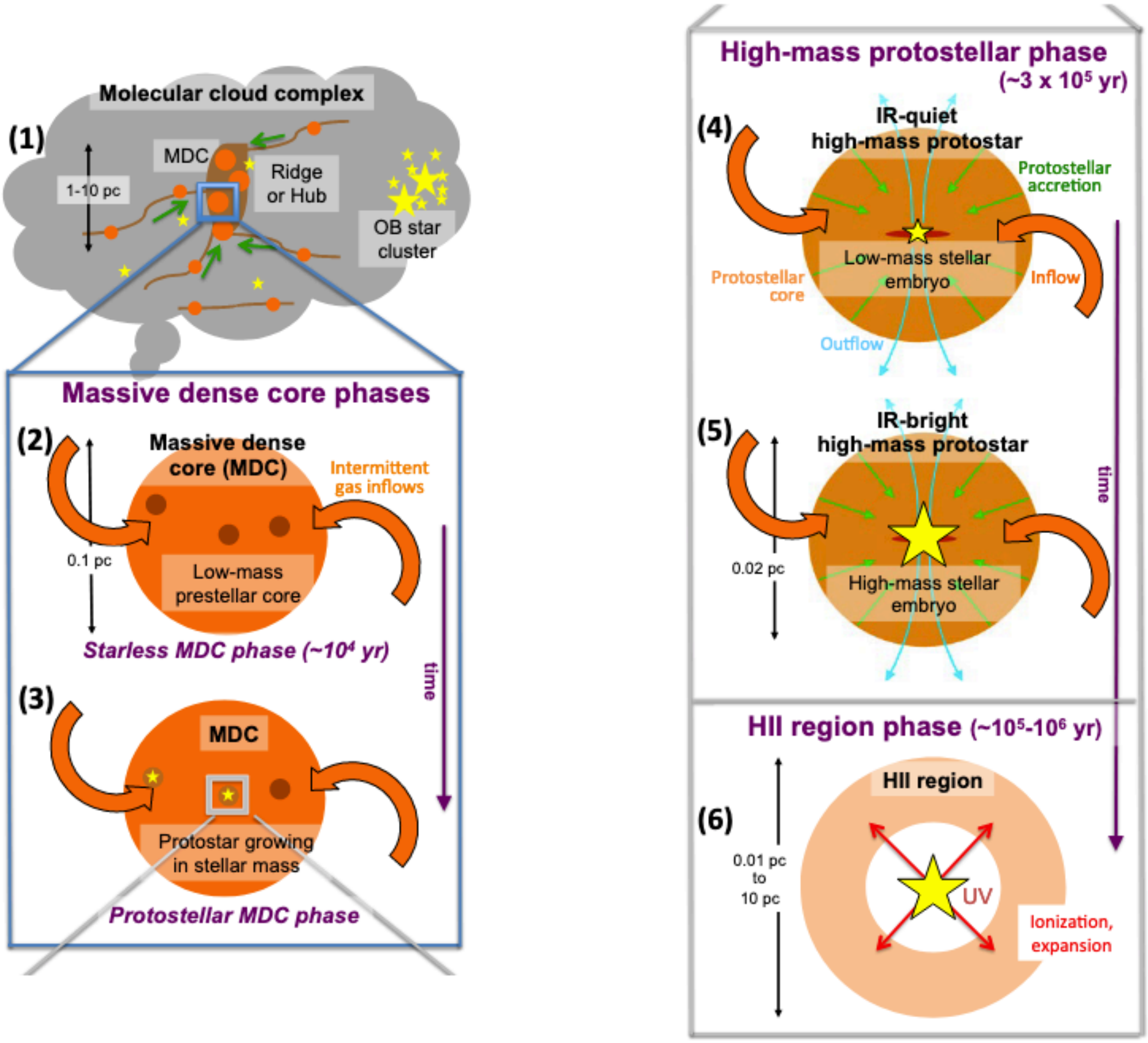

Figure 1.4: Schematic evolutionary diagram proposed for the formation of high-mass stars. (1) Massive filaments and spherical clumps, called ridges and hubs, host massive dense cores (MDCs, 0.1 pc) forming high-mass stars. (2) During their starless phase, MDCs only harbor low-mass prestellar cores. (3) IR-quiet MDCs become protostellar when hosting a stellar embryo of low-mass. The local, 0.02 pc, protostellar collapse is accompanied by the global collapse of MDCs and ridges/hubs. (4) Protostellar envelopes feed from these gravitationally-driven inflows, leading to the formation of high-mass protostars. The latter are IR-quiet as long as their stellar embryos remain low-mass. (5) High-mass protostars become IR-bright for stellar embryos with mass $> 8\,M_{\odot}$. (6) The main accretion phase terminates when the stellar UV field ionizes the protostellar envelope and an HII region develops. Image taken from Motte et al. (2018).

formed: NGC7129 FIRS2 (Fuente et al., 2005, 2014; van Dishoeck et al., 2011), Cep E-mm (Ospina-Zamudio et al., 2018) and OMC2-FIR4 (López-Sepulcre et al., 2015). They showed the importance of IM protostars in the study of the chemistry of protostellar envelopes and the diversity observed between solar-type objects and massive sources. While some IM protostars (e.g. FIRS2), have a chemical composition similar to that of massive hot cores, others show similarities with hot corinos in terms of chemical composition and molecular abundances Ospina-Zamudio et al. (2018). As a matter of fact, the latter authors concluded that there is no significant difference in the relative composition of O-bearing COMs between low-, high- and intermediate-mass protostars. However, they reported a significant relative abundance increase with luminosity for some N-bearing species (e.g. C_2H_5CN) when compared to methylformate $HCOOCH_3$.

1.3 Protostellar jets and outflows

The first indications of mass-loss phenomena from young stars appeared in the early 1950s with the discovery by Herbig (1951) and Haro (1952) of nebulosities observed in the visible domain traced by ionized atomic gas (Hα, [OII] and [SII]). These nebula objects were later referred to as Herbig-Haro (HH) objects and subsequently interpreted as the shock interaction of hypersonic stellar winds with the ambient material (Schwartz, 1975). Measurements of proper motions (Cudworth & Herbig, 1979) confirmed that the ejection originates from newly formed stars. Rapidly moving, highly collimated HH jets originating from young stars were discovered a years later (Mundt & Fried, 1983).

In the early 2000s, there were approximately 500 Herbig-Haro objects detected toward nearby star-forming regions such as Taurus and Orion. In the near- and mid-infrared, there have been several reports of emission from protostellar ejecta in the pure rotational and rovibrational transitions of molecular hydrogen H_2, in particular thanks to the Infrared Space Observatory (ISO) and the Spitzer space mission (see e.g. Lefloch et al., 2003; Maret et al., 2009). These observations revealed emission from dense $n(\mathrm{H_2}) = 10^4$–10^6 cm^{-3} and hot $T = 10^2$–10^3 K gas components accelerated up to speeds of a few $100\,\mathrm{km\,s^{-1}}$. This hot gas is also detected in the high-energy transitions of molecules such as CO ($J_u > 9$) and H_2O at far Infrared wavelengths (Benedettini et al., 2012)

The first evidence of CO outflows arrived in the mid-1970s with the discovery of broad wings in the Orion A molecular cloud (Kwan & Ko, 1976; Zuckerman et al., 1976). Soon afterwards, high-velocity CO emission was detected toward other objects, and the structure of the outflowing material was found to be bipolar (Snell et al., 1980; Rodriguez et al., 1980). The first surveys revealed that these bipolar outflows are extraordinarily common around young stars (Bally & Lada, 1983). Strong observational efforts led to the identification of a large number of molecular outflows in the following years. More than 200 objects were known in the mid-1990s (Fukui et al., 1993), an ever growing number which shows that outflow phenomena are ubiquitous in star-forming regions. Contrary to HH objects which can propagate several parsec away from the protostar, molecular outflows are more often confined to the limits of molecular clouds (Reipurth & Bally, 2001). However, large-scale surveys of CO emission show that molecular outflows can also propagate at parsec scale, and drive the formation of large-scale features within molecular clouds (Schuster et al., 2004). It is also established that molecular ejecta from protostars can sometimes propagate at parsec scale away from the powering protostar and leave the ambient cloud, as illustrated by HH 111 (Cernicharo & Reipurth, 1996).

It is now established that outflows are ubiquitous during the protostellar phase. They present different features observed with different tracers during the stage formation phase, depending on the mass of the central source. Throughout this section, I will describe the main characteristics of outflows, their morphology, formation and evolution. Also, I will review how outflows interact with the molecular cloud and the envelope that gave birth to the protostar powering them.

1.3.1 Molecular jets: observed properties

Most molecular outflows are usually bipolar, with two lobes ejected symmetrically on each side of the protostar. Together with CO, SiO is the most frequently used tracers to characterize protostellar ejections. The frequency of the emission of a molecular line is shifted by Doppler effect with respect to its rest value in the framework of the protostellar source. It means that when the outflowing gas moves towards the observer, the line frequency is actually higher (Doppler), or blueshifted, and the frequency shift in the spectrum can be directly converted into a (negative) velocity shift. Conversely, the gas moving away from the observer (positive velocity shift) is shifted to lower, redshifted, frequencies.

Figure 1.5 summarizes the now classical picture of a Class 0 protostellar outflow, here HH 211, where the H_2 emission (in greyscale) and the CO emission (contours) as mapped with the IRAM interferometer (Gueth & Guilloteau, 1999) are displayed. A detailed look at the spectra of protostellar ejections allows to distinguish two regimes, associated with two distinct components: first, the classical outflow with "standard" moderately high velocities, ranging from a few kilometers per second to about $20\,\mathrm{km\,s^{-1}}$; second, a weak, high-velocity and highly collimated jet consisting of accelerated/entrained gas up to sometimes much higher speeds $|\Delta V| \sim 100\,\mathrm{km\,s^{-1}}$; it appears on the spectrum separated from the central line (upper panel in Figure 1.5). Thanks to several single-dish and interferometric systematic studies, the paradigm is more established that protostellar jets in the Class 0 phase are mainly molecular. The low-velocity gas at lower speed forms the edges of a cavity around the jet (lower panel).

The word "outflow" is often used to refer to these two components. The limit between these two regimes is generally in the order of $|\Delta V| \sim 10 - 30\,\mathrm{km\,s^{-1}}$ and varies depending on the source, its geometry, and the evolutionary stage of the protostar. On the example of HH 211 shown in Figure 1.5, the high velocity component of CO J=2–1 is obtained for $|\Delta V| > 10\,\mathrm{km\,s^{-1}}$, while the low velocity is $|\Delta V| \leq 7\,\mathrm{km\,s^{-1}}$.

It is now well established that high-velocity jets from Class 0 and Class I protostars can be traced by CO emission (Gueth & Guilloteau, 1999; Lee et al., 2007; Santiago-García et al., 2009; Plunkett et al., 2015), which allows to estimate the molecular gas density and the mass-loss rate in the jets. Their knots and bow shocks can be traced by specific molecular tracers, such as: H_2 (McCaughrean et al., 1994; Hirano et al., 2006), SiO (Gueth et al., 1998; Lefloch et al., 1998) and SO (Lee et al., 2007, 2014). SiO is a shock tracer, tracing uniquely the jets within $\sim 10^4$ au of the central sources down to the bases where the density is high, allowing to probe the jet launching and collimation regions. In the Class II phase, jets are mainly detected in atomic and ionized gas (OI, Hα, and SII) (Reipurth & Bally, 2001; Bally, 2016), appearing as Herbig-Haro flows at optical and infrared wavelengths.

Figure 1.6 summarizes the morphology and the main components that constitute protostellar outflows. The protostellar disk (in purple) and its magnetic field (in red) produce a strongly collimated jet which substructures into several observable called "knots", often traced by CO, SiO, H_2O that are created due to ejecta with different velocities that collide, then propagates reaching out the parental cloud (pink arrows) and will heat and excite the

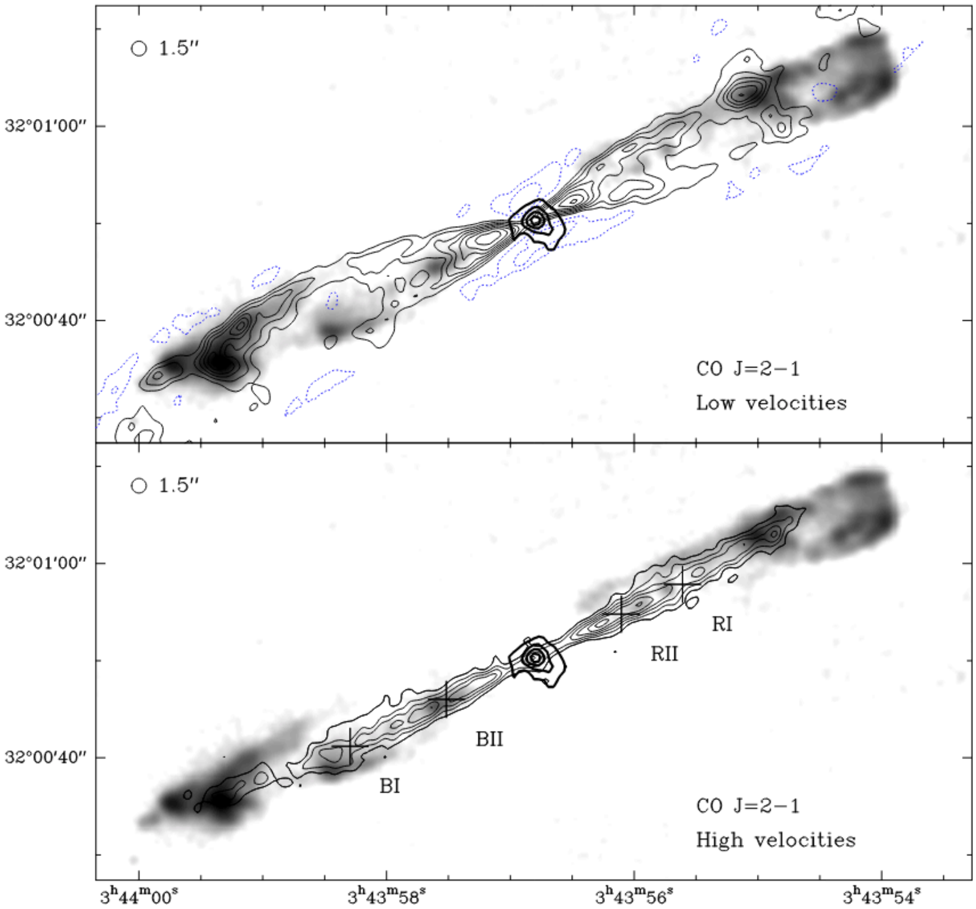

Figure 1.5: CO J=2–1 emission (thin contours) of the HH 211 outflow, integrated in two different velocity intervals and superimposed on the H_2 v=1–0 S(1) emission (in greyscale; from McCaughrean et al., 1994) and the 230 GHz continuum emission (thick contours). The angular resolutions are 0.75″ for the H_2, 1.7″ × 1.3″ for the CO, and 1.6″ × 1.3″ for the continuum observations. Velocities 2.2 and 18.2 $\mathrm{km\,s^{-1}}$ (the systemic velocity is 9.2 $\mathrm{km\,s^{-1}}$); Lower panel: CO J=2–1 emission integrated for velocities lower than 2.2 $\mathrm{km\,s^{-1}}$ and larger than 18.2 $\mathrm{km\,s^{-1}}$. Image taken from Gueth & Guilloteau (1999).

gas environment at the level of shock zones (magenta and green lines). The low-velocity outflow (cavity walls) is shown in yellow, the walls are made up of several layers represented in blue and green (low and high-J CO) then in yellow (H_2) with increasing levels of excitation.

The characteristics of protostellar ejections are directly linked to those of the protostar, and in particular to its accretion rate. The link between the mass-loss $\dot{M}_{jet}$ and the accretion rate $\dot{M}_{acc}$ on the central object. While the mass-loss rate is computed through the amount of mass ejected in a certain amount of time, the accretion can be obtained as follows (Lee, 2020):

$$\dot{M}_{acc} \sim \frac{(L_{bol} + L_{jet})R_{star}}{G.M_{star}} \approx 6.44 \times 10^{-8} \frac{L_{bol} + L_{jet}}{\mathrm{L}_\odot} \frac{M_\odot}{M_{star}} M_{star} \cdot yr^{-1}, \tag{1.1}$$

where it was assumed that both the bolometric luminosity and the jet's mechanical luminosity come from accretion.

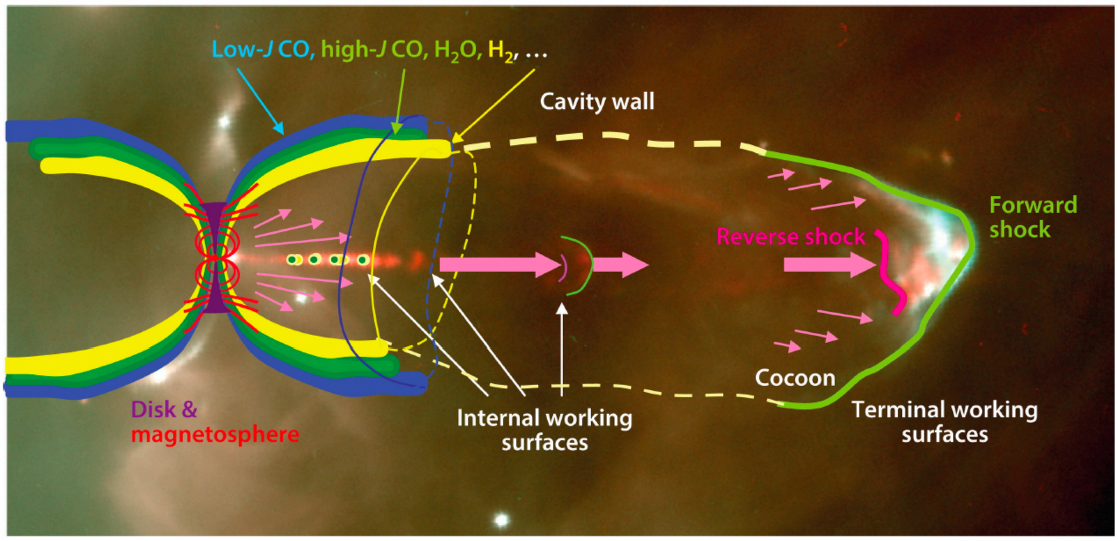

Figure 1.6: Diagram showing the main components linked to a protostellar ejection. The protostellar disk (in purple) and its magnetic field (in red) produce a strongly collimated jet which substructures into several observable nodes in CO, then propagates out of the parent cloud (pink arrows) and will heat and excite the gas environment at the level of shock zones (magenta and green lines). Around the jet develops a cavity made up of several layers represented in blue and green (CO) then in yellow (H_2) with increasing levels of excitation. The color image shows HH34 (in Orion A) and its jet in Hα (blue) and [SII] (red). Image taken from Bally (2016).

The ratio of the mass-loss rate to the accretion rate has been used to probe the mass-ejection efficiency that is then compared to the current jet-launching models. In Figure 1.7, it is shown the mass-loss rate versus the accretion rate. The Class 0 molecular jets are marked with blue stars in comparison to those found in different classes of young stellar objects (YSOs) associated with jets and outflows initially presented in the work of Ellerbroek et al. (2013). Despite a large dispersion, the average $\dot{M}_{jet}/\dot{M}_{acc}$ ratio remains in the same order of magnitude. It is also possible to note that $\dot{M}_{jet}$ decreases as protostars evolve from the Class 0/I stage (squares) to pre-main sequence phases (Herbig Ae/Be, T Tauri). In this last phase, $\dot{M}_{jet}$ is higher for Herbig Ae/Be stars (IM; triangles) than for T Tauri stars (LM; circles).

Other outflow properties change with time and the evolutionary status of the source. Arce & Sargent (2006) studied the gas and dust distribution in the circumstellar environment of a sample of 9 protostars at different stages of evolution (3 Class 0, 3 Class I, 3 Class II) to investigate how the effects of outflows on their immediate environment change over time. The authors observed that the opening angle of the low-velocity outflows (measured from the aperture of the cavity walls) increases with the outflow dynamical age, from $\theta \leq 55\,^{\circ}$ for Class 0 sources, to $\theta > 75\,^{\circ}$ for Class I sources. For the most evolved sources of the sample, Class II sources, outflows have even wider lobes or no definite shape or structure. Also, the authors observed that the proportion of atomic and/or ionized gas with respect to molecular gas increases for Class I sources.

The momentum flux is another interesting parameter of outflows as it allows to estimate

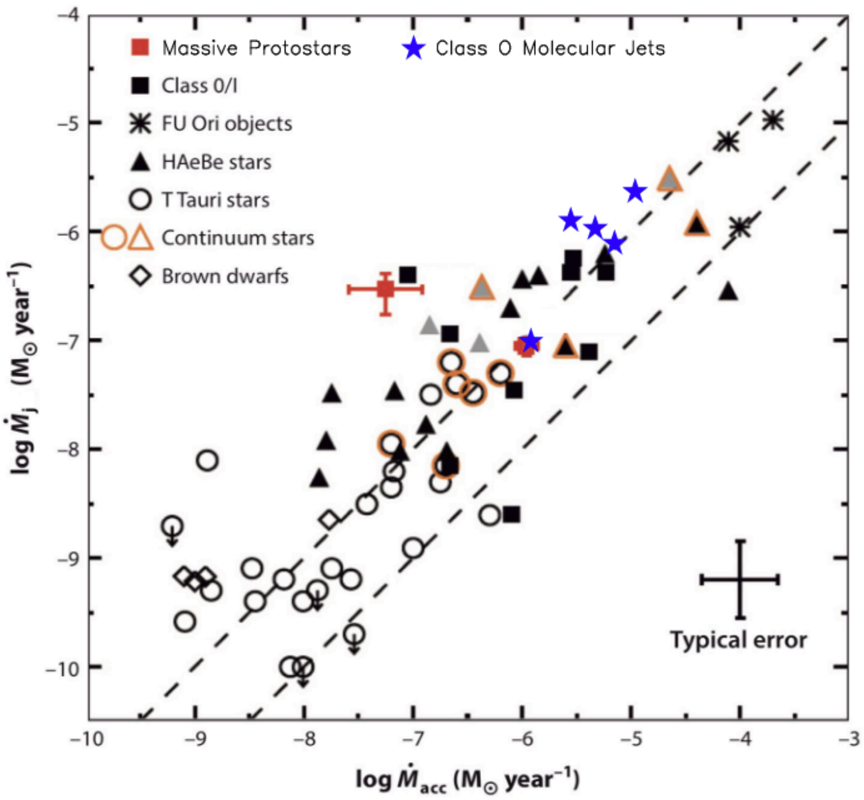

Figure 1.7: Observed mass-loss rate in the jets $\dot{M}_{jet}$ versus accretion rate $\dot{M}_{acc}$ of the class 0 sources (blue stars) compared with those in different classes of YSOs associated with jets and outflows presented in Ellerbroek et al. (2013). The dashed lines indicate $\dot{M}_{jet}/\dot{M}_{acc}$=0.01 and 0.1. Image taken from Lee (2020).

the flux deposited in the close environment of the protostars by the underlying driving winds/jets, and therefore to assess their dynamical properties. For instance, in the case of jet driven outflows, the combined momentum flux of all components (high-velocity jet and lower-velocity) is expected to be conserved along the flow. Bontemps et al. (1996) have studied the CO J=2–1 emission of a sample of 45 low-mass protostars ($M_{star} \simeq 0.01$–$3\,M_\odot$ and $L_{star} \simeq 0.3$–$30\,L_\odot$). They inferred that the outflow momentum flux (strength) of CO outflows F_{CO}, is very well correlated with the mass of the protostellar envelope, independently of the evolutionary stage of the driving source. They also showed that F_{CO} decreases from Class 0 to Class I. They interpreted this momentum flux decrease as the consequence of the decay of the mass accretion rate or infall with time, from $\sim 10^{-5}\,M_\odot$ yr^{-1} at the beginning of class 0 to $\sim 10^{-7}\,M_\odot$ yr^{-1} for protostars at the end of class I or class II.

We previously discussed that massive star formation are less constrained than the low-mass regime partly because of the difficulty to observe these regions, since they are complex structures composed of molecular gas and stars in the making, generally located at more than 1 kpc from the Sun, and largely embedded within high-density clouds (Motte et al., 2018). The same naturally applies to outflows from massive protostars, thus the observational results observed previously are regarding low- and intermediate-mass stars. In the review of Beuther & Shepherd (2005), the authors summarized the characteristics of 15 streams from massive protostars, observed at high angular resolution with interferometers. They found that both collimated jets and of wide-open cavities were present, which led them to propose a scenario in which the jet component disappears in favor of the outflow component with the evolution of the protostar. Massive outflows would therefore form in a similar way to solar-like ones, a mechanism already proposed by McKee & Tan (2003) in which massive stars and solar-type stars form with similar mechanisms. Furthermore, recently Nony et al. (2020) in their study of a cluster of 46 outflow lobes driven by 27 protostars with masses of 1–100 $M_{\odot}$ in the star forming region W43-MM1 at 5.5 kpc, have reported clear events of episodic ejection. Moreover, as noted by the authors, outflows observed at increasing angular resolution turn out to present several spatial (thus temporal) characteristic scales, and that's the topic we will cover in the next section: time variability in outflows.

1.3.2 Time variability in jets

We have described so far processes taking place in long time scales from 10^4 to 10^5 years that are associated to the protostellar evolution from class 0 to class II where a decrease of the accretion rate and opening of the outflow angle are observed.

The mass-ejection process turns out to be a non-steady process and there is wide observational evidence of time-variability in the ejection process in sources at all stages of protostellar evolution, from Class 0 to Class II and FU Orionis. Among the Class 0/I protostellar jets observed with millimeter interferometers, HH111, HH212, IRAS 04166+2706, and L1157 (Lefloch et al., 2007; Codella et al., 2007, 2014; Tafalla et al., 2010; Plunkett et al., 2015; Podio et al., 2016), provide nice examples of such variable outflow/jets in the early protostellar phase, with typical timescales of hundred to a few hundred years. Similar indications of mass-ejection variability are also reported in high-mass star-forming regions. A nice, recent example is provided by the signatures of episodic accretion detected by Nony et al. (2020) in his survey of 46 outflows in the W43-MM1 high-mass protocluster, who estimated a typical timescale of 500 yr for the phenomenon.

In order to study the kinematics of molecular outflows and jets, it is common to produce Position-Velocity (PV) diagrams along (across) the axis of propagation. These PVs consist of a succession of spectra in the propagation direction. The interpretation of these diagrams might be complex depending on the source, but their general patterns can be used to constrain the ejection mechanisms that give birth to the outflow. In the lower panels of Figure 1.8, one of the simplest cases is shown, where the gas velocity is seen to increase with distance from the source in a linear profile, a behaviour known as Hubble-law (Arce & Goodman, 2001b). On the other hand, in some sources only the high speed part of the Hubble-laws is visible, this draws a sawtooth profile in the PV diagram, it was called Hubble-wedges by Arce & Goodman (2001b). The vertices of this kind of profiles on the PVs correspond to the knots detected in the molecular (CO) emission maps (Plunkett et al., 2015). To explain these knots, the ejection must necessarily show velocity variability over time. This variability is mainly relative to two parameters: the quantity of gas ejected and the speed of the ejecta (Frank et al., 2014). An ejection episode can then be defined as an increase in one or both parameters compared to a steady state. Hubble-wedge profiles are best reproduced by bow-shock models (Lee et al., 2000). A bow-shock occurs in areas with a strong velocity gradient, it can be a terminal shock, where the jet propagating at high speed meets the interstellar medium, or internal shocks when a fraction of fast gas catches

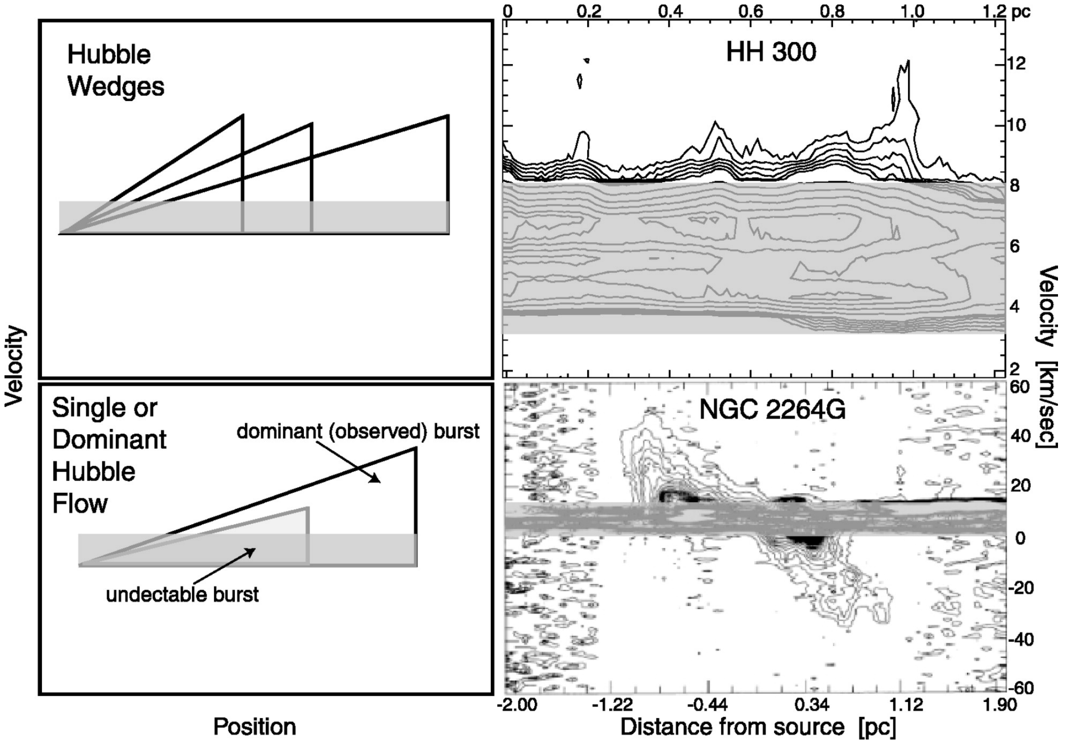

Figure 1.8: (Top left): Schematic picture of the Position-Velocity diagram of an episodic outflow. (Top right): Example of an episodic outflow HH 300 (Arce & Goodman, 2001a). (Bottom left): Schematic picture of the position-velocity diagram of an outflow with only one burst or with one dominant burst. (Bottom right): Example of a molecular outflow (NGC 2264G) with a single Hubble-law velocity distribution (Lada & Fich, 1996). The grey area represents the ambient cloud velocities, in which outflow emission cannot be detected since it is indistinguishable from the ambient cloud emission.

up with a fraction of slower gas. At the location of a bow-shock, the shocked gas is pushed aside and forms an parabolic shape (bow) (Raga & Cabrit, 1993).

Apart from the velocity or rate of ejections variations, there are also changes in the direction of velocities often seen as wiggling in the jets. The type of wiggling can be distinguish when both lobes of the jet are observed, in this case, wiggling jets are mainly detected with two shapes: "S" with central symmetry and "W" with mirror symmetry. These shapes are often caused due to the interaction with a binary companion or orbital motion (Terquem et al., 1999; Masciadri & Raga, 2002; Frank et al., 2014). We discuss more in detail the aspects and features of these shapes in Chapter 5.

Understanding the variability of the accretion and ejection processes is necessary in order to explain the whole structure of jets and outflows. Due to the direct link between accretion and ejection (Figure 1.7), the variability measured on the knots is an indirect way to measure that of the accretion. A more direct way is to follow the evolution of the luminosity of protostars, an approach which proved its efficiency in the case of FU Orionis stars (pre-main sequence stars), which undergo optical luminosity bursts of several magnitudes over periods ranging from one year to several decades (Audard et al., 2014). The models proposed to explain these accretion bursts fall into two categories: in the first class of models, accretion bursts are triggered by instabilities internal to the protoplanetary disk, that are activated, for instance, by a planet; in the second class, the burst are caused by disturbances external to the disk, typically a binary companion or the envelope. These external disturbances also cause a change in the jet orientation.

1.3.3 Mechanisms of formation: a paradigm

Protostellar ejections, which can propagate over several parsecs, come from the innermost parts of the protostellar core, on the scale of the astronomical unit. The exact origin of the jet is still a debated subject (see Arce et al., 2007; Frank et al., 2014), but most of the proposed ejection and acceleration processes rely on the combined effects of centrifugal force and magnetic field on matter accreted towards the protostar. Several outflow models have been proposed to explain how molecular outflows from protostars are formed. Currently, outflow models can be separated into four broad classes (see Figure 1.9 and Arce et al., 2007; Frank et al., 2014; Lee, 2020):

- *Wind-driven shell.* In this model, a wide-angle radial wind blows into the stratified surrounding ambient material, forming a thin swept-up shell that can be identified as the outflow shell (Shu et al., 1991; Li & Shu, 1996; Matzner & McKee, 1999). In these models, the ambient material is often assumed to be toroidal with density $\rho_a = \rho_{ao} \sin^2(\theta)/r^2$, while the wind is intrinsically stratified with density $\rho_w = \rho_{wo}/(r^2 \sin^2 \theta)$, where ρ_{ao} is the ambient density at the equator and ρ_{wo} is the wind density at the pole (Lee et al., 2001). Wind-driven models are attractive as they particularly explains more evolved outflows with low collimation.

- *Jet-driven bow shock.* In this model, a highly collimated jet propagates into the surrounding ambient material, producing a thin outflow shell around the jet (Raga & Cabrit, 1993). As the jet impacts the ambient material, a pair of shocks, a jet shock and a bow shock, are formed at the head of the jet. High pressure gas between the shocks is ejected sideways out of the jet beam, which then interacts with unperturbed ambient gas through a broader bow shock surface, producing an outflow shell surrounding the jet. An episodic variation in the mass-loss rate produces a chain of knotty shocks and bow shocks along the jet axis within the outflow shell. The physical origin of the jet is unclear and could even be considered as an extreme case of a highly collimated wide-angle wind without a tenuous wide-angle component.

- *Jet-driven turbulent flows.* In the jet-driven turbulent model, Kelvin-Helmholtz instabilities along the jet/environmental boundary lead to the formation of a turbulent viscous mixing layer, through which the cloud molecular gas is entrained (Canto & Raga, 1991; Raga et al., 1993; Cantó et al., 2003). The mixing layer grows both into the environment and into the jet, and eventually the whole flow becomes turbulent. However, these models produce decreasing molecular outflow momentum and velocity with distance from the powering source, opposite to that observed in most molecular outflows.

- *Circulation flows.* In these models the molecular outflow is not entrained by an underlying wind or jet, it is rather formed by infalling matter that is deflected away from the protostar in a central torus of high MHD pressure through a quadrupolar circulation pattern around the protostar, and accelerated above escape speeds by local heating (Fiege & Henriksen, 1996). The molecular outflow may still be affected by entrainment from the wind or jet, but this would be limited to the polar regions and it would not be the dominant factor for its acceleration (Lery et al., 2002).

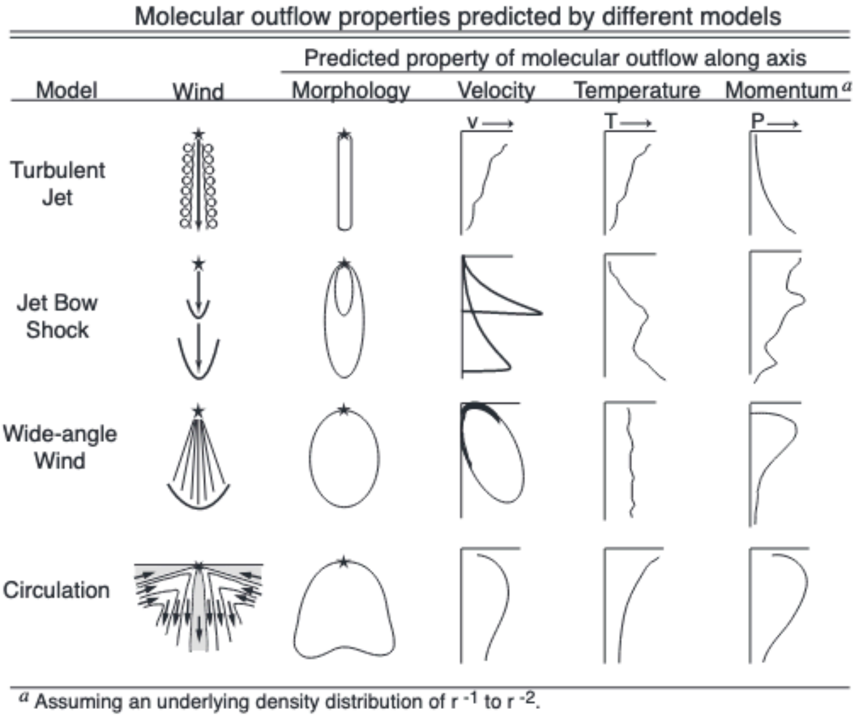

Figure 1.9: Properties of molecular flows along the axis of the jet predicted by different models (from top to bottom): interaction of the surrounding gas with the jet by turbulent movements; by jet-driven bow-shocks; interaction with a wide-angle wind coming from the disk; and finally a circulation flow. Image taken from Arce et al. (2007).

In the past decades, molecular outflows have been mapped at high angular resolutions with millimeter interferometers, allowing us to confront the outflow models in detail. Most of the numerical simulations concentrate on the Jet-driven bow-shock and the wide-angle wind models since they seem to be the most promising models so far.

Current jet-driven bow shock models can qualitatively account for the PV structure, where the outflow velocity increases rapidly toward the position of the internal and leading bow shocks, the broad range of CO velocities near H_2 shocks, and the morphological relation between the CO and H_2 emission seen in young and collimated outflows. These models are able to produce the observed outflow width for highly collimated outflows, such as L1448, HH 211, HH 212, Cep E-mm, IRAS04166+2706, among others (Bachiller, 1996; Gueth & Guilloteau, 1999; Lee et al., 2001; Santiago-García et al., 2009; Lefloch et al., 2015). However, jet-driven bow-shocks fail to account for poorly collimated outflows, as this model also have difficulty reproducing the observed outflow momenta.

On the other hand, Wide-angle winds can produce CO outflows with large widths but have trouble producing other commonly observed features. In this model, the outflow velocity also increases with the distance from the source, showing a lobe PV structure tilted with inclination that exhibits only a small velocity range at the tip. If the tip is not observed, the PV structure appears as parabolic (Li & Shu, 1996). Thus, the wind-driven model can produce widths consistent with observed molecular outflows in about 10^4 years. However, these models have problems producing discrete bow shock type features in the entrained molecular gas. Observations of sources such as L1221 and HH30 (Lee et al., 2001; Pety et al., 2006; Louvet et al., 2018) show a conical shape near the disc and seem better explained by disc winds. Finally, a single mechanism is therefore not sufficient to describe the diversity of observations, as in some cases jet-driven models reproduce better while in others disk-winds better reproduce the observations.

1.3.4 Chemistry in outflows

Bachiller et al. (2001) first led a systematic study of the chemical composition of outflow shocks in comparison with the envelope of the driving protostar. This systematic study of the outflow from low-mass protostar L1157-mm with the IRAM-30m telescope revealed a very rich and specific chemical composition of the ouflow with respect to the parental envelope, which led him to define a new class of outflows: "chemically active outflows". When the ejected material propagates into the ISM, it pushes and swept-up the surrounding material, forming molecular outflows around the jet axis. The surrounding medium is perturbed via shock waves that heat and compress the gas, triggering several processes, which do not occur in quiescent environments. These processes often trigger molecular dissociation, reactions with other compounds, disruptions of grain mantles and cores. Therefore, outflows can alter the chemical composition of the gas surrounding young stars and, depending on the outflow parameters, contribute to the local gas chemical enrichment (Bachiller et al., 2001).

The action of bipolar outflows on the surrounding gas can enhance some molecular abundances. A simple example is the case of SiO, whose abundance can be enhanced up to six orders of magnitude at the heads and along the axes of some molecular outflows (Bachiller et al., 1998; Nisini et al., 2007; Tafalla et al., 2015). The SiO enhanced abundance is due to the sputtering (gas-grain collisions) of the grain mantles and shattering (grain-grain collision) of the grain refractory cores, both releasing in the gas-phase SiO (about $\sim 5\%$) and Si, which is quickly oxidized in SiO, via reactions with OH or atomic O (Flower & Pineau des Forets, 1994; Schilke et al., 1997; Gusdorf et al., 2008a,b).

As for Complex Organic Molecules, they were largely detected in chemically active outflows. Indeed, CH_3OH and H_2CO were firstly seen to be enhanced in several outflows by a factor of 100 (Bachiller & Pérez Gutiérrez, 1997; Maret et al., 2004; Jørgensen et al., 2004). They were found tracing material at high density and high temperature, namely shocked regions. Later on, Arce et al. (2008) and Codella et al. (2009) reported the first detection associated to the B1 shock in the L1157 outflow (hereafter L1157-B1) of more complex organics like: CH_3OCHO, CH_3CN and C_2H_5OH. In the molecular survey of Lefloch et al. (2017, 2018), they have detected a large amount of organics and COMs: $HCOCH_2OH$, CH_3OCH_3, CH_3OCHO, CH_3CHO, C_2H_5OH, t-HCOOH, H_2CCO, among others.

Besides L1157-B1, there are a few detections of COMs reported in other low-mass protostellar outflows. So far, COMs other than methanol have been detected toward a handful of sources with single-dish facilities: formamide (NH_2CHO) toward L1157-B2 (Mendoza et al., 2014), acetaldehyde (CH_3CHO) toward IRAS 2A (Holdship et al., 2019), acetaldehyde and dimethyl ether (CH_3OCH_3) in the source SMM4-W (Öberg et al., 2011). It is worth mentioning that all these detections are based on observations at relatively low angular resolution, which fail to reveal a detailed picture of the spatial distribution emission. In contrast, interferometric studies have been able to map and resolve the spatial distribution of *a few* COMs toward a few chemically rich outflows: methanol, methyl cyanide, formamide, acetaldehyde in L1157-B1 (Codella et al., 2017, 2020), methanol, acetaldehyde, formamide, and dimethyl ether towards IRAS 4A (De Simone et al., 2020), methanol in Cep E-mm (Ospina-Zamudio et al., 2018). The main limitation here is the reduced spectral bandwidth covered in these observations, in comparison with the single-dish unbiased line surveys carried out at IRAM. As a consequence, interferometric observations give access only to a very limited number of detected transitions per molecular species. This has an obvious impact on the determination and the uncertainties of the physical conditions and column density.

As a matter of fact, most of the emission from organic species (including COMs) are associated to low-velocity outflows or bow shocks, and little is detected in high-velocity jets. Several studies were carried out but mostly SiO, SO and CO were detected. Only few systematic studies carried out, mostly using single-dish observations, toward jets found unusual chemical composition: IRAS04166+2706, L1448mm and Cep E (among others), therefore quite distinct from that of most Class 0 protostellar jets (Santiago-García et al., 2009; Tafalla et al., 2010; Ospina-Zamudio et al., 2019). In L1448mm, Tafalla et al. (2010) reported for the first time the presence of CH_3OH in the high-velocity jet, but the spatial distribution remains to be observed. Recently, by observing 16 protostellar jets with Atacama Large Millimeter Array (ALMA), Tychoniec et al. (2021) mapped several molecular tracers in the high-velocity jets and found the presence of H_2CO. The lack of detection of organics and COMs in high-velocity jets/bullets is not a surprise first because they can be easily dissociated in these regions, added to the fact that they require high integration time, even where these molecules are abundant (e.g. prestellar cores, hot corinos). Therefore, more systematic and sensitive studies must be performed in order to search for (complex) organic molecules in protostellar jets.

1.4 Context and goals of the thesis

1.4.1 Chemical inheritage

The Solar System started from a cold ($\sim 10\,\mathrm{K}$) and dense ($\sim 10^4\ \mathrm{cm}^{-3}$) molecular cloud clump, called the Proto-Solar Nebula, and ended up becoming the planetary system that we know, with the Earth as its habitable planet. Indeed, planets are a very common product of the star formation process and there are an incredible variety of planetary systems in the Galaxy. What makes such diversity is quite certainly the history of the system formation. Therefore, in order to comprehend our own origins, we need to understand what happened during the earliest phases of the formation of the Solar System.

One of the key elements of the chemical inheritage is the origin of the abundant deuterated water HDO present on Earth: given the distance of Earth to Solar, it implies that the corresponding HDO was brought from the outer regions of the Solar system. The presence of extremely rich organics in meteorites, with highly deuterated isotopologues also indicates that a rich chemistry took place in the outer regions of the Solar system. Such deuteration levels require very low temperature to take place. The occurrence of super-deuteration in the pre stellar phase, still in the Class 0 and Class I phase, naturally rise the question of a possible chemical inheritage of deuteration of the Solar System. The same question arises for phosphorus which plays a key role in biogenic processes on Earth and whose presence was detected in comet 67P/Churyumov-Gerasimenko (Altwegg et al., 2016). Its chemistry and its main carriers (only PO and PN until now) are now being investigated in early star forming regions (see Lefloch et al., 2016; Bergner et al., 2022).

In this direction, we have the final products of the formation process of the Solar System, i.e. the Earth, other planets, small bodies and the "leftovers" of the process, namely comets, asteroids and Interplanetary Dust Particles (IDPs). Traces of the earliest phases of the Solar System formation are hidden in the chemical composition of some material of its most primitive objects: comets, the unaltered meteorites class of "carbonaceous chondrites" and the IDPs. On the other hand, we have the possibility to study the earliest phases of the formation of Solar-like planetary systems via observations and physical-chemical models and simulations of their earliest stages: prestellar cores, protostars and protoplanetary disks, the three major first steps in the Solar-like star formation process. Each step is characterised by a specific chemical composition, which depends on the physical status and previous history of the object. These objects provide us with a key to unveil the message hidden in the objects of the early Solar System. Therefore, studies on the early stages of protostellar systems could allow us to draw a comprehensive, evolutionary chemical and physical inventory of these objects and compare their properties with the conditions of our present Solar system and its origin, such as we understand it from its exploration.

To conclude, the ultimate scientific goal of the project my Ph.D. is part of, is to use the chemical composition of present Solar-like planetary-forming systems to unveil the history of our own Solar System.

1.4.2 ACO project

My thesis is part of the AstroChemical Origins (ACO) network, which is a project funded by the Marie Curie program from the European Comission under the grant agreement number 811312. The project counts with 17 Ph.D. students spread in five countries around Europe. It started in May 2019 and will officially finish in May 2023. Within the framework of the thesis, I had to attend to four different ACO schools, accounting for more than 2 months of lectures on astrophysics and chemistry. As far as I am concerned, I had to dedicate part of my time to produce and manage the outreach content, that would be displayed in the ACO facebook page. Three network meetings of one week duration each were organized in the time of the ACO project. Besides, I spent one week of virtual short-visits to Nature Astronomy in order to work under the supervision of the journal editors. All these duties were carried out as part of my involvement in ACO, in addition to all the research activities done and reported in the thesis manuscript.

On the scientific side, the basic idea of ACO is to observe the chemical proxies linked to the Solar System primitive objects towards pre-stellar cores, protostars and protoplanetary disks and interpret them via astrochemical models. The project has the following four specific objectives:

1. To improve the detection capabilities of radio/millimetre receivers, in order to observe weak sources and low abundance molecules;

2. To build up a large and homogeneous database of astronomical spectral observations, in order to derive the chemical composition of forming Solar-like systems as a function of evolution and environment;

3. To understand the chemical processes in the exotic interstellar conditions via *ad hoc* quantum chemistry computations and laboratory experiments, in order to establish a reliable network of reactions occurring in Solar-like forming systems;

4. To develop sophisticated astrochemical models and tools, using modern techniques in order to predict the chemical composition of forming Solar-like planetary systems and compare it with observations, to finally build up a new model for the Proto Solar Nebula.

My project is part of building a large database of astronomical observations. More specifically, providing information regarding the molecules and physical processes taking place during the early stages of star formation. I describe below the specific goals of my thesis.

1.4.3 Specific goals of this thesis

As we have seen earlier in this Introduction (Section 1.3), the earliest stages of star formation are accompanied by powerful mass ejections in the form of hypersonic jets and bipolar outflows, which interact with the parental envelope through shocks. Thereby, these shocks inject mass and energy, modifying the properties of the protostellar material which feeds the nascent star. There is mounting evidence that they strongly alter the molecular complexity of the protostellar gas (Bachiller et al., 2001), while they can serve to probe the chemical composition of the molecular gas and dust during the pre-stellar phase, as evidenced by the many studies of L1157-B1 with ASAI and SOLIS (see e.g., Codella et al., 2017; Mendoza et al., 2018; Lefloch et al., 2021, among others). However, although L1157 has been extensively studied, more templates are needed to understand whether this source is indeed unique or simply more systematic studies toward other sources are required.

The kinematics of high-velocity outflow/jets and their interaction with the protostellar envelope is still not well understood and part of the problem lies in the lack of high enough angular resolution observations and a tight coupling with the numerical simulations, which could allow to interpret the observational signatures in terms of constraints on the processes occurring and feeding the protostar and its disk. The chemical composition and molecular richness of jets and outflows are yet to be explored and this is the first objective of this thesis: to obtain a detailed and as complete as possible inventory of the physico-chemical properties of an isolated protostar and map its molecular emission, to investigate the interaction between the high-velocity bullets present in the jet and its surroundings. Our choice fell on Cep E-mm, an object which appears to be valuable for understanding the formation and chemical properties of objects of intermediate mass (Chapter 2).

The main major questions I tried to tackle during my thesis is: How is organized the Cep E-mm jet structure? What are the gas dynamics? How are the molecules spatially distributed in the jet? Considering the richness in outflows, I wanted to understand whether the richness found in chemically rich outflows is indeed produced through gas phase or gas-grain reactions in the outflowing gas or the chemistry is simply carried away from the protostellar envelope, preserving the initial chemical composition. My motivation could be resumed by the question "are chemically rich outflows an illusion?"

The structure of the present manuscript is organized as follows. In Chapter 2, we present the past works done for the isolated intermediate-mass protostellar region of Cep E-mm and its outflow. The main concepts regarding interferometry and radiative transfer are discussed in Chapter 3. In Chapter 4, we present the interferometric data obtained with NOEMA used throughout this thesis and the different projects where the data initially belong to. The kinematic analysis performed towards the Cep E jet, with our highest angular resolution data, is presented in Chapter 5. In Chapter 6, it is shown the systematic search for molecules in the jet of Cep E and the spatial distribution of the detected species. In collaboration with Pedro Ruben Rivera-Ortiz, an expert in (chemo)-hydrodynamical simulations in our team at IPAG, we have modelled the different components of the outflow and the jet in order to explain the peculiar kinematical results of the CO gas. This study is presented in Chapter 7. The Cep E studies constitute the main part and the heart of my activity during my Ph.D. However, in addition (and in parallel) to the analysis and modelling of the Cep E ouflow/jet system, I also participated to other studies led in the group at IPAG: a) a model of the sulfur chemistry in the hot corino of Cep E-mm, in close collaboration with Ross O'Donoghue as part of my secondment in the ACO network; b) the behaviour of the HCN and HNC isotopologues in the shock region L1157-B1. These two molecular species (and isomers) are well known to play an important role in molecular cloud chemistry and the formation of complex molecules. This was the motivation to investigate the variations of abundance of both species and their rare isotopologues across the shock. The results of this study are presented in Appendix B.

Finally, the main results and perspectives of this present thesis are discussed in Chapter 8.

Chapter 2

The Cepheus E molecular cloud

2.1 Cepheus OB3

The Cep OB3 association is located close to the galactic plane near $108^{\circ} \leq l \leq 114^{\circ}$ and $0^{\circ} \leq b \leq 4^{\circ}$, or Equatorial coordinates (J2000): $22^h46^m00^s \leq \alpha \leq 23^h10^m00^s$. The distance to this region was first determined from photometric studies by Blaauw et al. (1959); Crawford & Barnes (1970); Sargent (1979) as being $d = 725\,\mathrm{pc}$ and recently revised to $d = (819 \pm 16)\,\mathrm{pc}$ thanks to the Gaia spacecraft (Karnath et al., 2019).

This region was first identified by Sargent (1979) in the course of the large scale CO 2-1 survey of the Cepheus region at an angular resolution of $2.5'$ with the Aerospace Corporation telescope (see Fig 2.1). As can be seen in Figure 2.1, the authors identified 6 main molecular clouds, labelled Cep A, B, C, D, E and F, all emitting at a velocity close to $V_{LSR} = -10\,\mathrm{km\,s^{-1}}$. Several detailed photometric studies toward the Cep OB3 association (Blaauw et al., 1959; Crawford & Barnes, 1970; Jordi et al., 1996) detected 42 Young Stellar Objects (YSOs), providing direct evidence for ongoing star formation in clouds. Sargent (1979) proposed that the observed Star formation was sequential - as opposed to spontaneous, - and could have been triggered by the propagation of Shock-Ionization front(s) driven by the OB stars of the association following the model proposed by Elmegreen & Lada (1977).

Among the molecular clouds mentioned, Cep A and Cep B were identified as sites of star formation. The first was early recognized as a high-mass star forming region, harbouring several compact HII regions (Beichman et al., 1979; Rodriguez et al., 1980) as well as maser's signatures in OH, H_2O and CH_3OH (Blitz & Lada, 1979; Lada et al., 1981; Cohen et al., 1984; Mehringer et al., 1997; Patel et al., 2007). Moreover, several sources in the early stages of star formation were detected in the near and far-infrared domain (Koppenaal et al., 1979; Beichman et al., 1979; Evans et al., 1981). Cepheus B is located near the HII region S155 (Felli et al., 1978; Panagia & Thum, 1981) inside Cepheus OB3, making the interface between them, a region where induced star formation could prevail (Felli et al., 1978; Panagia & Thum, 1981).

Unlike molecular clouds A, B and C (Heyer & Ladd, 1995), no indication of star formation was detected toward clouds Cep D, E and F at that time. It may then seem surprising that Cep E was the second most massive cloud in the OB3 region, with a mass of $2100\,M_{\odot}$ (Few & Cohen, 1983). Yu et al. (1996) using data at $2.7'$ from the Nagoya University Telescope of 4m at the molecular transition $C^{18}O$ $J = 1$–0 and together with Sargent

(1977) observations, estimated the size, H_2 density and temperature for Cepheus E as being $r \sim 1.5\,\mathrm{pc}$, $n(H_2) \simeq 2.1 \times 10^3\ \mathrm{cm}^{-3}$ and $T_{ex} \simeq 17\,\mathrm{K}$, respectively.

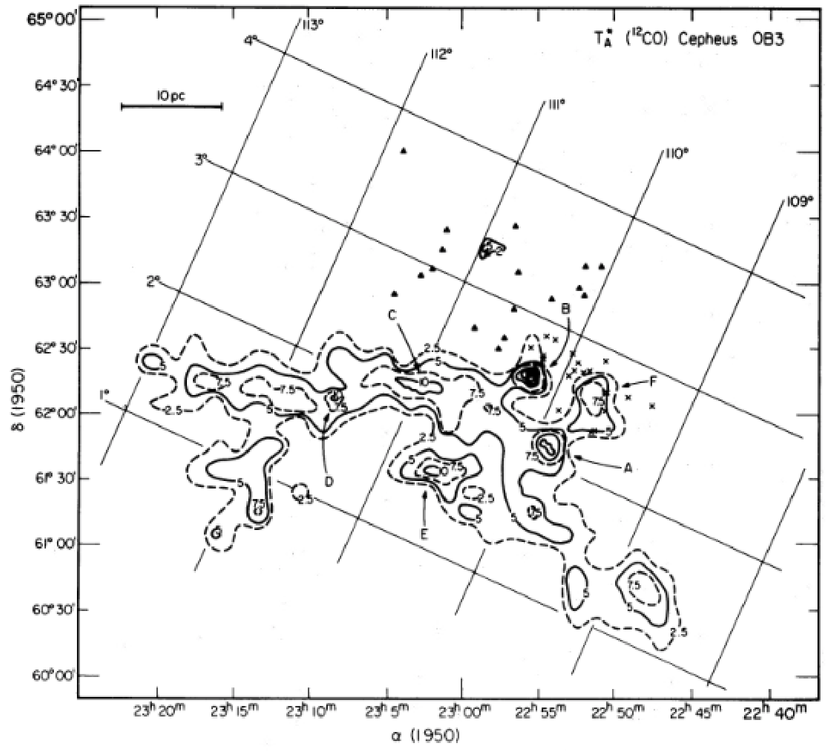

Figure 2.1: CO J=1-0 emission map of the association Cep OB3. The region in a more advanced stage (Cep OB3a) are represented with triangles while the younger regions (Cep OB3b) are the crosses. The squares on the other hand are associated to stars pre-main-sequence. Although the labeling comes from Blaauw et al. (1959), the image was taken from Sargent (1977).

2.2 Cepheus E

2.2.1 The protostellar region: Cep E-mm

With coordinates $\alpha(J2000) = 23^h03^m12.8^s$, $\delta(J2000) = +61\,^{\circ}42'26''$, the center of the Cep E cloud hosts the Infrared source IRAS 23011+6126, herein Cep E-mm. One of the first evidences of this source in this region came with the detection of H_2O maser emission at 22 GHz obtained by Wouterloot & Walmsley (1986) with the Effelsberg telescope of 100 meters. Using the fluxes obtained in the *Infrared Astronomical Satellite* (IRAS) bands (Wouterloot & Walmsley, 1986), Palla et al. (1993) have classified the region as a candidate to ultra compact HII region since it was above the threshold proposed by the authors in their classification. Eisloffel et al. (1996), on the other hand, failed to detect any emission from the source in the near-IR K-band at 2.2 μm down to a magnitude of 20.9 and concluded that the protostellar system was deeply embedded.

The first maps of the millimeter dust and molecular gas emission were obtained by Lefloch et al. (1996). Using the 19 channels bolometer installed at the IRAM-30m telescope, Lefloch et al. (1996) observed the 1.25 mm thermal dust emission of the region around IRAS 23011+6126 at an angular resolution of 11″. They detected a bright source ($S^{peak}_{1.25mm} \approx$ 460 Jy/beam) coinciding with the position of IRAS23011+6126, embedded in an envelope of 20″–40″. With a size of $\sim$ 7000 au (9″), the central source was only marginally resolved by the telescope. The authors estimated a peak of hydrogen column density N(H$_2$)= $1.8 \times 10^{23}\left(\frac{T}{20K}\right)^{-1}$cm^{-2} and a core mass of $\sim 18\,M_{\odot}$. Using the flux measurements from the IRAS satellite, they estimated a bolometric luminosity of about $100\,L_{\odot}$. This yields a ratio $\frac{L_{bol}}{10^3 \times L_{1.25mm}} \sim 7$. Therefore, an important fraction of the source luminosity comes from the the cold protostellar envelope, which Andre et al. (1993) showed a criterion to identify the early Class 0 protostar candidates. This observational study showed that Cep E-mm was a Class 0 protostar candidate of intermediate-mass, one of the first (if not the first) object at that time. As noticed by the authors, a fraction of the continuum emission was also detected along the outflow suggesting that the presence of a substantial amount of dust grains in the outflowing gas.

The continuum properties of the source were revisited a few years later by the group of Noriega-Crespo and their collaborators. Using observations from the *Infrared Space Observatory* (ISO) in the range 5–17 *mu*m and 40–200 *mu*m (Moro-Martín et al., 2001), the *James Clerk Maxwell Telescope* (JCMT) in the 850 *mu*m band (Chini et al., 2001), *Spitzer* in the range 3.5–70 *mu*m (Noriega-Crespo et al., 2004), the team built the Spectral Energy Distribution (SED) with the most sensitive and complete spectral coverage until then. It allowed them to derive the total envelope mass, which they estimated in the range 7–25 $M_{\odot}$, hence consistent with an intermediate-mass protostellar system.

Envelope Physical conditions

The systematic study of Crimier et al. (2010) was the first to determine the radial structure (temperature and density) of the Cep E-mm envelope. We recall here only the principles of their approach, bearing in mind that a detailed description of the method is given in the corresponding article.

The authors modelled the SED (Spectral Energy Distribution) of the envelope from the fluxes measured from millimeter to infrared wavelengths, by Spitzer (24 *mu*m, 70 *mu*m), IRAS (60 *mu*m, 100 *mu*m), JCMT (450 *mu*m, 850 *mu*m) and IRAM-30m (1300 *mu*m). The angular resolution of the IRAM and JCMT observations lies in the range 7.5″–14.5″, which marginally resolves the central core.

The density profile is assumed to decrease with radius following a power law of the kind $n(r)= n_0 \times (r_0/r)^{\alpha}$ where r_0 and n_0 are free parameters in the model. The envelope starts at the inner radius r$_{in}$ and extends to r$_{out}$, which are both free parameters of the model. The OH5 dust model of Ossenkopf & Henning (1994) is adopted in order to describe the opacity of dust grains coated by ice and to compute the dust temperature. The authors modelled the SED of the source using the 1D radiative transfer code DUSTY (Ivezic & Elitzur, 1997), which assumes a central source at temperature T_* (5000 K in Crimier et al., 2010) embedded in a spherically symmetric envelope of dust grains and gas. The dust and density profiles obtained for the envelope are displayed in Fig. 2.2. Based on these results, the authors estimate an envelope mass and a bolometric luminosity of $35\,M_{\odot}$ and 100 L$_{\odot}$, respectively.

The 24 μm flux was unsuccessfully reproduced by their model, which the authors interpreted possibly due to a complex internal structure in the envelope, the contribution from a hot inner component, circumstellar disk or outflow. On the one hand, as firstly discussed by Jørgensen et al. (2005), a spherical cavity in the interior of the envelope could reduce the optical depth at this wavelength and therefore be responsible for the exceeding flux detected at 24 μm. The problem is still being debated at the time of writing.

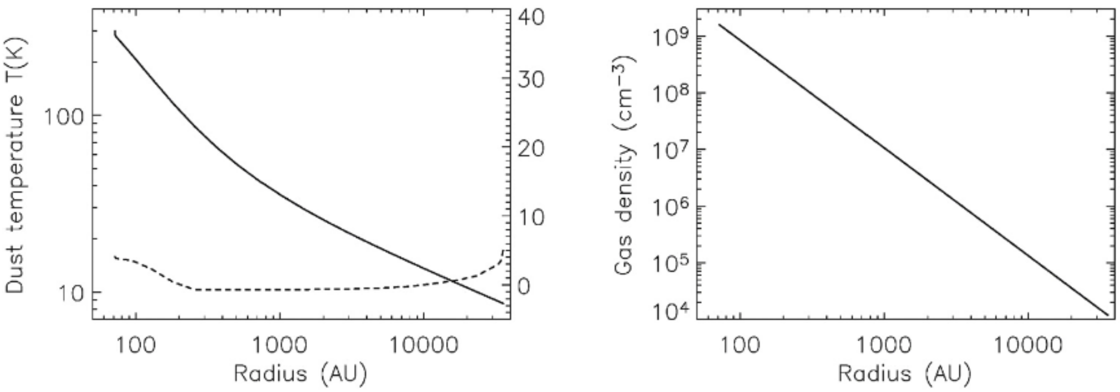

Figure 2.2: (Left panel): Dust temperature distribution as a function of radius (solid curve). The dashed line represents the difference between the dust and gas temperature derived using $X(H_2O)_{in} = 1 \times 10^{-5}$ and $X(H_2O)_{out} = 1 \times 10^{-7}$. (Right panel): H_2 density distribution as a function of radius, $n(H_2) \propto r^{-1.9}$. Image taken from Crimier et al. (2010).

The physical structure (n,T) obtained by Crimier et al. (2010) predict that within a radius of 200 au (0.24″) from the central protostar, the dust temperature is higher than 100 K, which makes possible for the ice mantles to evaporate (Ceccarelli et al., 2007) and, therefore, to release the main constituents into the gas phase. It is worth noticing that the signature of a hot corino with a rich chemical composition was indeed detected around protostar Cep E-A Ospina-Zamudio et al. (2018). Deuterated water observations with NOEMA provide an estimate of 330 au for the ice evaporation (hot corino) region (Lefloch et al. in prep). Despite the previous defaults noticed in Crimier's modelling of the SED, it is interesting to see that, in the end, the temperature structure is in reasonably good agreement with the observational constraints available from (deuterated) water.

Multiple system

The first direct indication of source multiplicity in Cep E came from the fact that two dust components were detected in the continuum at 222 GHz with the interferometric map observed at 1.4″ resolution with the *Owens Valley Radio Observatory* (OVRO) by Moro-Martín et al. (2001). Alonso-Albi et al. (2010) also raised the possibility of source multiplicity in the core that could cause small-scale deviation from spherical symmetry. The first component coincided with the infrared source but the second was shifted by 1.4″ (1000 au) southwest.

These results were confirmed by the sensitive interferometric observation of NOEMA at 1.4″ (see Figure 2.3, Ospina-Zamudio et al., 2018). Based on a 1.3 mm continuum emis-

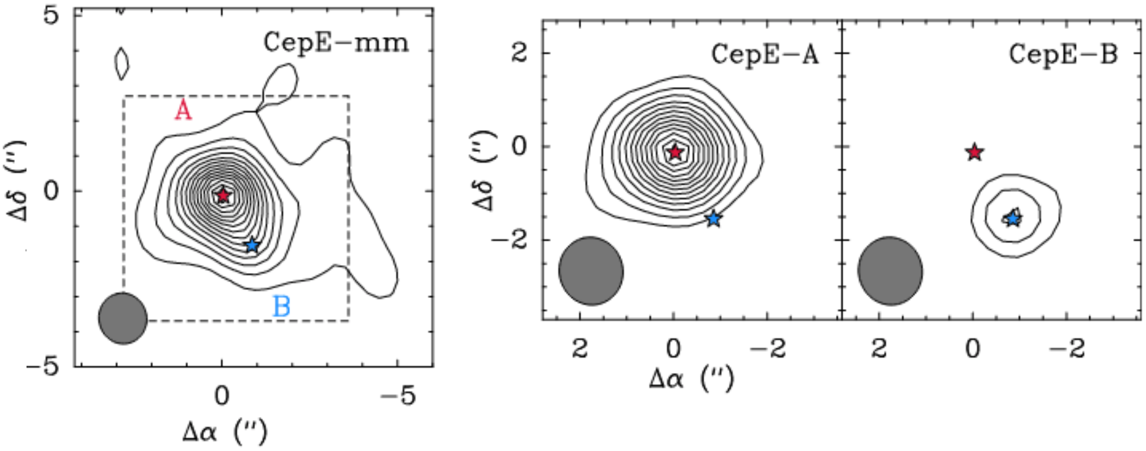

Figure 2.3: (Left): Cep E-mm 1.3 mm continuum map. First contour and steps are 3σ and 6σ respectively. The blue marks the position of Cep E-A and the red star is Cep E-B. Middle panel: continuum emission of component A; (Right) continuum emission of Cep E-B, the contours correspond to 3σ with steps of 9σ. Image adapted from Ospina-Zamudio et al. (2018).

sion map at 1.3″, Ospina-Zamudio et al. (2018) showed that the protostellar core emission actually arises from two components, referred to as Cep E-A and Cep E-B (see Figure 2.3), separated by 1.72″ ($\simeq$ 1400 au). Recently revised to 1.35″ ($\simeq$ 1100 au) with higher angular resolution data that will be presented in Chapter 3 (Lefloch et al. *in prep*). Moreover, Ospina-Zamudio et al. (2019) later showed that both components of the binary actually power a high-velocity jet, confirming the protostellar nature of each source.

Chemistry

Not much was known about the chemistry in Cep E-mm until the first study about a decade ago, using the IRAM-30m and the JCMT, by Alonso-Albi et al. (2010) who mapped the emission of the molecular tracers $C^{17}O$, $C^{18}O$, N_2H^+ and N_2D^+ at $12 - 24''$ in the cold envelope with the IRAM-30m. One main limitation of their work was the beamsize of their observations, which is larger the envelope size ($< 8''$, Lefloch et al., 1996, 2015).

More recently, the chemical content of the protostellar envelope Cep E-mm was the subject of an unbiased spectral line survey of the millimeter bands (3 mm, 2 mm, 1.3 mm, 0.8 mm) using the IRAM-30m telescope, carried out with ASAI (Lefloch et al., 2018). This survey was complemented with interferometric observations using IRAM/NOEMA at 1.4″ resolution. Ospina-Zamudio et al. (2018) carried out a full analysis of the line survey and identified a rich content in Complex Organic Molecules (COMs) and chemically related organic species. Overall, they detected rotational lines from a total of 9 Oxygen-bearing, 3 Nitrogen-bearing COMs (main isotopologues) plus a few rare isotopologues: E-/A-CH_3OH, $^{13}CH_3OH$, CH_2DOH, H_2CO, H_2CCO, t-HCOOH, $HCOOCH_3$, CH_3CHO, CH_3OCH_3, CH_3COCH_3, HNCO, NH_2CHO, CH_3CN, C_2H_5CN. This clearly points to the presence of a hot corino. Ospina-Zamudio et al. (2018) compared the molecular abundances of COMs (both O- and N-bearing) measured relatively to methylformate $HCOOCH_3$ to those measured in a sample of well-studied protostellar regions, from low to high-mass. They concluded that there was essentially no significant difference in the relative composition of low- and intermediate-mass protostars. As for high-mass protostars, it also came out that no difference was noticeable in the case of O-bearing COMs. However, the situation was somewhat different for N-bearing species. A positive gradient with source luminosity was identified in the case of C_2H_5CN.

In parallel, the cold envelope was found to display a rich content in C-chains, typical of WCCC sources (Sakai et al., 2008). Ospina-Zamudio et al. (2018) showed that the chemical composition of the cold envelope of Cep E-mm was very similar to that of L1544 (template of prestellar cores), which suggests that the protostar had preserved the inheritage of the prestellar phase, and developed a hot corino while the outer envelope displays signs of WCCC chemistry. Some marked differences were also observed in the Sulfur-composition, raising the question of possibly other chemical class of protostars.

In their study of the Cep E-A hot corino, Ospina-Zamudio et al. (2018) found no evidence of molecular signature from the binary component Cep E-B. The lack of molecular emission detected towards component B shows direct evidence for a marked chemical differentiation within the protobinary system. Similar cases of chemical differentiation have been reported in other sources such as IRAS 4A and IRAS 16293-2422 A (López-Sepulcre et al., 2017; Manigand et al., 2020). In the case of NGC 1333-IRAS 4A, the IRAS 4A1 component present a brighter continuum but no molecular emission at millimeter wavelengths, while 4A2 displays the spectral line of a hot corino. Observations of CH_3OH line emission with the VLA (*Very Large Array* from NRAO) at $1''$ resolution led De Simone et al. (2020) to prove that the lack of mm signature towards 4A1 was an observational bias. The VLA observations revealed CH_3OH emission from both sources. The authors showed that the opacity of the large amount of dust in the core was shadowing 4A1 (and 4A2 to some extent) to a level sufficient to absorb the methanol line emission from 4A1. In Cep E, the situation is quite different *a priori*, as the brightest continuum source is also the molecular rich hot corino. There is still the possibility that Cep E-B does not exhibit any line emission in the millimeter domain for dust opacity reason. This remains to be assessed by complementary observations at longer wavelengths. The conclusion of De Simone et al. (2020) is worthwile: VLA (or cm) observations are extremely useful to unveil and characterize the hot corino sources.

2.3 Outflow and jet

The low-resolution observations of Sargent (1977) and Fukui et al. (1989) showed the first evidence of a bright outflow in Cep E core. This was later on confirmed by the higher angular resolution (and higher sensitivity) observations of the molecular gas in the millimeter domain. Lefloch et al. (1996) obtained the first map of the CO millimeter line emission of the protostellar bipolar outflow, discovering the signature of a remarkably high-velocity molecular jet. Several rotational transitions from CO and SiO were detected later on (Lefloch et al., 1996; Ladd & Hodapp, 1997; Noriega-Crespo et al., 1998; Hatchell et al., 1999). Lefloch et al. (1996) could, using ^{12}CO and SiO 3-2 data, detect the presence of high velocity bullets (also reported by Hatchell et al., 1999) symmetrically located with respect to the powering source, Cep E-A.

Emission of the H_2 1-0 S(1) transition at 2.12 μ m was detected towards Cep E (Eisloffel et al., 1996; Noriega-Crespo et al., 1998, 2004). The line appears to trace the emission of specific gas layers in the low-velocity outflow and towards shocks in the Northern and Southern lobes, including the Southern terminal bowshock HH 377. One of the noteworthy characteristics of Cep E outflow is its high infrared luminosity ($3\,L_{\odot}$, see Giannini et al., 2001).

The isolation of the source limits the influence of external perturbations from the environment, such as shocks or FUV/ionizing radiation. Another advantage for the study of star formation processes is that it is one of the few sources in which the outflow proper motions have been determined and the 3-D geometry of the outflow/jet is relatively well constrained (Noriega-Crespo et al., 2014; Lefloch et al., 2015).

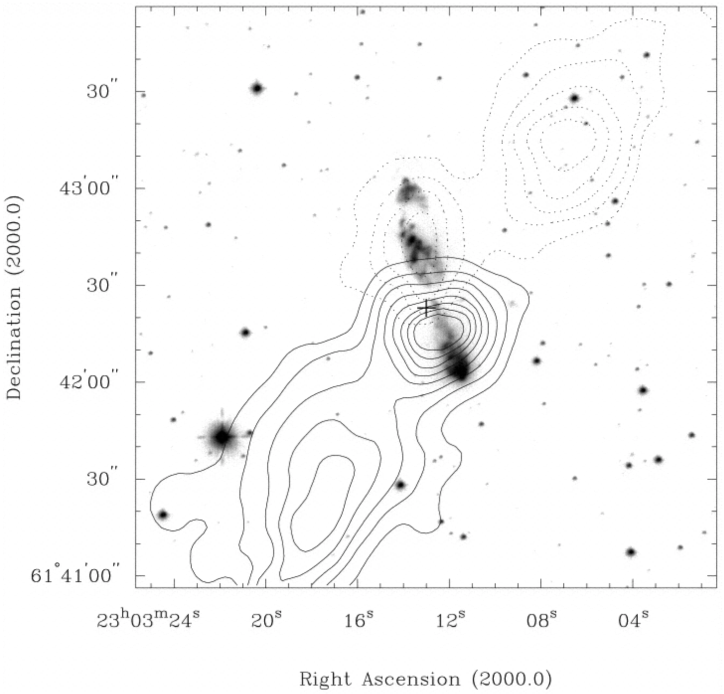

Figure 2.4: Gray scale corresponds to 2.12 μm S(1) line emission from H_2. The redshift (dotted) and blueshift (solid) contours correspond to ^{12}CO emission. The cross in the center marks the position of the 800 μm. The beamsize of the CO observation was 21″. Image taken from Ladd & Hodapp (1997).

Based on millimeter CO observations at low angular resolution (21″) with the JMCT, Ladd & Hodapp (1997) reported the emission of a second, more extended and slower outflow, propagating in a direction with a difference of position angle $\sim 52^{\circ}$ with respect to the high-velocity jet detected by Lefloch et al. (1996) (Figure 2.4). Recently, Ospina-Zamudio et al. (2019) detected the emission in the SiO J=5–4 line from a high-velocity molecular outflow powered by the binary companion Cep E-B (see Figure 2.5). Therefore, there is evidence for three outflows coming out of the protostellar region in Cep E-mm. No molecular signature of the second bipolar outflow of Ladd & Hodapp (1997) has been found in the many following studies of the region, in particular Lefloch et al. (2015). Therefore, my work was therefore naturally focused on the high-velocity outflow from Cep E-A.

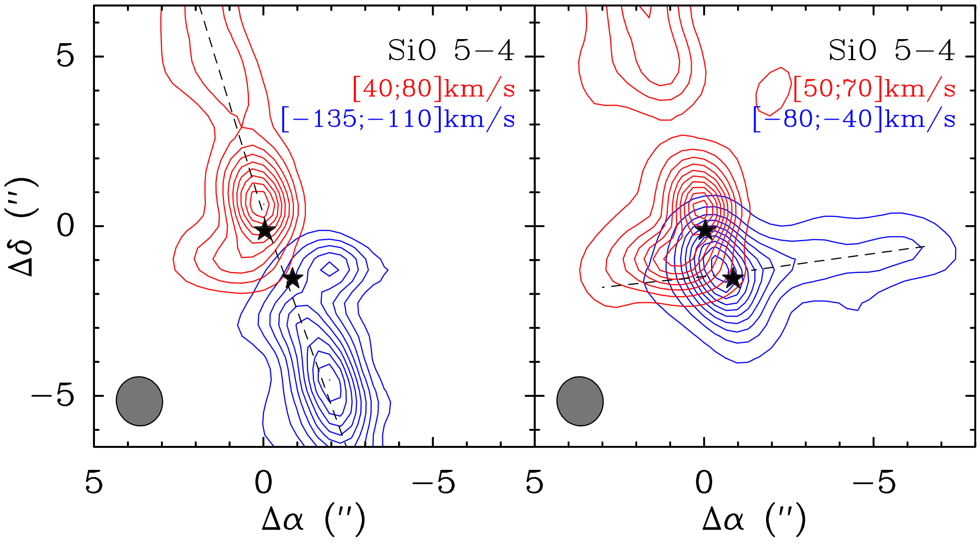

Figure 2.5: SiO J = 5–4 jet emission. (Left): the blue and red contours represent the integrated line emission between −135 and −110 km s^{-1} and between +40 and +80 km s^{-1}, respectively. Base contour and contour spacing of both jet emission are 10% of their maximum intensity. (Right): the blue and red contours represent the integrated line emission between −80 and −40 km s^{-1} and between +50 and +70 km s^{-1}, respectively. Base contour and contour spacing of both jet emissions are 5% and 10% of their maximum intensity, respectively. Image taken from Ospina-Zamudio et al. (2018).

2.3.1 Morphology

The physical conditions were well constrained mainly from CO and H_2O multi-transition studies. Firstly, Lefloch et al. (1996), using observations at 10″ with the IRAM-30m reported the presence of two outflow lobes with typical sizes of ≈ 30″ and transversal sizes of ≈ 10″, measured at half power. The peak velocities found by the authors are 80 km s^{-1} (northern lobe) and −125 km s^{-1} (southern) relative to ambient gas. Rotational transitions of H_2, CO and H_2O observed with the spatial telescope ISO (at 80″) and OVRO (at 8″) in the sub-millimeter have showed the presence of hot gas associated to the outflow (Moro-Martín et al., 2001). The angular resolution was far too low (80″) with ISO data to resolve the jet structure and, therefore, the physical conditions were averaged over the outflow cavities. The CO emission in the range J=14-27 comes from an extended gas with the temperature $T = 200 - 1000\,\mathrm{K}$ and the density $\mathrm{n(H_2)} = 4 \times (10^4 - 10^6)\ \mathrm{cm^{-3}}$.

2.3.2 Physical conditions

Concerning the physical conditions in the outflow, Lefloch et al. (2011) have reported the presence of protostellar shocks nearby the protostar at velocities involving the jet, by using IRAM-30m observations of H_2O $3_{1,3} - 2_{2,0}$ maser transition at 183.3 GHz. They have estimated the kinetic temperature and density for the shocked gas as $T_K \sim 200\,\mathrm{K}$ and $\mathrm{n(H_2)} \sim 10^6\ \mathrm{cm^{-3}}$ respectively.

Covering a large range of CO energy levels from 1 to 16, Lefloch et al. (2015) have systematically observed Cep E in both the (sub)millimeter and infrared domain, their data

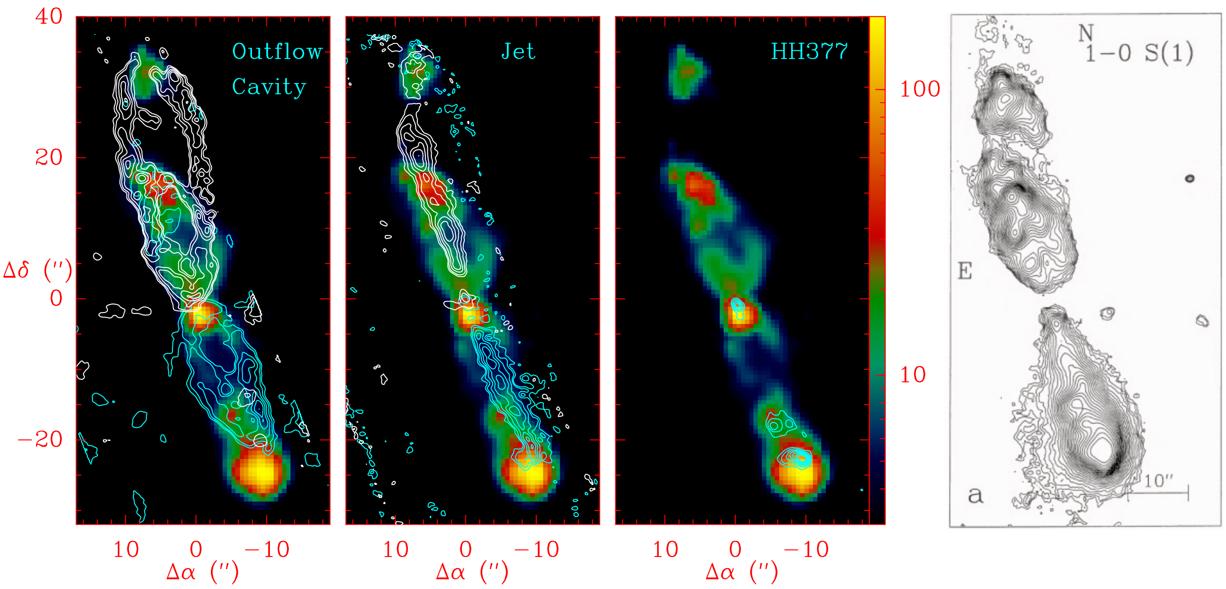

Figure 2.6: Cep E outflow emission observed in the CO J=2-1 transition at 1″ with PdBI in contours while the background corresponds to IRAC/Spitzer H_2 at 4.5 μm observations. (First panel): outflow cavity walls emission, flux was integrated in the velocity range [-15.2;8.7] km s^{-1} in the southern and [-2.2;-8.7] km s^{-1} in the northern lobe; (Second panel): High velocity jet emission, the southern corresponds to the flux integrated between [-135;-110] km s^{-1} while the northern [40;80] km s^{-1}; (Third panel): HH 377 emission, the contours correspond to the flux integrated in the velocity range of [-64;-77] km s^{-1}. (Fourth): Emission map of H_2 1-0 S(1). This figure taken from Lefloch et al. (2015) and Eisloffel et al. (1996).

were taken in the millimeter domain with observations in IRAM-30m and PdBI (see Figure 2.6) and, in the infrared with JCMT, Herschel and SOFIA (centered at the HH 377 position). With data at 1″, the highest angular resolution presented covering the whole jet so far, they have estimated a size of 1.7″ × 21″ for the jet and for the outflow cavity walls 22″ × 10″. In Figure 2.6, the outflow cavities moment 0 map is displayed by the white and light blue contours in the first panel, while the jet emission is shown in the second panel and the emission of the HH 377 is presented in the right panel. The emission velocity range of the low velocity outflow was reported as [-8;-2] km s^{-1}(North) and [-20;-14] km s^{-1}. The jet presents a velocity between [50;80] km s^{-1}(North) and [-150;100] km s^{-1}(South).

Lefloch et al. (2015) showed that in the southern lobe the jet carries enough momentum (1.7 $M_{\odot}$ km s^{-1}) to accelerate the ambient gas and drive the low-velocity outflow (2.6 $M_{\odot}$ km s^{-1}). CO knots emission were found inside the southern jet, with sizes of $2'' - 4''$ and peak velocity variations of several km s^{-1}. They proposed that these knots trace internal shocks, which would be responsible for the hot ($400 - 750$ K) gas component detected inside the jet. A colder component was also detected along the jet, with a temperature around T = $80 - 100$ K and density of n(H_2)= $(0.5 - 1.0)$ × 10^5 cm^{-3}.

Soon after, using observations of the CO lines J=1–0 to J=4–3 from the IRAM-30m and the JCMT telescopes, Ospina-Zamudio et al. (2019) constrained the physical conditions in the northern lobe of the outflow. They found that the northern high-velocity jet is somewhat warmer (T = $180 - 300$ K) and presents similar density n(H_2) = $(0.6 - 2.0) \times 10^5$ cm^{-3} gas.

The authors also observed that the low-velocity gas displays similar physical conditions in both lobes, with T $\sim$ 50 K and n(H_2) = $(1-7)\times 10^5$ cm^{-3}. The physical conditions of the outflow are summarized in Table 2.1, as obtained from Lefloch et al. (2015) and Ospina-Zamudio et al. (2019).

Table 2.1: Physical conditions determined in the northern and southern lobes for the high- and low-velocity outflow.

	Jet		Outflow	
	North	South	North	South
V ($\mathrm{km\,s^{-1}}$)	+50;+80	-150;-100	-8;-2	-20;14
Size	$2.7'' \times 21''$		$22'' \times 10''$	
T_{kin} (K)	180-300	80-100	50	50
n(H_2)(10^5 cm^{-3})	0.6-2.0	0.5-1.0	1-4	1-7
N(CO)(10^{17} cm^{-2})	2.7	0.9	1.2	1.4

2.3.3 Low-velocity Outflow: chemical composition

When analyzing the spectral line profiles detected toward Cep E with ASAI, Ospina-Zamudio et al. (2018) concluded that up to 3 velocity components could be detected, they are: a narrow velocity component ($1-3\,\mathrm{km\,s^{-1}}$; Narrow Line, NL) related to the hot corino, a broad component ($3-6\,\mathrm{km\,s^{-1}}$; Broad Line, BL) associated to the jet, and an extremely broad component ($> 7\,\mathrm{km\,s^{-1}}$; extremely Broad Line, eBL) related to the outflow cavities emission. They have in common the emission peak at a speed close (a few km/s) to the speed of the cloud $v_{LSR} = -10.9\,\mathrm{km\,s^{-1}}$. The eBL component presented a typical line width $\Delta V \geq 7\,\mathrm{km\,s^{-1}}$ and the species detected in families can be classified as:

- Hydrocarbons: C_2H, c-C_3H_2 and CH_3CCH;
- Oxygen-bearing: CO, HCO^+, H_2CO, CH_3OH, CH_3CHO and H_2CCO;
- Nitrogen-bearing: CN, HCN, HNC, HC_3N, CH_3CN and HNCO;
- Sulfur-bearing: CS, H_2S, SO, SO_2 and H_2CS.
- Silicon-bearing: SiO.

In Figure 2.7, we can see the emission of several of these aforementioned tracers. Some of them seem to be tracing the cavity (H_2CO, CH_3OH low-J and C_2H), while others (CH_3OH, HC_3N, C_2H_5CN and C_3H_2) are tracing the hot corino emission and the envelope. Following the classification proposed by Bachiller et al. (2001), Ospina-Zamudio et al. (2019) concluded that the Cep E outflow is chemically active and an important template to better constrain the impact and relation of outflows in their surroundings.

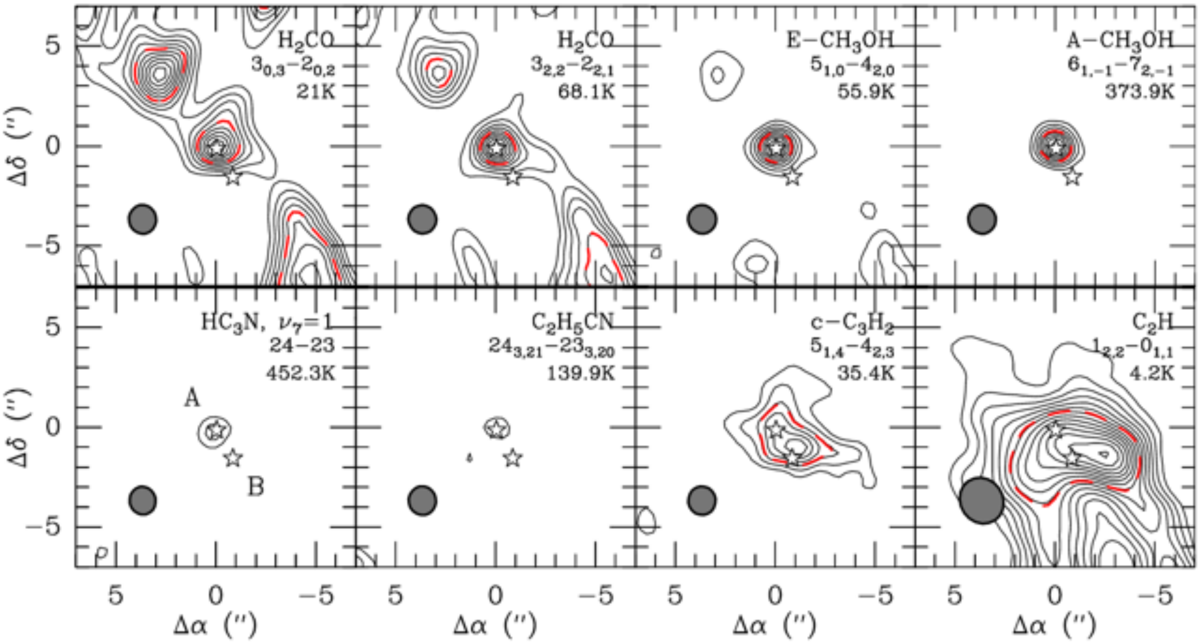

Figure 2.7: (Top): Emission map of two transitions of H_2CO and CH_3OH obtained with NOEMA towards Cep E with a spatial resolution around 1.4″. (Bottom): Emission map of HC_3N, C_2H_5CN, c-C_3H_2 and C_2H. White star marks the protostar Cep E-A and B and the HPBW is drawn by a grey circle. Image adapted from Ospina-Zamudio (2019).

2.3.4 Jet chemical composition

It was known that the Cep E molecular jet presented the emission of few molecular tracer, such as: H_2, CO, OI, H_2O and SiO (Lefloch et al., 1996; Gusdorf et al., 2017). But, the unbiased molecular survey in the millimeter domain with the IRAM-30m brough an unexpected view on the jet chemical composition with the detection of species: SO, CS, H_2CO, HCN, HCO^+. They also reported the presence of these species in the bowshock HH 377. The molecular abundances with respect to H_2 derived in the jet were of the order of 10^{-8}, and found to be similar to those determined in the low-velocity outflow gas. The detection of these species reveal an unusual chemical composition with respect to the species that are often observed in protostellar jets, such as CO, SiO and SO.

A chemical differentiation between lobes in the jet was observed. Among the aforementioned molecules, only CO, SO, SiO and HCO^+ were detected in the jet southern lobe. The authors proposed that this peculiar chemical composition could be caused by photochemistry driven by the UV field generated by shocks in the turbulent envelope as proposed by Viti et al. (2002). A difference of spectral signature between molecular species was reported by Ospina-Zamudio et al. (2019), they are shown displayed in Figure 2.8, molecules such as SiO, SO CS, H_2CO present a narrow line emission at $\sim 60\,\mathrm{km\,s^{-1}}$, while HCN and HCO^+ present a much broader emission. This suggests they are tracing different structures in the outflow/jet system, given the emission spread in a wide range of velocities, which highlights the importance of interferometric data to unveil how the molecular emission is distributed.

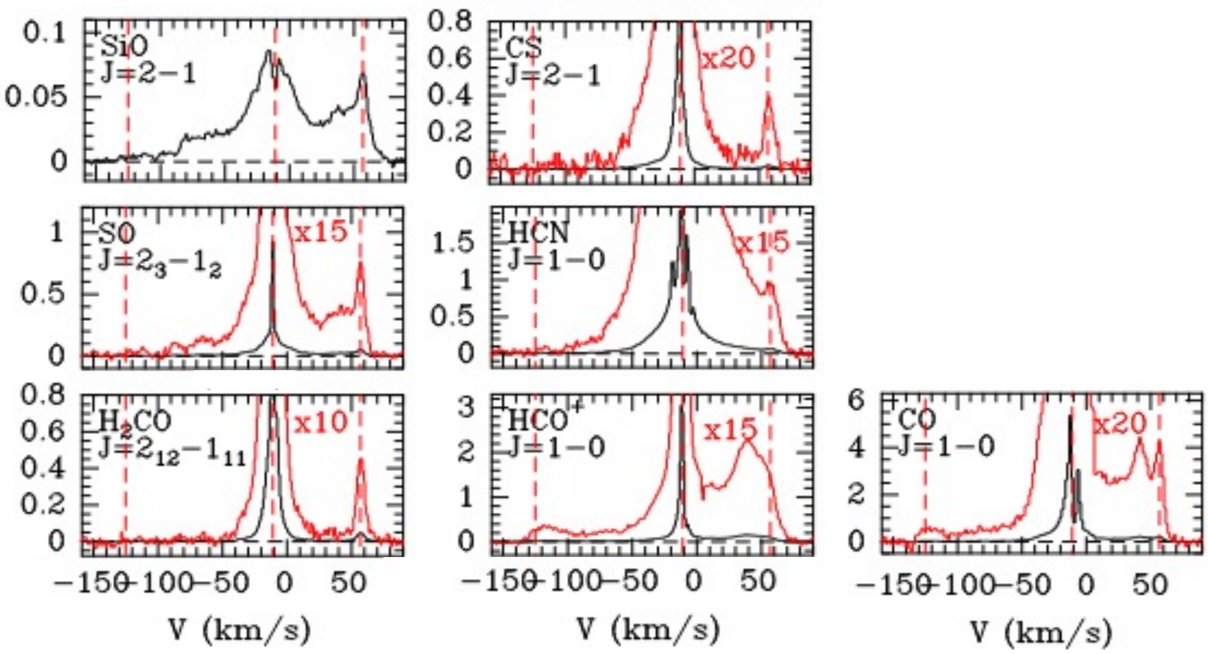

Figure 2.8: Molecular line emission detected towards the protostar. Original spectra are displayed in black. Spectra with a magnifying factor are drawn in thin red lines. Fluxes are expressed in units of antenna temperature T_A^*. The ambient cloud velocity ($v_{LSR} = -10.9\,\mathrm{km\,s^{-1}}$) and the mean jet velocity in the northern and southern lobes ($v_{LSR} = +57\,\mathrm{km\,s^{-1}}$ and $-125\,\mathrm{km\,s^{-1}}$, respectively) are marked by red, dashed lines. Image adapted from Ospina-Zamudio et al. (2019).

2.4 Conclusion

As a conclusion, Cep E is a clear-cut object to understand the formation and chemical properties of jet-driven protostellar outflows. The molecular spatial distribution remains to be characterized as well as the chemical differentiation in the outflows. The current challenges are regarding a full characterization of its kinematic properties that may shed new light on the formation, the dynamics and chemistry of outflows/jets. As being an intermediate-mass protostellar system, Cep E is in a privileged position for future comparisons with solar-type protostars as well as massive star formation.

Part II

Methodology

Chapter 3

Interferometric observations, data reduction and analysis in the millimeter domain

In this chapter, I will describe several aspects of radioastronomy, the principles of interferometry. I will also present the NOEMA interferometer, since it was the observatory where the dataset of this thesis was collected. I will finish this chapter by covering the main concepts of radiative transfer.

3.1 Atmospheric windows transmission

The Earth's atmosphere absorbs most part of the electromagnetic spectrum. Only optical, near infrared and radio wavelengths observations can be performed from the ground as shown in Figure 3.1, the other domains are often observed by making use of space telescopes (e.g. Chandra in the X-ray, Fermi in the γ-ray, etc.). Atmospheric windows delimit parts of the electromagnetic spectrum that are not absorbed by the Earth's atmosphere. There are only two windows in which the opacity is really low: the visible and the radio. Giving the framework of my thesis, I will be focusing in the radio domain throughout this discussion.

The radio band covers frequencies between $\nu \sim 15$ MHz ($\lambda \sim 20$ m) and $\nu \sim 1.5$ THz ($\lambda \sim 0.2$ mm). Radio wavelengths can be observed from the ground, but it must be avoided the observations nearby the wavelengths $\lambda \simeq 1$ m due to ionospheric effects and also larger than $\lambda \sim 2$ cm, due to atmospheric molecular lines that are dominating (in particular H_2O, O_2, O_3). The water vapour (H_2O) has an emission line at 22 GHz ($\lambda \sim 1.35$ cm) and 183 GHz (1.63 mm), molecular oxygen (O_2) has an intense band at 60 GHz (5 mm) and a line near 119 GHz (2.52 mm). Ozone (O_3) has a several lines in the mm wavelengths. Two other very abundant molecules in the atmosphere are N_2 and CO_2, but these do not have permanent dipole and therefore do not present rotational lines. Their lines are vibrational transitions and the frequencies are around $\nu \sim 300$ GHz, but to minimize the atmosphere effects in these frequencies, radio telescopes are often settled in high altitudes and dry sites with stable atmospheric conditions like the Atacama desert in Chile, for instance.

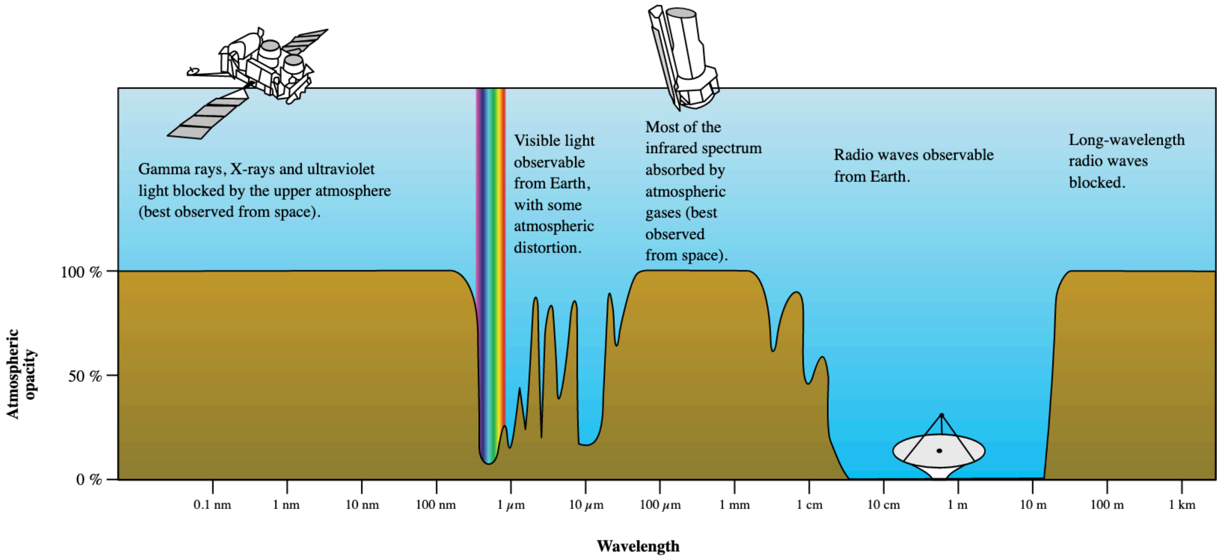

Figure 3.1: Schematic view of the atmosphere opacity of the electromagnetic radiation. Only a fraction, in the radio domain is is totally transparent. Credits: NASA.

3.2 Radioastronomy

In comparison to other disciplines like optical astronomy, *Radioastronomy* is a relatively young research field. It emerged in the early 20th century as a result of the pioneering work of K. Jansky and his colleagues from the Bell Laboratories, who were in charge of improving the quality of remote (radar) telecommunications. Radioastronomy nowadays covers the electromagnetic spectrum from far infrared to kilometer-scale wavelengths. This wavelength range allows to probe the cold and warm regions of the Universe and our Galaxy (3–100 K) as well as low-energy phenomena. It came out as a new field of investigation in the 1950s and some of its first results still remain as major discoveries in the field of Astrophysics: the 21 cm atomic hydrogen transition (Ewen & Purcell, 1951; Muller & Oort, 1951), the diffuse Cosmological Microwave Background (CMB; Penzias & Wilson, 1965), the first pulsar (Hewish et al., 1968), the fundamental rotational transition $J = 1–0$ of carbon monoxyde CO, a privileged tracer of the molecular gas in the interstellar medium (Wilson et al., 1970).

3.2.1 Single-dish telescopes

The first radiotelescopes were designed as single-dish devices to collect the sky radiation. The sensitivity of the instrument increases with the collecting area and one even built radiotelescopes with a main dish as large as several hundred meters (former Arecibo: 300m or FAST: 500m). The surface accuracy of these detectors bears direct limitation on the sensitivity of the signal which can be detected, in practice. The main dish of these telescopes is usually designed as a parabola, in order to preserve the astigmatism conditions along the optical path from the main dish to the focal plane. Among the several types of radiotelescopes designed, the Cassegrain telescope kind is commonly in use. The primary dish (a parabola, with a diameter of several tens of meters, like e.g. IRAM-30m) reflects the collected signal to a secondary mirror (a hyperbola, with a size of a few meters), which focuses and sends it to the focal plane, where the receivers to process the signal are installed.

Beam

Radio telescopes functioning as receiving antennas, the coupling between the incident radiation with the telescope has to be taken into account. The beam pattern P$_n$ is the response of the antenna as a function of direction. It can be described as the sum of the diffraction pattern of the antenna, including the main and secondary lobes, plus "error lobes" which represents the contribution induced by the diffraction/deviation of the antenna to a perfect collecting surface. The collected power can be expressed as:

$$P(\Omega) = \frac{1}{\Omega_A} \int\int P_n(\Omega - \Omega_0) B(\Omega_0) d\Omega, \tag{3.1}$$

where $B(\Omega_0)$ is the brightness distribution of the source and Ω_A is the beam solid angle defined by the equation:

$$\Omega_A = \int\int P_n(\Omega) d\Omega. \tag{3.2}$$

In practice, one aims at a telescope with the best possible directicity, i.e., the highest fraction of the energy to be collected in the main diffraction lobe. One defines the beam solid angle Ω_{MB} as:

$$\Omega_{MB} = \int\int_{\text{Main Beam}} P_n(\Omega) d\Omega. \tag{3.3}$$

The main diffraction lobe can be approximated by a Gaussian function and, as a result:

$$\Omega_{MB} \approx 1.113 \cdot \theta_{MB}^2, \tag{3.4}$$

where θ_{MB} is of the size of the beam pattern at half power. In practice, θ_{MB} defines the resolving power of the radio telescope at the frequency of the observation, i.e., the smallest angle between two objects that can be resolved by the instrument.

A diagram of radiation, presenting in two dimensions the power received as a function of the angle, is shown in Figure 3.2. As can be seen in this figure, the received power is maximum in the direction where the antenna is pointed, that it is inside the primary/main lobe, a small fraction of the total power is received in the secondary lobes of the antenna, located at larger angles and then the power decreases until it is zero. The main lobe of an antenna is characterized by two quantities: width at half power, called Half-Power Beam Width (HPBW) and; the total width between the first two minima, called Beam Width between First Null (BWFN). These quantities are angles with respect to the direction in which the antenna is pointed and they depend on the diameter of the antenna D and the wavelength λ of the observations. Therefore, in the ideal case of an uniform source, the angular resolution (θ) of an antenna is estimated as:

$$\theta \approx \text{HPBW} = 0.5 \cdot \text{BWFN} = 1.22 \cdot \frac{\lambda}{D}. \tag{3.5}$$

Currently, the biggest radio telescope observing in the millimeter domain is the Green Bank with a diameter D=100m - located in West Virgina in the USA,- and when it performs observations at 1.3 mm band - it can reach an angular resolution of $\theta \sim 2.6''$. Other larger telescopes like FAST with 500 m operates at large wavelengths in centimeter/meter domain.

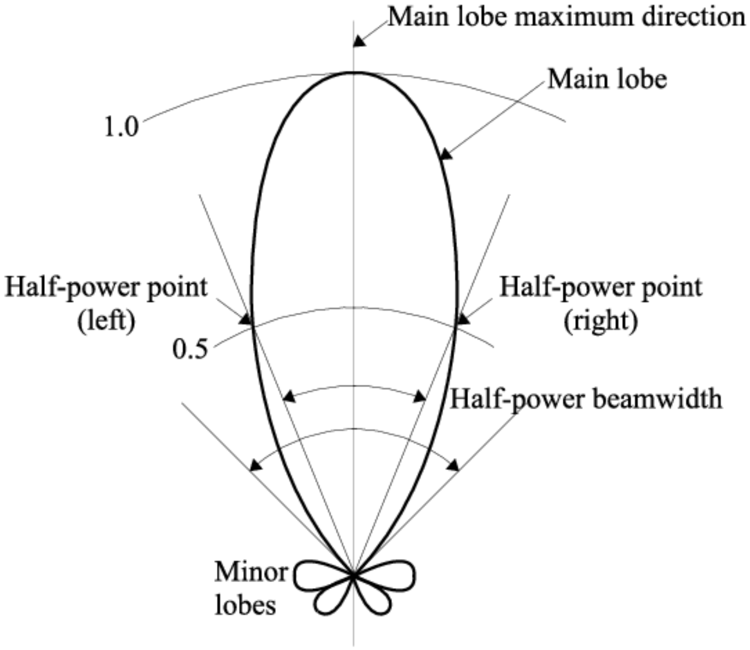

Figure 3.2: Diagram of a radiation patter of a parabolic antenna displaying the power received as function of the angle. The vertical axis corresponds to the direction in which the antenna is pointing, and the main lobe associated. The side (minor) lobes can only capture a small fraction of the radiation. Credit: Zúñiga et al. 2009.

Temperatures

The antenna temperature, T$_A$, is defined as the temperature of the black body whose flux is equal to that measured by the antenna, corrected for the atmospheric absorption, therefore, it can be written as:

$$T_A = \frac{1}{\Omega_A} \int\int \frac{\lambda^2}{2k_B} B(\Omega_0) P_n(\Omega - \Omega_0) d\Omega. \tag{3.6}$$

However, the above definition of the antenna temperature does not take into account the side lobes of the real beam pattern. What one wants is to measure what is coming from the 2π sr in front of the telescope, therefore, the corrected antenna temperature T$^*_A$ is defined:

$$T^*_A = \frac{T_A}{F_{eff}} \tag{3.7}$$

$$F_{eff} = \frac{\Omega_{2\pi}}{\Omega_A}, \tag{3.8}$$

being F_{eff} called *forward efficiency*. Another useful temperature in practice is the equivalent temperature of the source that produces the same flux as the one detected by filling the main-beam only:

$$T_{MB} = \frac{T_A}{B_{eff}} = \frac{F_{eff}}{B_{eff}} T^*_A, \tag{3.9}$$

where B_{eff} is the *beam efficiency*, defined by $B_{eff} = \Omega_{MB}/\Omega_A$.

3.3 Radio Interferometry

As previously discussed, angular resolutions are proportional to the antenna diameter, which in practice means that in order to unveil in detail the small scale structure (high angular resolution) in a given source, one needs a bigger antenna. Of course, there are several limitations in having huge antennas (e.g. wind and gravity deformation). To overcome these limitations, the astronomers had to appeal to a physical phenomena well known since the 19th century which is interferometry. The interferometry technique makes use of two or more antennas with the goal of create a virtual huge telescope in which the diameter is correspondent to the distance between two antennas. In this section, therefore, it will be described the main aspects of interferometry and long baseline interferometry.

3.3.1 General properties: Young's double slit experiment

The best way to understand the principle of an interferometer is to look at the Young experiment. In 1801, Thomas Young performed the famous optical experiment known as *the Young's slits*. This experiment was extremely important as it was the first time the wave behavior of light was seen, since at that time, it was thought that light behaves either as electromagnetic waves or particles (photons). The experiment consisted of an opaque surface with two slits separated by a distance S that was placed in the path of a monochromatic light with a wavelength λ. It was then observed the light that came out of the holes and hit an screen parallel to the surface distant by D. When a luminous source is locate at larger distances and the sizes of the slits are smaller than the wavelengths (Fraunhofer conditions), it is possible to observe a pattern created of succession of shiny and dark fringes, constructive and destructive interference, respectively. The intensity measured on the screen can then be expressed through the equation:

$$I(x) = 2I_0[1 + \cos\Phi(P)] = 2I_0[1 + \cos\left(\frac{2\pi\delta(P)}{\lambda}\right)], \tag{3.10}$$

I_0 corresponds to the intensity of the luminous source and $\Phi(P)$ the phase delay between two interfering waves measured in a point P on the screen. This delay can be expressed as a function of an optical path difference, $\delta(P)$. Through this experiment, Young managed to find a simple equation that relates the path difference and the difference y between the point P and the optical center, which is described by:

$$y = \frac{D \cdot \delta(P)}{S}. \tag{3.11}$$

The distance ΔW between two intensity extremes (fringes widths) is related to the wavelength by $\Delta W = \frac{\lambda D}{S}$. In the constructive (destructive) interference fringes, the intensities are added up (canceled). Therefore, it is possible to characterize these fringes by their visibility:

$$V = \frac{I_{max} - I_{min}}{I_{max} + I_{min}}, \tag{3.12}$$

in the simple case of Young's experiment, if the visibility is maximum, V is 1.

The Young experiment was a breakthrough on the understanding of interferometry but it is a simplified case, since it assumes a monochromatic light and a source infinitely far.

In more complex cases, the temporal (related to $\Delta\lambda$ only possible for non-monochromatic sources) and spatial (spatial extent of the emitting source) coherence have to be taken into account in order to describe the interference fringes intensities. The first application of interferometry in astronomy was to measure the diameter of Betelgeuse, a red giant evolved star located at 197 pc away (Michelson & Pease, 1921). Observations were performed in the so called Michelson interferometer which produces interference fringes by splitting a beam of light so that one beam strikes a fixed mirror and the other a movable mirror. When the reflected beams are brought back together, an interference pattern results. Michelson & Pease (1921) mounted this interferometer in the Mount Wilson telescope that had a diameter of 2.5m, they were able to measure an angular size of $0.048''$ for the red giant.

3.3.2 Principles of Interferometry

Radio interferometry consists of combining many single-dish telescopes placed apart to synthesize a large dish. Each dish receives radiation from the same object at the same time. Every pair of antennas makes a baseline and each baseline has an angular resolution $\theta \sim \lambda/d$, d being the distance between each pair. The field of view (often abbreviated to FOV) is defined as $\theta_{PB} \sim \lambda/D$, where D is the diameter of the single- dish telescopes. The simplest way to explain the functioning of an interferometer is to look at a 2 antenna system, as shown in Figure 3.3. Two antennas, 1 and 2, physically distant by a baseline ($|\vec{b}|$), both simultaneously observing a source at a given frequency ν in the $\hat{s}$ direction, and assuming the signal of the source is a plane electromagnetic wave. However, for the wave front to reach antenna 1, it needs to travel an extra path of:

$$\tau_g = \frac{< \vec{b}, \hat{s} >}{c} = \frac{|\vec{b}| \cdot \cos(\theta)}{c}, \tag{3.13}$$

where $< \vec{b}, \hat{s} >$ is the inner product of the baseline vector and the source direction vector. Antenna 2 obtains the same output as antenna 1 but the geometric delay, computed through Equation 3.13, causes the signal from both antennas to have different phases. In order to correct for the geometric delay of the wavefront, a new delay is inserted in antenna 2, called τ_0. The geometric delay of this antenna can be generated in two ways: causing the signal to travel a longer path within the electrical circuit (mechanically); or you can simply insert it through an electronic equipment into a digital system. As a consequence, the voltages received at each antenna are:

$$\begin{aligned} V_1(t) &= |V| \cdot \cos[\omega(t - \tau_g)] \qquad (3.14) \\ V_2(t) &= |V| \cdot \cos[\omega(t - \tau_0)]. \qquad (3.15) \end{aligned}$$

The output of a correlator as a function of the geometric delay R(τ_g), integrated over a time T can be expressed as Thompson et al. (1986):

$$R(\tau_g - \tau_0) = \lim_{t\to\infty} \frac{1}{2T} \int_{-T}^{T} V_1(t) V_2(t + \tau_0 - \tau_g) dt. \tag{3.16}$$

However, strictly, since the time integration cannot be infinite, the condition $T << \frac{1}{\Delta\nu}$ has to be satisfied so the average over several cycles is performed. The output of the correlator

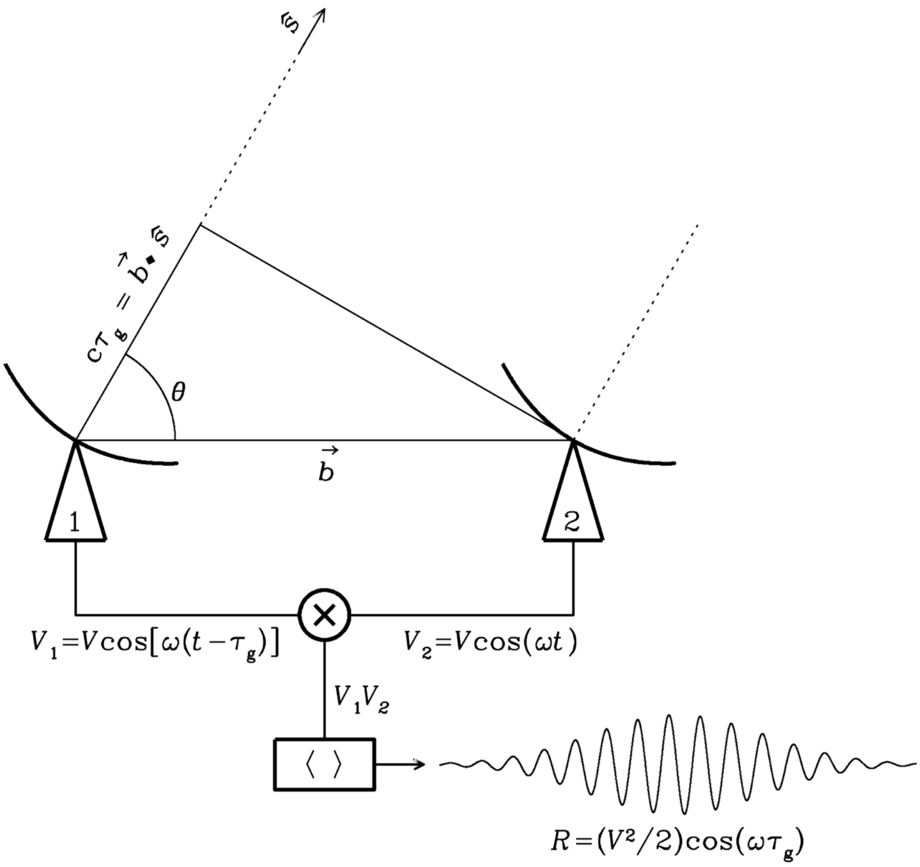

Figure 3.3: 1-D representation of an interferometer constituted by a pair of antennas (A_1,A_2) separated by a baseline $\vec{b}$. The antennas are pointed at the same source on the direction $\hat{s}$ which the signal is modelled by a plane electromagnetic wave. The geometric delay is τ_g. The voltages (V_1,V_2) obtained in each telescope are correlated to obtain a signal with output given by R. Credit: NRAO.

as a function of the frequency (ν) through the Fourier transform can be expressed as:

$$R(\nu) = \int_{-\infty}^{+\infty} R(\tau_g - \tau_0) e^{2\pi i \nu \cdot (\tau_g - \tau_0)} d(\tau_g - \tau_0). \tag{3.17}$$

Assuming that the voltages (V_1,V_2), with geometric delay corrections, are the same, we just need to multiply the equation 3.17 by $e^{-2\pi i \nu t}$ to obtain:

$$R(\nu) = V(\nu) \cdot V(-\nu) = |V(\nu)|^2, \tag{3.18}$$

with this, we can obtain the output $R(\tau)$ as the inverse Fourier transform of the output $R(\nu)$:

$$R(\tau_g - \tau_0) = \int_{-\infty}^{+\infty} R(\nu) e^{2\pi i \nu \cdot (\tau_g - \tau_0)} d\nu = \int_{-\infty}^{+\infty} |V(\nu)|^2 e^{2\pi i \nu \cdot (\tau_g - \tau_0)} d\nu. \tag{3.19}$$

The Fourier transform of the power spectrum $|V(\nu)|^2$ of the received signal corresponds to the output of the correlator, the correlator output depends on the time delay which varies because of the Earth's rotation. This results into the pattern of fringes, which is the response of the interferometer.

When observing a source with an intensity profile $I(\hat{s})$ through a section of solid angle $d\Omega$, the output of a correlator is calculated through the visibility equation with $\tau = \frac{<\vec{b},\hat{s}>}{c}$:

$$\vartheta = \int I(\hat{s}) e^{\frac{2\pi i \nu_0 <\vec{b},\hat{s}>}{c}} d\Omega. \tag{3.20}$$

The image synthesis built from the visibility data depends on the object being projected onto the plane in the sky with the coordinates: l and m, which are the coordinates of the celestial sphere, as shown in the Figure 3.4. The projection onto the plane perpendicular to $\vec{s}$ is called the u-v plane (u,v) that have units of inverse angle.

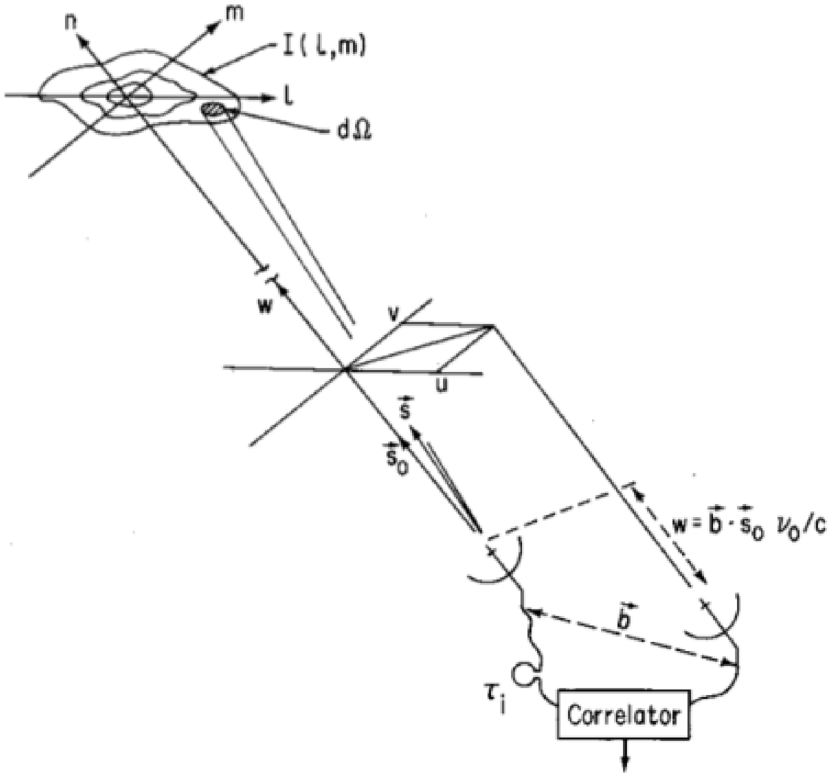

Figure 3.4: 2-D representation of an interferometer constituted by a pair of antennas separated by a base line ($\vec{b}$) that are simultaneously observing the same source. The local coordinate system in source is (l,m,n) and the perpendicular coordinate system from the Earth in the direction of the source (u,v,w). Credit: Wilson et al. (2009)

The visibility equation (Eq. 3.20) can be written as (Thompson, 1989):

$$\vartheta(u,v,w) = \int_{-\infty}^{+\infty}\int_{-\infty}^{+\infty} I(l,m) e^{-2\pi i[u\cdot l + v\cdot m + w\cdot(\sqrt{1-l^2-m^2}-1)]} \frac{dl\cdot dm}{\sqrt{1-l^2-m^2}}, \tag{3.21}$$

imposing the condition that the integral is zero when: $l^2 + m^2 \geq 1$. It is possible to display the Equation 3.21 in such a way that a Fourier transform appears in two dimensions, for this it is necessary that $\vec{b}$ and $\hat{s}$ are perpendicular, which translates as the inner product $< \vec{b}, \hat{s} >= 0$, and with that, w=0. So the visibility function becomes:

$$\vartheta(u,v) = \int_{-\infty}^{+\infty}\int_{-\infty}^{+\infty} I(l,m)e^{-2\pi i(u \cdot l + v \cdot m)}\frac{dl \cdot dm}{\sqrt{1-l^2-m^2}}. \tag{3.22}$$

Imaging consists in recovering the intensity distribution I(l,m) from the inverse Fourier transform of the visibility function $\vartheta(u,v)$. However, it is not possible to completely recover the true distributions of the sky brightness and the source, as we do not have a complete sample of the u-v plane. As a consequence, there is a fundamental limit on the level of detail in the source brightness distribution, which is defined as the resolution of the interferometer. The image resolution of an interferometer is defined by the sampling of available visibilities which, in general, is finite and discretized. On the other hand, the lack of information on angular scales not observed by the interferometer, such as the lack of coverage of spaces that are smaller than $\vec{b}_{min}$, end up resulting in a lack of sensitivity for the emission in large scale of the object. Therefore, two parameters are crucial in this phenomena, they are *resolution and sensitivity.* To summary, the angular resolution of an interferometer only depends on the longest baseline. On the other hand, the largest angular scale depends on the smallest baseline, and the incomplete sampling of the u-v plane is limiting sensitivity.

Dirty Beam and Dirty Image

The sampling of visibilities is called $S(u,v)$ and through the Fourier transform of the visibility function and the source brightness distribution, the following relation is obtained:

$$I^D(l,m) = \int_{-\infty}^{+\infty}\int_{-\infty}^{+\infty} S(u,v)\vartheta(u,v)e^{2\pi i(u \cdot l + v \cdot m)}du \cdot dv, \tag{3.23}$$

being I^D known as "Dirty image". Furthermore, the visibility is assumed to be zero where there is no coverage. To obtain the real brightness distribution through I^D, it is necessary to use the convolution theorem:

$$I^D(l,m) = I(l,m) * b(l,m). \tag{3.24}$$

The function $b(l,m)$, known as "dirty beam", is the Fourier transform of the visibility of a point source, and is calculated through the equation:

$$b(l,m) = \int\int S(u,v)e^{2\pi i(ul+vm)}dudv. \tag{3.25}$$

The real brightness distribution I(l,m) convolved with the PSF (Point Spread Function) generates the dirty map I^D, and the image synthesis, therefore, is directly related to the process of deconvolution of the dirty map. Deconvolution is always a non-linear process, and it is necessary to formulate a series of hypotheses and constraints to select plausible solutions. Some modern algorithms were developed in order to minimize limitations, the most well known is the CLEAN algorithm, developed by Högbom (1974). However, before performing the image synthesis, it is necessary to perform the so-called data calibration.

Data calibration

The data calibration is the first step in data reduction. The complex visibilities measured by an interferometer are decomposed into an amplitude A - equivalent to temperature (in K) - and a phase ϕ in degrees. Both are affected by many undesirable effects due to the atmosphere and electronic systems (e.g., detectors and correlators). Data calibration, therefore, has the aim of correcting for these effects. In order to determine the correction factors, some well known sources in the sky, called *calibrators*, must be chosen. Usually they are punctual sources with high and constant flux. The main data calibration usually done in interferometric data are summarized bellow:

- **Atmosphere calibration** The absorption lines of atmospheric components, more particularly H_2O and O_2 are often a constrain to millimeter observations. The amount of water vapor and turbulence in the atmosphere might cause attenuation and phase fluctuations. The phase and amplitude correction of the signal is done in real time from atmospheric models (e.g. model used in NOEMA, Pardo et al., 2001). Depending on the weather conditions, the data measured by an antenna should be discarded.

- **Bandpass calibration** Each receiver has an intrinsic amplitude and phase response for each frequency. This calibration corrects for amplitude and phase variations as a function of frequency for each baseline $\vec{b}$, and therefore for each pair of antennas and receivers. The correction is carried out using calibrators whose phase must be zero and the amplitude constant over time, independently of the frequency. Ideally, it is a strong source.

- **Phase and Amplitude calibration** The phase and the amplitude of the signal can be disturbed due to several phenomena over time (e.g. temporal atmosphere, electronic, pointing efficiency variation). As for the calibration of the bandwidth, the correction of the variation over time of the amplitude and the phase of the signal is carried out using calibrators which are chosen to be strong enough and as close as possible to the observed source.

- **Flux calibration** This calibration will make it possible to convert the visibilities into flux density units: the Jansky (Jy), with $1\text{Jy} = 10^{-26}$ W.m^{-2}.Hz^{-1}. Once all the calibrations have been carried out, the visibilities are entered in a table (u,v) containing the observation parameters. This table is used to reconstruct the brightness distribution of the observed source. Some with known flux density, spectral index, which are regularly monitored are used for that purpose (e.g. some quasars).

- **Self-calibration** The noise in the image can be higher than the thermal noise due to amplitude and phase errors that remain after performing the data calibrations cited above. The phase calibration performed is not always sufficient to calibrate the atmospheric phase. Self-calibration is one possible solution and consists of calibrating the instrument on the source itself if the latter is sufficiently intense: $S/N \geq 3$ for phase-only calibration and $S/N \geq 10$ for amplitude self-calibration. The resulting S/N of the image is improved. The corrections obtained after self-calibrating need to be applied to the spectral line data afterwards. This process may occur after a first clean is performed.

After the data is calibrated and the u-v table built, it is then performed the aperture synthesis to end up with a clean map, and the steps executed during this phase are described in the section bellow.

Cleaning process and algorithms

The cleaning procedure allows to reconstruct a dirty image from the visibilities and to deconvolve this image from the beam of the interferometer with the goal of getting a clean image after the process is finished. In the Section 3.3.2, it was described that the u-v plane sampling is discretized and, therefore, incomplete. To fill in the gaps in the u-v plane, extrapolations in the sampling have to be done. The most famous and common cleaning method known is the one developed by Högbom (1974). This method consists of a numerical deconvolution process applied in the image domain and the basic idea is that the true sky intensity is modeled as a delta function. The steps involved in the implementation of the algorithm are the following:

1. initially, the Fourier transform of the observed visibility function is calculated and the dirty map is produced;
2. a search for the highest intensity point/pixel on the dirty map where it is assumed that there is real emission from the source (although there may be contamination by secondary lobes);
3. at this point of highest intensity, it is subtracted the 'dirty beam' multiplied by the maximum intensity value and an attenuation factor. This step removes the contribution from part of the emission of the source in all points of the image, including the secondary lobes, generating a residual image of the first iteration;
4. the contribution to the intensities taken from the map in the previous item, as well as their respective positions, are added to a list called clean component;
5. steps 2 to 4 are repeated until the peak found on the map is compatible with the noise level of the data; and
6. finally, the clean point components are convolved with the beam that maintains the actual resolution of the data. This beam is normally a two-dimensional Gaussian elliptical function that it is fitted to the central lobe of the dirty beam. These elliptical Gaussians components are are then added to the last residual map. The image resulting is then called a clean map.

The outcome of this procedure and the steps are displayed in Figure 3.5. Högbom's algorithm is relatively slow and due to that few modifications to the original algorithm were proposed (e.g., Clark, 1980; Cotton & Schwab, 1983) in order to reduce the computational cost to clean the maps, however, they are considered unstable due to the non-linear operations solutions and, therefore, not always used. Another option to improve not just the cleaning but the velocity of the algorithm is the cleaning with masks. In this procedure, the optimization is done by telling the algorithm where the emission is located, therefore, an area around the emitting region is selected by the user, and it has to be done for all channels in the data cube.

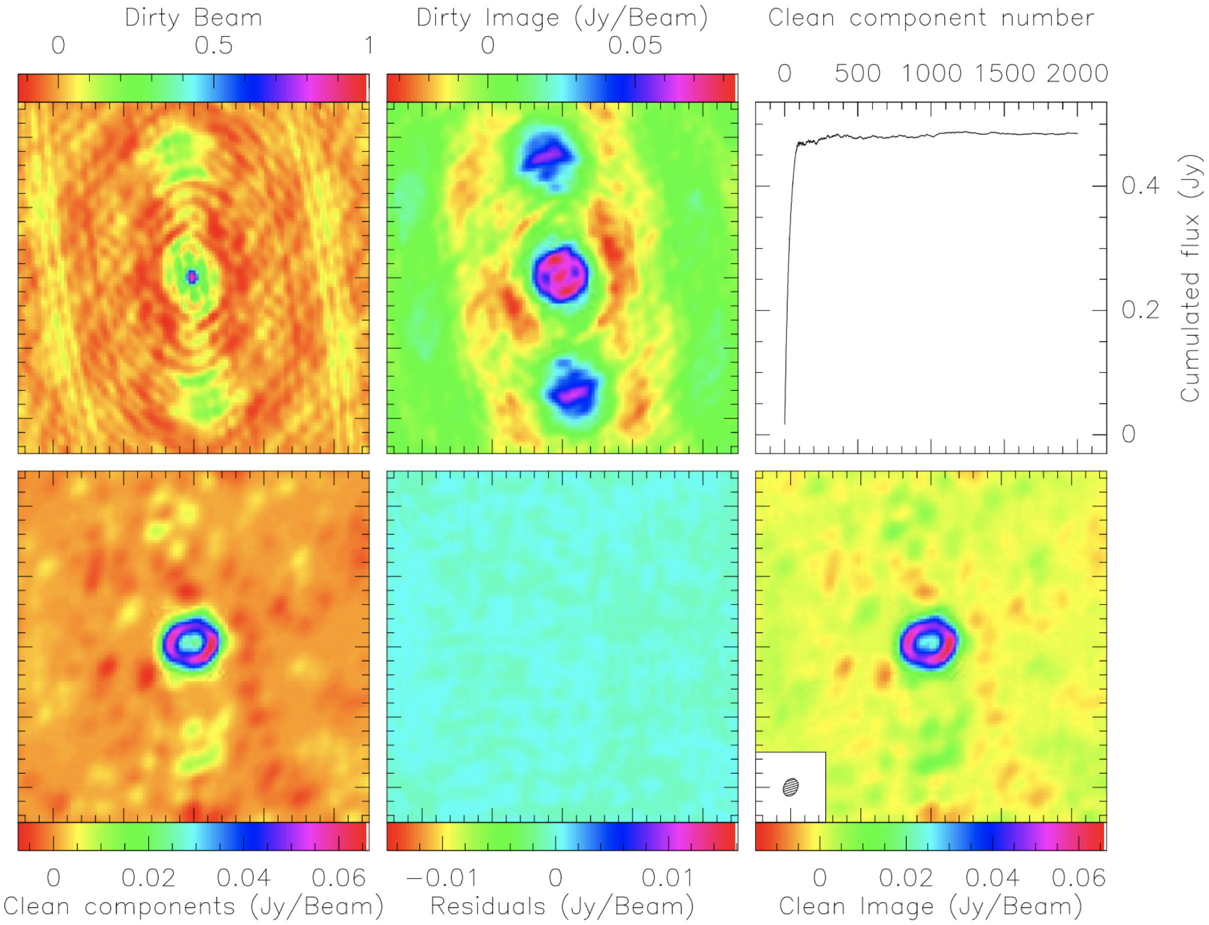

Figure 3.5: Interferometric image cleaning procedure. From left to right it is represented (top): the dirty beam, dirty image and the clean components number as a function of the cumulative flux; (bottom): map of the clean components, the residuals obtained from the cleaning and the final result which is the cleaned image. Credit: J. Pety during 10^{th} IRAM mm Interferometry School.

An important factor during the cleaning process is the weighting to be applied to the data. Since the observed visibilities are not uniformly distributed across the u-v plane but are usually concentrated towards the center, the most common weight used is known as *natural* weighting, where each visibility in a given weight $W(u,v) = 1/\sigma(u,v)$ with $\sigma(u,v)$ the noise of the visibilities (u,v). It favors the signal-to-noise (S/N) ratio to the resolution but provide a larger synthesized beam for the image. In the natural weighting, each cell is given a weight proportional to the number of visibility points in it. Another commonly used option is the *uniform* weighting that applies equal weights to each sample, decreasing the S/N as well as the beam, therefore, increasing resolution. In the latter, equal weights are given to the cell regardless of the number of measurements in each cell. A third frequently used option is the *robust* weighting, this one is considered an intermediate option (between natural and robust) and it is variant of the Clark algorithm (Clark, 1980). The Robust weighting (or Briggs method), allows a continuing variation using a robustness parameter R, between natural ($R = -2$) and uniform ($R = 2$) weights. This option makes it possible to obtain a good compromise between sensitivity and angular resolution by choosing R = 0.5. However, this is a relatively slow algorithm because the imaging step must be redone at each major cycle. During my thesis, I used only the natural weighting and the cleaning with masks in GILDAS.

3.4 NOrthern Extended Millimeter Array

The dataset used in the framework of my Ph.D. thesis was obtained in the IRAM (*Institut de Radio Astronomie Millimétrique*) interferometer, known as *NOrthern Extended Millimeter Array* (NOEMA) which is the successor of the *Plateau de Bure Interferometer* (PdBI). NOEMA is the most powerful millimeter radiotelescope of the Northern Hemisphere and one of the most advanced facilities existing today for radio astronomy, it is isolated and located in the French Alps on the *Plateau de Bure* (see Figure 3.6) at an altitude of 2560 meters.

Historically, the Plateau de Bure interferometer started with 3 antennas in 1988 and reached 6 antennas in 2001. Each antenna is a 15 m diameter Cassegrain telescope constructed largely of carbon fiber and the primary mirrors have a surface accuracy below 50 μm rms. The antenna mounts incorporate transporters for moving them between stations along the tracks. The interferometer was then re-named NOEMA after the addition of the 7th antenna in 2014. Nowadays, the array is composed of 12 antennas (last one was successfully integrated in December 2021) arranged in a "T" shape (N-S and E-W axes), with a maximum baseline of 760m. A baseline extension ($\sim$ 1700m) is expected by the end of the year 2022. Therefore, now at maximum operation, when the observations are performed with 12 antennas simultaneously, the number of baselines at NOEMA is $N = (N_a^2 - N_a)/2 = 66$.

The antennas are equipped with three receiver bands observing in dual polarization in two side-bands: upper (USB), and lower (LSB) in the 3 mm, 2 mm, and 1.3 mm in the atmospheric window. The receivers operate in 3 bands: band 1 (3 mm) covers frequencies between 71 and 119 GHz, band 2 (2 mm) from 127 and 182 GHz and; band 3 (1.3 mm) covering from 197 and 276 GHz. A forth band (0.8 mm), covering emission between 275 and 373 GHz will be available in the future. The receivers provide, in both USB and LSB simultaneously, two orthogonal linear polarization with a bandwidth of 7.744 GHz. The high-performance wide-band correlator named PolyFiX can process a total instantaneous bandwidth of $\sim$ 31 GHz for up to twelve antennas that are split into two polarization in each of the two available side-bands. The centers of the two 7.744 GHz wide side-bands are separated by 15.488 GHz. The channel spacing is 2 MHz throughout the bandwidth per polarization. Additionally, up to sixteen high-resolution chunks to obtain higher spectral resolution data (62.5 kHz) can be selected in each of the eight base-bands (i.e. up to 128 chunks in total), with a width of 64 MHz. A number of contiguous chunks defines one spectral window (SPW).

Three main configurations are available in NOEMA providing, consequently, different angular resolutions. These configurations are set and remain the same for months, given the time and cost to move the antennas. The D-configuration is the most compact allowing the interferometer to reach its maximum sensitivity and the lowest angular resolution of $4''$ at 100 GHz. The A-configuration is the most extended one and it is well suited to map compact and strong sources, providing an angular resolution of $1''$ at 100 GHz and reaching up to $0.4''$ at 230 GHz. Moreover, the C-configuration which is considered an intermediate

Figure 3.6: NOEMA antennas located in the French Alps on the wide and isolated Plateau de Bure. This image was taken from the IRAM photo Gallery (`https://www.iram-institute.org/EN/photo-gallery.php`).

array configuration and provides a complete coverage of the u-v plane with a synthesized beam of 2″ at 100 GHz. The shortest baseline possible is 24 m, to avoid shadowing and collisions between antennas. Additionally, short spacing observations, using the single-dish IRAM-30m telescope, can be done to minimize the limitation in the small baselines and improve sensitivity. Finally, these configurations might be used in different combinations in order to complement the u-v plane sampling, as well as to improve the sensitivity and the angular resolution. The HPBW of the antennas can reach up to $\sim 50''$ at 100 GHz or $\sim 20''$ at 230 GHz. Finally, A full description of the dataset obtained with NOEMA used during my thesis is given in Chapter 4.

3.5 Spectral lines and molecular analysis

Part of the work in this thesis relies on the analysis of molecular lines which are due to the emission/absorption of radiation at specific frequencies in the gas. Understanding the aspects of radiative transfer is thus important to be able to analyse the molecular lines. This section provides, therefore, some radiative transfer basics, and presents methods to compute the physical properties and chemical abundances of molecules.

3.5.1 Notions of radiative transfer

The propagation of a radiation emitting by a source with brightness I_ν at frequency ν in a certain medium of size ds (in the line of sight) is described by the equation of radiative transfer (for a very detailed formalism on radiative transfer, see Rybicki & Lightman, 1986;

Elitzur, 1992):

$$\frac{dI_\nu}{ds} = -\alpha_\nu I_\nu + j_\nu, \tag{3.26}$$

where α_ν and j_ν are the absorption and the emissivity coefficients of the medium, respectively. Another important factor to incorporate is the amount of material in the line of sight, this is usually quantified through the opacity factor $d\tau_\nu$. In a other words, the optical thickness $d\tau_\nu$ is related to the absorption coefficient of the radiation in a medium of thickness ds along the line of sight through:

$$\begin{aligned} d\tau_\nu &= -\alpha_\nu ds; \\ \tau_\nu(s) &= \int_{s_0}^{s} \alpha_\nu(s) \cdot ds \end{aligned} \tag{3.27}$$

As a consequence, a medium is considered *optically thin* if $\tau_\nu << 1$. In this case, and if the excitation conditions are known, the flux received by the observer makes it possible to compute the quantity of material that is located in the line of sight. On the other hand, if $\tau_\nu \geq 1$, the medium is considered *optically thick* and the intensity received by the observer generally gives only a lower limit of the amount of material present in the line of sight.

Taking into account the definition of opacity, it is possible to write the Equation 3.26 as:

$$\frac{dI_\nu}{d\tau_\nu} = -I_\nu + S_\nu, \tag{3.28}$$

where $S_\nu = j_\nu/\alpha_\nu$ is known as the source function. Therefore, the formal solution for the radiative transfer equation can be written as:

$$I_\nu(\tau_\nu) = I_\nu(0)e^{-\tau} + \int_0^{\tau_\nu} S_\nu(\tau_\nu^{'})e^{-(\tau_\nu - \tau_\nu^{'})}d\tau_\nu^{'}. \tag{3.29}$$

According to Rybicki & Lightman (1986), this equation can be interpreted as a sum of two terms: the initial intensity reduced by the absorption added to the integrated source diminished by absorption. For simplicity, it is assumed that the source function S_ν is constant, thus the Equation 3.29 could be written as:

$$I_\nu(\tau_\nu) = I_\nu(0)e^{-\tau_\nu} + S_\nu(1 - e^{-\tau_\nu}). \tag{3.30}$$

The processes of emission and absorption, defined by $S_\nu = j_\nu/\alpha_\nu$, are not independent in the framework of a medium in thermal equilibrium. The latter is reached when the radiation and the surrounding matter of a medium are in complete equilibrium with temperature T. Under the thermodynamic equilibrium (TE) assumption, and that the radiation is isotropic and its spectrum similar to that of a black body, which is described the Planck equation:

$$B_\nu(T) = \frac{2h\nu^3}{c^2}\frac{1}{e^{\frac{h\nu}{k_B T}} - 1} \tag{3.31}$$

where h, c and k_B are respectively the Planck constant, light speed and Boltzmann constant. However, the TE assumption only works in ideal systems. In the interstellar medium, considering that the temperature varies in different regions, it is more convenient to define a Local Thermodynamic Equilibrium (LTE). The LTE condition holds when a number of atoms collide so frequently with the colliders that the level populations are thermalized and, therefore, follow the Boltzmann distribution, which only depends on T. Therefore, a real system can be described as a collection of local regions each one characterized by a single temperature, thus under TE or LTE:

$$\begin{aligned} I_\nu &= B_\nu(T) \\ \frac{dI_\nu}{ds} &= 0, \end{aligned} \tag{3.32}$$

which by making use of the Kirchhoff law can be expressed as:

$$I_\nu = S_\nu = \frac{\alpha_\nu}{j_\nu} = B_\nu(T). \tag{3.33}$$

Inserting the relation above in Equation 3.30, it is possible to rewrite it as:

$$I_\nu(\tau_\nu) = I_\nu(0)e^{-\tau_\nu} + B_\nu(1 - e^{-\tau_\nu}), \tag{3.34}$$

which is a differential equation and to solve it, several conditions can lead to different solutions, they are:

- **Optically thick regime** ($\tau_\nu >> 1$) which leads to $I_\nu(\tau_\nu) = B_\nu(T)\tau_\nu$;
- **Optically thin regime** ($\tau_\nu << 1$) which implies to $I_\nu = I_\nu(0)(1 - \tau_\nu) + B_\nu(T)\tau_\nu$;
- **Rayleigh-Jeans approximation** ($h\nu/k_BT << 1$) thus $B_\nu(T) \approx 2k_BT\frac{\nu^2}{c^2}$. This condition in particular is valid at low temperatures (T=20-70K) and long wavelengths such as (sub)millimeter ones. Moreover, under LTE conditions, $I_\nu = 2k_B\frac{\nu^2}{c^2}T_B$, being T_B the brightness temperature.

Furthermore, it is possible to retrieve the true source brightness temperature T_B if the flux density F_ν and the source size both are known. The source total flux in a given frequency can be obtained by integrating the brightness I_ν over a solid angle $d\Omega$:

$$F_\nu = \int_\Omega I_\nu(\theta, \phi) cos\theta d\Omega. \tag{3.35}$$

Thus, replacing I_ν under LTE in the Rayleigh-Jeans approximation, a relation between flux and brightness temperature is obtained:

$$F_\nu = \frac{2k_B\nu^2}{c^2}T_B\Delta\Omega. \tag{3.36}$$

Finally, a general solution for the radiative transfer equation (Eq. 3.30), under the Rayleigh-Jeans regime, is as follows:

$$T_B = T_{bg}e^{-\tau_\nu} + T(1 - e^{-\tau_\nu}), \tag{3.37}$$

where T_B, T_{bg} and T is the brightness temperature of the source, the background temperature (usually 2.73 K) and the temperature of the object in between the source and the line of sight, respectively.

3.5.2 Molecular emission

Molecules usually found in star formation regions will not just interact with radiation but also between themselves through collision. The radiative and collisional processes in the gas will thus allow excitation or de-excitation of a given molecule. Assuming a single specie with only 2 levels of energy, with being l the lower energy level and u the upper energy level. The system can be excited or de-excited via various processes, such as collision with other species, or absorption/emission of a photon at the frequency ν_{ul}. At equilibrium, the rate of excitation of the lower level l is equal to the rate of the de-excitation of the upper level u. This is formulated by the statistical equilibrium equation:

$$n_l n_{coll} \gamma_{lu} + n_l B_{lu} J_\nu = n_u n_{coll} \gamma_{ul} + n_u A_{ul} + n_u B_{ul} J_\nu, \tag{3.38}$$

where γ_{lu} and γ_{ul} are respectively the excitation and de-excitation collisional coefficients, n_{coll} is the number density of the collisors. While n_l and n_u are the number density of the levels l and u, respectively. B_{lu}, B_{ul} and A_{ul} are the Einstein coefficients, and J_ν is the specific intensity of the radiation field at frequency. For a multilevel system, the equation above can be generalized by adding all the excitation and de-excitation transitions between the levels.

Excitation and de-excitation through radiation

Radiative transitions allow molecules to change their energy state of rotation by absorption or emission of a photon. Each transition occurs between an energetically lower level ("low") and an energetically higher level ("up") whose energy is quantized and depends on the wavelength λ of absorption or emission of the photon. The absorption of a photon of energy $h\nu_{lu}$ will excite a molecule in its ground state or in a low energy state. The probability of absorbing a photon is given by the Einstein coefficient B_{lu} given by the equation:

$$B_{lu} = B_{ul} \cdot \frac{g_u}{g_l}. \tag{3.39}$$

This coefficient is proportional to the induced emission coefficient B_{ul}. Moreover, it involves the ratio of the g_u and g_l degeneracies of the respective upper and lower states. A molecule in an excited state will always de-excite to a lower energy level and the radiative process can be generated by an external factor or spontaneously. For instance, the interaction with the radiation will allow the molecule to de-excite by stimulated emission. The probability of induced emission is given by the Einstein coefficient B_{ul}:

$$B_{ul} = \frac{A_{ul} c^3}{8\pi h \nu^3}. \tag{3.40}$$

This process of emission stimulated by interaction with a photon is considered to be the reverse of absorption.

Another possibility is that the molecule can de-excite by spontaneously emitting a photon of energy $h\nu_{ul}$. A_{ul} is the probability of spontaneous transition, and it is defined as follows:

$$A_{ul} = \frac{64\pi^4}{3hc^3} \nu_{ul}^3 S\mu^2, \tag{3.41}$$

where $\mathrm{S}\mu^2$ is the line intensity and μ the molecular dipole moment.

Excitation and de-excitation due to collision

The processes of excitation and de-excitation of molecules are generally induced by collision due to the high densities of molecular clouds in the interstellar medium, these collisions are essentially with H_2 and He. The probability of transitions $u \rightarrow l$ (or vice-versa) induced by collision is given by the coefficient γ_{ul} (or γ_{ul} for the opposite case). The collision coefficients C_{ul} (C_{lu}) depend on this probability, given by the following relation:

$$C_{ul} = n \cdot \gamma_{ul} = n < v\sigma_{ul} >, \tag{3.42}$$

with n the colliding particle density, and $< v\sigma_{ul} >$ the mean value of the collisional cross section computed through a Maxwell velocity distribution. Finally, as aforementioned, the molecular emission depends on the coupling between collisional and radiative processes, therefore, both must be taken into account.

3.5.3 Local Thermodynamic Equilibrium approach

The populations of the levels of the rotational transitions allows, with a molecular excitation model, to determine the abundance of molecular species. Considering a population at equilibrium for only radiative excitation and collisional, the ratio of the populations of the levels can be given in the case of a two-level system by:

$$\frac{n_u}{n_l} = \frac{g_u}{g_l} \frac{e^{-h\nu_{ul}/k_B T_k}}{1 + A_{ul}/C_{ul}}, \tag{3.43}$$

where g_l and g_u are the degeneracy coefficient for lower and upper levels, while A_{ul} and C_{ul} are the spontaneous and collision coefficients, respectively. T_k is the kinetic temperature of the medium, which is defined by the Maxwell distribution of the thermal velocities of the particles in the medium.

The hypothesis of a medium in local thermodynamic equilibrium is valid when the collisions between the molecule considered and the surrounding gas dominate the spontaneous radiative emission of the molecule: $C_{ul} >> A_{ul}$. In this case, the excitation temperatures of the rotational transitions of the molecule are equal to the kinetic temperature of the medium. The equation above can be, therefore, simplified and then it follows Boltzmann equilibrium law:

$$\frac{n_u}{nl} = \frac{g_u}{g_l} e^{-h\nu_{ul}/k_B T_{ex}}. \tag{3.44}$$

When the populations of the levels of the molecule follow the relation above, the transitions of the molecule are said to be thermalized.

Critical density

An important parameter is the critical density n_{cr}. This term represents for a given transition the density of the medium from which the collisional processes prevail over the radiative processes $(A_{ul} = \gamma_{ul} n_{cr})$. The degree of balance between the radiative and collisional transitions from the upper to the lower level, can be defined through the ratio:

$$\frac{n}{n_{cr}} = \frac{C_{ul}}{A_{ul}} \tag{3.45}$$

The transitions of a certain molecule is thermalized when the density of the medium - mainly H_2 - is much higher than the critical density ($n >> n_{cr}$). The smaller the spontaneous emission coefficient A_{ul}, the more the thermalization of the transitions will be favoured. This coefficient is dependent on the cube of the frequency and on the square of the dipole moment, the transitions of large energy difference just like those of the molecules of strong dipole moment will be difficult to thermalize. In some regions of stellar formation, the temperatures and densities do not allow the validation of the LTE for a given molecular tracer.

Brightness temperature and opacity

The brightness temperature T_B is defined from the brightness B_ν, thus:

$$B_\nu = B_\nu^{\text{Black Body}}(T_B) = \frac{2k_B}{\lambda^2} J_\nu(T_B), \tag{3.46}$$

$$\text{with } J_\nu(T_B) = \frac{h\nu}{k_B} \frac{1}{exp(\frac{h\nu}{k_B T}) - 1}. \tag{3.47}$$

The brightness temperature measured observationally depends on the excitation temperature T_{ex} of the studied transition, as well as on the background cosmic radiation T_{bg} and the opacity of the medium τ_ν:

$$J_\nu(T_B) = J_\nu(T_{ex})(1 - exp[-\tau_\nu]) + J_\nu(T_{bg})exp(-\tau_\nu). \tag{3.48}$$

Under the optically thin regime, the following approximation can be done: $1 - exp(-\tau_\nu) \sim \tau_\nu$. Therefore, the absorption coefficient can be rewritten as:

$$\alpha_\nu = \frac{c^2 n_l}{8\pi\nu^2} \frac{g_u}{g_l} A_{ul}\phi(\nu) \left(1 - exp\left[-\frac{h\nu}{k_B T_{ex}}\right]\right), \tag{3.49}$$

where ϕ is the profile of an emission line of a molecule. These two equations can be simplified by assuming that: first, the thermodynamic equilibrium is reached, thus the temperature of the transition is equal to the kinetic temperature T_K of the medium and; second the contribution of the cosmic microwave background can be neglected. In the dense clouds, such as Orion, it is common to neglect this contribution since $T \gg T_{bg}$ then $J_\nu(T) \gg J_\nu(T_{bg})$.

Column density and Rotational Diagram

The column density reflects the number of molecules per unit area measured along the line of sight. If enough transitions of a certain chemical specie are detected, the so-called Rotational Diagram (RD) analysis can be performed. The RD provides an estimate of the average gas kinetic temperature as well as of the column densities of the species from which the lines are emitted. However, in order to build these diagrams, two main assumptions have to be made: LTE and optically thin lines. Additionally, the background temperature T_{bg} has to be negligible. Combining Equations 3.48 and 3.49, it is possible to obtain a relation for the column density of a certain molecule:

$$\ln\left(\frac{N_u}{g_u}\right) = \ln\left[\frac{N_x}{Q(T)}\right] - \frac{E_u}{k_B T}, \tag{3.50}$$

where N_u, N_x and $Q(T)$ are the column density of the upper energy level, the total column density and partition function, respectively. N_u and $Q(T)$ are computed through:

$$Q(T) = \sum_{n=1}^{\infty} g_i e^{-E_{up}/k_B T},$$
$$N_u \approx \frac{8\pi k_B \nu^2 T_b \Delta\nu}{hc^3 A_{ul}}, \tag{3.51}$$

with g_i being the statistical weight of a level i and Q(T) is the partition function at a given temperature, that represents the statistical sum over all rotational energy levels in a given molecule. The partition function describes the distribution of energies of a single system and takes into account the rotational, vibrational, torsional and electronic energy components of a molecule: $Q = Q_{rot}Q_{vib}Q_{tor}Q_e$. When the temperature is low enough, only the first electronic level and possibly only the first vibrational level are populated, so $Q_e = 1$ and $Q_{vib} = 1$.

From Equation 3.50, it is possible to build a rotational diagram by plotting $\ln(N_u/g_u)$ as a function of E_u. A best fit procedure is performed and the slope is proportional to $1/T_{Rot}$, while the intercept is associated to the quantity $\ln(N_x/Q)$ which provides the total column density for the respective molecule. If the gas is truly under LTE and lines are optically thin, a straight line should be obtained. A correction for opacity is possible with the population diagram method (Goldsmith & Langer, 1999). As previously mentioned, rotational diagrams are great when several transitions are detected, but that's not always the case for molecules detected in outflows and jets. Lefloch et al. (2015) through a multi-line analysis of CO were able to compute the physical properties and distinguish components of the outflow. However, often few transitions from the same species are detected toward outflows and it is not possible to build a RD. In this case, the approach used to obtain the physical properties of these regions is known as Large Velocity Gradient (LVG) method which is described in the next section.

3.5.4 Large Velocity Gradient approach

The large velocity gradient (LVG) method is a step further in the interpretation of the observed lines compared to the rotational diagram. It is the application of the escape probability method to the problem of a gas with a systemic large velocity gradient. This method is often used either when only few transitions are available or when the lines are optically thick, LVG is an approach more sophisticated than the rotational diagrams to constrain the physical parameters (density, column density, kinetic temperature) of a source.

Escape probability method

The escape probability method was developed by Sobolev (1960) for the treatment of the radiative transfer in expanding envelopes and later extended to other physical problems. The method consists basically of an introduction of a local multiplicative factor describing the probability that a photon will escape the medium after it is generated.

Assuming lack of external source of radiation and that the source is completely opaque to its own radiation, J_ν would approach the local value of S_ν. A deviation of J_ν from S_ν reflects then the photons escaping the medium and the fraction of photons locally trapped is represented by the ratio J_ν/S_ν. Defining β_{esc} as the probability for a photon to escape, then the quantity $(1-\beta_{esc})$ is the fraction of photons that were absorbed.

Considering a two-level system and the following assumptions: the density, temperature and source function are constant across the slab. With the escape probability method, J_ν and β_{esc} might be expressed as:

$$\begin{aligned} J_\nu &= S_\nu(1-\beta_{esc}), \\ \beta_{esc} &= \frac{1}{4\pi}\int d\Omega \int \Phi(\nu) e^{-\tau_\nu} d\nu, \end{aligned} \tag{3.52}$$

where $\Phi(\nu)$ is the Gaussian line emission profile. Therefore, according to Equation 3.52, the probability β_{esc} depends on the source geometry and the optical depth τ_ν. For a semi-infinite slab (de Jong et al., 1975), the escape probability can be computed as:

$$\beta_{esc} = \frac{1-e^{-3\tau_\nu}}{3\tau_\nu}. \tag{3.53}$$

Besides, if the geometry of the source is considered a uniform sphere (Osterbrock, 1974):

$$\beta_{esc} = \frac{3}{4\tau_\nu}\left[1 - \frac{1}{2\tau_\nu^2} + e^{-2\tau_\nu}\left(\frac{1}{\tau_\nu} + \frac{1}{2\tau_\nu^2}\right)\right]. \tag{3.54}$$

The source function equation (Eq. 3.33) can be rewritten in terms of the Einstein coefficients such as:

$$S_\nu = \frac{n_u A_{ul}}{n_l B_{lu} - n_u B_{ul}}. \tag{3.55}$$

Therefore, substituting Equation 3.52 in the static equilibrium equation for a two-level system, is obtained the following:

$$\frac{n_u}{n_l} = \frac{g_u}{g_l} e^{-h\nu/k_B T} \frac{1}{1+\beta_{esc}\frac{n_{cr}}{n_{coll}}}, \tag{3.56}$$

Finally, the radiative intensity is decoupled from the statistical equilibrium equation. From the equation above, it can be inferred that the photons trapping scales reduces the spontaneous emission rate (as the critical density is linked to this coefficient) which corresponds to the fact that a photon is emitted only if it escapes the medium.

LVG codes

As previously discussed, the optical depth and geometry of the source is linked to the radiative mean free path of the photon. The denser the medium, the smaller the distance travelled by the photon and, thus, the less probable a photon will escape. In general, LVG codes allows calculating the line flux from a gas with a systemic gradient of velocity, constant density and temperature, for a given geometry (e.g. semi-infinite slab or uniform sphere). The flux F of a line emitted by a source at a distance d and can be computed as:

$$F = \frac{1}{4\pi d^2}\int_V h\nu A_{ul} n_u \beta_{esc} dV, \tag{3.57}$$

where the integral is on the volume of the emitting source. The flux computed by the LVG codes depends thus on the gas density and temperature, the column density of the molecule (for the line opacity), the velocity gradient (calculated from the linewidth), and the size of the emitting region.

With the data and the model issued by the LVG code, one can derive the H_2 density n(H_2), the species column density N, the gas temperature T_K and the source size if not already known (otherwise, the filling factor has to be corrected in the flux measuring, see Appendix A on how to compute the filling factor for Gaussian sources). Throughout this thesis, the LVG code used was *MadeX* (Cernicharo, 2012). The steps and methodology of the modelling carried out are detailed in Chapters 5 and 6.

Part III

Results

Chapter 4

Interferometric dataset

4.1 SOLIS Large program

The Large Program *Seeds of Life In Space* (SOLIS, Ceccarelli et al., 2017) is an observational project carried out with IRAM/NOEMA, whose goal is to have a global vision in the chemical evolution of iCOMs during the early stages of solar-like system's formation. The project was initially focused on the following O-bearing species: Methoxy (CH_3O), Methanol (CH_3OH), Dimethyl Ether (CH_3OCH_3), Methilformate ($HCOOCH_3$) and Formamide (NH_2CHO), since some of them are considered small bricks of the macro-molecules at the base of terrestrial life. The immediate goal is to pin down the location of iCOMs within each source, to estimate their abundances and sensitivity to evolutionary and environmental factors, the ultimate goal being the comprehension on the evolution of the chemical complexity in Sun-like objects, as well as the location, extent and distribution of iCOMs and how they evolve from the early to the more advanced stages of star formation. NOEMA provides the high sensitivity and spatial resolution observations in the Northern hemisphere needed for the objectives of SOLIS. In order to accomplish these goals, seven sources were selected amid pre- and proto-stellar sources and regions based on the results of two previous Large Programs: Chemical Herschel Surveys of Star-forming Regions (CHESS; Ceccarelli et al., 2010) and ASAI (Astrochemical Surveys at Iram; Lefloch et al., 2017). Both programs consisted of single-dish unbiased spectral surveys of representative star-forming regions: CHESS covers the 500–1900 GHz band with Herschel/HIFI, whereas ASAI covers the 3, 2 and 1.3 mm bands observable with the IRAM-30 m telescope. Among these sources selected, Cep E is present because of the evidences for a hot corino, as described in Chapter 2.

Cep E observations were performed in two configurations using the PolyFiX receiver in NOEMA. Observational parameters for both setups are summarized in Table 4.2, and full of the observations description of data reduction and calibration are described in the following sections.

4.1.1 The 1.3 mm band

The NOEMA array observed Cep E-mm in configuration A with 8 antennas on 23 and 30 December 2016 to observe the spectral band 204.0–207.6 GHz. The field of view of the interferometer was centered at position $\alpha(\mathrm{J2000}) = 23^h03^m13\overset{s}{.}00, \delta(\mathrm{J2000}) = +61\,^{\circ}42'21\overset{''}{.}00$.

The wideband receiver WideX covered the spectral band 204.0–207.6 GHz with a spectral resolution of 1.95 MHz ($\simeq 2.8\,\mathrm{km\,s^{-1}}$), which includes the rotational transition SO N_J= 5_4–4_3 at 206176.005 MHz among many others detected towards the hot corino (see Table 4.1). The precipitable water vapor (PWV) varied between 1mm and 2 mm (between 2 mm and 4 mm in the second night) during the observations. Standard interferometric calibrations were performed during the observations: J2223+628 was used for both amplitude and phase calibration. Bandpass calibration was performed on 3C454.3. Calibration and imaging were performed by following the standard procedures with GILDAS-CLIC-MAPPING[1]. The cleaning of the maps was done using natural weighting (see Chapter 3), with a typical synthesized beam of 0.4″–0.5″ and a position angle PA of 359 ° (see Table 4.2). Self-calibration was applied to the data. The shortest and longest baselines were 72 m and 760 m, respectively, allowing us to recover emission at scales up to 12″. The primary beam of the interferometer (≈ 24.4″) allowed us to recover emission up to ∼ 12″ (10^4 au) away from the protostellar core, while the synthesized beam gave access to spatial scales of ≈ 400 au.

Table 4.1: Molecules mapped within the SOLIS 1.3 mm band framework by Ospina-Zamudio (2019).

Molecules	ν (MHz)	Transition	E_{up} (K)
^{34}SO	201846	$5_4 - 4_3$	38.6
SO_2	204247	$18_{3,15} - 18_{2,16}$	180.6
A-CH_3OH	205791	$1_{1,+1} - 2_{0,+2}$	16.8
E-CH_3OH	206001	$12_{-5,7} - 13_{-4,9}$	317.1
CH_3CHO	205161	$11_{1,11} - 10_{1,10}$	61.5
CH_3OCH_3	204521	$12_{4,9} - 12_{3,10}$	93.5
CH_3OCH_3	204553	$8_{4,4} - 8_{3,5}$	55.3
CH_3OCHO	206379	$19_{1,19} - 18_{1,18}$	101.1
$CH_2(OH)CHO$	206340	$8_{5,3} - 7_{4,4}$	35.2

One of the first results of this data set came out with the continuum map displayed in the Figure 4.1 (top right panel), obtained with this setup at 0.4″. The data confirms the binarity of this source (as discussed in Chapter 2) and resolves without ambiguity the position of Cep E-B located at 1.35″ from Cep E-A (Lefloch et al *in prep.*). As described in Chapter 1, the main goal was to perform a comprehensive study in the outflow. The results related to this setup are presented in Chapter 5.

4.1.2 The 3 mm band

Setup 6 observations of the CepE-mm region were carried on 28 March and 19 April of 2018. The observational setup and the spectral bands covered are summarized in Table 4.2. The array was used in A and C configuration. The shortest and longest baselines were 24 m and 704 m, respectively, allowing us to recover emission up to the ∼ 32″.

In the 3mm range, the primary beam of the interferometer is wide enough (61″) to encompass the whole outflow. Observations were carried out with the PolyFiX correlator,

---

[1] http://www.iram.fr/IRAMFR/GILDAS/

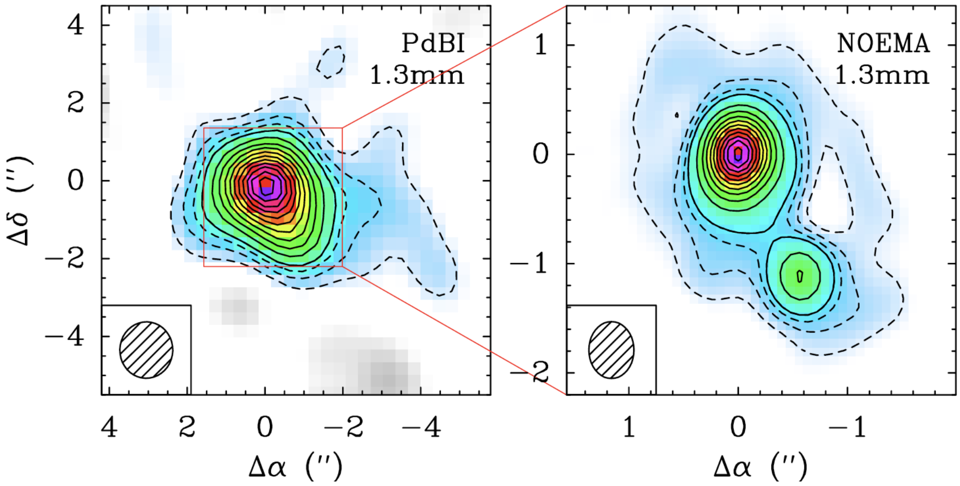

Figure 4.1: 1.3 mm band emission of the Cep E-mm protostellar core. (Left): mapped with NOEMA by Ospina-Zamudio et al. (2018) at 1.4″. (Right): mapped with NOEMA at 1.3 mm as part of SOLIS at 0.4″ note the two components of the protostellar system in the core Cep E-A (0″,0″) and B (−0.5″,−1.2″).

providing an spectral resolution of 2 MHz (Δv = 6.9 km s^{-1}). In addition to the broad PolyFiX band window, narrow spectral windows of high-spectral resolution ($\Delta\nu = 0.0625$ MHz) were placed on selected lines of interest. The amount of PWV ranged between 2mm and 5.5mm and system temperatures ranged between 60 and 100 K. The bandpass was calibrated using J2223+628 and 3C454.3, while the absolute flux calibration was fixed by observing MWC349, the phase rms is $\leq$ 77 °. Using a natural weighting, we obtained a synthesized beam of 2.10″ × 1.80″ (PA=−48 °) and 1.80″ × 1.61″ (PA=−50 °) in the spectral bands 80.5 – 88.0 and 95.0 – 103.4 GHz, respectively. The final uncertainty on the absolute flux scale is $\leq$ 10%. The typical rms noise of the SOLIS data per element of spectral resolution is 0.6 mJy.beam^{-1} (0.024 K) per spectral channel of 2 MHz.

Table 4.2: SOLIS Observational dataset properties: spectral bands, backend, spectral resolution $\Delta\nu$, configuration of the interferometer, synthesized beam size, positio angle PA, rms (mJy beam^{-1}) per element of spectral resolution Δv (km s^{-1}).

Setup	Range (GHz)	Backend	$\Delta\nu$ (MHz)	Δv (km s^{-1})	Config.	Synthesized beam (″×″)	PA (°)	rms (mJy.beam^{-1})
6	80.5 – 88.0	PolyFiX	2.0	7	AC	2.10 × 1.80	-48	0.6
			0.0625	0.2				3
	95.0 – 103.4	PolyFiX	2.0	7	AC	1.80 × 1.61	-50	0.6
			0.0625	0.2				3
5	204.0 – 207.6	WideX	2.0	2.8	A	0.41 × 0.34	-180	2.2
5	204.8 – 205.8	Narrow	0.625	0.9	A	0.43 × 0.33	-7	5.5

4.2 The W14AF project

This project (PI: B. Lefloch) observed Cep E-mm during the winter of 2014–2015 with the goal of mapping the outflow emission traced by usual outflow tracers (such as SiO and SO) at 3 mm and 1.3 mm bands. At 3 mm, the spectral band covering the frequencies 85.9–89.7 GHz was observed on 3 and 12 December, 2014 and on 6 and 7 March, 2015. The observations were carried out in configurations B and C of the interferometer, with baselines between the antennas ranging from 21 m to 443 m, which made it possible to recover the emission from spatial scales between 34″ and 1.6″. A single field of view centered on the nominal position of the Cep E-mm protostellar system was observed. During observations of this band, the phase had an rms $\leq 50\,^{\circ}$. The amount of PWV in the atmosphere was less than 10 mm and the temperature of the system was between 60 – 200 K. The observations were carried out under conditions suitable and only 1% of the data was not used for the calibration and the creation of the maps. The observational dataset properties are summarized in Table 4.3.

The spectral band 216.8–220.4 GHz was observed on 9 December, 2014, 13 and 24 April, 2015 and 7 December, 2015. The observations were made in the compact configurations C and D with baselines ranging from 19 m to 176 m, which made it possible to recover the emission in scales between 14.7″ and 1.5″. A mosaic of five fields was performed located at the following offset positions with respect to the nominal position of Cep E-mm: (−9″,−20.8″), (−4.5″,−10.4″), (0″, 0″), (+4.5″, +10.4″) and (+4.5″,+20.8″). During the observations of this band, the phase was stable with an rms $\leq 45\,^{\circ}$. The amount of water vapor PWV was less than 3 mm and the system temperature was between 100 – 200 K. Observations were made under suitable conditions with only 2% of the data being excluded from the final data set. The Wideband Express spectrometer (WideX) was connected to the receivers with a spectral resolution of 2 MHz, i.e. a radial velocity resolution $\Delta v = 6.8\,\mathrm{km\,s^{-1}}$ and $2.7\,\mathrm{km\,s^{-1}}$ in the band at 3 mm and 1.3 mm, respectively. Some particularly molecular transitions (e.g. SiO J=5–4, HCN J=1–0, $\mathrm{HCO^+}$ J=1–0) have been observed in parallel with a higher spectral resolution ($\Delta\nu = 625$ kHz) using the Narrow Band mode of the correlator.

Table 4.3: Observational dataset properties: spectral bands, backend, spectral resolution $\Delta\nu$, configuration of the interferometer, synthesized beam size, position angle PA, rms ($\mathrm{mJy\ beam^{-1}}$) per element of spectral resolution Δv ($\mathrm{km\,s^{-1}}$).

Range (GHz)	Backend	$\Delta\nu$ (MHz)	Δv ($\mathrm{km\,s^{-1}}$)	Config.	Synthesized beam (″×″)	PA (°)	rms (mJy.beam^{-1})
85.9 – 89.6	WideX	2.0	7.0-6.7	BC	2.38 × 2.13	60	1 – 3
86.0 – 86.2	Narrow	0.625	2.2	BC	2.46 × 2.20	52	3
86.7 – 86.9	Narrow	0.625	2.1	BC	2.46 × 2.19	48	3
88.5 – 88.7	Narrow	0.625	2.1	BC	2.39 × 2.07	-133	3
89.1 – 89.3	Narrow	0.625	2.1	BC	2.36 × 2.06	49	3
216.8 – 220.4	WideX	2.0	2.8–2.7	CD	1.46 × 1.39	72	3–5
217.3 – 217.6	Narrow	0.625	0.9	CD	1.42 × 1.41	40	10
218.7 – 218.9	Narrow	0.625	0.9	CD	1.46 × 1.37	-90	8

Data Calibration and reduction were carried out according to the standard procedure with the GILDAS software. The reconstitution of the images was carried out by adopting natural weighting. Thus, the sizes of the synthesized lobes produced at 3 mm and at 1.3 mm are equal to $2.38'' \times 2.13''$ (PA $= 60\,^{\mathrm{o}}$) and $1.46'' \times 1.39''$ (PA $= 72\,^{\mathrm{o}}$), respectively. The absolute flux calibration uncertainties are $\leq 10\%$ and $\leq 20\%$ at 3 mm and 1.3 mm, respectively. Finally, the typical rms noise per spectral channel is between 3–5 mJy/beam in the 3 mm band, and between 1–3 mJy/beam in the 1.3 mm band.

Chapter 5

Mass-ejection variability in the jet of Cep E

5.1 Context and motivation

The example of L1157-B1 very convincingly shows that significant progress in the understanding of the shock chemical composition became possible once the physical structure of the bowshock (velocity, temperature, density) was clarified (Lefloch et al., 2012; Benedettini et al., 2012) following the founding work of Gueth et al. (1996) on the kinematics of the outflow. Ultimately, the key question consists in retrieving, or at least constraining, the physical conditions and the abundance of molecular species, based on their spectral signatures. However, although L1157 has proven to be an outstanding chemically active outflow (Bachiller et al., 2001), more templates are needed to constrain whether this chemical richness is normal in young stellar objects or indeed this source is an exception.

Recently, Cerqueira et al. (2021), by carrying out hydrodynamical numerical simulations of the L1157-B1 flow, were able to show how the velocity field can be used to interpret spectral line profiles and identify the origin of the molecular emission: Mach disk and jet, low-velocity shock, entrained gas in the cavity. This approach may not be always applied to all objects once taking into account the complexity of some regions (source multiplicity or precession, for instance). As an additional degree of complexity, observations show that these different regions are dynamically interacting, transferring matter and momentum. Hence, the message remains: to understand the presence of molecular species in jets and outflows requires not only a chemical modelling but, equally importantly, an analysis of the outflow gas dynamics of the source.

The analysis with the IRAM-30m of the spectral line profiles detected towards the protostellar system Cep E-mm revealed a variety of signatures both in the outflowing gas and the jet, testifying of interaction and a complex physical structure, with internal shocks inside the jet. Although the studies of Lefloch et al. (2015) and Gusdorf et al. (2017) insisted on the presence of these knots to account for the emission of the high-J CO lines and the detection of OI with SOFIA, very few information about the knots was actually available, despite their importance as signatures of the time variability of mass-ejection phenomena. Therefore, the first part of this thesis was to obtain a picture as detailed as possible of the jet and the knots presence with their physical properties, as well as their interaction with the ambient gas.

After a first census of the chemical composition of the jet and outflow, and inspecting the spatial distribution of some of the detected species, it became obvious that in order to understand this rich chemistry detected (see Chapter 2), the first and necessary step is an in-depth investigation of the jet kinematics. Such a deep investigation, much deeper than until now, will provide a detailed and consistent view on the jet structure and its dynamics. With this work, we are then able to constrain the jet structure and its physical conditions (velocity, density and temperature). In a second step, we will be able to connect the kinematic and chemical properties of the high-velocity material. In this chapter, we will focus, therefore, in constraining the kinematic features of Cep E jet.

5.2 Two components in the jet

Previous studies showed evidence for time-variability in the molecular outflow/jet emission in Cep E, associated both with precession (Eisloffel et al., 1996) and internal bullets (Gómez-Ruiz et al., 2012; Lefloch et al., 2015; Gusdorf et al., 2017) which were possibly associated to CJ shocks. Therefore, the very first goal of my work was to characterize the physical properties of these knots by providing how many are present, their positions, sizes, masses, ages, contribution to the momentum ejecta. To accomplish with this, I have made use of the IRAM interferometer data, we have imaged the rotational transitions CO $J=$ 2–1 230538.00 MHz (Lefloch et al., 2015), a typical tracer of molecular outflows, along the full high-velocity jet at $1''$ resolution, and SO $N_J=5_4$–4_3 206176.013 MHz (part of the large program SOLIS, see Chapter 4 and Ceccarelli et al., 2017), a probe of molecular jets, at $0.4''$ resolution towards the central protostellar core. Information regarding the data reduction and the features of these maps were described in Chapter 4.

The flux-integrated map in CO and SO are presented in the Figure 5.1. Four main velocity components are detected: the outflow cavity walls (black) emitting at low velocities, the jet in red and blue contours emitting at high velocities; the southern terminal bow shock HH 377 in green; the northern terminal bullet NB in magenta. The jet displays velocities within the ranges $[-135;-110]$ km s^{-1} in the southern lobe and in the range $[+40;+80]$ km s^{-1} in the northern lobe.

We can immediately see from Figure 5.1 (left and middle panels) the presence of two components in the jet: a central, highly-collimated, component of diameter ≤ 320 au ($\sim 0.4''$) specifically probed by SO, surrounded by a radially extended gas layer traced by in CO ($\sim 2''$). On right hand panel, it is displayed the CO emission in the northern lobe where the upper panel shows the flux integrated within the range [55;80] km s^{-1} (so higher velocity) and the lower [40;55] km s^{-1}. The emission in the lower velocity range (lower panel) is broader, indicating an interaction with the low-velocity gas or the wings of the internal shocks. The high-velocity emission (upper panel) shows a narrow and highly-collimated jet, comparable to the one observed in SO, confirming the two components found in the jet and that it is detected in CO. This pattern of two components in the molecular jet revealed in our observations is consistent with the one recently reported by Podio et al. (2021) in the CALYPSO sample of young low-mass protostellar outflows.

Furthermore, from the distribution of the high-velocity CO emission, we have been able to determine the main axis of the northern and southern lobes of the jet. The former is found to make a position angle (PA) of $+20\,^{\circ}$ while the latter makes a PA of $+204\,^{\circ}$ which are displayed by the black arrows in Figure 5.1 on the left panel. On the middle

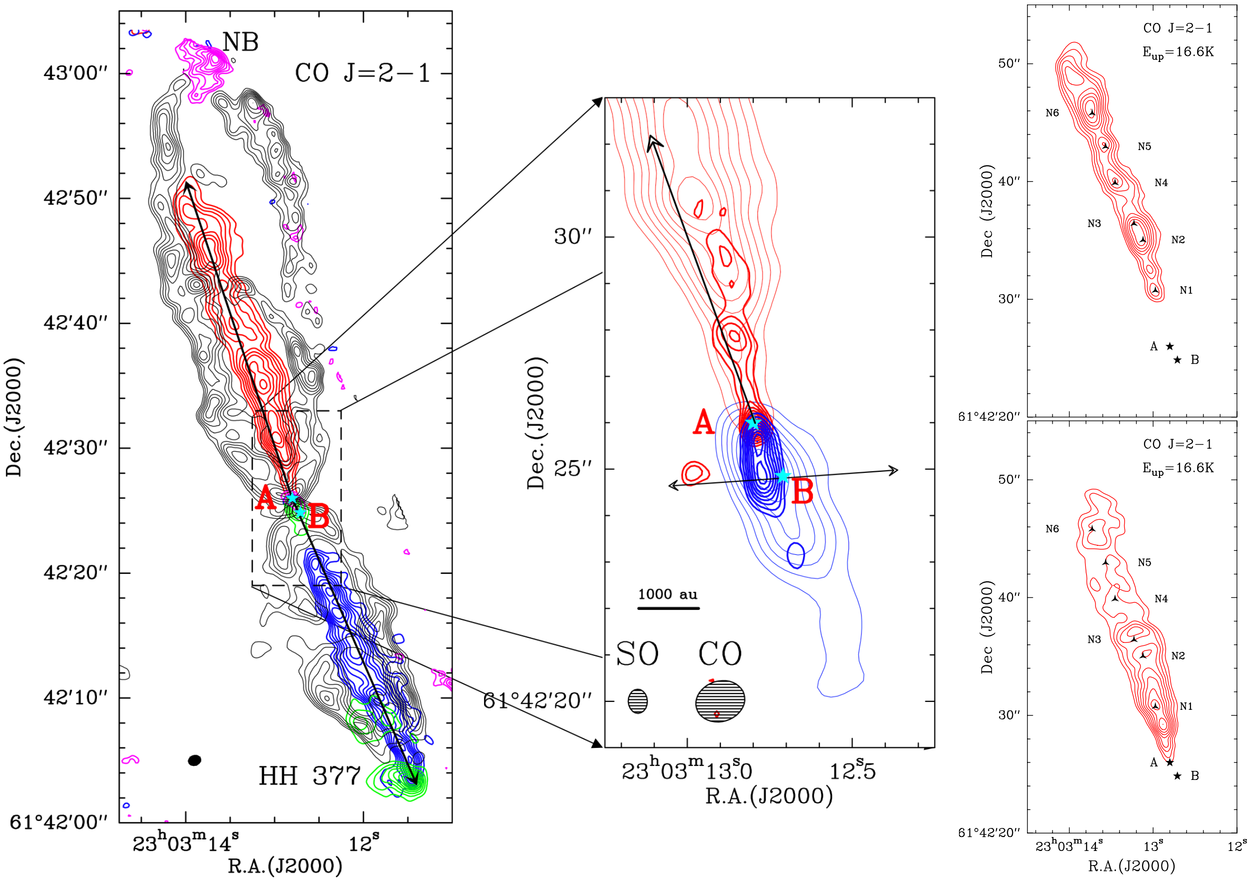

Figure 5.1: Molecular emission in the Cep E outflow as observed: (left) in the CO 2–1 line with the PdBI at 1″ resolution by Lefloch et al. (2015): a) the outflow cavity walls (black) emitting at low velocities, in the range [−8;−3] km s^{-1} and [−19;−14] km s^{-1} in the northern and southern lobe, respectively; the jet, emitting at high velocities in the range [−135;−110] km s^{-1} in the southern lobe (blue) and in the range [+40;+80] km s^{-1} in the northern lobe (red); the southern terminal bow shock HH 377, integrated in the range [−77;−64] km s^{-1} (green); the northern terminal bullet NB integrated in the velocity range [+84;+97] km s^{-1} (magenta). (middle panel): SO $N_J = 5_4$–4_3 flux-integrated emission is displayed is thick contours superposed by the CO in thin. The arrows correspond to the Cep E-B jet as determined by SiO J=5–4 transition. (right): emission integrated in the northern in the range [55;80] km s^{-1} (upper) and [40;55] km s^{-1} (lower). First contour and contour interval are 20% and 10% of the peak intensity in each component, respectively. The synthesized beams are shown in the bottom left corner.

panel however, the arrows in the West and East direction are indicating the direction of the outflow powered by Cep E-B. There is a misalignment of 4 °, already reported by Lefloch et al. (2015), between the northern and southern lobe, which required an extra effort to analyze them simultaneously in this work.

5.3 The jet is accelerating

In order to constrain the gas kinematics, we studied first the jet velocity distribution along its main axis by means of Position-Velocity (PV) diagram along both lobes of the jet by integrating them over the beamsize of the map, both the emission of CO and SO PV diagrams are displayed in Figure 5.2. Close to the protostar $\delta = 0''$, the emission is dominated by the ambient medium at $V_{lsr} = -10.9\,\mathrm{km\,s^{-1}}$. The velocity of the CO emission peak increases quickly as one moves away from the protostar and reaches its terminal value at about $5''$ (4000 au) from Cep E-A. In other words, the CO jet appears to accelerate from the protostar at scales of few arc second. The same behavior is observed in both lobes of the jet. At large distances from the source ($|\delta| > 10''$), the jet radial velocity V reaches a steady value of $\approx +65\,\mathrm{km\,s^{-1}}$ and $-125\,\mathrm{km\,s^{-1}}$ in the northern and southern lobe, respectively.

Close inspection of the position-velocity diagram of CO 2–1 and SO 5_4–4_3 (Figure 5.2) in the direction of the protostar reveals the presence of molecular gas components propagating at the full (terminal) velocity in both lobes. This is well illustrated by knots N0a at $\delta = 0''$, $V = +55\,\mathrm{km\,s^{-1}}$ and N0b at $\delta = +2''$, $V = +40\,\mathrm{km\,s^{-1}}$ in the northern lobe. In the southern lobe, some smaller features at $\delta = 0''$, $V = -70\,\mathrm{km\,s^{-1}}$ and $V = -120\,\mathrm{km\,s^{-1}}$, respectively, are detected and seen in SO 5_4–4_3, possibly as a consequence of their small size and the higher resolution of these observations.

As can be seen in Figure 5.2, the velocity gradually increases from ambient to the terminal value on a scale of a few arcseconds. The radial velocity profile V as a function of distance δ to the protostar along the jet main axis can be fitted by the simple relation:

$$\frac{V - V_{lsr}}{V_0} = \exp\left(\frac{-\delta_0}{\delta}\right), \tag{5.1}$$

where V_0 is the jet terminal velocity relative to the protostar and δ_0 the length scale of the jet acceleration process. The length scale δ_0 and the jet velocity V_0 (with respect to Cep E-A) were determined from a best fitting procedure to the CO Position-Velocity diagram. The procedure yields $\delta_0 = 693$ au (590 au) and a jet velocity $V_0 = +75\,\mathrm{km\,s^{-1}}$ ($-118\,\mathrm{km\,s^{-1}}$) in the northern (southern) jet. The agreement between the best fitting V_0 values and the observational determination of the jet velocity relative to the source is very good and supports our simple modelling. The close agreement between both values of δ_0 suggests that the physical conditions are similar at subarcsec scale around Cep E-A.

To conclude, we have found evidence for apparent CO jet acceleration in both lobes, or another process occurring at small-scales (600-700 au). The detection of extremely high-velocity knots at terminal velocity in the direction of Cep E-A plus the length scale of the acceleration process, which is much larger than the disk size and the hot corino (< 200 au) clearly proves this acceleration is not the jet launch mechanism we are observing. Most likely, we are probing the interaction of the protostellar envelope with the protostellar jet itself and this is what we are going to study in the next section.

5.4 Jet-envelope interaction

In order to search for evidence of interaction between the jet and the envelope material, we performed PV diagrams at various positions perpendicular to the main axis of the jet,

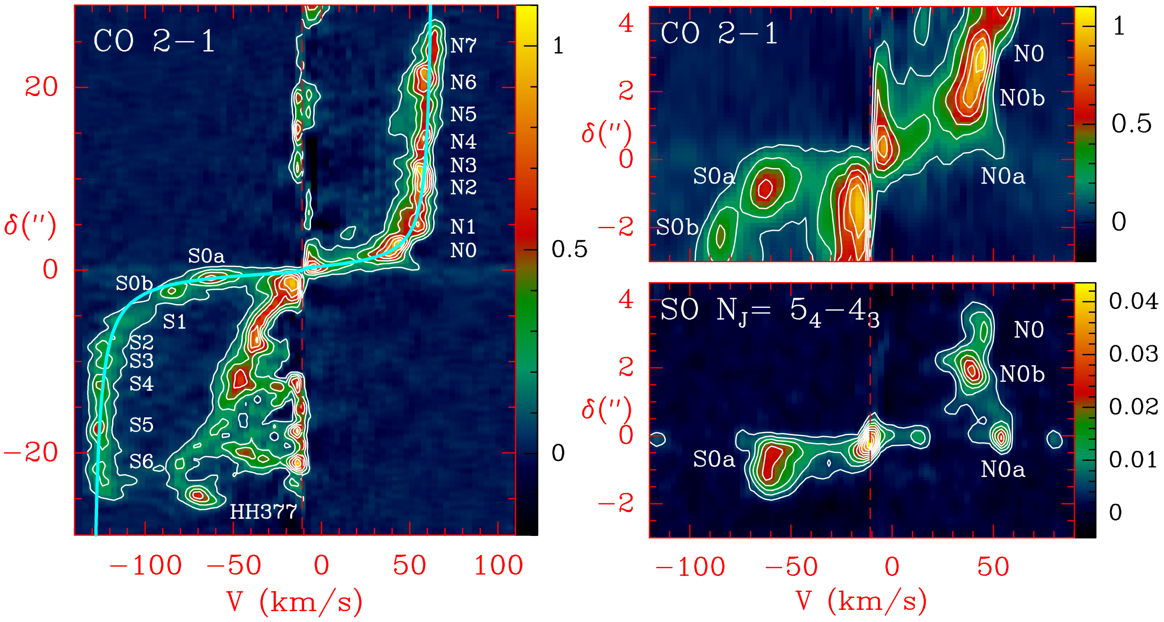

Figure 5.2: Position-velocity diagrams of the CO and SO emission along the jet main axis. (Left panel) CO 2–1 as observed at 1″ with the IRAM interferometer. The best fitting relation to the gas acceleration $|V - V_{lsr}|/V_0 = \exp(-\delta_0/\delta)$ is superimposed in cyan. (Right) Magnified view of the CO 2–1 emission in the top, while SO $N_J = 5_4$–4_3 as observed at 0.4″ resolution with NOEMA is in the bottom. First contour and contour interval are 10% and 15% of the peak intensity, respectively. The red dashed lines mark the ambient cloud velocity. The velocity resolution of the CO and SO observations is 3.3 km s^{-1} and 2.8 km s^{-1}, respectively. Fluxes are expressed in Jy/beam.

from the location of the protostar up to several arcsecond away. These PV diagrams are displayed in Figure 5.3.

We first concentrated in the northern lobe. Along the jet main axis, we see in CO that the ambient gas velocity is connected to the jet in a region of 4″ approximately, delimited by the knots S0b and N0 in the southern and northern lobe, respectively. In this region we observe a broad velocity range of emission from ambient to terminal, as discussed previously, and suggests gas acceleration. Across the jet main axis, we observe a velocity increase as one gets closer to the jet axis at $\alpha = 0''$. This velocity distribution is continuous from V$_{lsr}$ to V$_{jet}$ hence shows an increasing velocity field around the jet, which is better interpreted as evidence of ambient gas entrainment by the latter. The CO emission of this entrained component is brighter than the jet material launched from the protostar and its associated knots, hence suggesting an accelerated jet, as aforementioned. This process is best be seen at positions $\delta = +0''$ to $\delta = +1.5''$ across the jet main axis (see top panels in Fig. 5.3). However, when further away from the protostar ($\delta \geq 2.0''$), the jet signature gradually separates from the entrained gas emission. Finally, this suggests that the entrainment process loses its efficiency as the distance from the protostar increases beyond this distance in the northern lobe.

In the southern lobe, on the other hand, the evidence of jet entrained gas near Cep E-A at $\delta \sim 0$ is much weaker. The emission in the range [−70;−11] km s^{-1} appears collimated with a typical diameter of 1.5″. The main difference with the northern lobe lies in that there is no jet entrainment of material at distance $> 1''$ (800 au), i.e. that the amount of jet entrained material is much less in the southern lobe. The CO jet emission is inhomogeneous and displays a maximum between $\delta = -1''$ and $\delta = -3''$ (see Fig. 5.3). This maximum coincides with the region of propagation of the Cep E-B jet, as mapped in the SiO 5–4 line by Ospina-Zamudio et al. (2019) (as can be seen in Figure 2.5). The absence of gas entrainment in the southern lobe is most likely a result of the interaction between both outflows/jets, which means that the outflow from the B component is removing the material that could be entrained by the southern jet powered by Cep E-A.

As discussed by Lefloch et al. (2015), detailed analysis of the momentum budget in the outflow southern lobe showed that the high-velocity jet carries away the same amount of momentum as the low-velocity gas (1.7 vs 2.6 $M_\odot$ km s^{-1}, respectively). This led the authors to conclude that the low-velocity outflow is driven by the protostellar jet itself. This result is supported by the distribution of the CO emission in the Position-Velocity diagram along the main jet axis. As can be seen in the left panel of Fig. 5.2, the low-velocity gas appears to accelerate gradually from the protostar up to the terminal shock HH 377 following the relation: $(V - V_{lsr}) \propto \delta$ where δ is the angular distance to the protostar. This kinematic feature is an unambiguous signature of jet bowshock driven outflow (Raga & Cabrit, 1993; Wilkin, 1996; Cabrit et al., 1997).

5.5 The internal shocks in the jet

We performed a systematic search for knots along the jet in both the northern and the southern lobes from the CO jet intensity map (Fig. 5.1) and the CO Position-Velocity diagram along the jet main axis (Fig. 5.2). We identified ten knots in the northern and eight knots in the southern lobe, they are labeled N0a to N7, S0a to S6 in the northern and southern, respectively.

With an angular resolution of 0.4″, SO 5_4–4_3 observations allowed us to identify knots at a few arcseconds from the protostar. In the northern jet, for instance, we have detected the knot N0a at $\delta = +0.2''$ and $V = +54.6$ km s^{-1} and knot N0b at $\delta = +2.0''$ and $V = +39.8$ km s^{-1} (see bottom right panel in Fig. 5.2). In the southern jet, we have detected a knot, referred to as S0a, near offset position $\delta = -0.8''$ and $V = -62.5$ km s^{-1}. The SO emission looks elongated along the jet axis and it is hence unclear whether more than one knot is actually present. The emission from the southern jet close to Cep E-A does not display the same fragmented structure as in the north. The similarity in the ejection velocities of S0a and N0a, both at short distance from Cep E-A suggests that they are associated with the same ejection event and that the physical conditions of jet acceleration are comparable in both lobes.

5.5.1 Properties

After the knots were identified, we derived their main properties. Initially, we measured the coordinates in the plane of the sky then we computed their distance with respect to the protostar. The positions and sizes (beam-deconvolved) of the different knots were determined from a 2D Gaussian fit to the CO flux distribution, except for knots N0a-N0b, whose parameters were determined from the SO molecular emission. We also measured the radial

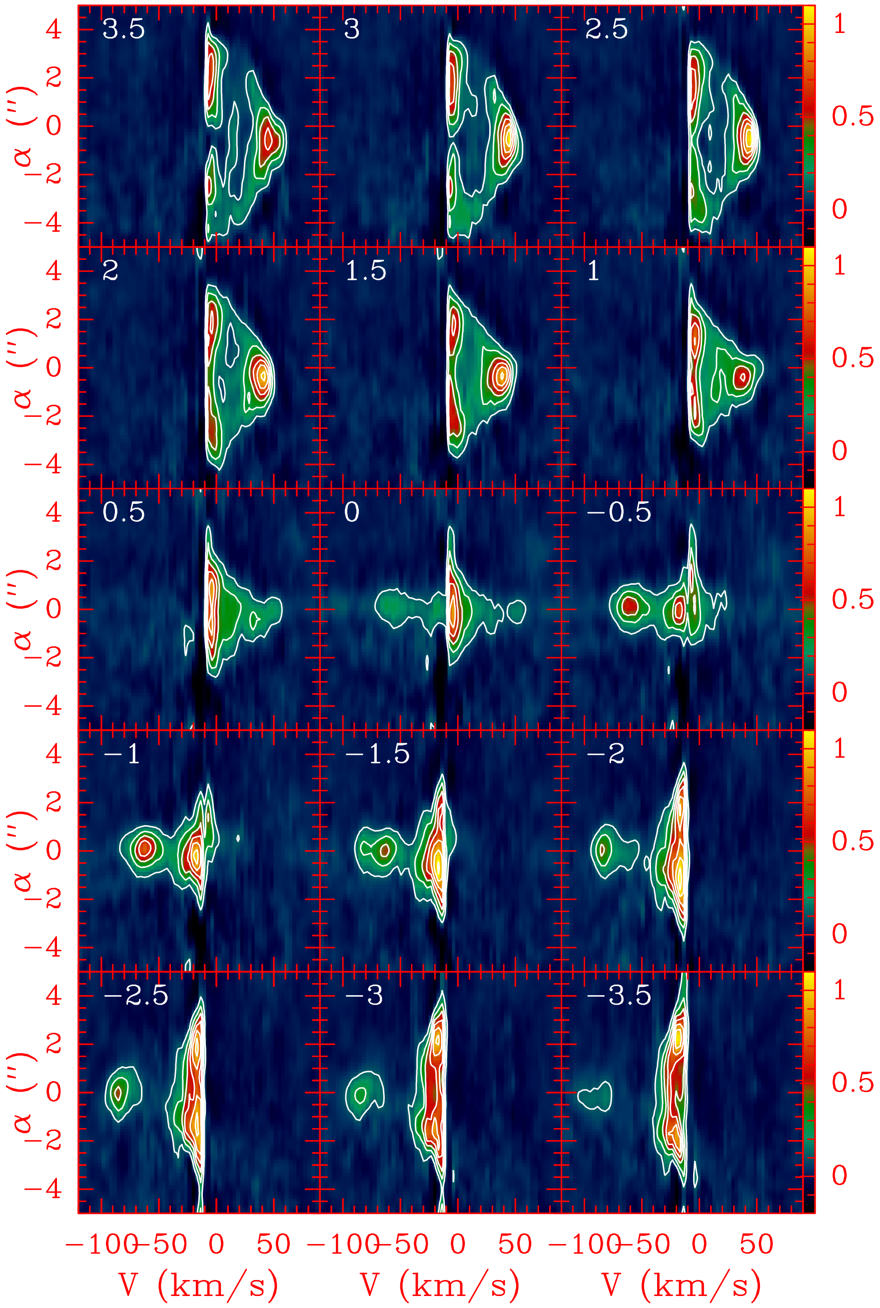

Figure 5.3: Position-velocity diagrams of CO 2-1 line across the jet main axis (see Fig. 5.1). The relative distance to the protostar δ (in arcsecond) is indicated in the top left corner. First contour and contour interval are 10% and 15% of the peak flux, respectively. Fluxes are expressed in Jy/beam.

velocity V and the line width, which were derived from the CO Position-Velocity diagram in Figure 5.2. Hence, the flux at the peak F_P was computed by multiplying the line width by the main beam temperature at the peak. Finally, from the velocity and the inclination angle of the jet with respect to the plane of the sky, we obtained the dynamical age $t_{dyn}= d/V \times \tan i$, where i is the inclination with respect to the plane of the sky. The knots dynamical ages are within the range 0–1500 yr. Interestingly, HH 377 and NB have comparable dynamical ages, therefore the series of knots in the northern and southern appear to cover the same time interval of mass-ejection events. Those knot properties aforementioned are summarized in Table 5.1. For the sake of comparison, we have included the parameters of the terminal shocks NB and HH 377.

Table 5.1: Coordinates, distance to Cep E-A along the jet main axis, size (beam deconvolved), radial velocity, line width, flux at the peak, dynamical age, period number and mass of the knots in the jet. Dynamical ages were obtained after correcting for the jet inclination angle.

ID	$(\Delta\alpha;\Delta\delta)$ ($''$;$''$)	δ ($''$)	Size ($''$)	V (km s^{-1})	ΔV (km s^{-1})	F$_P$ (K km s^{-1})	t_{dyn} (yr)	n	Mass (10^{-3} $M_\odot$)
North									
N0a	(+0.1; +0.2)	0.2	0.5	+54.6	12(3)	35(9)	12	0	0.08
N0b	(+0.3; +2.0)	2.0	0.9	+39.8	18.3(0.4)	430(9)	154	3	0.3
N0	(+0.6; +3.1)	3.2	1.4	+44.5	14.1(0.3)	289(7)	218	4	1.9
N1	(+1.2; +4.7)	4.9	1.8	+54.6	18.7(0.7)	351(13)	291	5	3.6
N2	(+2.3; +9.0)	9.3	1.7	+57.2	9.8(0.4)	270(10)	532	10	2.8
N3	(+3.0; +10.4)	10.8	3.0	+58.2	8.5(0.4)	261(12)	609	11	7.8
N4	(+4.6; +13.9)	14.6	2.6	+58.2	9.6(0.4)	197(7)	823	15	4.5
N5	(+5.4; +16.9)	17.8	2.0	+60.2	12.5(0.9)	189(14)	975	18	2.5
N6	(+6.6; +19.4)	20.5	2.9	+59.2	13.3(0.3)	281(6)	1139	21	7.6
N7	(+8.3; +22.9)	24.4	1.9	+63.2	10.2(0.3)	175(5)	1283	23	2.1
NB	(+6.3; +34.3)	34.9	4.0	+83.3	13(2)	70(9)	1440	26	1.3
South									
S0a	(−0.2; −0.8)	-0.8	0.9	-62.5	23.6(0.5)	389(9)	60	1	0.7
S0b	(−0.8; −2.1)	-2.2	1.1	-85.2	19(1)	216(16)	115	2	0.6
S1	(−1.8; −5.4)	-5.7	1.3	-113.5	20(2)	147(11)	218	4	0.5
S2	(−3.3; −7.6)	-8.3	1.7	-124.1	16.0(0.8)	135(7)	286	5	0.8
S3	(−3.6; −9.3)	-9.9	1.8	-124.1	14.7(0.7)	144(7)	341	6	0.9
S4	(−4.9; −11.6)	-12.6	2.3	-125.4	8.4(0.3)	114(4)	429	8	1.3
S5	(−6.8; −15.9)	-17.3	2.0	-126.1	8.4(0.3)	124(5)	585	11	1.1
S6	(−8.8; −19.9)	-21.8	1.4	-126.1	13.2(0.3)	114(6)	737	13	0.5
HH 377	(−9.5; −22.7)	-24.6	4.5	-67.0	10.9(0.2)	261(5)	904	16	6.0

Figure 5.4 displays the distribution of knot velocities relative to Cep E-A as a function of the distance to the protostar. We have superimposed the best fitting solution to the velocity profile along the main axis, following Equation 5.1. We adopted an uncertainty of $\pm 0.5''$ in position (one beam size) and a value of ± 5 km s^{-1} in velocity (mean knot line width). From this figure, we can see that all the knots but N0a trace the overall CO gas distribution in the jet. Moreover, it is also possible to observe the acceleration region close to the protostar and the terminal velocity of the jet, which were both discussed in Section 5.3.

Knots are not regularly distributed along the jet, at equal distance one from the other. At large distance from the protostar, typically $12''$, the separation between knots tends to

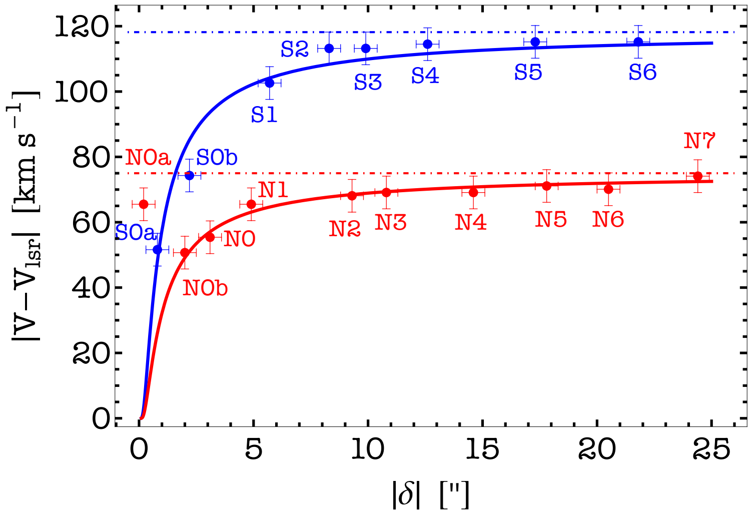

Figure 5.4: Distribution of knot velocity peaks along the main jet axis as a function of distance δ to Cep E-A in the northern (red) and southern (blue) jet components. The best fit to the northern (southern) jet velocity relative to the source is shown as a solid curve.

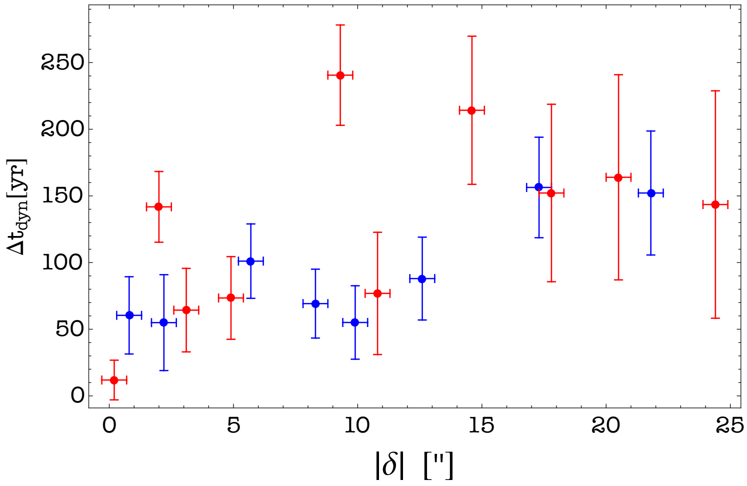

Figure 5.5: Distribution of time intervals between subsequent knots as a function of distance to the protostar along the jet main axis, both in the northern (red) and southern (blue) lobes.

increase from $\sim 2.5''$ (2000 au) to $\sim 4.5''$ (3700 au) in the southern lobe (see figure 5.4). The knot distribution is more complex in the northern lobe, but their separations are of the same order, $\sim 2.5''$ for "close" (e.g. N2/N3) and $4.5''$ for "remote" (N5/N6) knots. This distribution may be biased by the gas acceleration in the central protostellar regions. For this reason, in order to get more insight into the knot distribution, we have also computed the distribution of time intervals between subsequent knots as a function of distance to the protostar and the mean knot velocity, this is displayed in Fig. 5.5. A marked separation is observed in the southern lobe (in blue) between the knots located at $\leq 10''$–$13''$ (8000 au) from the protostar, with a short $\Delta t_{dyn} \sim$ 50–80 yr, and the more distant knots, with $\Delta t_{dyn} \sim$ 150–200 yr. A similar pattern is observed in the northern lobe (red), with similar time intervals close to and far away from the protostar. The case of knots N2/N3 at 9–11$''$ is peculiar, since they are found in unexpected regimes for their distances, N2 in large time interval and N3 at smaller interval. We suspect this anomaly is caused by the interaction of the knots with the ambient gas or the cavity walls.

To summarize, analysis of the knot interval distribution suggests the presence of two timescales: a short time interval $\Delta t \sim 50-80\,\mathrm{yr}$ close ($\leq 12''$) to the protostar and a longer timescale $\Delta t \sim 150-200\,\mathrm{yr}$ at larger distances from the protostar. Such knot interval distribution could be explained due to a periodic process in the ejection mechanism taking place at the base of the jet. We examine this hypothesis in more detail in the next section.

5.5.2 Masses

We have determined the mean gas column density of the knots from a radiative transfer analysis of the CO 2–1 line emission, using the radiative transfer code MadeX (Cernicharo, 2012) in the large velocity gradient approximation and the CO-H_2 collision coefficients from Yang et al. (2010). In this modelling, we assumed that the CO emission measured toward the knots arises from a single physical component. In other words, the contributions of the entrained gas layer and the inner jet material along the line of sight were neglected with respect to that of the knots. Line widths and intensities were obtained from a Gaussian fit to the line profiles at the flux peak of the knot. The peak intensity of the knot was sometimes found to lie off the jet main axis by a fraction of a beam which reveals a complex knot structure at few arcsecond scale, with some small velocity shifts between the intensity peak and the jet main axis. We have adopted the jet H_2 density and temperature derived by Lefloch et al. (2015) and Ospina-Zamudio et al. (2019) in the southern and northern lobes from a CO multi-transition analysis (see Table 2.1 in Section 2.3.2). The total H_2 mass and column density were subsequently obtained from N(CO) adopting a standard CO to H_2 relative abundance ratio of 10^{-4}.

We derived knot masses of the order of $10^{-3}\,M_\odot$ (see Table 5.1). It appears that the knots are more massive in the northern than in the southern lobe by a factor of a few. The masses of the knots tend to increase beyond $10''$ (8200 au), a distance corresponding approximately to knots N3 and S4 in the northern and southern lobe, respectively, or equivalently, to a dynamical timescale of $\sim 500\,\mathrm{yr}$. As previously discussed, the CO position-velocity diagrams show evidence of protostellar material entrainment by the northern jet close to Cep E-A; therefore, it seems unlikely that the observed knot mass increase is related to the jet-envelope interaction whose we address in more detail in the following section, in which we consider the possibility of dynamical interactions of the knots. The knots N3 and N6 appear as an exception in the northern lobe with mass of $8 \times 10^{-3}\,M_\odot$, a factor of $\sim$ 2–3 higher than the mass of the other knots. Interestingly, the mass of knot NB ($1.3 \times 10^{-3}\,M_\odot$) is similar to that of the other knots.

5.5.3 Mass-loss rate

After computing the knot properties, the masses and dynamical ages, we decided to retrieve the mass-loss history of Cep E and its variations. In order to approach this, we have first determined the cumulative mass of the knots as a function of time. The origin (t=0) is defined by the knots NB and S6 in the northern and southern lobes, respectively. We decided to use S6 instead of HH 377 simply because it is not a simple knot as indicated by its very high mass with respect to jet knots. The cumulative mass function is obtained by adding up the mass one after the other of subsequent ejected knots. The time scale is simply obtained from the knot dynamical age. We took as time reference the knots NB and S6 in the northern and southern lobe, respectively. This cumulative mass function is displayed in the Figure 5.6.

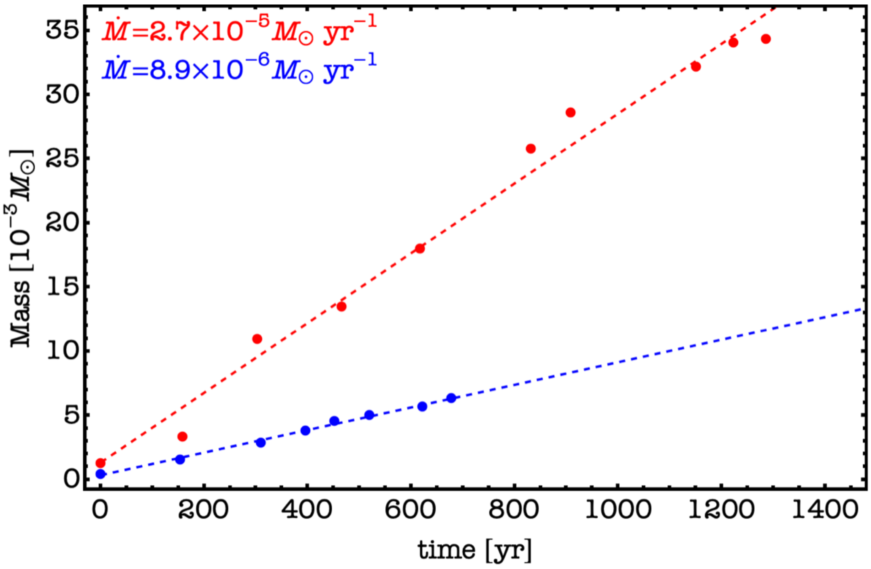

Figure 5.6: Cumulative knot mass function in the northern (red) and southern (blue) lobes. The best linear fits are drawn by dashed lines.

The cumulative mass function is therefore not an absolute distribution since the time (the ejection) we take as reference is not same in both lobes. However, what matters here is the mass evolution, as a function of time, not the absolute value, but the gradient with time. This function in both lobes are drawn in Fig. 5.6. The main result appears immediately that mass function increases linearly as a function of time, within observational uncertainties. We have performed a linear fit to both distributions, which yielded the mass increase with time $\dot{M} = 8.9 \times 10^{-6}\ M_\odot\ \mathrm{yr}^{-1}$ in the southern lobe (dashed blue line) and $\dot{M} = 2.7 \times 10^{-5}\ M_\odot\ \mathrm{yr}^{-1}$ in the northern lobe (dashed red line). The second result is the higher mass-loss rate increased in the northern lobe. This reflects the trend, reported previously in Section 5.5.2, that the knots appear 3 times more massive in the northern lobe, possibly as a result of the interaction with the protostellar envelope, which drives the entrainment (and acceleration) of ambient material by the knots. This process is much less efficient, if present, in the southern lobe. The third result is the relatively larger dispersion in the cumulative mass function in the North. Apart from uncertainties, it may reflect the interaction with ambient material.

5.5.4 Ballistic ejection

The distribution of time intervals, with a typical value of 55 yr, for the knots close to the protostar, suggests that the knot ejection process is periodic with a typical period of 55 yr. Based on their dynamical age, it is possible to attribute to each knot a number "n", referring to the specific ejection period (or time) which led to the formation of that knot. These period numbers are reported in Table 5.1. We have reported in Fig. 5.7 the distribution of knot dynamical ages as a function of their period number. The typical error assumed on the knot location corresponds to a synthetic beam size (HPFW) of the CO ($\sim 1''$) J=2-1 map, from these we could infer the error for Δn as being around 1 on the period n.

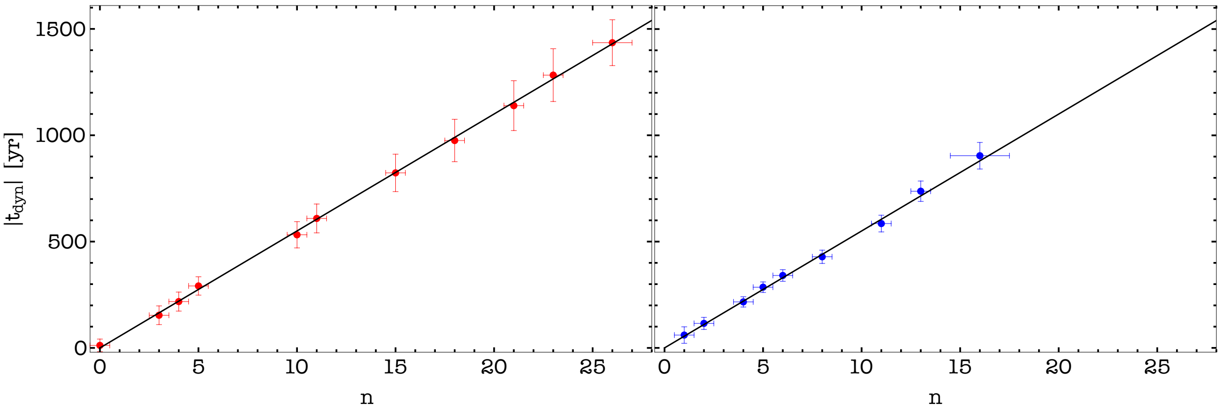

Figure 5.7: Distribution of knot dynamical ages as a function of the number of periods of the periodic mass-ejection mechanism n in the northern (left panel) and southern (right panel) lobes.

By inspecting Figure 5.7, it is possible to identify that several knots have a counterpart in the other lobe, suggesting then that they are associated to the same mass-ejection episode. For instance, N0 and S1 correspond to $n = 4$, N1 and S2 to $n = 5$ and N3 and S5 to $n = 11$. The knots with lower n values ≤ 12 are observed at close distances each other and are possibly associated with successive ejections. On the other hand, the further knots, with higher $n > 12$, do not share the same behavior displaying higher distances between themselves. We note a bimodal distribution between knots that is surprising, a priory, if the ejection process is periodic. Therefore, we have searched for a process that could explain why there is such distribution.

Analyzing the velocity distribution of knots, one can notice that N0a, N0b and N0 were ejected with different velocities. While N0a moves at $V \approx 55\,\mathrm{km\,s^{-1}}$, N0b is moving away at $V \approx 40\,\mathrm{km\,s^{-1}}$, but they are separated by $\sim 1.8''$ ($\sim$ 1500 au). Which means that in about 500 yr and at a distance of $\sim 8''$ from the protostar, N0a will catch up and collide with N0b. This collision time scale would correspond to a period $n \sim 11$, which is around the threshold in which no subsequent ejections are traced. This argument is also supported by the fact that knots with dynamical ages higher than 500 years have higher masses than younger knots.

We can, therefore, conclude that the bimodal knot distribution observed in the jet of Cep E can be explained as the result of collision(s) of subsequent knots ejected at different velocities. The knot S0a is quite elongated and we speculate that it might be a consequence of a knot collision. However, in order to resolve the spatial structure of knots, a higher angular resolution than it than the ones we have at the moment is necessary. Only with high resolution we will be able to fully resolve the structure of the knots and to search for the so called reverse shocks that are expected to form between colliding knots ejected.

The case of HH 377

As previously discussed, HH 377 does not have the same physical properties as jet knots. Ayala et al. (2000) carried out a detailed study based on optical and infrared spectroscopy, in particular H_2 lines. They derived rotational temperature of $\sim 2000\,\mathrm{K}$ and concluded that the emission arises from shock in dense gas. Not having spectral resolution high enough, their estimate of shock velocity is based on models and they found that a wide range of solutions was possible.

An important result of the study of Ayala et al. (2000) is that the line emission they detect arises from a shock propagating in ambient dense gas $\sim 10^5$ cm^{-3} or more, results latter confirmed by the multi-line analysis performed by Lefloch et al. (2015). This density is much higher than the estimated in the northern lobe, as evidenced by the morphology of the low-velocity outflow which is widely open, unlike the southern lobe which remain compact up to the terminal bowshock. The mass of HH 377 is estimated to be $6 \times 10^{-3}\, M_\odot$, which corresponds to the moss of 5–6 knots. This is probably a lower limit as a standard CO/H_2 ratio was assumed in the mass derivation. It is worth remembering the size of HH 377 is somewhat larger than that of the knots. Whereas they have typically circular sizes of $1.5''$–$2''$ in the southern lobe, HH 377 is actually more extended in the direction transverse to the jet, which results into a transverse size of $\sim 4.5''$ (Lefloch et al., 2015).

The conclusion is that HH 377 is massive enough that several knots from the jet may have impacted into the terminal shock and produced this extended and bright shock region. If we follow our cumulative mass-loss rate analysis, the mass of HH 377 corresponds to an age of 670 yr, therefore, the dynamical age of the southern jet would be actually $\sim 1410\,\mathrm{yr}$ which is the 670 added to the dynamical age of S6. This value actually agrees with the lack of knots in the period number range $n = 17 - 26$ in the southern lobe, whereas in the same range, there are four knots in the northern lobe.

5.6 Jet wiggling

Another feature that can be noticed from Figure 5.1 is that the jet lobes have their main axis, which we determined and are displayed by the black arrows, but the knots central peaks do not follow exactly all over these axis which implies therefore that the jet is wiggling. Few models have been proposed to account for the change in the ejection direction, some of them are:

- jet precession due to tidal interactions between the associated protostellar disk and a non-coplanar binary companion (Terquem et al., 1999). Since jets are expected to originate from the disk inner parts, their orientation relative to the orbital plane will be determined by that of the disk inner regions;

- the orbital motion of a binary system initially introduced by Masciadri & Raga (2002), which explains by simply implying that the source driving the jet is orbiting a companion, and the orbital movement is responsible for producing the wiggling;

- a misalignment between the disk rotation axis, and the ejection mechanism (Frank et al., 2014) attributed to the disk magnetic field of the disk. In this scenario, only a single protostar is required.

Since the angular resolution of our observations (0.5″ for SO and 1″ for CO) does not allow us to probe the disk scale or the jet launch region, we had to limit our exploitation and therefore consider only the two following classes of periodic mass-ejection models to account for the wiggling: a) jet precession and b) orbital motion around a binary companion. Both models produce a garden-hose effect (Raga et al., 1993): close to the source, the jet propagates almost parallel to the main jet axis, while further downstream, the side-to-side wiggling is amplified as the fluid parcels ejected in different directions diverge from each other. The outflow morphology allows distinguishing between the two models: an antisymmetric S-shape is observed in the precession scenario, while a mirror-symmetric W-shape is observed in the orbital motion scenario (e.g., Raga et al., 1993; Masciadri & Raga, 2002; Noriega-Crespo et al., 2011; Velázquez et al., 2013; Hara et al., 2021). A simple representation of these two scenarios are presented in Figure 5.8, on the left panel it is displayed the S-shape to account for the precession and on the right hand side, it is shown the binary interaction causing the jet to have a projection of W-shape. It is important to remember that it is a simple illustration, since several factors were not included for sake of simplicity (e.g. magnetic field, ejection material coming from the protostellar disk, and others).

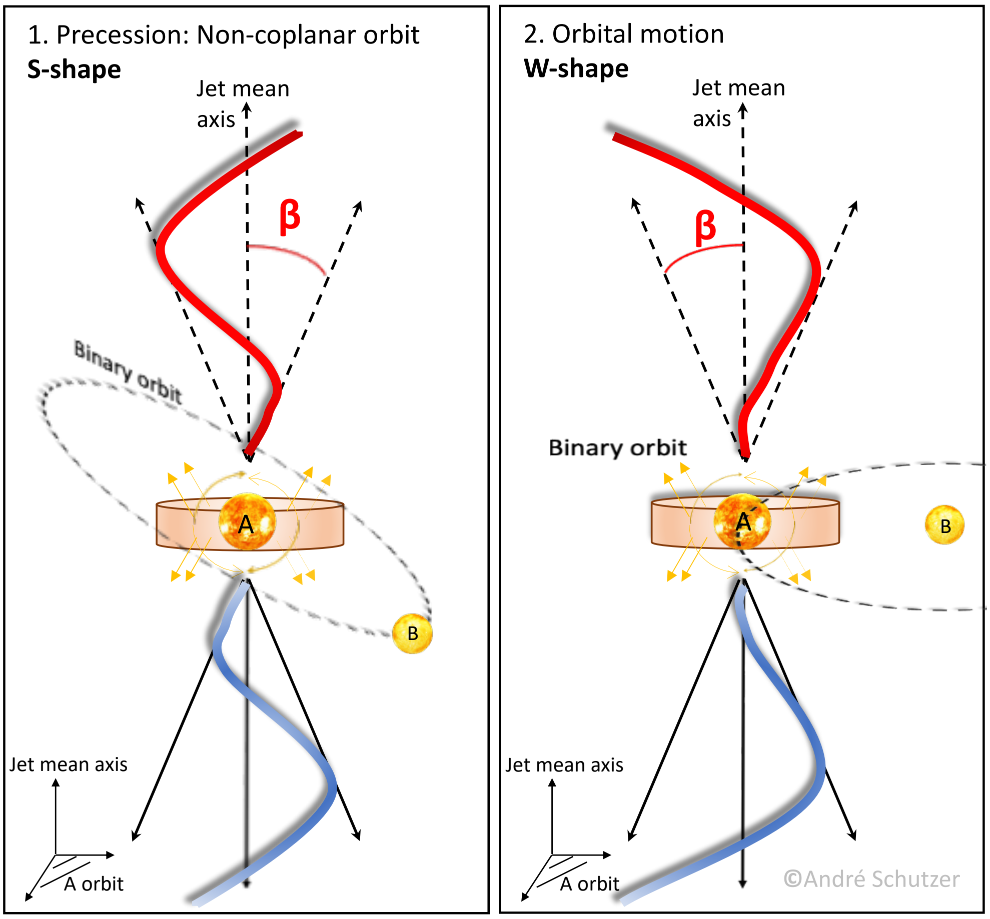

Figure 5.8: Scenarios to account for the jet wiggling in Cep E. (Left): Jet precession that displays an S-shape projection of the jet, this process is often caused due to non-coplanar orbits from a binary companion. (Right): Orbital motion scenario that shows a mirror-symmetric W-shape in the jet, it is due to orbital motion of the star powering the jet around a binary.

5.6.1 Precession

Eisloffel et al. (1996) and Noriega-Crespo et al. (2014) have already presented precession models for the jet of Cep E in the past, but with less accuracy than the one discussed here, thanks to the high resolution of the CO and SO data. In our model, we consider a jet precessing inside a cone of main axis z and half opening angle β. The jet makes a spiral pattern described by the following parametric equations (Raga et al., 1993):

$$x = z \tan\beta \sin\left(\frac{2\pi}{\lambda} z + \phi\right) \tag{5.2}$$

$$y = z \tan\beta \cos\left(\frac{2\pi}{\lambda} z + \phi\right), \tag{5.3}$$

where λ is the spatial period and ϕ is the phase angle. In general, the precession axis makes an inclination angle i with respect to the plane of the sky and the projected coordinates (α',δ') in this plane are given by

$$(x', \alpha', \delta') = (x\cos i + z\sin i, y, z\cos i - x\sin i). \tag{5.4}$$

We adopted an inclination angle $i = 47°$ (see Chapter 2). We first determined the parallactic angle of the jet precession axis z in the plane of the sky, from the average position angle of the lines formed by the source and the knots, including NB and HH 377. Since the wiggling presents different behavior in the northern and southern lobes we, therefore, proceeded independently for the different lobes. We were able to find a misalignment of about 7° between both axes.

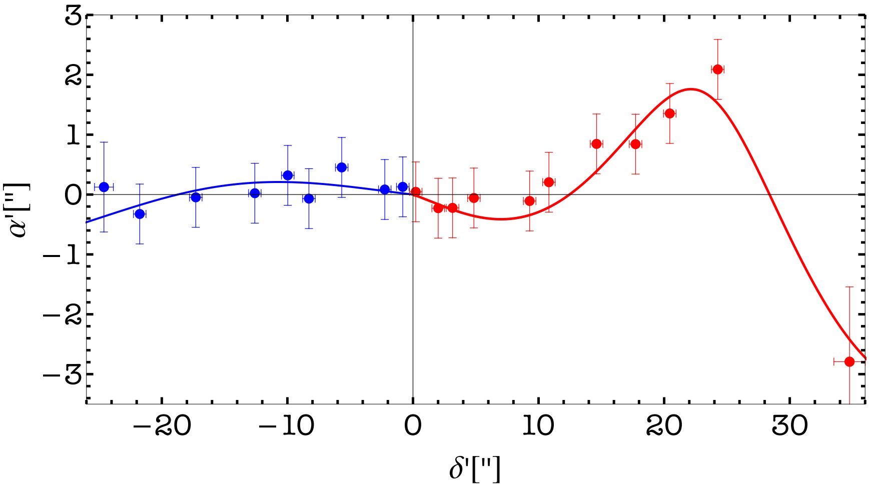

Figure 5.9: Positions of the CO knots with respect to the precession axis in the northern (red) and southern (blue) lobe. The solid line draws the best fitting precession model to the observational data.

After determining the orientation of the jet precession axis z, different from the main jet axis (from Figure 5.1), we computed the coordinates (α',δ') of each knot in the plane of the sky, reported in Figure 5.9. The northern (red) knots show an increasing deviation in the positive α' direction until $\delta' = 26''$. Further away, NB is detected at negative offsets

$\alpha'= -3''$ from the precession axis (west direction in the plane of the sky). In the southern lobe, (blue) knots appear to lie along the precession axis, with small positive offsets at less than $10''$ (8000 au) from the Cep E-A, no significant deviation is seen in this lobe, which is obviously limited by the angular resolution of our observations ($1''$).

The knot spatial distribution displayed in Fig. 5.9 around the driving protostar at $\delta'= 0''$ is consistent with an S-shape symmetry. On the contrary, a W-shape symmetry would require a knot distribution with negative offsets in the Southern lobe, which is not compatible with the observational data. We conclude that comparison of the northern and southern knot spatial distributions unambiguously **favors the S-Shape geometry** to account for the jet wiggling in Cep E.

Table 5.2: Parameters of the jet precession model: length period λ, half-opening angle β, total deprojected jet velocity $V_t = V_j/\sin i$ (with $i = 47°$), where V_j is the jet velocity measured from CO 2–1, precession time period τ_p used in the precession model for each outflow lobe and the phase angle ϕ.

	λ ($''$)	V_t ($\mathrm{km\,s^{-1}}$)	β ($°$)	τ_p (yr)	ϕ ($°$)
North	53.3 ± 0.5	106	3.3 ± 0.2	1960 ± 20	154 ± 5
South	76.7 ± 4.5	163	1.2 ± 0.2	1840 ± 120	168 ± 10

From Equations 5.2, 5.3 and 5.4, we have searched for the parameter set (λ, β, ϕ) which best reproduces the knot positions in the plane of the sky. The northern and southern lobes were modelled separately. We also derive the precession period $\tau_p= \lambda/V_t$, where V_t is the total jet velocity. The best fitting model was obtained through a least-squares method and is drawn as a red (northern lobe) and blue (southern) continuous curve in Fig. 5.9. The output of the best fitting model is shown in Table 5.2.

In order to reduce the number of free model parameters, we have placed an upper limit $\beta \sim 1.2\,°$ on the half opening angle of the southern precession cone. This value was obtained from the maximum deviation of about $1''$ (CO beamwidth) across the jet axis at the position of knot S6. Besides, our model succeeds in reproducing the knot spatial distributions specially in the northern but also in the southern jet. In the latter case, we note however that the variations in the knot distribution are smaller with respect to the position uncertainties, thus the parameters uncertainties computed through the best fitting solution (see Table 5.2) are naturally larger.

The values of the phase angle ϕ and the precession period τ_P are similar in the northern and southern lobes. This is an important result which shows that the same process can account for the properties of both lobes and the symmetry of the mass-ejection. The higher radial velocity of NB can also be account for by our model. Finally, as can be seen in Table 5.2, the differences in the alignment of the precession axes, the jet velocities and the half-opening precession angle can be interpreted as different environmental conditions between the outflow lobes, which already has been discussed by Hirth et al. (1994) and Velázquez et al. (2014).

5.6.2 Orbital motion

It was Masciadri & Raga (2002) who first proposed that the orbital motion of a binary system could account for the wiggling morphology of outflows. In their model, the half-opening angle is determined by the ratio between the orbital velocity and the total jet velocity $\tan\beta = V_o/V_t$. Also, the authors related the distance Δz ($\sim 23''$ for Cep E) between a maximum and a minimum in y, to the separation r_0 of the two binary components:

$$\Delta z = \frac{2\pi r_0}{\tan\beta}, \tag{5.5}$$

which implies $r_0 \sim 140$ au and an orbital period τ_o of

$$\tau_0 = \frac{2\pi r_0}{V_o} = \frac{\Delta z}{V_t} \sim 700\text{yrs}, \tag{5.6}$$

at the distance of Cep E-mm (819 pc). Then, we estimate a typical mass

$$M_s = \frac{16\pi^2 r_0^3}{\tau_o^2 G} \sim 20\mathrm{M}_\odot \tag{5.7}$$

for both protostars from the binary system. In the original work of Masciadri & Raga (2002), they derived the relation above under the assumption of same mass for both components, which is not true for Cep E. The value obtained in equation 5.7 can not be related to the luminosity reported for the protostellar core (see Chapter 2 and Lefloch et al., 1996), as well as the core masses derived from the dust thermal emission at arcsecond scale by Ospina-Zamudio et al. (2018). Moreover, if it is assumed the same orbital period and we apply Equation 5.7 to Cep E-B, which is $1.2''$ distant (~ 9000 au) from Cep E-A, the mass required would be even larger than the one obtained in Equation 5.7.

Therefore, the orbital motion scenario can not be accounted for the shape of the jet wiggling as determined by the knot spatial distribution along the jet which, as discussed, follows an S-shape. Together with the values obtained for the orbital motion, which are inconsistent with the properties of the protostellar core, we confirm that the jet wiggling is caused due to the tidal interaction between the protostellar disk driving the jet and a non-coplanar binary companion.

In the past, based on the parameters estimated by Eisloffel et al. (1996), Terquem et al. (1999) have applied their precession model to Cep E and concluded that the system is a very close binary separated by $r_0 = 4$–20 au, and a disk significantly small of radius $R \simeq 1$–10 au. Therefore, in the scenario proposed by Terquem et al. (1999), Cep E-B cannot be responsible for the precession observed in the jet from Cep E-A. Taking into account the much longer precession timescale implied by our new model (≈ 1900 yr) in comparison with the 400 yr, the separation of the binary increases by a factor 2 up to 8–40 au ($0.01''$–$0.05''$) but unfortunately, with our NOEMA observations at $0.4''$ it is impossible to unveil this region.

5.7 Summary and conclusions

My first work (de A. Schutzer et al., 2022) was dedicated to building a kinematic scenario for the jet of Cep E and to do so, I took advantage of the highest angular resolution data available to me, which were CO J=2 − 1 at 1″ and SO N_J=5_4 − 4_3 at 0.5″. We identified two components in the jet: an internal, narrow and collimated (∼ 0.5″, 400 au); and an external broader gas layer (∼ 1.2″, 1000 au). The jet shows evidence for mass-ejection variability, traced by the many internal shocks detected (18) along the high-velocity lobes. A dynamical timescale of 55 years between subsequent ejections close to the protostar (< 1000 au) with velocity variability that could permit knot collisions at < 10″ was found. Moreover, a gas acceleration is taking place at arcsecond scale. At this scale, we also observed that part of the material from the envelope is being entrained by the high velocity jet and dragged away, a process which occurs up to several 1000 au from the protostar. We computed the mass-loss rate through a cumulative mass function for both lobes of the jet and obtained $\dot{M}= 8.9 \times 10^{-6}\, M_\odot\, \mathrm{yr}^{-1}$ in the southern and $\dot{M}= 2.7 \times 10^{-5}\, M_\odot\, \mathrm{yr}^{-1}$ in the northern lobe, therefore, three times higher in the northern. In this lobe, we also reported two knots N3 and N6 which present higher masses than others, with values two to three times higher, that could indicate an interaction with ambient gas at these locations. Finally, we investigated the wiggling measured by the knots spatial distribution along the jet main axis, and we propose that jet precession originates in tidal perturbations of the associated protostellar disk by a binary companion.

The results presented throughout this chapter are key on the understanding of the processes taking place at small and large scale in the jet of Cep E, as well as the interaction between the jet and the low velocity material: ambient gas entraining and interaction with the low-velocity outflow.

This work has been published in Astronomy and Astrophysics. Title: SOLIS. XVI. Mass ejection and time variability in protostellar outflows: Cep E. (de A. Schutzer et al. A&A, 662, A104). It can be accessed through this link. The published version is also found bellow.

A&A 662, A104 (2022)
https://doi.org/10.1051/0004-6361/202142931

Astronomy & Astrophysics

SOLIS

XVI. Mass ejection and time variability in protostellar outflows: Cep E

A. de A. Schutzer[1], P. R. Rivera-Ortiz[1], B. Lefloch[1], A. Gusdorf[2,3], C. Favre[1], D. Segura-Cox[4,5,⋆],
A. López-Sepulcre[1,6], R. Neri[6], J. Ospina-Zamudio[1], M. De Simone[1], C. Codella[7,1], S. Viti[8,9], L. Podio[7],
J. Pineda[4], R. O'Donoghue[9], C. Ceccarelli[1], P. Caselli[4], F. Alves[4], R. Bachiller[10], N. Balucani[11,1,7], E. Bianchi[1],
L. Bizzocchi[4,12], S. Bottinelli[13,14], E. Caux[13], A. Chacón-Tanarro[10], F. Dulieu[15], J. Enrique-Romero[1,16],
F. Fontani[7], S. Feng[4], J. Holdship[8,9], I. Jiménez-Serra[17], A. Jaber Al-Edhari[1,18], C. Kahane[1], V. Lattanzi[4],
Y. Oya[19], A. Punanova[20], A. Rimola[16], N. Sakai[21], S. Spezzano[4], I. R. Sims[22], V. Taquet[7], L. Testi[23,7], P. Theulé[24],
P. Ugliengo[25], C. Vastel[13,14], A. I. Vasyunin[20], F. Vazart[1], S. Yamamoto[19], and A. Witzel[1]

(Affiliations can be found after the references)

Received 16 December 2021 / Accepted 8 March 2022

ABSTRACT

Context. Protostellar jets are an important agent of star formation feedback, tightly connected with the mass-accretion process. The history of jet formation and mass ejection provides constraints on the mass accretion history and on the nature of the driving source.

Aims. We characterize the time-variability of the mass-ejection phenomena at work in the class 0 protostellar phase in order to better understand the dynamics of the outflowing gas and bring more constraints on the origin of the jet chemical composition and the mass-accretion history.

Methods. Using the NOrthern Extended Millimeter Array (NOEMA) interferometer, we have observed the emission of the CO 2–1 and SO $N_J = 5_4$–4_3 rotational transitions at an angular resolution of 1.0″ (820 au) and 0.4″ (330 au), respectively, toward the intermediate-mass class 0 protostellar system Cep E.

Results. The CO high-velocity jet emission reveals a central component of ≤400 au diameter associated with high-velocity molecular knots that is also detected in SO, surrounded by a collimated layer of entrained gas. The gas layer appears to be accelerated along the main axis over a length scale $\delta_0 \sim 700$ au, while its diameter gradually increases up to several 1000 au at 2000 au from the protostar. The jet is fragmented into 18 knots of mass $\sim 10^{-3}\ M_\odot$, unevenly distributed between the northern and southern lobes, with velocity variations up to 15 km s^{-1} close to the protostar. This is well below the jet terminal velocities in the northern (+65 km s^{-1}) and southern (−125 km s^{-1}) lobes. The knot interval distribution is approximately bimodal on a timescale of ∼50–80 yr, which is close to the jet-driving protostar Cep E-A and ∼150−20 yr at larger distances >12″. The mass-loss rates derived from knot masses are steady overall, with values of $2.7 \times 10^{-5}\ M_\odot$ yr^{-1} and $8.9 \times 10^{-6}\ M_\odot$ yr^{-1} in the northern and southern lobe, respectively.

Conclusions. The interaction of the ambient protostellar material with high-velocity knots drives the formation of a molecular layer around the jet. This accounts for the higher mass-loss rate in the northern lobe. The jet dynamics are well accounted for by a simple precession model with a period of 2000 yr and a mass-ejection period of 55 yr.

Key words. ISM: jets and outflows – ISM: kinematics and dynamics – stars: formation

1. Introduction

The earliest stages of the low-mass star formation process are associated with powerful mass-loss phenomena in the form of high-velocity (∼100 km s^{-1}) collimated jets. These jets accelerate the ambient circumstellar gas and drive the formation of low-velocity (∼10 km s^{-1}) molecular outflows (Raga & Cabrit 1993), commonly observed in the millimeter lines of CO (Bachiller 1996). Although the actual jet launch mechanism is still debated (e.g., Bally 2016), it is well established that mass-loss phenomena take their origin in the inner 1–100 au around the nascent star, and their interaction with the dense surrounding protostellar gas is expected to play a major role in the formation of protostellar jets themselves (Frank et al. 2014). Jet-outflow systems have also been proposed to remove angular momentum from the central protostellar regions and in this way to allow material accretion from the disk onto the central object (Frank et al. 2014). Therefore, the formation of jet-outflow systems seems to be an indispensable mechanism in the process of mass accretion by the protostar. Retrieving the history of the jet may provide some constraints to the mass accretion history.

The time variability of the mass-ejection phenomena associated with young stellar objects was identified a long time ago in studies of Herbig–Haro (HH) objects. These studies revealed knots and wiggling structures. Measurements of the proper motion of HH objects showed direct evidence of velocity variations (Reipurth & Bally 2001). Close to the powering source(s) of the HH jet(s), chains of aligned knots are detected, while at larger distances, disconnected heads with lower velocities trace the impact against the ambient cloud. Raga et al. (1990) showed that velocity variability in the ejection process drives the formation of internal working surfaces, where the fast jet material catches up with the slow material. This results in bright emission knots along the jet, while the ejection direction variability produces a garden-hose effect in which the ejected material diverges from an equilibrium-axis position. The distribution of knot dynamical ages measured in class I atomic jets suggests

---

[⋆] NSF Astronomy and Astrophysics Postdoctoral Fellow.

that there are up to three superposed ejection modes with typical timescales of a few 10 yr, 10^2 yr, and 10^3 yr, respectively (Raga et al. 2002).

The wiggling structure observed in molecular outflows has been interpreted and successfully modeled in terms of variability of the ejection direction (see, e.g., Gueth et al. 1996; Eisloeffel et al. 1996; Ferrero et al. 2015; Podio et al. 2016; Lefèvre et al. 2017). Several theoretical models have been proposed to explain this phenomenon (Masciadri & Raga 2002; Terquem et al. 1999; Frank et al. 2014), but direct observational constraints are still lacking. It seems, however, that most of the identified precessing jets arise from multiple protostellar systems, which suggests that the presence of companion(s) probably plays a role in the origin of the phenomenon. The precession periods derived toward class 0/I objects range from ~400 yr to 5×10^4 yr (Frank et al. 2014).

Recently, the IRAM Large Program Continuum And Lines in Young ProtoStellar Objects (CALYPSO) has significantly enhanced the statistics for the properties of molecular protostellar jets and their outflows by targeting a sample of 30 nearby (d < 450 pc) protostellar sources, mainly in the class 0 stage, which were observed in selected millimeter transitions of CO, SiO, and SO (Podio et al. 2021). A high detection rate (>80%) of high-velocity collimated jets was reported for sources with $L > 1\,L_\odot$, with a velocity asymmetry between the jet lobes for ~30% of the sample. Interestingly, half of the 12 protostellar jets detected in SiO display evidence for bending axes, which is suggestive of precession or wiggling.

High-angular resolution observations of class 0/I protostellar jets with ALMA and NOEMA, such as HH111, HH212, IRAS 04166+2706, and L1157 (Lefloch et al. 2007; Codella et al. 2007, 2014; Tafalla et al. 2010; Podio et al. 2016; Plunkett et al. 2015), bring strong evidence of time variability of the ejection process in the early protostellar phase. A few observational estimates on timescales have been obtained, as illustrated by Plunkett et al. (2015), who reported an average value of 310 ± 150 yr between subsequent ejection events in outflow C7 in the cluster Serpens South, with a large scatter in the knot distribution. In their study of a cluster of 46 outflow lobes in the star forming region W43-MM1 at 5.5 kpc, Nony et al. (2020) moreover reported clear events of episodic ejection. The typical timescale between two ejecta is estimated as $\sim500^{+300}_{-100}$ yr, consistent with the values reported in nearby low-mass protostars. Uncertainties remain high because of the poorly constrained geometry and the outflow inclination angle with respect to the line of sight. Moreover, as noted by the authors, outflows observed at increasing angular resolution turn out to present several spatial (thus temporal) characteristic scales. Therefore, more observational work is needed in order to make progress on these questions.

In this article, we present a detailed study of the high-velocity molecular jet from the young class 0 intermediate-mass protostellar system CepE-mm (Lefloch et al. 1996, 2015; Ospina-Zamudio et al. 2018). Previous studies showed evidence for time-variability in the molecular outflow/jet emission, associated both with precession (Eisloeffel et al. 1996) and with internal bullets (Gómez-Ruiz et al. 2012; Lefloch et al. 2015; Gusdorf et al. 2017). Using the IRAM interferometer, we have imaged the rotational transitions CO J = 2–1 230 538.00 MHz, a typical tracer of molecular outflows, along the full high-velocity jet at 1″ resolution, and SO $N_J = 5_4–4_3$ 206 176.013 MHz, a probe of molecular jets, at 0.4″ resolution toward the central protostellar core, as part of the SOLIS Large Program (Ceccarelli et al. 2017). We have carried out an observational study of the dynamics of the molecular outflow-jet system and the bullets. We show that the main jet kinematical features can be accounted for by a simple analytic model of the mass-ejection process. In a forthcoming paper (Schutzer in prep.), we will present a detailed study of the unusually rich chemical composition of the jet, and we will show that it originates from the jet structure and its dynamics.

The paper is organized as follows. Section 2 summarizes the main properties of the Cep E-mm protostellar source. We present in Sect. 3 our interferometric observations of the outflow-jet in the CO 2–1 and SO $N_J = 5_4–4_3$ lines. In Sect. 4, we analyze the kinematics of the CO jet-outflow, and we show that the observed jet acceleration traces the jet interaction with the parental envelope. In Sect. 5, we present a detailed study of the molecular knots detected along the jet, and by means of a simple ballistic model, we constrain their formation mechanism and their physical properties (age, mass, and dynamical age). In Sect. 6, we propose a new jet precession model that aims to account for the outflow morphology. Our conclusions are summarized in Sect. 7.

2. Source

Cep E-mm is an intermediate-mass class 0 protostellar system with an luminosity of 100 $L_\odot$ (Lefloch et al. 1996; Chini et al. 2001), embedded in an envelope of 35 $M_\odot$ (Crimier et al. 2010), located in the Cepheus OB3 association at a distance of 819 ± 16 pc (Karnath et al. 2019). Using the NOEMA interferometer, Ospina-Zamudio et al. (2018) presented evidence of a protobinary system with a separation of 1″.35 (1100 au) between component A located at $\alpha_{J2000} = 23^{\rm h}03^{\rm m}12^{\rm s}.8$, $\delta_{J2000} = +61°42'26''.0$ and component B at $\alpha_{J2000} = 23^{\rm h}03^{\rm m}12^{\rm s}.7$, $\delta_{J2000} = +61°42'24''.85$. While both protostars power a high-velocity jet, the outflow from component A attracted attention because of its high luminosity in the near-infrared, in particular in the H_2 rovibrational line S(1) v = 1–0 at 2.12 μm (Eisloeffel et al. 1996), a probe of shocked molecular gas. We refer to the driving protostar as “A” or “Cep E-A” below.

High-velocity molecular jet emission was discovered for the first time by Lefloch et al. (1996) with the IRAM 30m telescope, and it was subsequently imaged at 1″ in the CO 2–1 line using the PdBI by Lefloch et al. (2015). The CO 2–1 velocity-integrated emission of the jet is displayed in Fig. 1. The northern and southern lobes propagate at radial velocities of approximately +65 km s^{-1} and −125 km s^{-1}, respectively, in the ambient cloud ($V_{\rm lsr}$ = −10.9 km s^{-1}). Both lobes have a similar length ~20–25″. The southern jet terminates with the bright object HH377 (Ayala et al. 2000), located at the tip of the molecular jet itself. In the north, the CO jet emission drops at 10″ from the apex of the low-velocity outflow cavity (see Fig. 1), where another more extended bullet, dubbed NB is detected near V = +100 km s^{-1}.

The proper motions of the H_2 bright shock structures, NB and HH377, were determined by Noriega-Crespo et al. (2014) and correspond to tangential velocities of (70 ± 32) km s^{-1} and (106 ± 29) km s^{-1} for the northern and southern components, respectively, after correcting for the recently revised distance to Cep E-mm (820 pc instead of 730 pc). When the radial jet velocity determination from the CO observations is taken into account, this results in a revised jet inclination angle of 47° with respect to the plane of the sky, which is close to the determination by Lefloch et al. (2015). The first indications of precession in the Cep E-mm outflow were reported by Eisloeffel et al. (1996), who detected a wiggling structure and sideways positional effects in the H_2 1–0 S(1) 2.12 μm emission map of the outflow. The evidence for precession in the Cep E-mm

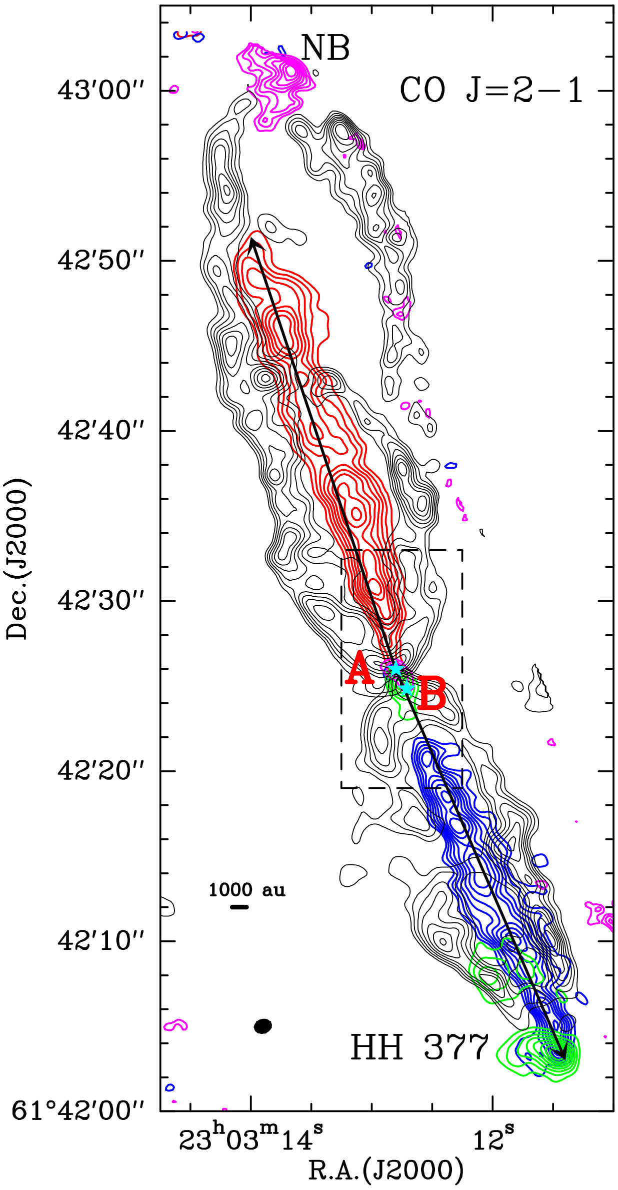

Fig. 1. Emission of the Cep E-mm outflow as observed in the CO 2–1 line with the PdBI at 1″ resolution by Lefloch et al. (2015). Four main velocity components are detected: a) the outflow cavity walls (black) emitting at low velocities, in the range [−8;−3] km s^{-1} and [−19;−14] km s^{-1} in the northern and southern lobe, respectively; b) the jet, emitting at high velocities in the range [−135;−110] km s^{-1} in the southern lobe (blue) and in the range [+40;+80] km s^{-1} in the northern lobe (red); c) the southern terminal bow shock HH377, integrated in the range [−77,−64] km s^{-1} (green); and d) the northern terminal bullet NB integrated in the velocity range [+84,+97] km s^{-1} (magenta). First contour and contour interval are 20% and 10% of the peak intensity in each component, respectively. The synthesized beam (1.″07 × 0.″87, HPBW) is shown in the bottom left corner. The dashed black box encloses the central protostellar region studied with the SO $N_J = 5_4$–4_3 line (see Fig. 2). The main axes of the northern and southern lobes of the jet are shown with black arrows.

outflow appears when inspecting the orientation of the two outflow cavities in the northern outflow lobe, which display a misalignement of ~7°, as shown in Fig. 1. Interestingly, this value also corresponds to the difference between the current jet orientation (red in Fig. 1) and the direction of the line connecting the northernmost knot NB (δ = +35″) to protostar A.

A simple model, assuming an outflow velocity of 200 km s^{-1} and neglecting the inclination of the flow with respect to the plane of the sky, led Eisloeffel et al. (1996) to estimate an opening angle of 4°. More recently, based on numerical simulations, Noriega-Crespo & Raga (2014) showed that the proper motions measured in the infrared in bow shocks could be explained by a jet precession angle of 10°. Although several parameters are markedly different from more recent observational determinations (jet inclination angle of 30° and assumed time-dependent velocity variations of 50% over a 60 yr period), the authors qualitatively succeeded in accounting for the overall features of the Cep E-mm outflow.

An accurate determination of the gas physical and dynamical properties (density, temperature, mass, and momentum) in the low-velocity outflow and the jet were obtained from a detailed CO multiline analysis by Lefloch et al. (2015) and Ospina-Zamudio et al. (2019). The authors showed that in the southern lobe, the jet carries enough momentum (1.7 $M_\odot$ km s^{-1}) to accelerate the ambient gas and drive the low-velocity entrained gas (2.6 $M_\odot$ km s^{-1}). CO emission knots were found inside the southern jet, with sizes of 2″–4″ and peak velocity variations of several km s^{-1}. They proposed that these knots trace internal shocks, which would cause the hot (400–750 K) gas component detected inside the jet. As a conclusion, CepE -mm is a clear-cut case of a jet-driven protostellar outflow, whose in-depth study may shed new light on the formation and the dynamics of outflows-jets.

3. Observations

3.1. SO $N_J = 5_4$–4_3

The NOEMA array was used in configuration A with eight antennas on 23 and 30 December 2016 to observe the spectral band 204.0–207.6 GHz toward the Cep E-mm protostellar system as part of the Large Program Seeds Of Life In Space (SOLIS; Ceccarelli et al. 2017). The field of view of the interferometer was centered at position $\alpha(J2000) = 23^h03^m13.^s00$ $\delta(J2000) = +61°42'21.''00$. The wideband receiver WIDEX covered the spectral band 204.0–207.6 GHz with a spectral resolution of 1.95 MHz (≃2.8 km s^{-1}), which includes the rotational transition SO $N_J = 5_4$–4_3 at 206 176.005 MHz. The spectroscopic parameters of the transition were taken from CDMS[1] (Müller et al. 2005). The precipitable water vapor (PWV) varied between 1 mm and 2 mm (between 2 mm and 4 mm in the second night) during the observations. Standard interferometric calibrations were performed during the observations: J2223+628 was used for both amplitude and phase calibration. Bandpass calibration was performed on 3C454.3. Calibration and imaging were performed by following the standard procedures with GILDAS-CLIC-MAPPING[2]. The emission of the SO $N_J = 5_4$–4_3 line was imaged using natural weighting, with a synthesized beam of 0.52″ × 0.41″ and a position angle PA of 359° (see Table 1). Self-calibration was applied to the data. The shortest and longest baselines were 72 m and 760 m, respectively, allowing us to recover emission at scales up to 12″. The primary beam of the interferometer (≈24.4″) allowed us to recover emission up to ~12″ (10^4 au) away from protostars Cep E-A and Cep E-B, while the synthesized beam gave access to spatial scales of ~400 au.

In order to estimate the fraction of the IRAM 30m flux collected by NOEMA, we compared the SO $N_J = 5_4$–4_3 molecular

---

[1] CDMS database: https://cdms.astro.uni-koeln.de/cdms/portal/

[2] http://www.iram.fr/IRAMFR/GILDAS/

Table 1. Properties of the observational dataset.

Line	Frequency (MHz)	Backend (MHz)	$\Delta\nu$ (MHz)	ΔV (km s^{-1})	Config.	Synthetic beam ($'' \times ''$)	PA (°)	rms (mJy beam^{-1})
SO $N_J = 5_4$–4_3	206 176.013	WideX	2.0	2.8	A	0.52×0.41	359	2.2
CO 2–1	230 538.000	WideX	2.5	3.3	AB	1.07×0.87	+73	1.8

Notes. The following properties are presented: spectral bands, backend, spectral resolution $\Delta\nu$, configuration of the interferometer, synthesized beam size, position angle PA, and rms (mJy beam^{-1}) per element of spectral resolution ΔV (km s^{-1}).

spectrum of the ASAI millimeter line survey of the Cep E-mm protostellar core from Ospina-Zamudio et al. (2018) and the NOEMA spectrum degraded at the same angular resolution. We found that about 34% of the IRAM 30 m flux was recovered by the interferometer.

3.2. CO 2–1

We made use of the CO $J = 2$–1 data obtained at a spatial resolution of ~1″ with the IRAM Plateau de Bure Interferometer (PdBI). The observation procedure and the data were presented in Lefloch et al. (2015). In order to map the molecular emission along the outflow, the 1.3mm band was observed over a mosaic of seven fields centered at the offset positions (−9.0″, −20.8″), (−4.5″, −10.4″), (+0″, +0″), (+4.5″, +10.4″), (+4.5″, +20.8″) with respect to Cep E-A.

As explained by the authors, the emission at scales larger than 10″ was recovered by combining the PdBI data with the synthetic visibilities derived from an IRAM 30 m map of the region. The jet total flux was recovered by the interferometer in both lobes (Lefloch et al. 2015). The intensities were converted from Jy beam^{-1} into K using a conversion factor of 26.88.

4. Jet-envelope interaction

4.1. Molecular gas distribution

The CO and SO emissions from the high-velocity jet in the protostellar region around Cep E-A are displayed in Fig. 2. The line fluxes were integrated in the velocity range [+40;+80] km s^{-1} and [−110;−50] km s^{-1} in the northern and southern lobe, respectively. We observe a very good morphological match between the SO and CO emission distributions at close distance (<2″) from the protostar. Both species trace a strongly collimated jet with a diameter ≤0.4″ (~320 au), unresolved in our observations. At a larger distance (>2″) from protostar A, the CO emission gradually broadens until it reaches a diameter of about 2″ (FWHM), while the SO emission is mainly unaffected. Comparison of CO position-velocity diagrams across the jet main axis in Fig. 3 confirms that the high-velocity emission ($V = 60$ km s^{-1}) is unresolved near the protostar (offset $\delta = 0''$), while it reaches a diameter of 2″ at $\delta > 1.5''$.

Hence, these observations draw the picture of a two-component jet: a central, highly collimated component of diameter <320 au, specifically probed by SO, surrounded by a radially extended gas layer detected in CO. The pattern revealed in our observations is consistent with the pattern recently reported by Podio et al. (2021) in the CALYPSO sample of young low-mass protostellar outflows.

The situation is more complicated in the southern lobe by the high-velocity jet powered by protostar B, which propagates in the east-west direction at 1″ south of protostar A (Ospina-Zamudio et al. 2018). A signature of the B jet is detected as a redshifted clump near 23$^{\rm h}$03$^{\rm m}$13$\overset{\rm s}{.}$0 +61°42′25″ (Fig. 2). We note that the southern (blueshifted) lobe of the A jet displays a highly collimated SO emission, with a diameter similar to that of the northern lobe.

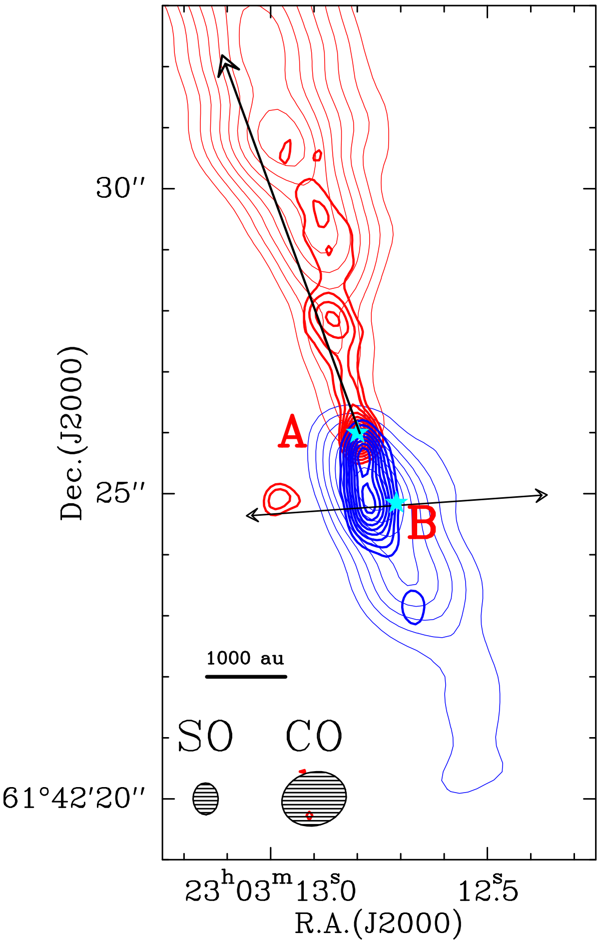

Fig. 2. Distribution of the CO 2–1 and SO $N_J = 5_4$–4_3 velocity-integrated emission in the central protostellar region. Northern lobe (red): emission is integrated in the velocity range [+40;+80] km s^{-1} and is displayed in thin and thick contours for CO and SO, respectively. Southern lobe (blue): emission is integrated in the velocity range [−110;−50] km s^{-1} and is displayed in thin and thick contours for CO and SO, respectively. The velocity interval was chosen in order to include the region of jet acceleration close to the protostar (see Sect. 4.2). The beam sizes (HPBW) of the CO and SO observations (1.07″ × 0.87″ and 0.52″ × 0.41″, respectively) are shown with ellipses in the bottom left corner. The velocity resolution of the CO (SO) observations is 3.3 km s^{-1} (2.8 km s^{-1}). The first contour and contour interval are 20% and 10% of the peak intensity in each component. The arrow draws the main axis of the jet from protostar B (from Ospina-Zamudio et al. 2018).

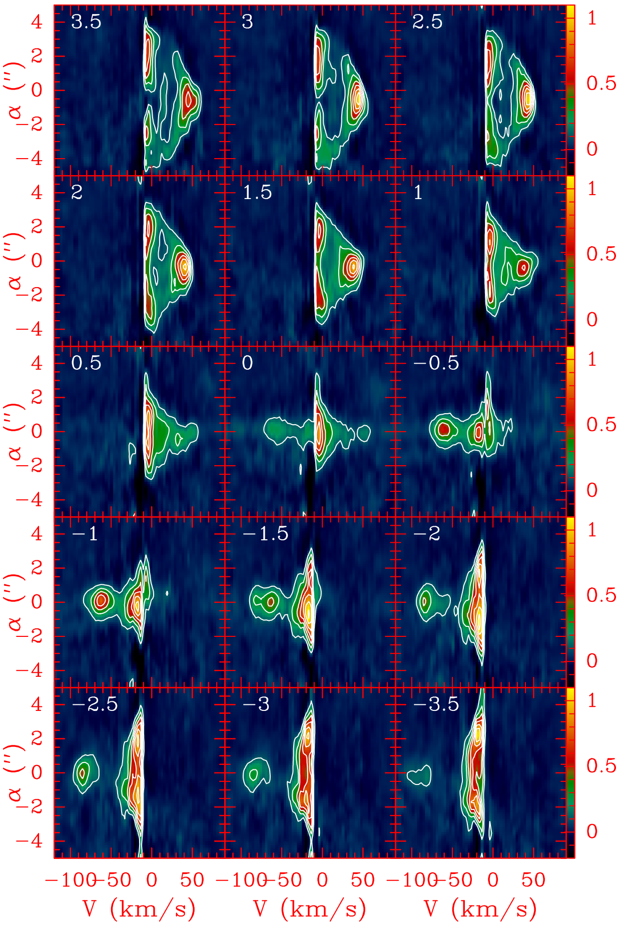

Fig. 3. Position–velocity diagram of the CO 2–1 line emission across the jet main axis (see Fig. 1). The beam size (HPBW) of the CO observations is 1.07″ × 0.87″. The velocity resolution of the observations is 3.3 km s^{-1}. The relative distance to the protostar δ (in arcsecond) is indicated in the top left corner. The first contour and contour interval are 10% and 15% of the peak flux, respectively. Fluxes are expressed in Jy beam^{-1}.

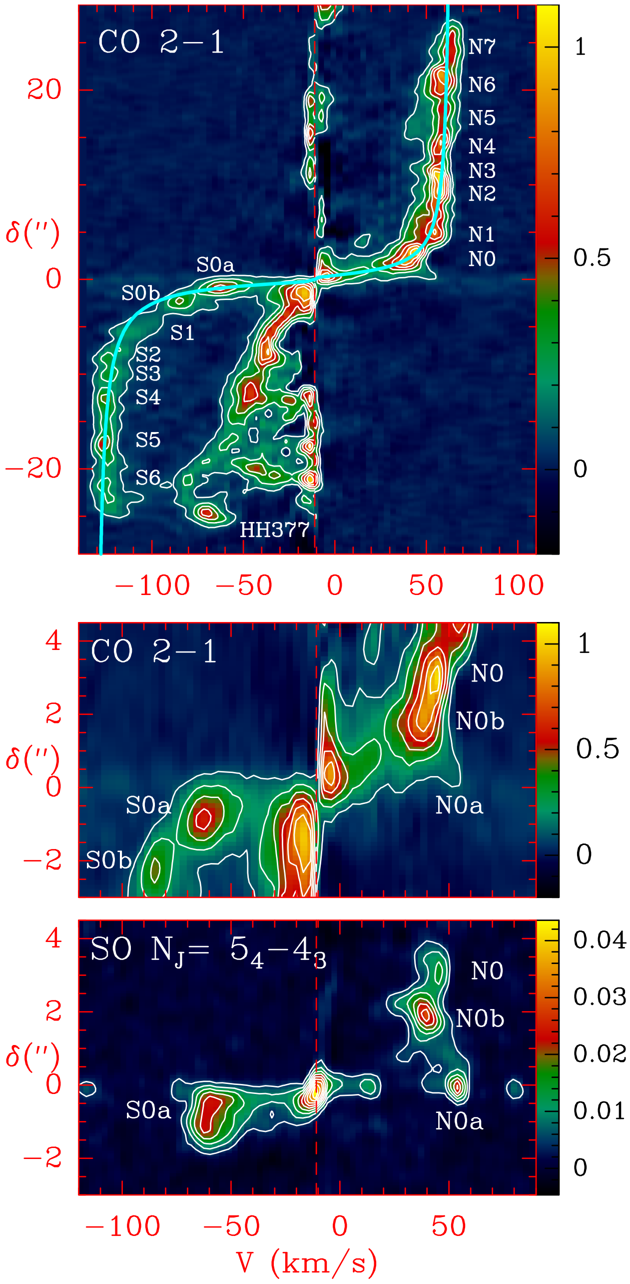

Fig. 4. Position–velocity diagrams of the CO and SO emission along the jet main axis (see Fig. 1). *Top*: CO 2–1 as observed at 1″ with the IRAM interferometer. The different knots identified close to the protostar are indicated. The best-fitting relation to the gas acceleration $|V - V_{\rm lsr}|/V_0 = \exp(-\delta_0/\delta)$ is superimposed in cyan. *Middle*: Magnified view of the CO 2–1 emission in the central protostellar region near Cep E-A. *Bottom*: SO $N_J = 5_4$–4_3 as observed at 0.4″ resolution with NOEMA. The first contour and the contour interval are 10% and 15% of the peak intensity, respectively. The dashed red lines mark the ambient cloud velocity ($V_{\rm lsr} = -10.9$ km s^{-1}). The velocity resolution of the CO and SO observations is 3.3 km s^{-1} and 2.8 km s^{-1}, respectively. Fluxes are expressed in Jy beam^{-1}.

4.2. Jet acceleration

The orientation of the main axis of the jet at large scale was determined from the distribution of the high-velocity CO emission integrated in the intervals [+40; +80] km s^{-1} and [−135; −110] km s^{-1} in the northern and southern lobe, respectively (see Fig. 1). The former is found to make a position angle (PA) of +20°, while the latter makes a PA of +204°. These values based on the large-scale CO distribution are somewhat indicative because of the complexity of the outflow kinematics and the evidence of changes in the direction of propagation along the outflow, as illustrated at large scale by the difference of orientation of the two northern outflow cavities (Fig. 1). This point is discussed in Sect. 6.

The distribution of the CO emission as a function of velocity along the main jet axis is displayed in Fig. 4. The emission is dominated by the protostellar source Cep E-A at $V_{\rm lsr} = -10.9$ km s^{-1}. At large distance from the source ($|\delta| > 10''$), the jet radial velocity V reaches a steady value of ∼+65 km s^{-1} and −125 km s^{-1} in the northern and southern lobe, respectively.

However, in the inner 5″ (∼4000 au) around the protostar, the CO jet displays much lower velocities than the asymptotic values measured at large distances. More precisely, the velocity gradually increases from ambient at $V_{\rm lsr} = -10.9$ km s^{-1} to the terminal value on a scale of a few arcseconds. The radial velocity profile V as a function of distance δ to the protostar along the jet main axis can be fit by the simple relation

$$(V - V_{\rm lsr})/V_0 = \exp(-\delta_0/\delta),$$

where V_0 is the jet asymptotic radial velocity relative to the protostar, and δ_0 is the length scale of the jet acceleration process.

The length scale δ_0 and the jet velocity V_0 (relative to Cep E-A) were determined from a best-fitting procedure to the CO position-velocity diagram. The procedure yields $\delta_0 = 693$ au (590 au) and a jet velocity $V_0 = +75$ km s^{-1} (-118 km s^{-1}) in the northern (southern) jet. The agreement between the best-fitting V_0 values and the observational determination of the jet velocity relative to the source is very good (+76 km s^{-1} and -114 km s^{-1} for the northern and southern lobes, respectively; see Sect. 2 and Fig. 4) and supports our simple modeling. The close agreement between the two values of δ_0 suggests that the physical conditions are similar at subarcsecond scale around Cep E-A.

Intriguingly, the jet appears to be accelerated on a scale of 700 au and exceeds the size of the protostellar disk and hot corino of Cep E-A ~200 au by far (Lefloch et al., in prep.). Inspection of the CO and SO position-velocity diagrams along the major axis of the jet in the central protostellar regions reveals a more complex situation, as shown in the middle and bottom panels of Fig. 4. The CO emission distribution reveals that a small fraction of material is accelerated at velocities up to ~60 km s^{-1} at a few 100 au from protostar A, which is similar to the jet terminal velocity.

The SO $N_J = 5_4$–4_3 emission distribution obtained at 0.4″ resolution, a factor of 2 higher than in the CO observations, brings more insight into the gas acceleration, as shown in Fig. 4 (bottom panel). The bulk of the SO emission arises from three compact knots: N0a, located at less than 0.2″ (~160 au) from Cep E-A, with velocity $V = +54.6$ km s^{-1}, and N0b and N0, detected in the northern jet at $\delta = +2''$, $V = +39.8$ km s^{-1} and $\delta = +3.1''$, $V = +44.5$ km s^{-1}, respectively. Figure 2 shows that the SO emission in the velocity range of these three knots ([+40; +80] km s^{-1}) is unambiguously located in the northern lobe of the Cep E-A jet. As shown by Ospina-Zamudio et al. (2018), the second high-velocity collimated jet powered by the secondary companion Cep E-B propagates in the east-west direction about 1″ south of Cep E-A (see their Fig. 2), nearby enough to raise the question of a possible contamination in the distribution of the molecular gas emission.

However, the spatial distribution of the SO emission at 0.4″ resolution integrated between +40 and +80 km s^{-1} (Fig. 2) shows that all three knots are associated with the Cep E-A northern jet. Interestingly, the bulk velocity of the SO gas appears to vary monotonically between these knots.

To summarize, the analysis of the jet kinematics reveals two components: a component with an extremely high velocity that is highly collimated and originates from the protostar, detected in SO and CO, and a secondary, more extended layer of accelerated gas detected mainly in CO.

4.3. Envelope entrainment

4.3.1. Northern lobe

Inspection of the CO position-velocity diagrams across the jet main axis (Fig. 3) shows that the ambient gas emission extends up to distances of ±4″ from the jet (see, e.g., panel $\delta = +2''$). The CO jet is well identified at $V \simeq +65$ km s^{-1}. In the close environment of the protostar at $\delta = 0''$, the velocity distribution between the outer quiescent regions of the envelope and the jet is continuous, as shown in Figs. 3–4. This means that the ambient quiescent protostellar material from the envelope is dragged away and accelerated by the jet. The CO emission of this entrained component is brighter than the jet material launched from the protostar and its associated knots, hence suggesting an accelerated jet. The gas entrainment is best seen in the PV diagrams $\delta = +0''$ to $\delta = +1.5''$ across the jet main axis (see the top panels in Fig. 3). At larger distances from the protostar, $\delta \geq 2.0''$, the jet signature ($V = +65$ km s^{-1}) gradually separates from the entrained gas emission. This suggests that the entrainment process loses its efficiency as the distance from the protostar increases beyond ~2″ (1600 au).

4.3.2. Southern lobe

The evidence of jet-entrained gas near Cep E-A at $\delta = 0.0$ is much weaker. The emission in the range [−70;−11] km s^{-1} appears to be collimated with a typical diameter of 1.5″, consistent with the value measured in the northern jet in the range [+40;+60] km s^{-1}. The main difference with the northern lobe is that there is no jet entrainment of material at distance >1″ (800 au), that is, that there is far less jet-entrained material in the southern lobe. The CO jet emissivity is inhomogeneous and displays a maximum between $\delta = -1''$ and $\delta = -3''$ (see Fig. 3). This maximum coincides with the region of propagation of the Cep E-B jet, as mapped in the SiO 5–4 line by Ospina-Zamudio et al. (2019). We speculate that the absence of gas entrainment in the southern lobe could result from the interaction between the two outflows-jets.

As discussed by Lefloch et al. (2015), a detailed analysis of the momentum budget in the outflow southern lobe showed that the high-velocity jet carries away the same amount of momentum as the low-velocity gas (1.7 versus 2.6 $M_\odot$ km s^{-1}, respectively). This led the authors to conclude that the low-velocity outflow is driven by the protostellar jet itself. This result is supported by the distribution of the CO emission in the position-velocity diagram along the main jet axis. The top panel of Fig. 4 shows that the low-velocity gas appears to be gradually accelerated from the protostar up to the terminal shock HH377 following a Hubble law relation: $(V - V_{\rm lsr}) \propto \delta$, where δ is the angular distance to the protostar. This kinematical feature is an unambiguous signature of a jet bowshock-driven outflow (Raga & Cabrit 1993; Wilkin 1996; Cabrit et al. 1997).

5. Mass ejection

Bright knots of CO gas in the molecular jet were first reported by Lefloch et al. (2015). In this section, we present a detailed study of the knots and show that a simple ballistic modeling can account for their dynamical properties.

5.1. Kinematics

We have searched for knots along the jet in both the northern and the southern lobes from the CO jet intensity map in Fig. 1 and the CO position-velocity diagram along the jet main axis (Fig. 4). We identified ten (eight) CO knots in the northern (southern) lobe, labeled N0a to N7 (S0a to S6) (see Table 2).

The SO 5_4–4_3 observations provide a more concentrated view of the knots located at a few arcseconds from the protostar. In the northern jet, we detect knot N0a at $\delta = +0.2''$ and $V = +54.6$ km s^{-1} and knot N0b at $\delta = +2.0''$ and $V = +39.8$ km s^{-1} (see the bottom panel in Fig. 4). In the southern jet, we detect a knot, referred to as S0a, near the offset position $\delta = -0.8''$ (and $V = -62.5$ km s^{-1}). We note that the SO emission looks elongated along the jet axis and it is hence unclear whether more than one knot is present. The emission from the southern jet

Table 2. Knot identification and properties.

ID	($\Delta\alpha$;$\Delta\delta$) (″;″)	δ (″)	Size (″)	V (km s^{-1})	ΔV (km s^{-1})	$F_{\rm P}$ (K km s^{-1})	$t_{\rm dyn}$ (yr)	n	Mass (10^{-3} $M_\odot$)
North									
N0a	(+0.1; +0.2)	0.2	0.5	+54.6	12(3)	35(9)	12	0	0.08
N0b	(+0.3; +2.0)	2.0	0.9	+39.8	18.3(0.4)	430(9)	154	3	0.3
N0	(+0.6; +3.1)	3.2	1.4	+44.5	14.1(0.3)	289(7)	218	4	1.9
N1	(+1.2; +4.7)	4.9	1.8	+54.6	18.7(0.7)	351(13)	291	5	3.6
N2	(+2.3; +9.0)	9.3	1.7	+57.2	9.8(0.4)	270(10)	532	10	2.8
N3	(+3.0; +10.4)	10.8	3.0	+58.2	8.5(0.4)	261(12)	609	11	7.8
N4	(+4.6; +13.9)	14.6	2.6	+58.2	9.6(0.4)	197(7)	823	15	4.5
N5	(+5.4; +16.9)	17.8	2.0	+60.2	12.5(0.9)	189(14)	975	18	2.5
N6	(+6.6; +19.4)	20.5	2.9	+59.2	13.3(0.3)	281(6)	1139	21	7.6
N7	(+8.3; +22.9)	24.4	1.9	+63.2	10.2(0.3)	175(5)	1283	23	2.1
NB	(+6.3; +34.3)	34.9	4.0	+83.3	13(2)	70(9)	1440	26	1.3
South									
S0a	(−0.2; −0.8)	−0.8	0.9	−62.5	23.6(0.5)	389(9)	60	1	0.7
S0b	(−0.8; −2.1)	−2.2	1.1	−85.2	19(1)	216(16)	115	2	0.6
S1	(−1.8; −5.4)	−5.7	1.3	−113.5	20(2)	147(11)	218	4	0.5
S2	(−3.3; −7.6)	−8.3	1.7	−124.1	16.0(0.8)	135(7)	286	5	0.8
S3	(−3.6; −9.3)	−9.9	1.8	−124.1	14.7(0.7)	144(7)	341	6	0.9
S4	(−4.9; −11.6)	−12.6	2.3	−125.4	8.4(0.3)	114(4)	429	8	1.3
S5	(−6.8; −15.9)	−17.3	2.0	−126.1	8.4(0.3)	124(5)	585	11	1.1
S6	(−8.8; −19.9)	−21.8	1.4	−126.1	13.2(0.3)	114(6)	737	13	0.5
HH377	(−9.5; −22.7)	−24.6	2.2	−67.0	10.9(0.2)	261(5)	904	16	6.0

Notes. Coordinates, distance to Cep E-A along the jet main axis, size (beam deconvolved), radial velocity, line width, flux at the peak, dynamical age, period number, and mass of the knots in the jet. The dynamical ages for NB and HH377 were directly computed from the proper motions measured by Noriega-Crespo et al. (2014) after correcting for the difference of inclination angle induced by the jet precession.

close to Cep E-A does not display the same fragmented structure as in the north. The similarity in the ejection velocities of S0a and N0a, both at short distance from Cep E-A, suggests that they are associated with the same ejection event and that the physical conditions of jet acceleration are comparable in both lobes.

We derived the main physical properties of the identified knots: coordinates, size (beam-deconvolved), distance d from the protostar, radial velocity V, dynamical age $t_{\rm dyn} = d/V \times \tan i$, and mass. The positions and sizes of the different knots were determined from a 2D Gaussian fit to the CO flux distribution, except for knots N0a-N0b, whose parameters were determined from SO. The velocities were measured in the CO position-velocity diagram in Fig. 4. These parameters are summarized in Table 2. For the sake of completeness, we included the parameters of the terminal shocks NB and HH377 (see Fig. 1).

The knot dynamical ages appear to span the time range 60–1500 yr. Interestingly, HH377 and NB have comparable dynamical ages, so that the two series of knots in the northern and southern appear to cover the same time interval of mass-ejection events.

Figure 5 displays the distribution of knot velocities relative to Cep E-A as a function of the distance to the protostar. We superimposed the best-fitting solutions to the CO position-velocity diagrams in blue and red for the southern and northern lobes, respectively. We adopted an uncertainty of ±0.5″ in position (one beam size) and a value of ±5 km s^{-1} in velocity (mean knot line width) (see Table 2). It immediately follows that all the knots but N0a trace the overall CO gas distribution in the jet. The amplitude of the velocity fluctuations with respect to the bulk of jet material velocity is weak, on the order of a few km s^{-1}.

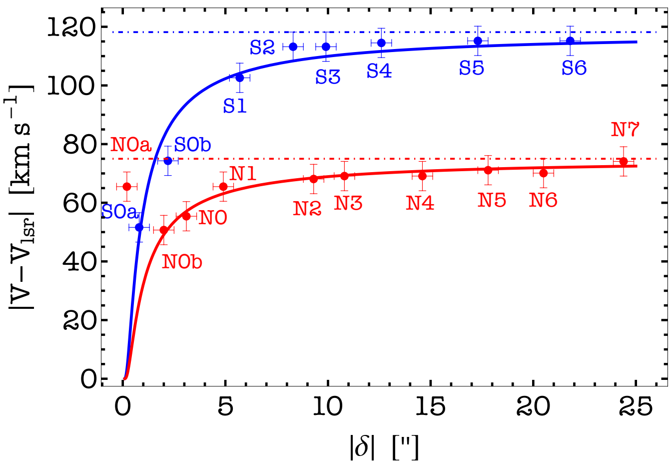

Fig. 5. Distribution of knot velocity peaks along the main jet axis as a function of distance δ to Cep E-A in the northern (red) and southern (blue) jet components. The best fit to the northern (southern) jet velocity relative to the source $(V - V_{\rm lsr})/V_0 = \exp(-\delta_0/\delta)$ with $\delta_0 = 693$ au (δ_0= 590 au) and $V_0 = +75$ km s^{-1} ($V_0 = -118$ km s^{-1}) is drawn by the solid curve.

Knots are not regularly distributed along the jet at equal distances one from the other. At large distance from the protostar, typically 10″, the separation between knots tends to increase from ∼2.5″ to ∼4.5″ in the southern lobe (see Fig. 5). The

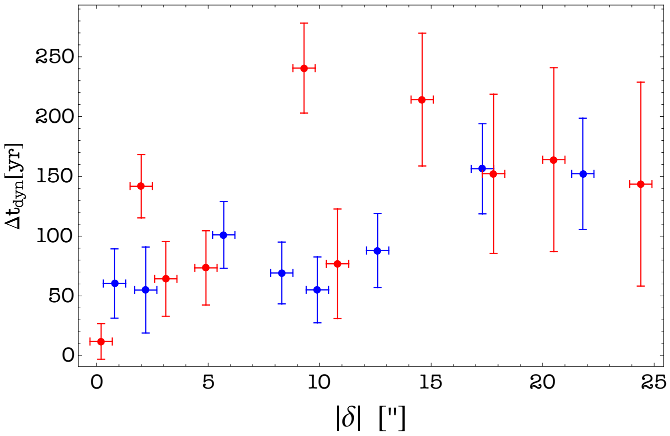

Fig. 6. Distribution of time intervals between subsequent knots as a function of distance to the protostar along the jet main axis in the northern (red) and southern (blue) lobes.

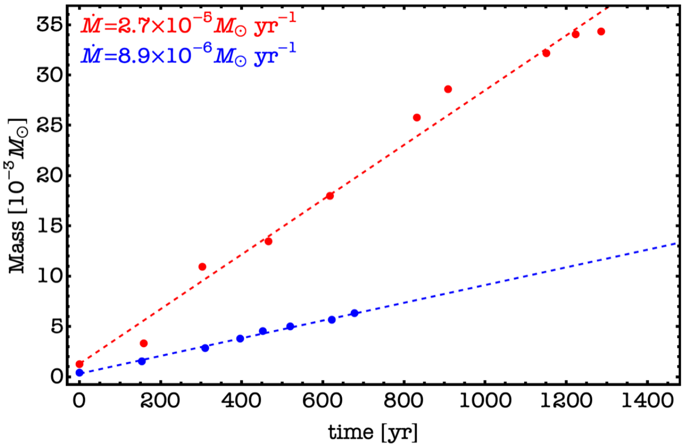

Fig. 7. Cumulative knot mass function in the northern (red) and southern (blue) lobes. Knot NB (S6) and its associated dynamical timescale is taken as reference in the northern (southern) lobe. The best linear fits are drawn by dashed lines.

knot distribution is more complex in the northern lobe, but their separations are on the same order, ~2.5″ (2000 au) and 4.5″ (3700 au) for close (e.g., N2/N3) and remote (N1/N2) knots, respectively. This distribution may be biased by the gas acceleration in the central protostellar regions. For this reason, in order to obtain more insight into the knot distribution, we computed the distribution of time intervals between subsequent knots as a function of distance to the protostar. This is displayed in Fig. 6. A marked separation is observed in the southern lobe (in blue) between the knots located at ≤10–13″ from the protostar, with a short $\Delta t_{\rm dyn}$~50–80 yr, and the more distant knots, with $\Delta t_{\rm dyn}$ ~150–200 yr. A similar pattern is observed in the northern lobe (red), with similar time intervals close to and far away from the protostar. We consider the case of knots N2/N3 at 9–11″ as peculiar; we suspect that this anomaly is caused by the interaction of the knots with the ambient gas.

To summarize, the analysis of the knot interval distribution suggests the presence of two timescales: a short time interval Δt ~ 50–80 yr close (≤12″) to the protostar, and a longer timescale Δt ~ 150–200 yr at larger distances from the protostar. This knot interval distribution could be explained as due to a periodic process that takes place at the base of the Cep E-mm jet. We examine this hypothesis in more detail in the next section.

5.2. Knot mass distribution

We have determined the mean gas column density of the knots from a radiative transfer analysis of the CO 2–1 line emission, using the code MadeX (Cernicharo 2012) in the large velocity gradient approximation and the CO-H_2 collisional coefficients from Yang et al. (2010). In this simple model, we assumed that the CO emission measured toward the knots arises from a single physical component. In other words, the contributions of the entrained gas envelope and the inner jet material along the line of sight, both discussed in Sect. 4.3, were neglected with respect to that of the knots. Line widths and intensities were obtained from a Gaussian fit to the line profiles at the flux peak of the knot (see Table 2). The peak intensity of the knot was sometimes found to lie off the jet main axis by a fraction of a beam. This indirectly reveals a complex knot structure at subarcsecond scale, with some small velocity shifts between the intensity peak and the jet main axis. We adopted the jet H_2 density and temperature derived by Lefloch et al. (2015) and Ospina-Zamudio et al. (2019) in the southern and northern lobes from a CO multitransition analysis. The total H_2 mass and column density were subsequently obtained from N(CO) adopting a standard CO to H_2 relative abundance ratio of 10^{-4}.

We derived knot masses of the order of 10^{-3} $M_{\odot}$ (see Table 2). The knots are more massive in the north than in the south by a factor of a few. In both lobes, the masses of the knots tend to increase beyond 10″ (8000 au), a distance corresponding to knots N3 and S4 in the northern and southern lobe, respectively, or, equivalently, to a dynamical timescale of 500 yr. As discussed in Sect. 4.3, the CO position-velocity diagrams show evidence of protostellar material entrainment by the northern jet only in the central 2″–3″ close to Cep E-A; therefore, it seems unlikely that the observed knot mass increase is related to the jet-envelope interaction. This point is addressed in more detail in the following section, in which we consider the possibility of dynamical interactions of the knots.

The mass of knot NB (1.3×10^{-3} $M_{\odot}$) is similar to that of the other knots, in agreement with the interpretation that NB is the jet terminal bow shock. Our estimate of the HH377 mass was found to agree well with the previous estimate obtained by Lefloch et al. (2015) (≃6×10^{-3} $M_{\odot}$), based on a detailed CO multiline analysis. In other words, the mass of HH377 amounts to that of four to five knots, consistent with the number of undetected knots in the southern lobe. The derived value must be considered a lower limit as the CO abundance could be lower if dissociative J-type shock components were present (see Gusdorf et al. 2017).

5.3. Mass-loss rate

The determination of knot masses and their dynamical timescales allows us to retrieve the mass-loss history of Cep E-A and its variations. We report in Fig. 7 the cumulative mass of ejected knots as a function of time. In this analysis, the origin of the time axis $t = 0$ is defined by the knots NB and S6 in the northern and southern lobes, respectively (strictly speaking, HH377 is not a simple knot, as discussed in the next section). Then, the cumulative mass is obtained by summing one after the other the mass of the subsequently ejected knots; the corresponding time is simply obtained from the distribution of knot dynamical timescales, starting again from the most distant ones

(NB/S6). We note that the reference time $t = 0$ in Fig. 7 differs between outflow lobes as the reference knots NB and S6 taken as reference to compute the cumulative mass function have different dynamical ages.

Figure 7 shows that the cumulative mass function is well fit by a linear function of slope $\dot{M} = 8.9 \times 10^{-6}\, M_\odot\, \mathrm{yr}^{-1}$ in the southern lobe (dashed blue line) and $\dot{M} = 2.7 \times 10^{-5}\, M_\odot\, \mathrm{yr}^{-1}$ in the northern lobe (dashed red line), respectively. We can draw two conclusions from this figure.

First, the mass-loss rate appears steady over the whole knot ejection process in both lobes. We note that the possibility of knot interactions along the jet, as discussed in Sect. 5.4, should not affect the slope of the cumulative mass function, but only the mass of specific ejecta.

Second, the mass-loss rate appears to be higher in the northern lobe by about a factor 3. The main difference between both lobes lies in the fact that northern knots are entraining and accelerating a layer of protostellar material. This phenomenon is not detected in the southern lobe (see Sect. 4.3). It naturally explains the higher amount of high-velocity material in the northern lobe and the difference in the mass-loss rates observed between both lobes. The scatter of the knot mass distribution is also larger, and we propose that it might result from the jet interaction with the ambient medium.

5.4. Ballistic modeling

The observed variability of the separation between knots, as discussed in Sect. 5.1, has usually been interpreted as the result of the superposition of several ejection modes with different periodicity (Raga et al. 2012), related to velocity or density variations in the ejection process. Here, we propose that the minimum time interval between two consecutive knots corresponds to the period of the variable ejection process and that the radial velocity fluctuations reported in Table 2 result from this variability. Then, the apparent bimodal distribution of knot separation can simply be accounted for by dynamical interactions in the nearby environment of protostar A.

From the knot dynamical ages (see Table 2), we estimate a period $\tau_{\mathrm{ej}} = 55$ yr for the ejection process. It is then possible to translate the knot dynamical age into the number of elapsed periods since its formation, so that each knot can be uniquely identified from its associated period number n. This is represented in Fig. 8, where the ages of the individual knots are plotted as a function of the number n of periods of the ejection process. The typical uncertainty on the knot location corresponds to $\sim 1''$, the synthetic beam size (HPFW) of the CO observations, which results in an uncertainty $\Delta n \sim 1$ on the period number n.

Inspection of the knot dynamical ages shows that some events in the northern jet exhibit a counterpart in the southern jet, suggesting that they are associated with the same mass-loss event. This is the case, for example, of knots N0/S1 ($n = 4$), N1/S2 ($n = 5$) and N3/S5 ($n = 11$). As discussed in Sect. 5.1, the knots with low n values ($n < 10$), which are observed at close distance from the protostar, tend to be associated with subsequent ejections, while knots with large period numbers appear to be unevenly distributed (see Fig. 8).

The bottom panel in Fig. 4 shows that the young knots N0a-N0b-N0 are ejected with marked velocity variations. The youngest knot N0a moves at a velocity that is 15 km s^{-1} faster than N0b, while they are separated by 1500 au ($\sim 1.8''$). Hence, it should take about 500 yr for N0a to catch up and collide with N0b. The collision is bound to occur at the typical distance of 6500 au, that is, $8''$ from the protostar. This collision timescale corresponds to a period number $n \simeq 11$. As discussed above (see also Fig. 8), this value of n is the threshold beyond which the knot distribution no longer displays evidence of subsequent ejections. We also note that on average, the mass of the knots is higher for dynamical timescales longer than 500 yr. We conclude that the bimodal knot distribution observed in the jet is most likely the result of collisions between subsequent knots ejected with markedly different velocities.

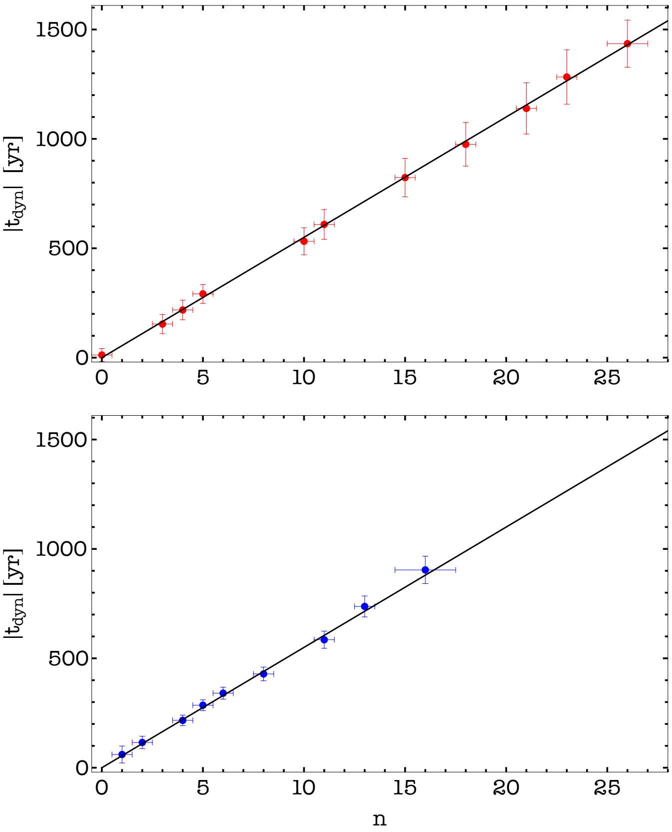

Fig. 8. Distribution of knot dynamical ages as a function of the number of periods of the periodic mass-ejection mechanism n in the northern (*upper panel*) and southern (*lower panel*) lobes.

We speculate that the elongated appearance of knot S0a might trace the interaction of two subsequent ejections. The spatial structure of knots is out of reach at the angular resolution of the CO data. Observations at higher angular and spectral resolutions are required in order to fully resolve the structure of the knots and to search for the reverse shocks that are expected to form between colliding mass ejecta.

Ayala et al. (2000) proposed that HH377 traces the impact of the southern jet in a dense molecular gas clump, explaining that HH377 propagates at a velocity $V \simeq -67$ km s^{-1}, strongly reduced with respect to the jet velocity itself (-125 km s^{-1}). We propose that the southern knots, after they reached the terminal jet velocity $V \simeq -125$ km s^{-1}, propagate along the jet until they finally impact the terminal bow shock. In the impact, their velocity suddenly drops, while their material feeds the HH object. The distance between S6 and HH377 is $\sim 4''$ (3300 au), so that it takes about 270 yr for a knot to cover this distance, which is far shorter than the duration of the mass-loss phase, as estimated from the dynamical age of the oldest northern knots (~ 1500 yr; see Fig. 8).

The mass of HH377 is ~$6 \times 10^{-3}\ M_{\odot}$, which amounts to the mass of ~6 knots (adopting an average knot mass of $10^{-3}\ M_{\odot}$). This number agrees reasonably well with the lack of knots in the range $n = 17$–26 in the southern lobe, whereas four knots are detected in the northern jet. According to our mass-loss rate analysis, the HH377 mass corresponds to the amount of jet material ejected for ~670 yr. This would imply a dynamical age of ~1410 yr for the southern jet, which agrees very well with the dynamical age of knot NB (1440 yr; Table 2), at the tip of the northern jet.

6. Jet wiggling

As recalled in Sect. 1, the cause of the wiggling structure observed in molecular outflows is not completely understood. Several models have been proposed to account for the variability of the ejection direction: orbital motion of a binary system (Masciadri & Raga 2002), jet precession due to tidal interactions between the associated protostellar disk and a noncoplanar binary companion (Terquem et al. 1999), misalignment between the disk rotation axis, and the ejection mechanism (Frank et al. 2014). The latter model requires only a single protostar.

The limited angular resolution of our observations (320–800 au) does not allow us to probe the disk scale or the jet launch region. Here, we consider the two following classes of periodic mass-ejection models proposed to account for the wiggling pattern of protostellar outflows: (i) jet precession and (ii) orbital motion around a binary companion. Both models produce a garden-hose effect (Raga et al. 1993): close to the source, the jet propagates almost parallel to the main jet axis, while further downstream, the side-to-side wiggling is amplified as the fluid parcels ejected in different directions diverge from each other. Outflow morphology allows distinguishing between the two models: an antisymmetric S shape is observed in the precession scenario, while a mirror-symmetric W shape is observed in the orbital motion scenario (e.g., Raga et al. 1993; Masciadri & Raga 2002; Noriega-Crespo et al. 2011; Velázquez et al. 2013; Hara et al. 2021).

6.1. Precession

We adopted a more detailed modeling of the jet precession than the previous works by Eisloeffel et al. (1996) and Noriega-Crespo et al. (2014) by making use of the spatial distribution of knots to constrain the dynamical parameters of the ejection process, under the assumption of ballistic motion. We considered a jet precessing inside a cone of main axis z and half-opening angle β (see the top panel of Fig. 9). The jet produces a spiral pattern described by the following parametric equations (Raga et al. 1993):

$$x = z \tan\beta \sin\left(\frac{2\pi}{\lambda} z + \phi\right) \tag{1}$$

and

$$y = z \tan\beta \cos\left(\frac{2\pi}{\lambda} z + \phi\right), \tag{2}$$

where λ is the spatial period and ϕ is the phase angle. In general, the precession axis makes an inclination angle i with respect to the plane of the sky, and the projected coordinates (α',δ') in this plane are given by

$$(x', \alpha', \delta') = (x \cos i + z \sin i, y, z \cos i - x \sin i). \tag{3}$$

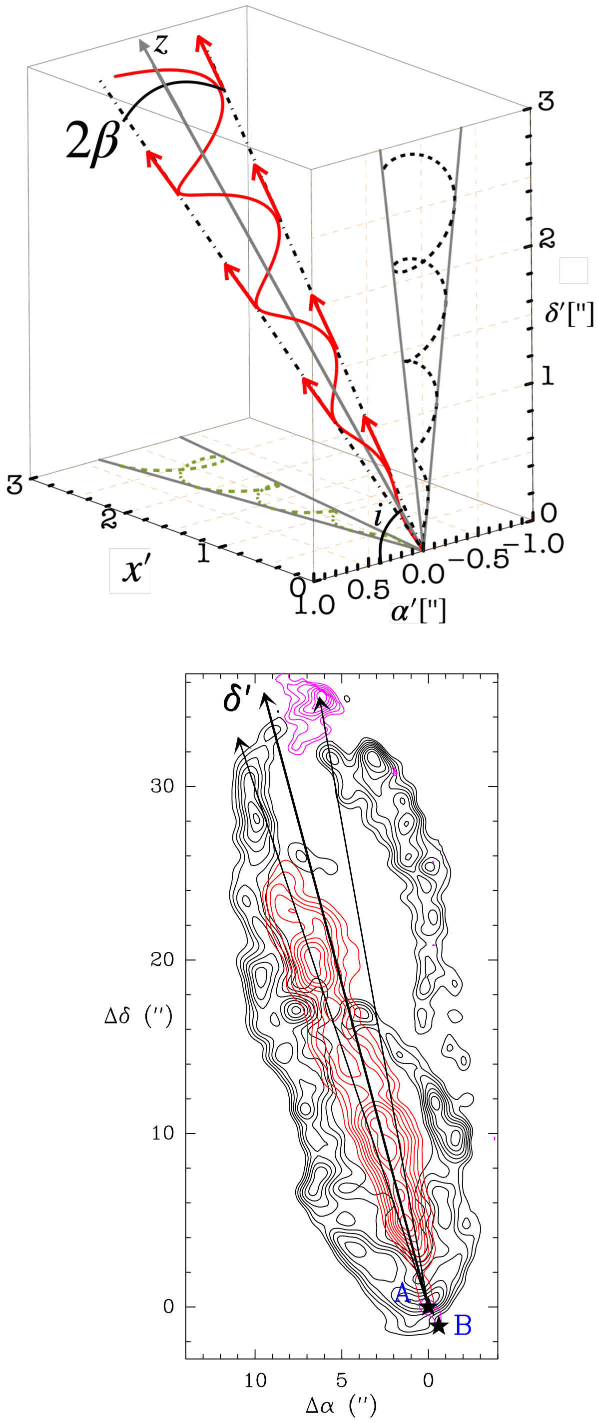

Fig. 9. Jet precession in Cep E. *Top*: wiggling model. The jet precession axis is represented by the continuous gray line. The jet moves over a cone of half-opening angle β. It makes an inclination angle i with respect to the plane of the sky (α',δ'). The locus of the ejection direction is drawn by the red curve. In the plane of the sky (α',δ'), the projection of the locus is represented by the black line. *Bottom*: projected view of the jet axis associated with the current high-velocity emission, the previous ejection associated with knot NB, and the precession axis δ', superimposed on the CO 2–1 outflow emission (see Fig. 1).

We adopted for Cep E an inclination angle $i = 47°$, as mentioned in Sect. 2. We first determined the parallactic angle of the jet precession axis z in the plane of the sky from the average position angle of the lines formed by the source and the knots, including

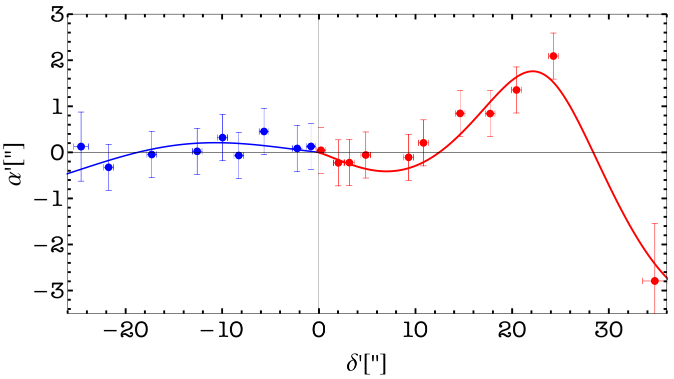

Fig. 10. Positions of the CO knots with respect to the precession axis in the northern (red) and southern (blue) lobe. The solid line draws the best-fitting precession model to the observational data.

Table 3. Parameters of the jet precession model.

	λ (″)	V_t $^{(a)}$ (km s^{-1})	β (°)	τ_p (yr)	ϕ (°)
North	53.3 ± 0.5	106	3.3 ± 0.2	1960 ± 20	154 ± 5
South	76.7 ± 4.5	163	1.2 ± 0.2	1840 ± 120	168 ± 10

Notes. Length period λ, half-opening angle β, total deprojected jet velocity $V_t = V_j/\sin i$ (with $i = 47°$), precession time period τ_p used in the precession model for each outflow lobe, and phase angle ϕ. $^{(a)}$Measured from the CO observations.

NB and HH377. Proceeding independently for the northern and southern lobes, we find a misalignment of about 7° between the two axes. The configuration in the northern outflow is summarized in the bottom panel of Fig. 9: the loci of the current jet, the precession axis δ' , and the direction of the previous ejection associated with knot NB.

After determining the orientation of the jet precession axis z, we computed the coordinates (α',δ') of each knot in the plane of the sky. They are reported in Fig. 10. The northern (red) knots show an increasing deviation in the positive α' direction until $\delta' = 26''$. Farther away, NB is detected at negative offsets $\alpha' = -3''$ from the precession axis. In the southern lobe, (blue) knots appear to lie along the precession axis, with small positive offsets at less than 8000 au from the protostar. The spatial distribution of the knot displayed in Fig. 10 around the driving protostar at $\delta = 0''$ is consistent with an S-shape symmetry. A W-shape symmetry would require a knot distribution with negative offsets in the southern lobe, which is not compatible with the observational data. We conclude that comparison of the northern and southern knot spatial distributions unambiguously favors an S-shape geometry.

Using Eqs. (1)–(3), we then searched for the parameter set (λ, β, ϕ) that best reproduces the location of the knots in the plane of the sky. We modeled the northern and southern lobes separately. From the total jet velocity V_t, we derived the precession period $\tau_p = \lambda/V_t$. The best-fitting model was obtained through a least-squares method and is drawn as a (red/blue) continuous curve in Fig. 10. The parameters of the best-fitting model are presented in Table 3.

Our model succeeds in reproducing the spatial distributions of the knots both in the northern and the southern jet. In the latter case, we note, however, that the variations in the knot distribution are smaller than the position uncertainties, hence enlarging uncertainties in the parameters of the best-fitting solution (see Table 3). The values of the phase angle ϕ and the precession period τ_P are found to be similar between the northern and southern lobes. This is consistent with symmetric ejections, in agreement with the observational data.

Table 3 shows that differences are observed between the northern and southern lobes in the alignment of the precession axes, the jet velocities, and the half-opening precession angle. We propose that this is related to the different environmental conditions between the outflow lobes (Hirth et al. 1994; Velázquez et al. 2014).

Precession changes the direction of the jet propagation with respect to the plane of the sky, and therefore affects the knot radial velocity. Taking into account the inclination of the Cep E jet with respect to the plane of the sky, the half-opening angle of its precession cone can yield velocity variations up to 15 km s^{-1}. Hence, the combined effect of the ejection variability and precession is expected to generate velocity variations of 25 km s^{-1} or more, which could explain the higher radial velocity reported for NB. To conclude, velocity variations as large as those measured between NB and younger knots are consistent with the wiggling dynamics of the Cep E jet; variations like this are expected to be rare as the jet dynamical age is similar to the precession period.

6.2. Origin of the jet wiggling

Masciadri & Raga (2002) first proposed that the orbital motion of a binary system could account for the wiggling morphology of outflows. The authors found that the same description of a precessing jet model could be applied at a distance from the precession axis larger than the binary separation r_0. In this case, the half-opening angle is determined by the ratio of the orbital velocity and the total jet velocity $\tan\beta = V_o/V_t$. Moreover, the authors related the distance Δz between a maximum and a minimum in y ($\Delta z \sim 23''$ for Cep E) to the separation r_0 of the two binary components,

$$\Delta z = \frac{2\pi r_0}{\tan\beta}, \tag{4}$$

which implies $r_0 \sim 140$ au and an orbital period τ_o of

$$\tau_0 = \frac{2\pi r_0}{V_o} = \frac{\Delta z}{V_t} \sim 700\ \mathrm{yr} \tag{5}$$

at the distance of Cep E-mm (819 pc). Then, we estimate a typical mass

$$M_s = \frac{16\pi^2 r_0^3}{\tau_o^2 G} \sim 20\ M_\odot \tag{6}$$

for the components of the binary. In their original work, Masciadri & Raga (2002) derived this relation under the assumption of equal-mass components. This value is too high to be reconciled with the luminosity of the protostellar core (100 $L_\odot$) and the core masses derived from the dust thermal emission at arcsecond scale by Ospina-Zamudio et al. (2018). Applying Eq. (6) to protostar B, which lies at a distance of 1.2″ (~9000 au) from A and assuming the same orbital period, the mass required would be even higher than ~20 $M_\odot$.

As discussed in the previous section, the spatial distribution of the knot along the jet (Fig. 10) appears to agree better with an S-shape than with a W-shape symmetry. The symmetry of the distribution therefore supports jet precession rather than an orbital motion scenario as the origin of the change in outflow direction in Cep E.

To summarize, the orbital motion scenario fails to account for the properties of the spatial distribution of the knot in the Cep E protostellar jet. Our analysis favors a jet precession scenario as origin of the outflow wiggles. As mentioned above in this section, Terquem et al. (1999) proposed that jet precession originates in the tidal interaction between the protostellar disk driving the jet and a noncoplanar binary companion. The authors applied their analytic model to the case of Cep E based on the parameters estimated by Eisloeffel et al. (1996). They concluded that the system is a very close binary with a distance in the range 4–20 au and a small disk radius $R = 1–10$ au. Taking into account the much longer precession timescale implied by our new model, 2000 yr instead of 400 yr, the separation of the binary increases by a factor ~2 up to 8–40 au (0.″01–0.″05), but unfortunately, the linear scales involved remain beyond the reach of the NOEMA interferometer. We note that also in the scenario proposed by Terquem et al. (1999), protostar B cannot be responsible for the precession observed in the jet from protostar A.

7. Conclusions

We have carried out a detailed kinematical study of the high-velocity jet of the intermediate-mass class 0 protostar Cep E-A using observations from the IRAM interferometer at (sub)arcsecond resolution in the CO 2–1 and SO $N_J = 5_4–4_3$ lines. Our conclusions are listed below.

- The CO high-velocity jet consists of two components: a central component with a diameter of ≤400 au associated with high-velocity molecular knots (also detected in SO), and a surrounding gas layer accelerated on a length scale δ_0 ~700 au, whose diameter gradually increases up to several 1000 au at about 2000 au from the protostar.
- Along the main jet axis, the CO gas velocity can be simply fitted as a function of distance δ to the protostar by the relation $(V_r - V_{\rm lsr})/V_0 = \exp(-\delta_0/\delta)$, where $V_{\rm lsr} = -10.9$ km s^{-1} is the ambient cloud velocity, V_0 is the terminal velocity in the jet lobe relative to the source ~+75 km s^{-1} (−118 km s^{-1}), and δ_0 is the length scale ~700 au (600 au) in the northern (southern) hemisphere. Analysis of the CO position-velocity diagrams shows that the jet layer consists of quiescent protostellar material entrained by extremely high velocity knots. The material entrainment appears to be more efficient in the northern than in the southern lobe.
- The jet molecular gas emission reveals 18 bright knots in either lobes of the jet with a dynamical timescale of 55 yr between subsequent ejections close (<1000 au) to the protostar. The knots have a typical size of 2″, with a tendency to increase with distance to the protostar. We have identified knots NB and HH377 as the terminal bow shocks of the northern and southern lobes, respectively.
- Assuming a standard CO abundance of 10^{-4} relative to H_2, a simple radiative transfer analysis in the LVG approximation with MadeX yields a typical mass of $10^{-3}\ M_\odot$ for the bullets. SO observations at 0.4″ show that the knots leave the inner protostellar regions (~200 au) at high velocity, with marked velocity fluctuations between subsequent ejections. The cumulative knot mass function allows us to estimate mass-loss rates of $2.7\times10^{-5}\ M_\odot$ yr^{-1} and $8.9\times10^{-6}\ M_\odot$ yr^{-1} in the northern and southern lobes, respectively. The jet mass-loss rates appear steady with time. The higher mass-loss rate in the north is consistent with protostellar material entrainment by the jet.
- The knot interval distribution between subsequent knots is approximately bimodal with intervals of ~55 yr and ~150 at short (<12″) and large (>12″) distance from the protostar. In the northern jet, the velocity fluctuations are large enough (~15 km s^{-1}) that the spatial separation between knots can be overcome in a dynamical timescale of ≃500 yr, when knots will have traveled a typical distance of 12″ (10^4 au) from the protostar. This naturally explains the lack of knots at large distances from the source. This result is also supported by the higher masses found for the knots at larger distances.
- Analysis of the knot spatial distribution suggests precession as the origin of the wiggling structure of the outflow. Applying the Masciadri-Raga formalism, we obtained an accurate description of the jet morphology, taking into account the outflow inclination angle with respect to the plane of the sky. The same model allowed us to discard binary orbital motions as the source of the Cep E-mm jet wiggling, since it would require protostellar masses too high to be reconciled with the source luminosity and mass. We propose that jet precession originates in tidal perturbations of the associated protostellar disk by a binary companion, yet to be identified, in agreement with previous work by Terquem et al. (1999).

The results discussed throughout this article not just present the kinematic information about the Cep E outflow-jet system the but also allow us to have a closer understanding on the processes involved in the jet formation and interaction of its surroundings. In fact, this study contributes for a better comprehension of the difference between low- and high-mass star formation feedback processes.

Acknowledgements. Based on observations carried out with the IRAM NOEMA interferometer. IRAM is supported by INSU/CNRS (France), MPG (Germany) and IGN (Spain). AS, BL, PR-RO, acknowledge support from the European Union's Horizon 2020 research and innovation program under the Marie Skłodowska-Curie grant agreement No 811312 for the project "Astro-Chemical Origins" (ACO) and the European Research Council (ERC) under the European Union's Horizon 2020 research and innovation program for the Project "The Dawn of Organic Chemistry" (DOC) grant agreement No 741002. DSC is supported by an NSF Astronomy and Astrophysics Postdoctoral Fellowship under award AST-2102405. A.V. and A.P. are the members of the Max Planck Partner Group at the Ural Federal University. A.P. and A.V. acknowledge the support of the Russian Ministry of Science and Education via the State Assignment Contract no. FEUZ-2020-0038.

References

Ayala, S., Noriega-Crespo, A., Garnavich, P. M., et al. 2000, AJ, 120, 909
Bachiller, R. 1996, ARA&A, 34, 111
Bally J. 2016, ARA&A, 54, 491
Cabrit, S., Raga, A., & Gueth, F. 1997, in Herbig–Haro Flows and the Birth of Stars; IAU Symp. 182, eds. B. Reipurth, & C. Bertout (Kluwer Academic Publishers), 163
Ceccarelli, C., Caselli, P., Fontani, F., et al., 2017, ApJ, 850, 176
Cernicharo, J. 2012, EAS, 58, 251
Chini, R., Ward-Thompson, D., Kirk, J. M., et al. 2001, A&A, 369, 155
Codella, C., Cabrit, S., Gueth, F., et al. 2007, A&A, 462, L53
Codella, C., Cabrit, S., Gueth, F., et al. 2014, A&A, 568, L5
Crimier, N., Ceccarelli, C., Alonso-Albi, T., et al. 2010, A&A, 516, A102
Eisloeffel, J., Smith, M. D., Davis, C. J., & Ray, T. P. 1996, AJ, 112, 2086
Ferrero, L. V., Gómez, M., Gunthard, G. 2015, BAAA, 57, 126
Frank, A., Ray, T., Cabrit, S., et al. 2014, Protostars and Planets VI, eds. H. Beuther, R. S. Klessen, C. P. Dullemond, & T. Henning (Tucson, AZ: University of Arizona Press), 451
Gómez-Ruiz, A. I., Gusdorf, A., Leurini, S., et al. 2012, A&A, 542, L9
Gueth, F., Guilloteau, S., & Bachiller, R. 1996, A&A, 307, 891
Gusdorf, A., Anderl, S., Lefloch, B., et al. 2017, A&A, 602, A8
Hara, C., Kawabe, R., Nakamura, F., et al. 2021, ApJ, 912, 34
Hirth G. A., Mundt, R., Solf, J., & Ray, T. P. 1994, ApJ, 427, L99

Karnath, N., Prchlik, J. J., Gutermuth, R. A., et al. 2019, ApJ, 871, 46
Lefèvre, C., Cabrit, S., Maury, A.J., et al. 2017, A&A, 604, A1
Lefloch, B., Eisloeffel, J., & Lazareff, B. 1996, A&A, 313, L17
Lefloch, B., Cernicharo, J., Rodríguez, L. F., et al. 2002, ApJ, 581, 335
Lefloch, B., Cernicharo, J., Reipurth, B., et al. 2007, ApJ, 658, 498
Lefloch, B., Gusdorf, A., Codella, C., et al. 2015, A&A, 581, A4
Maret, S., Bergin, E. A., Neufeld, D. A., et al. 2009, ApJ, 698, 1244
Masciadri, E., & Raga, A. C. 2002, ApJ, 568, 733
Nony, T., Motte, F., Louvet, F., et al. 2020, A&A, 636, A38
Noriega-Crespo, A., Raga, A. C., Lora, V., Stapelfeldt, K. R., & Carey, S. J. 2011, ApJ, 732, L16
Noriega-Crespo, A., Raga, A. C., Moro-Martín, A., et al. 2014, NJPh, 16, 105008
Ospina-Zamudio, J., Lefloch, B., Ceccarelli, C., et al. 2018, A&A, 618, A145
Ospina-Zamudio, J., Lefloch, B., Favre, C., et al. 2019, MNRAS, 490, 2679
Plunkett, A. L., Arce, H. G., Mardones, D., et al. 2015, Nature, 527, 70
Podio, L., Codella, C., Gueth, F., et al. 2016, A&A, 593, L4
Podio, L., Tabone, B., Codella, C., et al. 2021, A&A, 648, A45
Raga, A. C., & Cabrit S. 1993, A&A, 278, 267
Raga, A. C., Cantó, J., Binette, & Calvet, N. 1990, ApJ, 364, 601
Raga, A. C., Cantó, J., & Biro, S. 1993, MNRAS, 260, 163
Raga, A.C., Velázquez, P. F., Cantó, J., & Masciadri, E. 2002, ApJ, 395, 647
Raga, A.C., Rodríguez-González A., Noriega-Crespo A., & Esquivel A. 2012, ApJ, 744, L12
Reipurth, B., & Bally, J. 2001, ARA&A, 39, 403
Tafalla, M., Santiago-García, J., Hacar, A., & Bachiller, R. 2010, A&A, 522, A91
Terquem, C., Eislöffel, J., Papaloizou, C. B., & Nelson, R. P. 1999, ApJ, 512, L131
Tychoniec, Ł., Hull, C. L. H., Kristensen, L. E., et al. 2019, A&A, 632, A101
Velázquez, P. F., Raga, A. C., Cantó, J., et al. 2013, MNRAS, 428, 1587
Velázquez, P. F., Riera, A., Raga, A. C., & Toledo-Roy, J. C. 2014, ApJ, 794
Wilkin, F. P. 1996, ApJ, 459, L31
Yang, B., Stancil, P. C., Balakrishnan, N., & Forrey, R. C. 2010, ApJ, 718, 1062

---

[1] Univ. Grenoble Alpes, CNRS, IPAG, 38000 Grenoble, France
e-mail: `andre.schutzer@univ-grenoble-alpes.fr`
[2] Laboratoire de Physique de l'ENS, ENS, Université PSL, CNRS, Sorbonne Université, Université de Paris, 75005 Paris, France
[3] Observatoire de Paris, PSL University, Sorbonne Université, LERMA, 75014 Paris, France
[4] Max-Planck-Institut für extraterrestrische Physik, Giessenbachstrasse 1, 85748 Garching, Germany
[5] Department of Astronomy, The University of Texas at Austin, 2500 Speedway, Austin, TX 78712, USA
[6] Institut de Radioastronomie Millimétrique (IRAM), 300 rue de la Piscine, 38406 Saint-Martin-D'Hères, France
[7] INAF, Osservatorio Astrofisico di Arcetri, Largo E. Fermi 5, 50125 Firenze, Italy
[8] Leiden Observatory, Leiden University, PO Box 9513, 2300 RA Leiden, The Netherlands
[9] Department of Physics and Astronomy, University College London, Gower Street, London, WC1E 6BT, UK
[10] IGN, Observatorio Astronómico Nacional, Calle Alfonso XII, 28004 Madrid, Spain
[11] Dipartimento di Chimica, Biologia e Biotecnologie, Via Elce di Sotto 8, 06123 Perugia, Italy
[12] Dipartimento di Chimica "G. Ciamician" via F. Selmi 2, 40126 Bologna, Italy
[13] Université de Toulouse, UPS-OMP, IRAP, Toulouse, France
[14] CNRS, IRAP, 9 Av. Colonel Roche, BP 44346, 31028 Toulouse Cedex 4, France
[15] LERMA, Université de Cergy-Pontoise, Observatoire de Paris, PSL Research University, CNRS, Sorbonne Université, UPMC, Univ. Paris 06, 95000 Cergy Pontoise, France
[16] Departament de Química, Universitat Autònoma de Barcelona, 08193 Bellaterra, Catalonia, Spain
[17] Centro de Astrobiología (CSIC, INTA), Ctra. de Ajalvir, km. 4, Torrejón de Ardoz, 28850 Madrid, Spain
[18] University of AL-Muthanna, College of Science, Physics Department, AL-Muthanna, Iraq
[19] Department of Physics, The University of Tokyo, 7-3-1, Hongo, Bunkyo-ku, Tokyo 113-0033, Japan
[20] Ural Federal University, 620002, 19 Mira street, Yekaterinburg, Russia
[21] The Institute of Physical and Chemical Research (RIKEN), 2-1, Hirosawa, Wako-shi, Saitama 351-0198, Japan
[22] Univ. Rennes, CNRS, IPR (Institut de Physique de Rennes) – UMR 6251, 35000 Rennes, France
[23] ESO, Karl Schwarzchild Srt. 2, 85478 Garching bei München, Germany
[24] Aix-Marseille Université, PIIM UMR-CNRS 7345, 13397 Marseille, France
[25] Università degli Studi di Torino, Dipartimento Chimica Via Pietro Giuria 7, 10125 Torino, Italy

Chapter 6

Chemistry in the jet of Cep E

6.1 Scientific context and goals

One of the key-questions in modern astrochemistry is to understand the evolution of interstellar matter from the cold molecular clouds to the protoplanetary systems. It is well established that the early stages of star formation are accompanied by powerful mass ejections in the form of hypersonic jets and bipolar outflows (see Bally et al., 2007, for a review). These jets interact with the parental envelope and the ambient cloud through shocks and modify the morphology, the physical conditions (temperature and density) as well as the chemical composition of the protostellar gas and dust. There is mounting evidence that they alter the molecular complexity of the protostellar gas (Arce et al., 2008; Lefloch et al., 2017; De Simone et al., 2020), while they can serve to probe the chemical composition of the molecular gas and dust during the pre-stellar phase. This has led to the concept of chemically active outflows (Bachiller & Pérez Gutiérrez, 1997), whose prototype is the L1157 and has triggered numerous observational and modelling studies.

On the observational side, it has been recognized since the pioneering work of (Bachiller & Pérez Gutiérrez, 1997; Bachiller et al., 2001) that outflows from Class 0 protostars can be chemically active. Considerable efforts with the major ground-based and space facilities in the (sub)millimeter and the infrared have been dedicated to investigate the chemical richness of a few prototypical objects (e.g. IRAS04166+2706, L1448mm, IRAS 4A, among others), in particular L1157-B1 (Bachiller & Pérez Gutiérrez, 1997; Bachiller et al., 2001; Mendoza et al., 2014; Codella et al., 2017; Lefloch et al., 2017). The goal of these studies is not only to provide an inventory of the chemical richness but to constrain the formation and evolution of outflows, how they interact with the ambient cloud by modifying the morphology, the temperature and density.

Some molecular species were soon identified as specific tracers of outflow activitied, like: SiO, a probe to constrain the shock speed and the preshock density (Gueth et al., 1998); the ion HCO^+ and its isotopologues, since they are sensitive to magnetic field (Olofsson et al., 1982); CH_3OH, a tracer of the grain mantle composition and the sputtering region (Tafalla et al., 2010); and S-bearing species such as SO, OCS and SO_2 (depleted onto grains with short chemical timescales). Different molecular species probe different regions of the outflow and, therefore, provide powerful tools to explore their inner structures. The content and the origin of molecules in protostellar jets is still a main issue in star formation studies. Carbon monoxide (CO) was detected in protostellar jets already a long time ago (e.g. HH 111 and H 211 Cernicharo & Reipurth, 1996; Gueth & Guilloteau, 1999). Subsequent studies based on single-dish or interferometric observations have succeeded in detecting only a few molecular species in low- and intermediate-mass jets. Protostellar jets in the Class 0 phase are mainly molecular, they can be traced by CO emission (Gueth & Guilloteau, 1999; Lee et al., 2000; Plunkett et al., 2015). Their knots and bow shocks can be traced by shock tracers like H_2 (McCaughrean et al., 1994), SiO (Lefloch et al., 1996; Gueth et al., 1998; Hirano et al., 2006; Podio et al., 2014), and SO (Lee et al., 2007; Codella et al., 2014). In the Class I and Class II phases, the class I sources SVS13AB (Bachiller et al., 1998), NGC 1333 IRAS2 (Jørgensen et al., 2004) and HH 211 (Palau et al., 2006) showed SiO emission probing the molecular jet and not strong shocks against the ambient gas. Nevertheless, protostellar jets from Class I and II are mainly detected in atomic and ionized gas (OI, Hα, and SII) (Reipurth & Bally, 2001; Bally, 2016), appearing as Herbig-Haro flows at optical and infrared wavelengths.

A few systematic studies were first carried out using single-dish observations toward the jets: IRAS04166+2706, L1448mm and Cep E (among others), which display an unusual chemical composition, quite distinct from that of most Class 0 protostellar jets (Santiago-García et al., 2009; Tafalla et al., 2010; Ospina-Zamudio et al., 2019). Episodic events are commonly observed toward jets, the detection of high-velocity molecular bullets toward young protostars (L1448-mm and I04166) show abundant Oxygen-bearing species (e.g. SiO and SO) but intriguingly a decrease in Carbon-bearing species, such as HCN and CS. The jet spectral signatures detected by single-dish telescopes differ markedly between molecular species, indicating the presence of several physical components. The low-angular resolution of these data (10$''$ at best) limits the conclusions on the spatial origin of the emission inside the jet.

The unbiased millimeter line survey of the Cep E intermediate-mass protostellar jet with the IRAM 30m telescope has brought an additional degree of complexity Ospina-Zamudio et al. (2019). The authors reported an unusual composition including the presence of both O-rich species (SiO, SO) and Carbon-rich (HCN, CS) species, among other species such as HCO^+ and H_2CO. The chemical composition was thought all the more unusual as CS, SO and H_2CO appeared to be the most abundant species. Internal shocks have been proposed to contribute to jet molecular complexity. In Chapter 5, we have characterize these shocks in the jet of Cep E as well as the interaction between the high velocity jet and the molecular rich parental envelope (de A. Schutzer et al., 2022).

In order to shed light on the peculiar chemical composition of the Cep E jet and to better understand the origin of molecular emission in protostellar jets, we have taken advantage of the IRAM Large Program SOLIS and the W14AF project (presented in Chapter 4) at arcsecond resolution to perform an unbiased systematic search for molecules in the high velocity jet of Cep E. The goal of this work is, therefore, to unveil the spatial distribution of molecules in the jet/outflow, as well as the interaction between the structures in the outflow and, to investigate further the chemical differentiation reported between lobes with IRAM-30m observations performed by Ospina-Zamudio et al. (2019). More specifically, we want to verify: whether all species are detected with single-dish are also observed with the interferometer; how the transitions detected are spatially distributed and what they can tell us about the complex jet structure, by learning about the velocity field in and around the jet; better quantify the interaction between the jet/outflow and the ambient/envelope material.

6.2 Systematic search for molecular emission

By means of inspecting the spectral data cubes produced at 2 MHz resolution, we have carried out a systematic search for molecular line emission in the northern and southern lobes of the jet, associated with the velocity intervals [+40;+80] $\mathrm{km\,s^{-1}}$ and [−135;−110] $\mathrm{km\,s^{-1}}$, respectively, as reported by Lefloch et al. (2015). Firstly, we performed a general cleaning of the data cubes in order to search for molecules emitting at the jet velocity ranges. This search was done using the CASSIS software (Vastel et al., 2015), where we only considered molecular transitions with a peak intensity above the 3σ level. Hence, we performed individual and dedicated cleaning of the maps of all transitions that showed jet emission.

In total, we detected 15 rotational transitions from 7 following species (Table 6.1): SiO (Silicon monoxide), HCN (Hydrogen cyanide), HCO^+ (Formyl cation), CS (Carbon monosulfide), CH_3OH (Methanol), H_2CO (Formaldehyde) and SO (Sulfur monoxide). The spectroscopic properties (quantum numbers, frequency, upper level energy) of the detected molecular transitions detected are listed in Table 6.1. Comparison of the emission maps of the molecular species confirms that all the species identified by Ospina-Zamudio et al. (2019) are indeed associated with the protostellar jet. As it was already mentioned, SiO and SO are commonly found in protostellar jets, but the presence of organic species such as HCN and H_2CO, or high-density gas tracers such as CS and HCO^+ has been significantly less reported in extremely high-velocity gas (Tychoniec et al., 2019). We report, for the first time, the presence of methanol in the high velocity jet. The presence of the complex organic molecule CH_3OH, as indicated by the detection of the five rotational transitions $5_{-1,0}$–$4_{0,0}$, $2_{-1,0}$–$1_{-1,0}$, $2_{0,+0}$–$1_{0,+0}$, $2_{0,0}$–$1_{0,0}$, and $4_{2,0}$–$3_{1,0}$ along the jet came as a surprise as this species had been detected only towards L1448m (Tafalla et al., 2010), but since they observed with single-dish observations the nature of the emission could not be disentangle.

Table 6.1: Molecules detected in the jet of Cep E with SOLIS and W14AF data.

Molecule	Transition	ν (MHz)	E_{up} (K)	Molecule	Transition	ν (MHz)	E_{up} (K)
E-CH_3OH	$5_{-1,0} - 4_{0,0}$	84521.17	40.4	SiO	$5 - 4$	217104.98	31.3
E-CH_3OH	$2_{-1,0}$–$1_{-1,0}$†	96739.36	12.5	HCN	$1_1 - 0_1$†	88630.42	4.3
A-CH_3OH	$2_{0,+,0}$–$1_{0,+,0}$†	96741.37	7.0		$1_2 - 0_1$†	88631.85	4.3
E-CH_3OH	$2_{0,0}$–$1_{0,0}$†	96744.55	20.1		$1_0 - 0_1$†	88633.94	4.3
E-CH_3OH	$4_{2,0}$–$3_{1,0}$	218440.06	45.5	HCO^+	$1 - 0$	89188.53	4.3
SO	$2_2 - 1_1$	86093.95	19.3	CS	$2 - 1$	97980.95	7.1
	$3_2 - 2_1$	99299.87	9.2	p-H_2CO	$3_{0,3} - 2_{0,2}$	218222.19	21.0
	$5_4 - 4_3$	206176.01	38.6	p-H_2CO	$3_{2,2} - 2_{2,1}$	218475.63	68.1
	$6_5 - 5_4$	219949.40	35.0	p-H_2CO	$3_{2,1} - 2_{2,0}$	218760.06	68.1
SiO	$2 - 1$	86846.96	6.3	CO	2-1	230538.00	16.6

The transitions marked with a † are blended. These parameters were obtained from JPL (Pickett et al., 1998) and CDMS (Endres et al., 2016) databases.

6.3 Dataset comparison: Jet misalignment?

I checked the consistency of the full dataset by comparing emission maps of some bright lines observed in the W14AF and SOLIS datasets, I noticed a shift in the spatial distribution both in right ascension and declination between the data from SOLIS and W14AF.

Initially, I produced the moment 0 maps and superposed CO and SiO emission for both datasets. On one hand, the W14AF data presented a good agreement in comparison with CO at 1″ (left panel in Figure 6.1) as illustrated by the SiO 2–1 contours in black. While comparing the spatial distribution of the CO jet emission and molecular tracers of the W14AF project (SiO, SO, H_2CO) it appears they are well-aligned. A shift of −0.20″ in $\Delta\alpha$ and +0.35″ in $\Delta\delta$ is observed between SiO 2–1 observed by W14AF and SOLIS (right panel in Figure 6.1). The same shift is observed between for other molecular transitions (same molecular specie), like when compared SO between W14AF and SOLIS (middle panel).

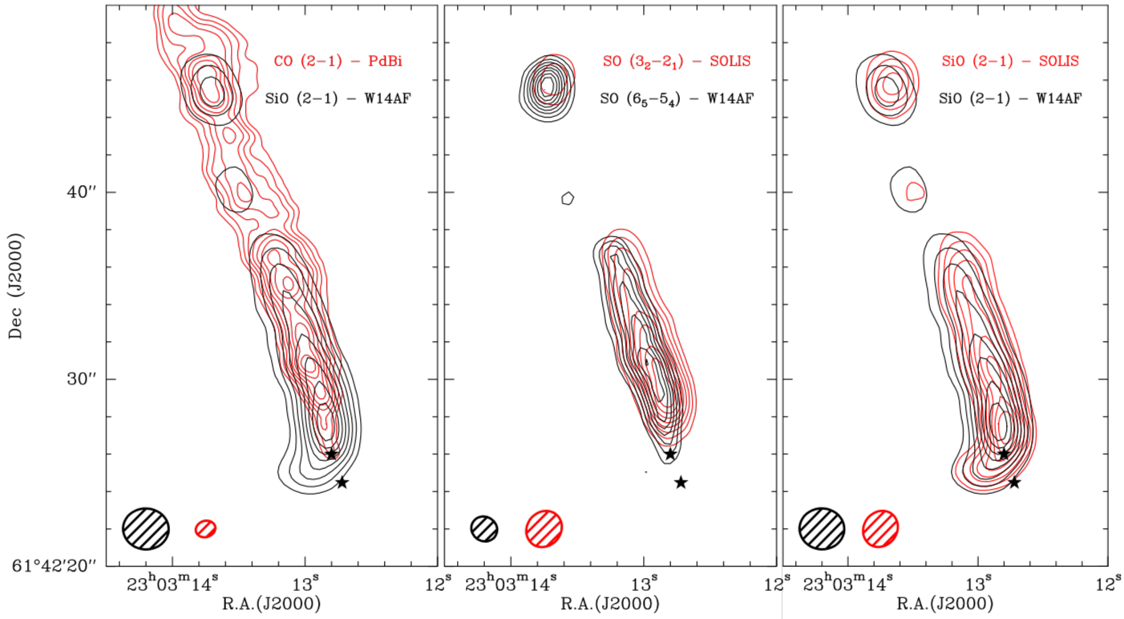

Figure 6.1: Superposition moment 0 maps of SiO, SO and CO jet emission coming different dataset. (Left): Emission of CO J=2–1 (Lefloch et al., 2015) and SiO J=2-1 from W14AF, contours are in red and black, respectively. (Middle): Emission of SO N_J=3_2-2_1 and SO N_J=6_5–5_4 with contours in red (SOLIS) and black (W14AF), respectively. (Right) Emission from both SiO J=2–1 with contours W14AF data contours in black and SOLIS in red. First contour and contour interval are 20% and 10% of the peak intensity in each component, respectively.

Therefore, I decided to investigate further the nature of this spatial shift in SOLIS 3 mm band with respect to the CO and the W14AF data. Hence, first I checked the origin of the misalignment by identifying whether the shift was seen in the continuum maps of SOLIS 3 mm and W14AF, since it could be that the continuum central positions between 3 mm band from SOLIS and W14AF data are different and this computed difference would probably be the offset expected.

The continuum emission for both W14AF and SOLIS data are displayed in the Figure 6.2,

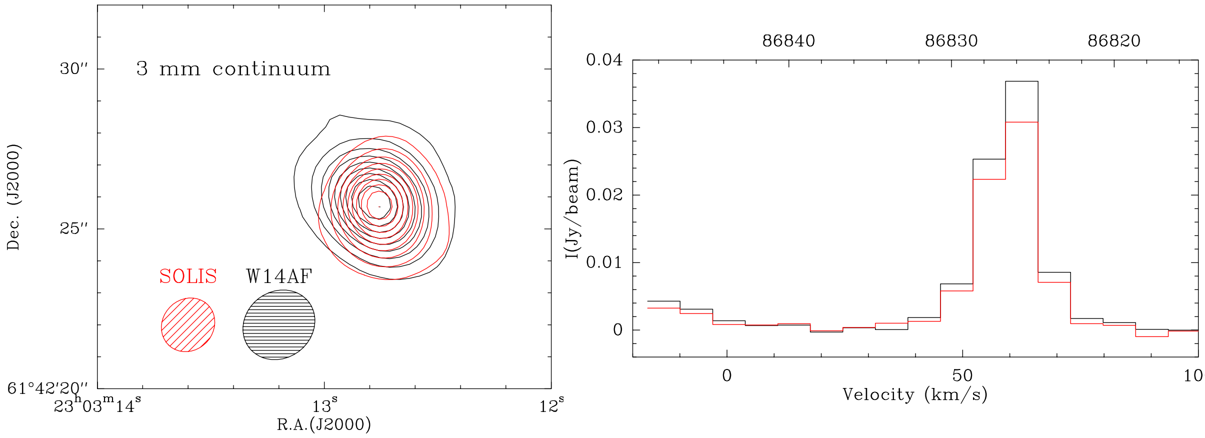

Figure 6.2: (Left):Continuum emission comparison W14AF and SOLIS in the 3 mm band with beamsizes of 2.35″ × 2.08″ and 1.76″ × 1.59″, respectively. W14AF data contours are in black and SOLIS in red. First contour and contour interval are 10% and 10% of the peak intensity in each component, respectively. (Right): black line correspond to SiO 2–1 spectra from SOLIS toward the peak position after correcting by the offset (−0.2″,+0.35″), and in red is the spectra without applying the offset correction.

the location of the continuum peak in both datasets agree. I also investigated the spectra peaks toward few positions in the jet, in the right panel of Figure 6.2, I present the SOLIS spectra of SiO J=2–1 extracted from the position (6.6″;19.4″) in black superposed with the spectra shifted by (−0.2″;+0.35″) in red, which corresponds to the shift seen between W14AF and SOLIS 3 mm data. The line profiles are exactly the same with a difference in the peak intensities, being the shifted one smaller than the black one indicating we are tracing the same gas but loosing flux.

Therefore, after checking the excellent agreement in the continuum distribution obtained with W14AF and SOLIS, the conclusion is that the spatial shift observed between the molecular line distribution is not an observational or an astrophysical problem. Most likely, it is an artefact that occurred in the process of self-calibration. Finally, we decided to simply adopt the shift (−0.2″,+0.35″) whenever analyzing or superposing data from SOLIS 3 mm.

6.4 Spatial distribution

In Figure 6.3, we present the moment 0 maps of the different species detected along the jet. The emission was integrated in the range [+40;+80] $\mathrm{km\,s^{-1}}$ in the northern lobe (in red contours), in the southern lobe, the jet emission (blue contours) is integrated in the range [−140;−110] $\mathrm{km\,s^{-1}}$. The emission of HH 377 integrated in the range [−77;−64] $\mathrm{km\,s^{-1}}$ is displayed in black. We also included the CO J=2-1 emission at 1″ already presented in Chapter 5 superposed to IRAC/Spitzer H_2 at 4.5 μm in color scale; due to the spectral resolution of the 3 mm data, blending of the three of transitions CH_3OH and the three hyperfine components of HCN J=1–0 are observed in the spectral signatures (see Table 6.1). We do not display the H_2CO $J=3_{2,2}-2_{2,1}$ since it has the similar E_{up} and Einstein coefficients as the transition $J=3_{2,1}-2_{2,0}$, and it does not bring any complementary information. Half of the transitions are from low upper energy levels ($E_{up} \leq 10$ K) but few lines are coming from upper energy levels as high as E_{up}= 40.4 K (CH_3OH) and 68 K (H_2CO) which could indicate more than one component in the jet or a gradient of temperature depending on the spatial distribution.

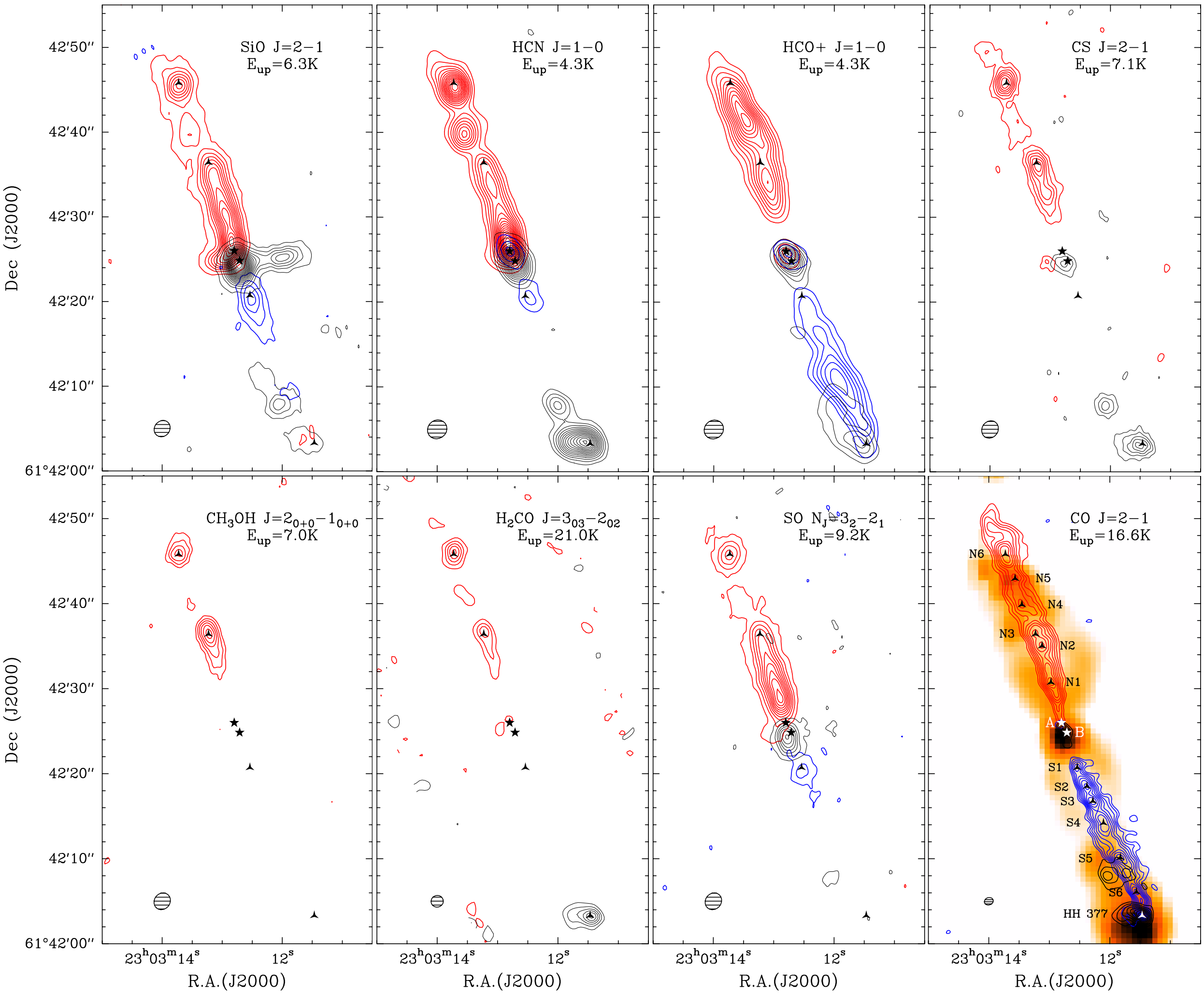

Figure 6.3: Montage of moment 0 maps of the lowest-J transitions of the different molecular species detected in the Cep E jet: SiO, HCN, HCO^+, CS, CH_3OH, H_2CO, SO, CO. In the northern lobe, the jet emission (red contours) is integrated in the range [+40;+80] km s^{-1}. In the southern lobe, the jet emission (blue contours) is integrated in the range [−140;−110] km s^{-1}. The emission of HH377 integrated in the range [−77;−64] km s^{-1} is displayed in black contours. First contour is at the 3σ level; contour interval is 6σ for SiO, HCN and HCO^+ and 3σ for CS, CH_3OH, SO and H_2CO. For the sake of comparison, we show in the bottom right panel, the CO jet emission in the same velocity intervals and the IRAC/Spitzer H_2 at 4.5 μm in color scale (Lefloch et al., 2015). CO first contours and steps are 20% and 10% of the peak intensity in each lobe.

6.4.1 Northern lobe

In Figure 6.3, we display the low-J transitions of the different tracers detected in the jet. The emission of these transitions are clearly probing different regions in the high-velocity gas. The first noticeable feature is that CO and HCO^+ are the only species which trace both the northern and southern lobes of the jet. Their respective distributions actually display similar morphologies with the difference, however, that the HCO^+ intensity distribution looks somewhat smoother in these velocity ranges - [+40;+80] $\mathrm{km\,s^{-1}}$ in northern and [−140;−110] $\mathrm{km\,s^{-1}}$ in southern lobe). In comparison with CO, HCO^+ does not display the signature of the knots unambiguously detected in the CO jet in the velocity range displayed. Nevertheless, when we integrate the CO flux in a lower velocity range [40;55] $\mathrm{km\,s^{-1}}$ (bottom right panel in Figure 5.1), CO emission shows the same spatial distribution that is seen in HCO^+. Furthermore, the HCO^+ emission appears wider than that of the other species observed at a similar angular resolution ($\approx 2''$). The mean deconvolved transverse size measured from the FWHM is ($\approx 4''$) much broader than other tracers ($\approx 2 - 3''$).

In the northern lobe, SiO, HCN, SO and CS appear to trace the well characterized jet collimated structure with a diameter of $\approx 3''$ (2400 au at the distance of Cep E, beam-deconvolved) and a length of 25″. Along this collimated molecular layer, compact roundish clumps of a few arcsec diameter are detected, which coincide with CO knots identified along the jet and analysed in Chapter 5. Knots N3 and N6 are, for instance, good examples of such regions (see Figure 6.3). However, in the environment of the protostar ($< 5''$), there is almost no emission from H_2CO and CS, their emission is dominated by the knots N3 and N6 in this lobe although they show emission beyond 6″ along the jet. However some emission from these molecules is detected in the lower-velocity range [40;50] $\mathrm{km\,s^{-1}}$ in the inner protostellar environment. To summarize, all the species detected in the high-velocity gas reveal an inhomogeneous structure made of a long ($\sim 25''$) and collimated, smooth layer, and a few small ($\sim 2''$) emission knots.

The situation in the higher excitation lines ($E_{up} > 30\,\mathrm{K}$, except SO $N_J = 2_2$–2_1 at $E_{up} = 19.3\,\mathrm{K}$ also included) is different, as can be seen in Figure 6.4. The emission is not so much radially extended, which indicates a gradient of excitation inside the high-velocity gas with higher excitation in the central region of the jet. In the northern lobe, only two transitions of SO $N_J = 2_2 - 1_1$ and $N_J = 6_5 - 5_4$ and SiO J= $5 - 4$ trace the jet direction and not continuous from knot N3 to N7 (compared to SiO and SO in Figure 6.3), their emission is also knotty in at positions N4, N5 and N6. On the other hand, H_2CO J=3_{21}–2_{20}, CH_3OH J=4_2–3_{10} are mainly associated to the shock positions N3 and N6. The excitation conditions are more favorable in N3 and N6, which are different from other knots. This directly raises the question on the nature of N3 and N6 as the excitation conditions and the line brightness are higher.

6.4.2 Southern lobe

The situation is different in the southern jet lobe, only SiO, HCN, SO and HCO^+ are the species detected, while CH_3OH, H_2CO and CS are not detected along the jet. SiO particularly is fragmented but quite extended. Their emission is located within short distance ($\sim 6''$, 5000 au) from the protostar except for HCO^+ which traces the whole lobe until the terminal bowshock HH 377, as mentioned previously. Like in the northern lobe, there is a lack of emission at the terminal velocity ($-125\,\mathrm{km\,s^{-1}}$) within the $< 5''$ close to the

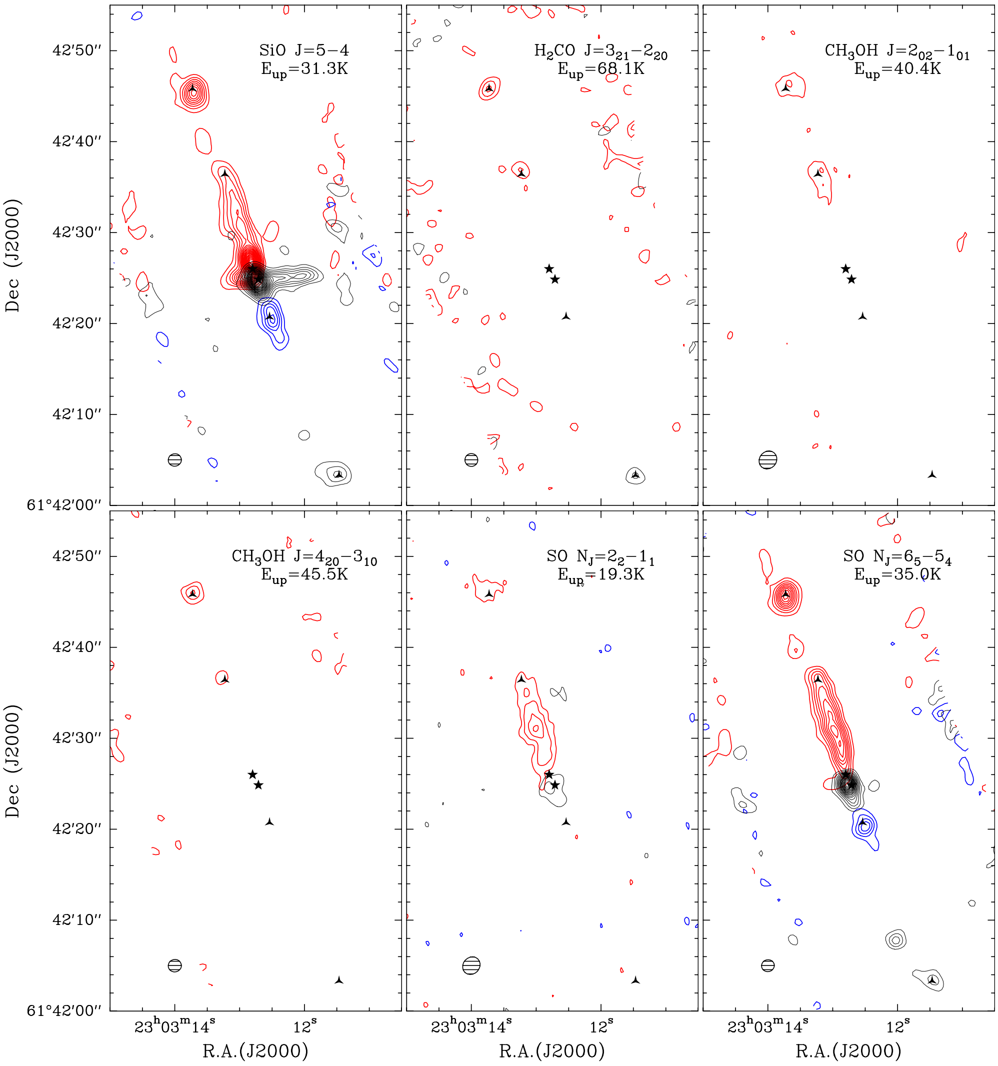

Figure 6.4: Montage of moment 0 maps of the high-J transitions of the different molecular species detected in the Cep E jet: SiO, H_2CO, CH_3OH and SO. The emission intervals were integrated in the same velocities ranges as in figure 6.3. Here, the first contour is at the 3σ level and contour interval is 3σ for each component.

protostar. We note, however, that the emission in Figure 6.3 in black contours are displayed in this region ($< 5''$), this emission corresponds to the flux integrated in the velocity range [−77;−64] $\mathrm{km\,s^{-1}}$ and it is the acceleration region discussed in Chapter 5 for the southern lobe of the jet. We will come back to this feature in more detailed later in this chapter. The CO and HCO^+ jets propagate at terminal velocity $V_r \simeq -110\,\mathrm{km\,s^{-1}}$ with respect to the ambient gas until it reaches the location of the Herbig Haro object HH 377 (see Figure 5.2).

In the high-J regime, the situation is not very different in the southern lobe. Only SiO and SO are detected, their emission is associated mainly to the knot S1, and to the terminal bowshock HH 377, which displays also the presence of formaldehyde (see Figure 6.4). All of them show an emitting area smaller than the low-J transitions which is expected given the different excitation conditions.

Towards the terminal bowshock HH 377 ($V_r = -67\,\mathrm{km\,s^{-1}}$), the species SiO, HCN,

HCO^+, CS and SO are detected. The molecular emission of these species looks extended in the transverse direction with respect to the jet, which is consistent with a bow shock morphology where part of the material is ejected sideways after impacting the environment (Raga & Cabrit, 1993). Their emission peaks (including CO), do not coincide with the H_2 peak from IRAC (see CO panel in Figure 6.3), as well as the emission size is way smaller around 3″ beam-deconvolved for most of the low-J transitions. The H_2 emission toward HH 377 is roundish and larger when compared to the molecules that we detected. Moreover, it is located southwards of the peak of the molecular emission of all species we detected which indicates that the peak traced by H_2 is quite dense and the molecular emission from SiO, HCN, HCO^+, CS and SO are tracing the shock impact of the jet in this clump.

6.4.3 Recovered flux

In order to estimate the fraction of the flux filtered out by the NOEMA interferometer in the protostellar jet, we compared molecular spectra extracted from the NOEMA maps and degraded at the angular resolution of the IRAM 30m telescope with spectra from the ASAI millimeter line survey of Cep E-mm (Ospina-Zamudio et al., 2019). We report in Table 6.2 the ratio of NOEMA to IRAM 30m flux measured in the velocity interval [+40;+70] km s^{-1}. Taking into account the calibration uncertainties, the agreement between the fluxes collected by the IRAM 30m telescope and the NOEMA interferometer is very satisfying. This implies that NOEMA is probing the same structures as those detected with the single-dish telescope. The only two exceptions are the transitions CS 2–1 at 97980.95 MHz and SO 5_4–4_3 at 206176 MHz, whose NOEMA to IRAM 30m flux ratio is much smaller, ∼ 49% and 34%, respectively.

Table 6.2: Fraction of the IRAM 30m flux recovered by the interferometer in the velocity range [50;70] km s^{-1} in a field of same solid angle on the IRAM-30m centered on protostar Cep E-A.

Line	Frequency (MHz)	Synth. Beam (″×″)	Fraction	Project
SiO 2–1	86846.96	2.1 × 1.8	0.87	SOLIS
HCN 1–0	88631.85	2.4 × 2.1	0.73	W14AF
HCO^+ 1–0	89188.53	2.4 × 2.1	0.66	W14AF
CS 2–1	97980.95	1.8 × 1.6	0.49	SOLIS
SO 3_2–2_1	99299.89	1.8 × 1.6	0.76	SOLIS
SO 5_4–4_3	206176.01	0.4 × 0.3	0.34	SOLIS
SiO 5–4	217104.98	1.5 × 1.4	0.82	W14AF
SO 5_6–4_5	219949.44	1.5 × 1.4	> 0.95	W14AF

6.4.4 Chemical differentiation between lobes

Taking in consideration what we described in the previous sections on the spatial distribution, we report a chemical differentiation between the lobes of the jet, which corresponds to the asymmetries observed between the different molecular tracers in Figures 6.3 and 6.4, especially when comparing the emission distributions of CH_3OH, H_2CO and CS. Hence, the question arises as if the difference in chemical signatures between the northern and southern lobes could be due to an observational bias (sensitivity) or whether it testifies of an intrinsic difference in gas composition, whose nature remains a puzzle.

In the work of Lefloch et al. (2015), with a multi CO line analysis with J_{up} from 1 to 21, the authors reported two components with different excitation conditions detected in the southern jet: one low-excitation component with $T = 80–100\,K$ and $n(H_2) \approx 1 \times 10^5$ and a high-excitation one with $T = 400–750\,K$ and $n(H_2) \approx 1 \times 10^6$, displaying, therefore, a gradient of temperature and density along the southern jet. As for the northern lobe, Ospina-Zamudio et al. (2019) studied a position $12''$ north of the protostar by analysing lines with J_{up} ranging from 1 to 4. They found a $T = 180–300\,K$ and $n(H_2) \sim 10^5$, under the assumption that the physical conditions are the same along the northern jet lobe. Also, they report higher column density for the molecules than in the southern.

We first checked whether the lack of emission of several species in the southern is due to a sensitivity issue or not. In order to test this, we initially assumed that molecular abundances are similar in both lobes, then the line intensity ratios between different tracers are expected to display similar values. Therefore, the non-detection of CH_3OH, H_2CO, CS in the southern could simply be a result of a lack of sensitivity of our observations. To check this hypothesis, we computed the flux ratio of the low-J transition of those species (CH_3OH, H_2CO, CS) relative to SiO J=2–1 at the positions N3 and N6, and assuming at 0^{th} that these ratios should be similar in the Northern and Southern lobes. Hence, we computed the intensity ratio between CH_3OH $2_{-1,0}$–$1_{-1,0}$/SiO 2–1 at the position of knots N3 and N6 in the northern lobe. We obtained a ratio value of 0.34 and 0.19, respectively. Thus, assuming the ratio is the same in knot S1, in the southern lobe, we obtain a I_{peak} (CH_3OH) in the range $0.11\,K - 0.19\,K$. This is more than one order of magnitude higher than the noise measured at the S1 position ($\sigma = 0.0076\,K$). Therefore, we conclude that the lack of CH_3OH detection in S1 is not due to the lack of sensitivity but rather to the chemical and physical conditions taking place in S1.

In the work described in Chapter 5, we have shown an important difference between both lobes: the northern shows entrainment by the jet traced by CO while the southern was too weak to be observed in CO 2–1 and SO 5_4–4_3 in few arcsecond from the protostar. Therefore, we decided to investigate further whether this entrainment material is traced or not in the other species, since it could have implications to the presence or not of some species, as part of this material might come from the chemically rich protostellar envelope.

6.4.5 Chemical differentiation between jets

In the SiO J=2–1 and J=5–4 moment 0 maps (Figures 6.3 and 6.4), we find the presence of emission associated to Cep E-B jet. The jet from the binary companion is emitting mainly in the velocity range [-80,-40] $km\,s^{-1}$ in black and [+50,70] $km\,s^{-1}$ in red contours. The SiO emission is extended in the Western direction with a length of $\sim 7''$, with a transversal size of $\sim 3''$. The eastern part is less extended with a length $\sim 4''$ and transversal size $\sim 2''$. We are not able to confirm that the emission shown by the SO transitions (especially $N_J = 3_2$–2_1) in this inner part corresponds or not to the B-jet. Therefore, in the inner close environment ($\lesssim 2''$) of the protostars, the contours of the jets powered by Cep E-A and B can not be disentangle in our observations as the B-jet has similar velocity with respect to the A-jet in the northern and the acceleration region of the southern lobe.

Intriguingly, CS is present but only in the Eastern direction (see red contours in Figure 6.3) at a position around ΔRA $= 1.5''$ and ΔDec $\approx -1''$. Therefore, we confirm that with the exception of SiO and CS, no other species are detected in the Cep E-B jet lobes. To summarize, we are able to report a chemical differentiation between the jets of Cep E-B and A, with the latter being much chemically richer.

6.5 Gas entrainment

Initially, we aimed to investigate the detection of gas entrainment by the jet at subarcsecond scale, we have performed Position-Velocity diagrams of the low-J transitions from the species detected in the jet. These PVs diagrams were computed in $\delta = 0''$ (declination offset) across the jet main axis and were integrated over a beam size of each transition, that varies between $1.5''$ and $2.4''$ depending on the species. The diagrams are reported in Figure 6.5 for SiO 2–1, HCN 1–0, HCO$^+$ 1–0, CS 2–1, CH$_3$OH 2_{0+0}–1_{0+0}, H$_2$CO 3_{03}–2_{02}, SO 3_2–2_1 and CO 2–1.

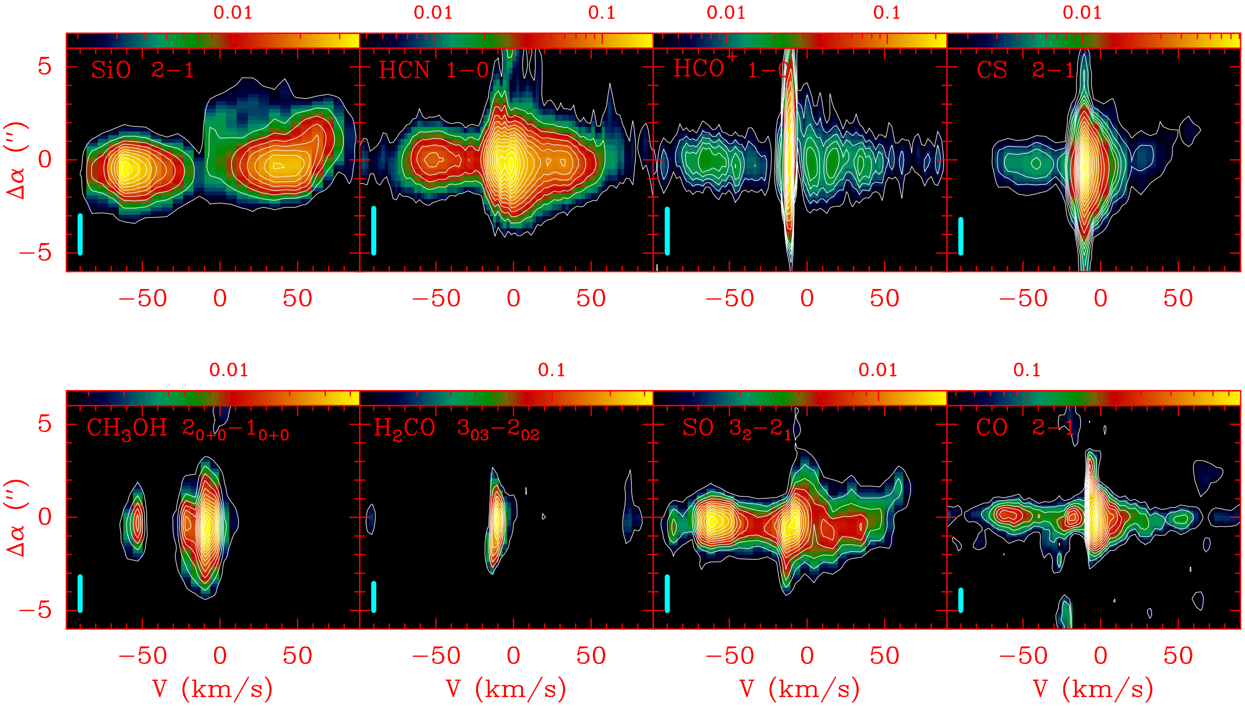

Figure 6.5: Montage of the Position-Velocity diagrams of molecular transitions across the jet in the position $\delta = 0''$. We show the lowest-J transitions of the molecular species detected in the CepE-A jet: SiO, HCN, HCO$^+$, CS, CH$_3$OH, H$_2$CO, SO, CO. In each map, the first contour is 3σ; contour interval 6σ for SiO, CH$_3$OH and SO, and 12σ for HCN, HCO$^+$, CS and H$_2$CO. For CO first contour and contour interval are 10% of the peak flux. The synthetic beam sizes are marked by a thick light blue line of each panel. The units are Jy/beam $\cdot$ arcsec.

In Figure 6.5, we can see that HCN, HCO$^+$, CS and SO are showing emission from the ambient ($V_{lsr} = -10.9\,\mathrm{km\,s^{-1}}$) to the jet velocity ($V \sim 57\,\mathrm{km\,s^{-1}}$) in the northern lobe, indicating that they are tracing the entrainment material of the ambient gas by the jet in this lobe. On the other hand, H_2CO, CH_3OH emissions are present around the ambient velocity range, the emission at this velocity is tracing the low-velocity outflow (cavity walls), but no emission from ambient to jet velocities is detected indicating they are not tracing the entrainment gas. The spots seen at $\sim -55\,\mathrm{km\,s^{-1}}$ in Methanol are actually probing the hot corino emission associated to the line: CH_3OH $2_{1,1}$–$1_{1,0}$ at 96755.5 MHz and $E_{up} = 28\,\mathrm{K}$. Moreover, Silicon monoxide (SiO) displays already high velocity emission $\sim 50\,\mathrm{km\,s^{-1}}$ at this scale, but weak entrainment from ambient by the high velocity jet is detected. The 'tail' shape in the SiO PV diagram (also seen in CS) with $\Delta\alpha > 0$ and velocities $V_r > 50\,\mathrm{km\,s^{-1}}$, correspond actually to the jet of Cep E-B powered almost perpendicular to the jet ejected by component A, the jet from B can also be seen in the SiO moment 0 map in Figure 6.3 in red to the Eastern and in black contours to the Western directions (in the plane of the sky). We interpret the lack of emission from CH_3OH and H_2CO at this scales, and as a consequence no/weak entrainment, due to the fact that these species are frozen onto the grains. We see the presence of these species associated mainly to the internal shocks N3 and N6 at further distances from the protostars. In the southern lobe, the situation is different, there is a very weak if any sign of entrainment, for all species detected.

As described in Chapter 5, where we analyzed the CO and SO emission at $1''$ and $0.4''$, we observed an acceleration at arcsecond scale that it is tightly linked to the gas entrainment detected in CO. This acceleration was determined by analyzing knots at few arcsecond from the protostar before they reach the terminal velocity, in order to unveil this acceleration and inner knotty structure as seen for the species detected in the jet, we have performed PV diagrams along the whole jet main axis without taking into account the misalignment between the lobes of 4°, these PVs are displayed in Figure 6.6.

By inspecting Figure 6.6, one can note that in the southern lobe, the bulk of the emission comes from the inner protostellar environment $\Delta\delta < 5''$, then we can see the emission of the species in the S1 shock of SiO, SO and HCN mainly with velocities of $-120\,\mathrm{km\,s^{-1}}$, as seen in the moment 0 maps, but then it suddenly stops beyond $\sim 10''$. CS is particularly interesting in this case, because it shows emission $-70\,\mathrm{km\,s^{-1}}$ but not faster than this, which means that CS is initially present in the jet (in the acceleration region) but further downstream, it is destroyed, possibly due to the dissociation caused by the high velocities or radiative process to UV radiation. Yet in this lobe, we see the emission from HH 377 in the same tracers reported. The HCN and HCO^+ emission in the Herbig Haro object is linked to the cavity walls emission, traced by the continuous contours from the ambient velocity ($-11\,\mathrm{km\,s^{-1}}$) to the HH 377 one ($\sim -67\,\mathrm{km\,s^{-1}}$). Other species, such as H_2CO, SiO and CO, for instance, do not show any interaction with the ambient material at these distances ($\Delta\delta \approx 25''$).

In the northern lobe, the PV diagrams along the jet (Figure 6.6) displays mainly two profiles: a knotty one, seen in SiO, CS, CH_3OH, H_2CO; and the one that shows no knotty structure but a connection between the ambient material and the high-velocity jet, it corresponds to the HCO^+. It is important to notice that SiO and HCN PVs also show a gradual emission from the low-velocity gas ($\approx -11\,\mathrm{km\,s^{-1}}$) up to the high velocity jet ($\approx 60\,\mathrm{km\,s^{-1}}$) in distances that correspond to the knot N6, which indicates an interaction between the jet and the cavity walls in the outflow. Furthermore, we can see that the shock positions, displayed in the CO PV diagram, have a correspondence, or in other words, knotty structures at the similar distances but low-velocities. Therefore, we can see that at the same

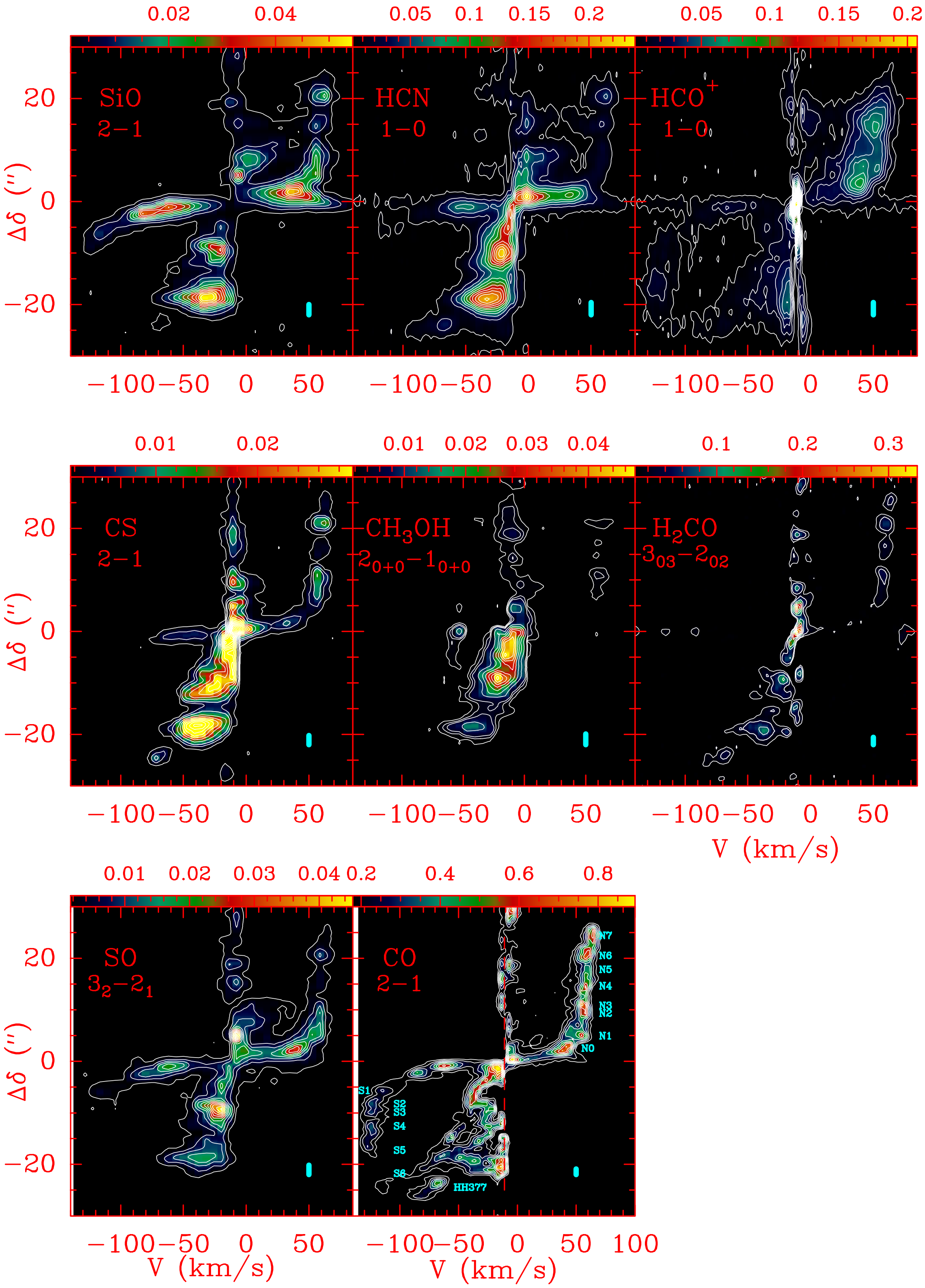

Figure 6.6: Montage of Position-Velocity diagrams, from left to right, it is displayed: (Top panels) SiO, HCN, HCO$^+$ and CS; (Bottom): CH$_3$OH, H$_2$CO, SO and CO. First contours are 3σ with steps of 3σ (CH$_3$OH), 6σ (HCO$^+$, CS, H$_2$CO and SO), 9σ (SiO) and 12σ (HCN) of each component, with exception of CO which presets first contour as 20% peak intensity with steps of 10%. The units are Jy/beam · arcsec.

positions where the internal shocks in the jet are located, we find a peak of emission in the low velocity gas, these positions are brighter at distances that correspond to N3 ($\sim 11''$) and N6 ($\sim 20''$). These results indicate that the jet is interacting closely or hitting the cavity walls in these positions, which is supported by the fact the jet changing direction due to precession, as shown in Chapter 5.

Knowing that the positions N3 and N6, in the northern lobe of the jet, show some particularities such as: interaction with the cavity walls, higher masses, brighter emission and presence of methanol, we have decided to investigate further them by means of radiative transfer and line analysis. The situation in the southern lobe is certainly different, we will also investigate the Herbig Haro object (HH 377) which we showed as an accumulation of several shocks (de A. Schutzer et al., 2022), but also the position S1 in more detail since it is the brightest and richer high-velocity knot in this lobe. The results regarding the analysis of the shocks N6, N3, S1 and HH 377 are presented in the Section 6.6.

6.5.1 Interaction between A and B outflows?

One of the main remaining questions concerning the Cep E outflow is the notably difference of the spatial distribution and presence of molecules between the northern and southern lobes of the jet. It is known that the physical conditions between the lobes are different from the works of Lefloch et al. (2015) and Ospina-Zamudio et al. (2019). While Lefloch et al. (2015) obtained from their CO multi-line analysis a $T_K = 80 - 100\,K$ and $n(H_2) = (0.5 - 1.0) \times 10^5\,cm^{-3}$ for the southern lobe of jet, Ospina-Zamudio et al. (2019) computed $T_K = 180 - 300\,K$ and $n(H_2) = (0.6 - 2.0) \times 10^5\,cm^{-3}$ for the northern lobe, i.e., at least factor of two warmer and denser in the northern with respect to the southern jet lobe. Therefore, its known that there is a difference in excitation conditions between both lobes, but is there another phenomena taking place that could affect or explain the weak entrainment in the southern and therefore related to the chemical differentiation? We decided to further investigate this.

We have superimposed in Figure 6.7 the CO J=2–1 emission (left panel) and H_2CO $J=3_{03}–2_{02}$ (middle) and H_2CO $J=3_{22}–2_{21}$ (right) probing the cavity walls (low-velocity outflow) and the Cep E-B jet being traced by CS $J = 2–1$ (left) and SiO J=5–4. We also report the direction of the other B-jet lobe with the light blue arrow. By inspecting this figure, one can note that around position $\Delta\delta = -1''$ and $\Delta\alpha = 1.5''$ the emission of the B-jet is peaking and the cavity walls show no contours (or a "gap"). It seems that at this position the B-jet is interacting and changing the morphology of the low-velocity outflow, the interaction is quite clear when observing the left panel, as if the B-jet is removing the material in this position. The emission of CS in this position ($-1.0''$,$1.5''$) is shifted in velocity with respect to SiO, as the latter peaks around $75\,km\,s^{-1}$ and CS at $56\,km\,s^{-1}$.

We propose that the interaction between the low-velocity outflow in the southern and the B-jet toward the Eastern direction (on the plane of the sky) is affecting the entrainment in the southern jet lobe powered by Cep E-A, presented in the previous sections. In this scenario, the jet powered by Cep E-B is somewhat removing the ambient/envelope material southwards of Cep E-A that would be entrained by its jet, as it happens in the northern. This would lead to the lack of molecules that are often trapped into the dust mantles, such as H_2CO and CH_3OH and is released after the pass of shock at further distances. However, since there is no entrainment due to the B-jet removal of material, the dust mantles were not

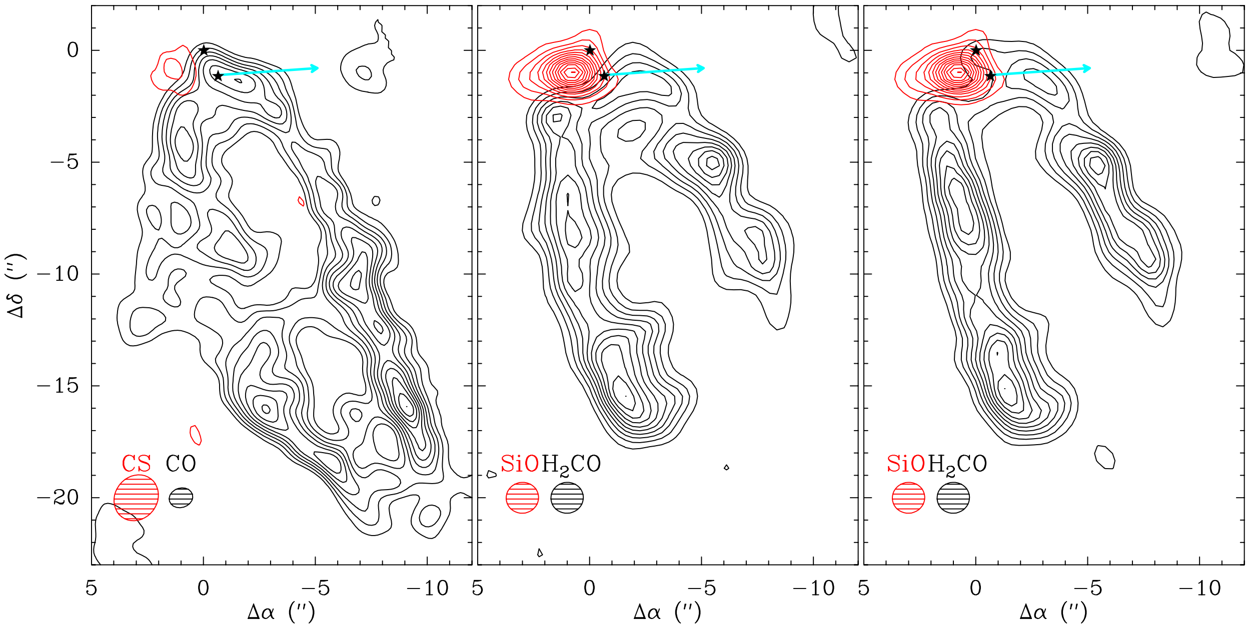

Figure 6.7: Molecular emission of the low-velocity outflow (cavity walls) integrated in the range [−19;−14] km s^{-1} black and the jet from Cep E-B in red contours. (Left) flux integrated map of CO J=2–1 in the cavity walls and the jet as traced by CS J=2–1 integrated in the range [48;65] km s^{-1}. (Middle and Right) Flux integrated map of H_2CO J=3_{03}–2_{02} (middle), H_2CO J=3_{22}–2_{21} (right) in the cavity walls and the jet as traced by SiO J=5–4 integrated in the range [65;80] km s^{-1}. The blue arrow corresponds to the other lobe of the Cep E-B jet detected in SiO J=5-4 towards the western direction. In the low-velocity outflow, first contour and contour interval are 10% and 10% of the peak intensity in each transition, respectively. The synthesized beams are shown in the bottom left corner. As for the jet, the contours are 3σ with steps of 3σ for each tracer.

preserved and carried away inside the jet implying, therefore, that shocks would not be able to release this material at further distances, as happened at N3 in the northern. In order to really constrain what is happening and what are the consequences in this interaction, one would need to numerically model this phenomena, as the observations are not able to disentangle this jet collision.

6.6 Shocked knots

In order to analyse the shock N6, N3, S1 and HH 377, the very first thing we did was to extract their spectra at their respective positions. Thus, a simple Gaussian fit was applied in order to estimate the line properties of the transition: the values of peak velocity (v_{peak}), Full Width at Half Maximum (Δv) and peak temperature (T_{peak}) for the four positions N3, N6, S1 and the bow shock HH 377. The Gaussian fit parameters are summarized in Table 6.3. One notes that the line parameters of N3 and N6 are quite similar, with line width $\sim$ 10 km s^{-1}. Significant differences are observed towards S1, where line profiles are twice as large as those of N3, N6 and HH 377. We will come back to this point in the following discussion.

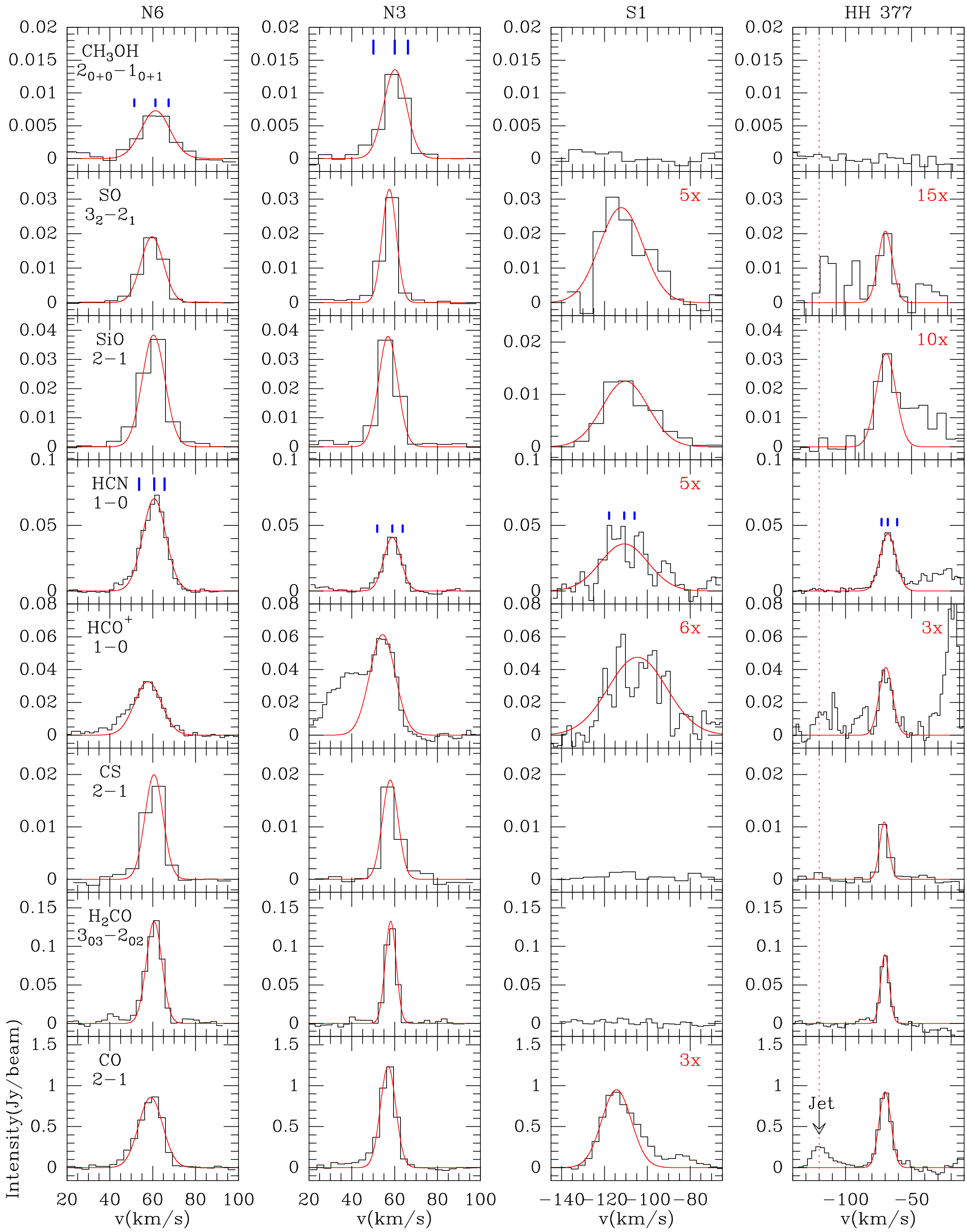

Figure 6.8: Montage of line profiles of CH_3OH, SO, SiO, HCN, HCO^+, CS, H_2CO and CO as observed towards the positions N6, N3, S1 and to the HH 377 object (from left to right). The Gaussian fits are displayed in red (see Table 6.3). The locations of the HCN hyperfine satellites and the CH_3OH multiple components are marked with blue lines.

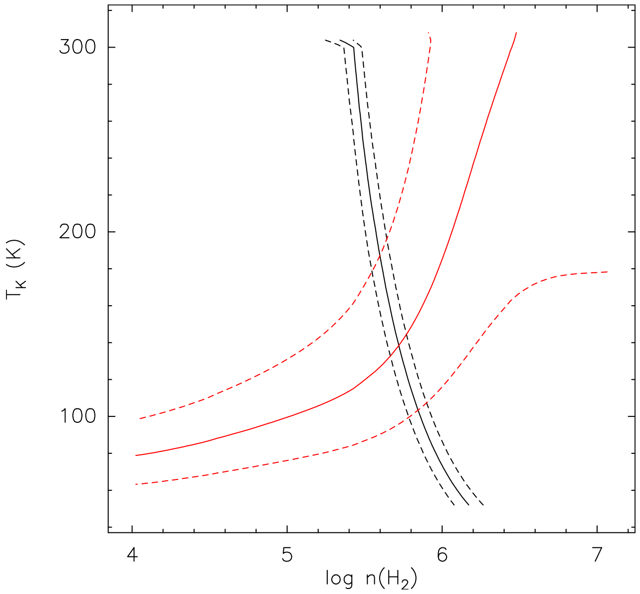

Figure 6.9: LVG grid performed to reproduce the physical conditions in N3 with SiO ratio 2-1/5-4 in black contours and H_2CO line intensity ratio $3_{2,1} - 2_{2,0}/3_{0,3} - 2_{0,2}$ in red. The dashed lines correspond to a 10% uncertainty on line intensity ratios. We assumed the column density of both species to be 10^{14} cm^{-2}.

We have constrained the physical conditions and the abundances of the detected molecular species from modelling of the line fluxes using the radiative transfer code MadeX in the Large Velocity Gradient (LVG) approximation (Cernicharo, 2012), the collision coefficients used are summarised in Table 6.5. We have used the line intensity ratio 5–4/2–1 of SiO as a probe of density n(H_2) whereas this ratio is barely sensitive to kinetic temperature changes, as can be seen in Figure 6.9. Therefore, in order to constrain the kinetic temperature for the regions, we analyzed the line intensity ratio H_2CO $3_{2,1}$–$2_{2,0}/3_{0,3}$–$2_{0,2}$. For both species, we have built a grid of models with density between 10^4 cm^{-3} and 10^9 cm^{-3}, temperature between 50 K and 450 K, and we initially assumed a column density of 10^{14} cm^{-2}. Hence, we superposed both line intensity ratios in the parameter space (n(H_2),T_K) to obtain the range of solutions (n(H_2,T_K) which can account simultaneously for the line intensities measured. The kinetic temperature and density ranges as being the intersection regions such as presented in the Figure 6.9 for N3, the results ranges are displayed in Table 6.4. Before comparing with the line intensity ratio, they were corrected by the beam dilution of the interferometer.

6.6.1 Knots N3 and N6

For the position N6, we have obtained T_K=110–200 K and n(H_2)=(5–13)×10^5 cm^{-3}, while for N3 the temperature range is between T_K=100–190 K and density n(H_2)=(3–8)×10^5 cm^{-3} which is consistent to what was reported by Ospina-Zamudio et al. (2019). The best solutions are: T_K=150 K and n(H_2)= 8×10^5 cm^{-3} for N6; T_K=135 K and n(H_2)=5×10^5 cm^{-3} for N3.

We can immediately see that the shocks N3 and N6 present similar temperatures and

Table 6.3: Spectroscopic and observational properties of lines detected at shock positions N6, N3, S1 and HH 377 in the jet. The observational properties are obtained from a Gaussian fitting to the line profiles.

						N6			N3			S1			HH377		
Molecule	Transition	ν (MHz)	E$_{up}$ (K)	TAG	Conversion (1 Jy/beam = x K)	v$_{peak}$ (km/s)	Δv (km/s)	T$_{peak}$ (K)	v$_{peak}$ (km/s)	Δv (km/s)	T$_{peak}$ (K)	v$_{peak}$ (km/s)	Δv (km/s)	T$_{peak}$ (K)	v$_{peak}$ (km/s)	Δv (km/s)	T$_{peak}$ (K)
E-CH$_3$OH	$5_{-1,0}-4_{0,0}$	84521.17	40.4	32003	44.5	59.5(0.7)	13(1)	0.24(0.02)	58(2)	9(3)	0.49(0.05)	-	-	-	-	-	-
E-CH$_3$OH	$2_{-1,0}$–$1_{-1,0}$†	96739.36	12.5	32003													
A-CH$_3$OH	$2_{0,+,0}$–$1_{0,+,0}$†	96741.37	7.0	32003	43.9	61.3(0.5)	16(1)	0.32(0.03)	60.0(0.3)	12.4(0.8)	0.59(0.06)	-	-	-	-	-	-
E-CH$_3$OH	$2_{0,0}$–$1_{0,0}$†	96744.55	20.1	32003													
E-CH$_3$OH	$4_{2,0}$–$3_{1,0}$	218440.06	45.5	32003	12.9	61.1(0.7)	9.6(0.7)	0.61(0.06)	57.7(0.6)	5(1)	0.48(0.05)	-	-	-	-	-	-
SO	2_2-1_1	86093.95	19.3	48501	44.5	61(1)	10(2)	0.18(0.02)	59(1)	11(1)	0.18(0.02)	-	-	-	-	-	-
	3_2-2_1	99299.87	9.2	48501	42.9	59.7(0.2)	12.2(0.4)	0.82(0.08)	57.5(0.3)	7.7(0.5)	1.4(0.1)	-112.1(0.9)	24(2)	0.24(0.02)	-70(2)	13(4)	0.058(0.006)
	6_5-5_4	219949.40	35.0	48501	13.8	60.3(0.1)	10.5(0.1)	0.45(0.05)	57.3(0.1)	6.9(0.1)	3.1(0.3)	-116.0(0.6)	18(2)	0.75(0.08)	-70.1(0.4)	10(1)	0.77(0.08)
SiO	$2-1$	86846.96	6.3	44505	44.5	60.4(0.2)	12.8(0.6)	1.7(0.2)	57(1)	10(3)	1.7(0.2)	-110.3(0.4)	25(1)	0.56(0.06)	-69(2)	16(4)	0.14(0.01)
	$5-4$	217104.98	31.3	44505	12.9	61.2(0.2)	10.9(0.1)	5.1(0.5)	58.1(0.1)	6.3(0.2)	3.3(0.3)	-110.9(0.9)	22(2)	0.89(0.08)	-70(1)	13(2)	0.82(0.08)
HCN	1_1-0_1†	88630.42	4.3	27501													
	1_2-0_1†	88631.85	4.3	27501	31.5	60.7(0.2)	12.8(0.4)	2.2(0.2)	58.9(0.5)	9(1)	1.3(0.1)	-110.8(0.8)	26(2)	0.23(0.02)	-67.9(0.5)	14(1)	1.4(0.1)
	1_0-0_1†	88633.94	4.3	27501													
HCO$^+$	$1-0$	89188.53	4.3	29507	31.7	57.8(0.5)	14(1)	1.0(0.1)	55(1)	12.8(0.6)	2.0(0.2)	-104.6(0.9)	32(2)	0.25(0.03)	-69.5(0.9)	12(2)	0.40(0.04)
CS	$2-1$	97980.95	7.1	44501	43.9	60.6(0.4)	10(1)	0.88(0.09)	58.0(0.9)	8.5(0.5)	0.83(0.08)	-	-	-	-70.7(0.4)	8.4(0.8)	0.48(0.05)
p-H$_2$CO	$3_{0,3}-2_{0,2}$	218222.19	21.0	30581	12.9	60.7(0.2)	8.7(0.4)	1.7(0.2)	58.2(0.2)	6.0(0.4)	1.7(0.2)	-	-	-	-70.2(0.3)	8.0(0.7)	1.2(0.1)
p-H$_2$CO	$3_{2,1}-2_{2,0}$	218760.06	68.1	30581	12.7	60.0(0.3)	9.7(0.6)	0.72(0.07)	57.9(0.2)	5.2(0.4)	0.79(0.08)	-	-	-	-70.6(0.4)	7(1)	0.47(0.05)
CO	2-1	230538.00	16.6	28503	24.7	59.1(0.5)	13.3(0.3)	21(2)	57(0.5)	8.5(0.4)	31(3)	-113(2)	20(2)	7.3(0.7)	-70.1(0.5)	10.9(0.2)	23(2)

The transitions marked with a † are blended in the jet line profile. TAGs were obtained from JPL (Pickett et al., 1998) and CDMS (Endres et al., 2016) databases.

densities (Table 6.4). Thus, with the temperature and densities from the best fitting solutions, we computed the column densities for the species detected in these positions, which are summarized in Table 6.5. In both knots, the column density of SiO and H_2CO are of the same order $\approx 10^{14}$ cm^{-2} and $\approx 8 \times 10^{13}$ cm^{-2}, respectively. The values obtained in N6, lies between 5×10^{13} (HCO^+) and 9×10^{14} cm^{-2} (SO), for N3 the values are similar from 5×10^{13} (HCO^+) to 5×10^{14} cm^{-2} (SO). We report in Table 6.3 the column density and abundances with respect to H_2 that were computed assuming the relative abundance between CO and H_2 is 10^{-4}.

In our CO analysis, discussed in Chapter 5, we obtained masses for all knots detected along the jet, and the knots N3 and N6 caught our attention since they were 2-3 times more massive ($8 \times 10^{-3}\ M_\odot$) than other knots in the northern lobe. Additionally to the masses, in our spatial distribution maps, we could see that these shocks are actually chemically richer than the other internal knots, with the presence of CH_3OH for instance which is quite unusual in internal knots of jets. This rich composition and higher masses can be explained by the fact that the jet is impacting the cavity walls at the positions of N3 and N6, as we know from the work of Ospina-Zamudio et al. (2019) that the low-velocity outflow is rich in COMs. Therefore, to explain the presence of CH_3OH, known to be formed through oxygenation of CO (Watanabe et al., 2004) in the grain surfaces mantles, the ice mantles have to be (at least partially) preserved in the cavities and after the shocks N3 and N6 hit the walls, they release the material to the gas-phase through sputtering. As for other possible grain surface products like SiO and H_2CO, the first is unlikely to be that abundant coming from grain processing (Gusdorf et al., 2008a,b), and H_2CO can be formed both in grain surface and gas-phase but it is unclear in our study what is the contribution of processes in N3 and N6.

To summary, it is clear that these shocks are not normal internal knots in the jet when compared to other knots in the northern lobe of the jet and we propose N3 and N6 are actually shocks against the cavity walls but to observationally disentangle it, we will need higher spatial resolution.

Table 6.4: Physical conditions in knots N6, N3, S1 and terminal bowshock HH 377 as derived from LVG approach.

ID	Size ($''$)	T_{kin} (K)	n(H_2) ($\times 10^5$ cm^{-3})	N(SiO) (10^{13} cm^{-2})	N(H_2CO) (10^{13} cm^{-2})
N6	1.7	110 – 200	5.0 – 12.6	14.0	11.0
N3	2.1	100 – 190	3.2 – 7.9	7.3	6.5
S1	1.7	60 – 190	1.6 – 10.0	9.6	≤ 4.0
HH377	1.8	210 – 350	7.9 – 15.8	2.4	8.3

6.6.2 Knot S1

As for the position S1, the situation is diverse as H_2CO is not present and therefore, we can not constrain the temperature, we have assumed that it would have similar temperatures to N3 or N6, so we establish the range to be between T_K=60-190 K, and thus, with the SiO ratio, we obtained the density range as $n(H_2)=(2\text{-}10)\times10^5$ cm^{-3}. Among the species detected in S1, we have reported the column densities in the range 8×10^{12} (HCO^+) to 4×10^{14} cm^{-2} (SO), for the molecules not detected in this knot (CS, H_2CO and CH_3OH), we computed the upper limit in their column densities by assuming that the $I_{\rm peak}$ is three times the noise (3σ) of the spectra extracted from this knot.

From the line analysis and spatial distribution, it is clear that the situation is different in the knot S1. It has a simpler composition typical of jets. The line widths are broader ($\Delta v \sim 24.0\,\mathrm{km\,s^{-1}}$) with some spectra (e.g. SiO 5–4 and SO 6_5–5_4) show even an almost double peak profile, which testify complex kinematics in S1. As we showed with the CO jet kinematics knots collisions are likely possible, and we propose that the collision between knots are producing this emission arising from S1, which could explain the large line widths. This collision can produce a head and reverse shocks internals in the jet. It is possible that the molecular emission is probing the internal knot and the reverse shock caused by a collision of knots, but unfortunately to disentangle both shocks, higher angular and spectral resolutions are required.

6.6.3 HH 377

Likewise for HH 377, we obtained T_K=210–350 K and density $n(H_2)=(7.9\text{–}15.8)\times10^5$ cm^{-3}. The best solution was found as T_K=225 K and $n(H_2)=9\times10^5$ cm^{-3} for HH 377. In the bowshock HH 377, we obtained almost the double of the kinetic temperature with respect to the internal knots and also higher density. With the physical conditions estimated for these positions we computed the column density of the other species detected in the respective knots. They lie in the range of 8×10^{13} (SiO) to 3×10^{14} cm^{-2} (SO). The column densities can be retrieve in Table 6.5.

The presence of methanol was not detected toward the terminal bow shock we reported an upper limit of 1.1×10^{14} cm^{-2}, and the emission seen in Figure 6.11 for the transition is lower than 3σ, as the map is quite noisy. As we discussed, CH_3OH most likely is processed in the dust mantles and sputtered out by shocks as no clear gas-phase formation path is possible. However, H_2CO can be formed through both dust mantles (Garrod & Herbst, 2006) and gas-phase (Vazart et al., 2020), but we can assume that the presence of H_2CO in HH 377 is likely due to gas phase reactions at high temperatures produced in the terminal bow shock.

6.6.4 Comparison between knots

In Figure 6.10 we report the relative abundances with respect to SiO for the four positions N6, N3, S1 and HH 377. Among them, N3 and N6 display a very similar relative abundance for all molecules detected in our work, as should be expected for shocks under the similar physical conditions in the same lobe. As for HH 377, it shows 2 to 5 times higher relative abundances when compared to the previous knots (N3 and N6) with the exception of Methanol which we report the upper limit. For the knot S1 we display only the molecules detected and not the ones that we computed the upper limit for the column density, we can see that HCN and HCO^+ are under abundant when compared to other three knots we studied in Cep E, SO and CO show abundances similar to those for N3 and N6.

Table 6.5: Molecular gas column densities and abundances obtained from an LVG analysis of the CH_3OH, SO, SiO, HCN, HCO+, CS and H_2CO line emission detected towards shock positions N6, N3, S1 and HH377. A standard CO abundance of 10^{-4} relative to H_2 was adopted. Herein, the convention $a(b) = a \times 10^b$ was followed.

Species	N6		N3		S1		HH377		Collisional Coefficients
	N (cm^{-2})	X	N (cm^{-2})	X	N (cm^{-2})	X	N (cm^{-2})	X	
CH_3OH	7.6(14)	1.3(−7)	3.5(14)	6.8(−8)	$\leq$ 1.2(14)	$\leq$ 4(−8)	$\leq$ 1.1(14)	$\leq$ 1.1(−8)	Pottage et al. (2001)
SO	9.0(14)	1.5(−7)	4.6(14)	8.9(−8)	4.4(14)	1.5(−7)	3.3(14)	3.7(−8)	Lique et al. (2006)
SiO	1.4(14)	2.3(−8)	7.3(13)	1.4(−8)	9.6(13)	3.3(−8)	2.4(13)	2.7(−9)	Dayou & Balança (2006)
HCN	1.5(14)	2.4(−8)	6.0(13)	1.2(−8)	2.0(13)	6.8(−9)	1.2(14)	1.3(−8)	[1]
HCO^+	5.0(13)	8.3(−9)	4.9(13)	9.5(−9)	7.9(12)	2.7(−9)	3.1(13)	3.4(−9)	Flower (1999)
CS	2.5(14)	4.2(−8)	9.6(13)	1.9(−8)	$\leq$ 1.1(13)	$\leq$ 3.9(−9)	1.4(14)	1.6(−8)	Lique & Spielfiedel (2007)
H_2CO	1.1(14)	1.8(−8)	6.5(13)	1.3(−8)	$\leq$ 4.0(13)	$\leq$ 1.4(−8)	8.3(13)	9.2(−9)	Green (1991)
CO	6.0(17)	1.0(−4)	5.2(17)	1.0(−4)	2.9(17)	1.0(−4)	9.0(17)	1.0(−4)	Yang et al. (2010)

[1]: Unpublished results taken from http://www.giss.nasa.gov/data/mcrates#hcn

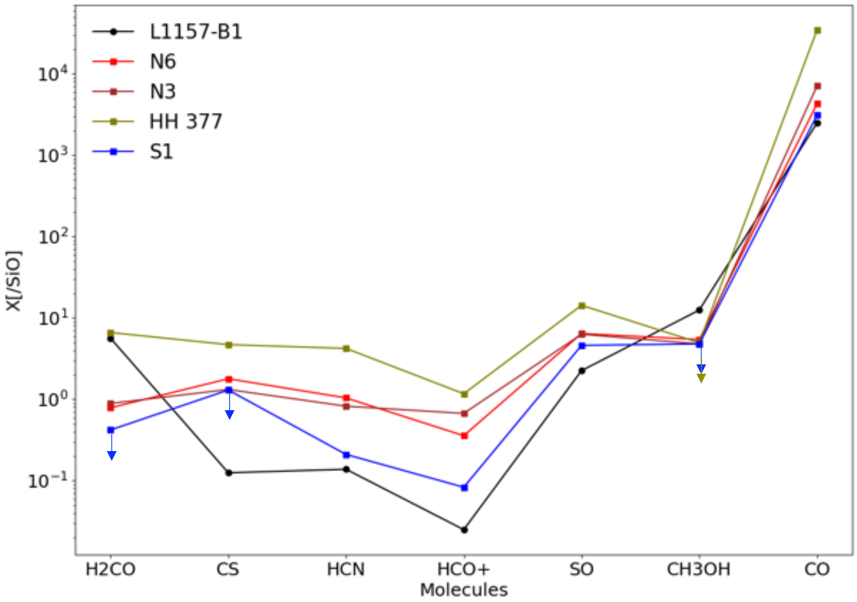

Figure 6.10: Comparison of relative abundances in N3, N6, S1, HH 377 in Cep E and L1157-B1. As presented in Table 6.5, for methanol in the HH 377 object the abundance is presented as an upper limit.

We have also included the relative abundances with respect to SiO for L1157-B1 in Figure 6.10 (black line). As we previously discussed, this shock has been extensively studied for displaying a very rich chemical composition (see e.g., Mendoza et al., 2014; Codella et al., 2017; Lefloch et al., 2017, among others). The results from H_2CO, SiO, CS and HCN were retrieved from Mendoza et al. (2014), Nisini et al. (2007), Gómez-Ruiz et al. (2015) and Lefloch et al. (2021). While the abundances of HCO^+, SO and CH_3OH came from Podio et al. (2014), Holdship et al. (2019), Lefloch et al. (2017), respectively. As can be seen in this figure, the relative abundance of SO, CO and CH_3OH are similar to ones of N3 and N6, while H_2CO has the same relative abundance ($\sim$ 10) as HH 377. The other species (CS, HCN and HCO^+) are under abundant by a factor of 10 with respect to the shocks we are studying but, intriguingly, HCN and HCO^+ have similar relative abundances when compared S1. We note that SiO production depends also on the shock parameters not only environmental (chemical) conditions, making it not a good probe of COMs, for instance.

This comparison between Cep E shocks and LL157-B1 tell us that, when relative to SiO, the richness in B1 could be biased since Cep E is even more abundant and possibly richer but given the distance to probe the complex molecules, one would need a high amount of integration time in the interferometer to detect COMs in toward the shocks in Cep E.

6.7 Conclusions

We have carried out a systematic search for molecular species in the high-velocity jet of the intermediate-mass Class 0 protostar Cep E-A using observations from the IRAM interferometer. We have identified and mapped the spatial distribution of 7 species, including one new detection with respect to previous studies: SiO, HCN, HCO^+, CS, H_2CO, SO and CH_3OH (for the first time). It's clear from maps that a chemical differentiation is present between both lobes of the jet, as in the southern CS, H_2CO and CH_3OH are not detected. The emission in the northern is knotty and associated to the internal shocks N3 and N6. In the southern, only HCO^+ is present along the jet, while the other species SiO, SO and HCN are associated to S1 and the terminal bow shock HH 377.

Analysis of gas kinematics along the jet show clear evidence for gas acceleration in the northern lobe, similarly to CO. PV diagrams along and across the main axis of the jet show that many of the species detected are actually entrained from the protostellar envelope: CS, HCO^+, HCN and SO. Some species (CH_3OH and H_2CO) are detected only in the protostellar envelope around the protostar. This is consistent with the fact those species being on icy mantles of dust grains. The detection CH_3OH at several arcsecond from Cep E-A arises from the cavity walls of the outflow, probably sputtering in the low-velocity shock. As for the southern, PVs across the jet show weak entrainment in the close environment of the protostar. By analyzing PVs along the jet, gas acceleration is seen close to the protostar but the molecular emission (except for CO and HCO^+) suddenly stops around $10''$ already at terminal velocity $V_r = -125\,\mathrm{km\,s^{-1}}$, which is located just after the knot S1. We found evidence of the B-jet to be hitting the cavity walls in the southern lobe and to explain the weak entrainment in this lobe by the A-jet, we propose that Cep E-B jet is removing part of the envelope material that could be entraining. In order to understand the phenomena behind this interactions and the consequences, numerical models are required.

We analysed in more detail the shocks N6, N3, S1 and HH 377. We have first obtained the physical conditions where we N3 and N6 present similar temperatures and densities $\approx$ 100–200 K and (5–10 $\times\ 10^5$ $\mathrm{cm^{-3}}$). We found evidence of interaction between the high-velocity jet and low-velocity outflow at positions N3 and N6, as if the jet is hitting the cavity walls which is supported by the wiggling observed in the jet (see Chapter 5) and the fact that the methanol, a grain surface chemistry product, is found at these locations. In the shock S1 we assumed a range of temperature between 60–190 K as we could not constrain it due to the lack of emission of some species in this shock, but the large linewidths ($\sim 24\,\mathrm{km\,s^{-1}}$)

indicate this knot is different from the others we studied, to explain this we proposed S1 is an internal shock in the jet and the linewdiths measured are possibly due to knot collisions and/or the presence of a reverse shock, which can not be disentangle with our current angular resolution. The terminal bow shock HH 377 presents higher temperature (210–350 K) and density (8–16 $\times$ 10^5 cm^{-3}) when compared to the internal knots. Finally, we computed the abundances for all species reported toward these positions by assuming the physical conditions mentioned above and report them in the range 10^{14} and 10^{15} cm^{-3}. We compared the relative abundances with respect to SiO and found that the Cep E knots are mostly more abundant by a factor of few with respect to L1157-B1.

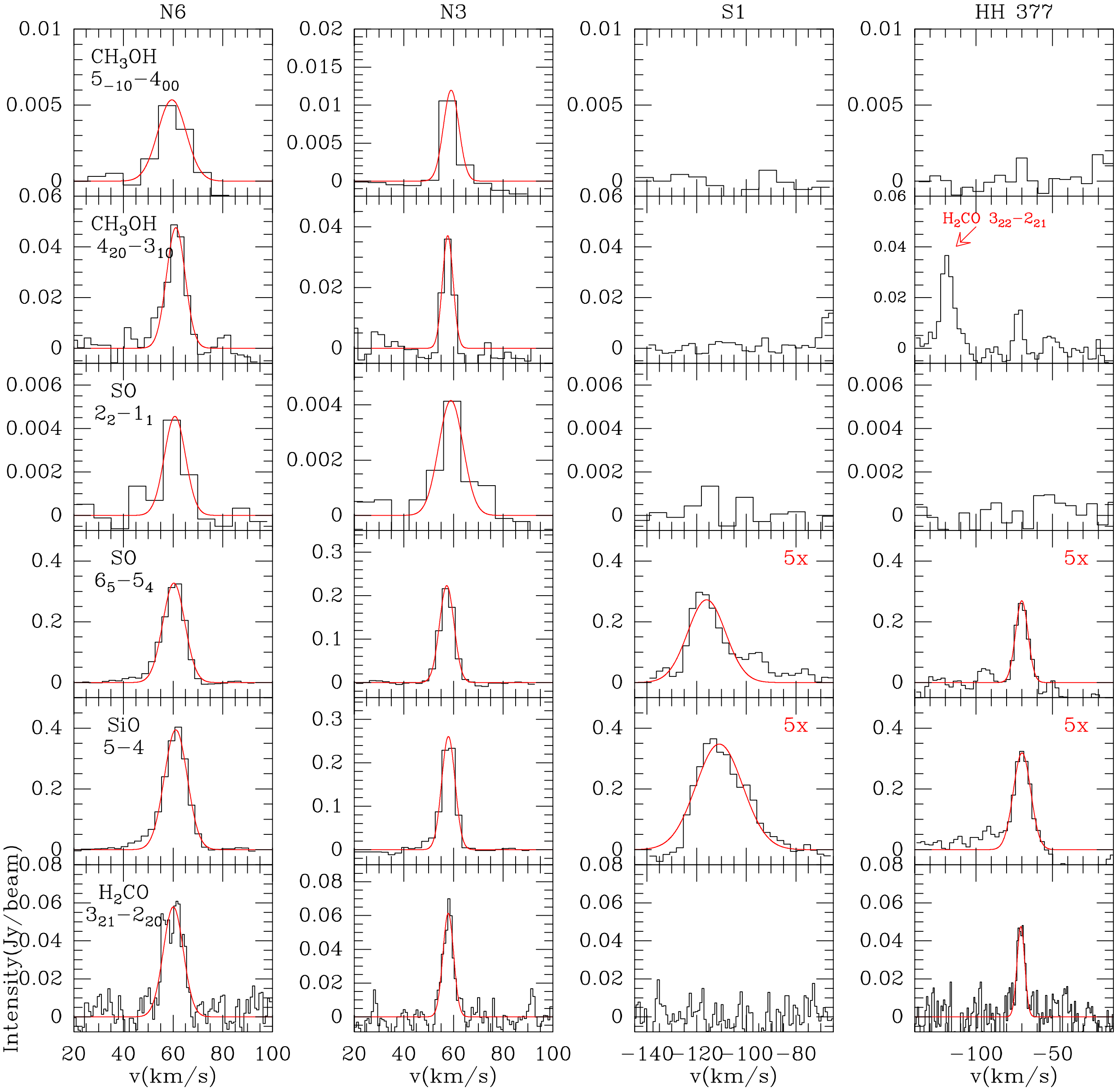

Figure 6.11: Spectra from high-J transitions CH$_3$OH, SO, SiO and H$_2$CO as observed towards the positions N6, N3, S1 and to the HH 377 object (from left to right). The Gaussian fits are displayed in red (see Table 6.3).

Chapter 7

Numerical simulations

7.1 Scientific context and goals

Commonly, the high relative molecular abundance of CO relative to H_2 (assuming the canonical value of 10^{-4}) and its low-energy transitions in the millimeter domain makes it a good tracer of protostellar outflow in the conditions of cold molecular clouds. Even more, the morphology, velocity, and sizes of a molecular outflow depend on the observed tracer, the luminosity, mass and age of the outflow, which indicates its evolution and its inner structure (Bally, 2016).

Over the years, there have been intense numerical efforts to simulate the chemical and dynamical structure of protostellar outflows and their evolution in the ambient interstellar gas, which have led to a general model for the star formation process. Two main class of models are currently in use to describe the structure of outflows (see for a review Frank et al., 2014): the first one considered is wide-angle wind radially expanding at high speed (Shu et al., 1995) and a fast jet surrounded by a MHD disk wind ejected in a narrow solid angle (Matzner & McKee, 1999; Ferreira et al., 2006).

On the numerical side, Smith et al. (1997) carried out 3D simulations of dense molecular jets drilling through a molecular environment where the CO density is considered as a fixed fraction of H_2 density and chemical evolution is not taken into account. They succeeded in reproducing the morphology of the classical CO bipolar outflows, which image the accumulated and accelerated cool gas. They showed that the simulations predict infrared shock structures remarkably similar to those found in highly collimated Class 0 outflows. They proved that in spite of the limitations in their description of the physical conditions (e.g. dust and magnetic field), these hydrodynamical models could provide a meaningful description of the dynamics of bipolar outflows from young stars and accurate enough images for comparison with observations.

On the other hand, most of the hydrodynamical codes developed so far do not include a chemical network and thereby do not address the molecular gas composition, in contradiction with the observational evidence that outflows from Class 0 protostars are often chemically active (e.g. Bachiller et al., 2001; Arce et al., 2007; Lefloch et al., 2017; Ospina-Zamudio et al., 2018; De Simone et al., 2020). It is only with the advent of the first generation of chemo-hydrodynamical codes that it is now possible to model the outflowing gas evolution and to build spectroscopic diagnostics which can be tested against the observational constraint interferometric data has provided, and to investigate in detail the physical processes at work in the jet.

We decided to use a chemo-hydrodynamical code in order to model and reproduce the properties of the CO emission in the Cep E protostellar outflow and its jet, as presented in Chapter 5. The goal was to improve our understanding of observational properties revealed by our interferometric study. To do so, in collaboration with Dr. Pedro Rivera-Ortiz, we carried out a numerical study of Cep E with WALKIMYA, a 2D hydrodynamical code coupled to a chemical a reduced chemical network allowing to follow the evolution of the CO chemistry in molecular outflows (Castellanos-Ramírez et al., 2018). The advantage of this code is that it computes the time evolution of chemical species in a full gas dynamic simulation. As an expert in HD simulation and a numerical modeller, P. Rivera-Ortiz has had a major contribution in developing WALKIMYA-2D (Castellanos-Ramírez et al., 2018).

My contribution in this work was on the observational side, providing the constraints and helping on the interpretation of the results. In this chapter, after a briefing presentation of WALKIMYA-2D, I will present and discuss the results and the advances obtained by WALKIMYA-2D in our understanding of Cep E.

7.2 Numerically modelling the CO emission

7.2.1 Introduction to WALKIMYA-2D

We have used the 2D chemo-hydrodynamical WALKIMYA-2D that solves the hydrodynamic equations and a chemical network, on an axisymmetric numerical adaptive mesh. A complete description of the code is presented in Castellanos-Ramírez et al. (2018).

The chemical network is designed mainly to follow the evolution of the CO chemistry, as induced by the heating and cooling processes in the jet propagation and the shock interaction(s) with the ambient gas. For computational reasons (to keep computational times within reach), the network is reduced to 14 chemical species (and 146 reactions): H, H_2, H^+, CH, CH_2, H_2O, OH, CO, C, C_2, O, O_2, HCO and CO_2. The reaction rates were taken from the UMIST database (McElroy et al., 2013) in the astrochemical context, the code was successfully benchmarked against the model of dark molecular cloud presented in McElroy et al. (2013) and the chemical network was benchmarked with laboratory experiments to study the Nitric Oxide (NO) formation by electrical discharges using both a zero-dimensional and a gas dynamic model approach (Castellanos-Ramírez et al., 2018).

The energy loss-rate is calculated adopting the same prescription as follows: for temperatures larger than 5800 K the cooling function considers the atomic contribution while in the lower temperature range, it uses a parametric molecular cooling function based on CO and H_2 (Rivera-Ortiz et al., 2019). The adaptative mesh uses 7 levels of refinement, yielding 4096×1024 cells, in a computational domain $(5 \times 1.25) \times 10^4$ au, allowing a resolution as high as 12.2 au per cell side. We used a reflective boundary condition for the symmetry axis and a free outflow boundary condition for all the other borders. The size of the mesh is large enough that the outer boundaries do not affect the simulation.

7.2.2 Initial conditions

The protostellar region

The first step was to adopt "reasonable" initial conditions as close as possible from the physical environment in which the Cep E jet propagates. To start with, we have adopted the physical model of the protostellar envelope derived by Crimier et al. (2010), from a 1D modelling of the dust Spectral Energy Distribution (SED) between 24 μm and 1300 μm, using the radiative transfer code 1D DUSTY (Ivezic & Elitzur, 1997). The temperature is fitted by a broken radial power law $T \propto r^{\beta}$ with $\beta = -0.8$ in the range 50–300 K and $\beta = -0.4$ in the range 7 K–50 K.

In their model of density distribution, Crimier et al. (2010) assumed the density profile starts at a radius $r_{in} = 70$ au and follows a single radial power law distribution $n(r) = n_0 \times (r_0/r)^{\alpha}$. In order to avoid density singularities in the limit $r \to 0$ in the numerical modelling, we have adopted a slightly version of the density profile derived by Crimier et al. (2010):

$$n(r) = \frac{n_0}{1 + (r/r_0)^{\alpha}}, \tag{7.1}$$

where $n_0 = 10^9$ cm^{-3}, $r_0 = 100$ au and $\alpha = 1.9$. The simulation takes into account the role of gravity, in agreement with the source density stratification evidenced from Crimier et al. (2010). Our model included a resulting gravitational force as a source term, which is:

$$g = -\frac{2\, c_0^2\, r}{r_0^2\, (1 + (r/r_0)^{\alpha})} \tag{7.2}$$

where c_0 is the local sound speed. The inclusion of this gravity term ensures hydrostatic equilibrium close to the source.

The jet

In our simulations, we adopted as initial jet parameters a nuclei density n(H_2)$= 2 \times 10^6$ cm^{-3} and a temperature $T_j = 300$ K, which are in reasonable agreement with the previous CO jet studies of Lefloch et al. (2015) and Ospina-Zamudio et al. (2019). We adopted an initial velocity of $V_j = 200\,\mathrm{km\,s^{-1}}$ and a jet radius of 100 au. In order to account for the knot formation in the jet, we imposed a velocity variability of 8% with a period τ of 130 years, following the equation:

$$V_j = V_{j,0}\,[1 + \delta_v \cos(2\pi t/\tau)] \tag{7.3}$$

where $\tau = 130$ yr is the injection mass period and t is the evolutionary time. The jet injection velocity $V_{j,0}$ and the relative amplitude variability δ_v are free parameters of the simulation. We adopted $\delta_v = 0.05$–0.08, which implies velocity variations of 10–15 $\mathrm{km\,s^{-1}}$, consistent with variations measured in Cep E (de A. Schutzer et al., 2022).

We explored the influence of the jet radius, the velocity variability and the initial jet velocity by considering slightly different values of these parameters. This led to run the four simulations listed in table 7.1. In our simulation, we did not include the effect of jet precession. The comparison between numerical simulations and our CO observations was made with the northern outflow lobe of Cep E, whose entrained gas dynamics is better revealed in the CO interferometric observations (de A. Schutzer et al., 2022): morphology, gas acceleration, time-variability and knot formation.

Table 7.1: Initial parameters of the four models M1–M4 computed with WALKIMYA-2D: jet radius r_j, injection velocity $v_{j,0}$, relative velocity variability amplitude δ_v. M1 is the model which best fits the Cep E outflow.

Parameter	M1	M2	M3	M4
r_j[au]	100	50	50	150
$v_{j,0}$ [km s^{-1}]	200	165	200	200
δ_v	0.08	0.08	0.05	0.08

Filtering the emission of the high- and low-velocity components allows direct comparison between the simulations and the observational signatures of the distinct outflow components. In order to compare our numerical simulations with the observations, the CO emissivity has been computed directly from the hydrodynamical simulations assuming LTE. The assumption of LTE is justified given the high-density and temperature of the gas in the jet and the protostellar envelope, with n(H_2)$\sim 10^4$ cm^{-3} at 25000 au from the protostar. We have built synthetic CO J= 2–1 maps of the outflow cavity and the jet, by integrating the emission in the velocity intervals [3;7 km s^{-1}] and [50;150 km s^{-1}], respectively. Those maps were subsequently convolved with a Gaussian profile whose size (FWHM) corresponds to the synthetic beamsize of the interferometer for our CO observational (820 au).

We first explored the parameter space and searched for the model which best reproduces the qualitative and quantitative properties of the Cep E northern outflow lobe. Overall, we found that all four models M1–M4 give approximately similar results. In the next section we present the results of model M1, the simulation which best accounts for the molecular gas observations of Cep E. The initial jet velocity is 200 km s^{-1}, with a velocity fluctuation amplitude of 0.08, and an ejection radius of 100 au.

7.3 Outflow formation

In Figure 7.1, we show the molecular gas density distribution at five subsequent steps of the simulation which are from t=0 to t= 2000 yr with steps of 500 yr. The jet is launched at z=0 in gas of density 10^9 cm^{-3}. The difference in density between the jet (10^6 cm^{-3}) and the ambient gas (10^9 cm^{-3}) creates a shock into the ambient gas, at a velocity much lower than the injection velocity of the jet $v_{j,0} = 200$ km s^{-1}.

The first ejection interacts with the very dense gas envelope (10^7–10^8 cm^{-3}) and this process repeats with the subsequent ejecta several times until a few hundred years. At t = 500 yrs, one can see that a small outflow cavity of 5000 au has formed and the jet is now propagating along its central axis. The overpressure resulting from the accumulation of knots, pushes the protostellar envelope transversely away from the jet, causing the formation of a wide-angle outflow cavity, and the density increase in the low-velocity cavity walls at the basis of the jet. This implies that a kinematic age computed from the bowshock position and velocity is actually a lower limit to the real age of the outflow.

At t = 1000 yr, the model shows now a leading jet head and a series of Internal Working Surfaces (IWS). They are usually formed as the result of the ejection time-variability and are observed as "knots" with a small size of a few $\sim$ 100 au. 3 knots are easily detected along the jet, while at t = 2000 yr, 8 eight knots are identified. It is possible to note that these

Table 7.2: Outflow physical properties derived from CO emissivity maps at 1500 yr in the four numerical simulations (M1– M4) and comparison with the observational values of the Cep E outflow: jet mass M_j, outflow mass M_o, jet length z_{bs}, maximum outflow radius r_{max}.

Parameter	M1	M2	M3	M4	Cep E North	 South
$M_j\,[10^{-2}\mathrm{M}_\odot]$	2.25	0.75	1.5	5	3.6	2.6
$M_o[\mathrm{M}_\odot]$	2.3	1.3	1.2	2.9	2.0	0.4
$z_{bs}[\,10^3\mathrm{au}]$	27	23	29	31	41	30
$r_{max}[\,10^3\mathrm{au}]$	3.7	1.5	3.6	5.3	5	4

knots tend to expand radially as they propagate along the jet, tracing the wings of inner bowshocks, since the slower material interacts with the faster material ejected at later times. These wings appear to drive the formation of complex structures inside the outflow cavity as can be seen in the bottom panel of Figure 7.1. Fast moving knots tend to accumulate at the head of the bow, increasing the density at the tip of the jet. After 1500 yr, the knots located at distance $>$ 15000 au display wings with a typical size of 1000 au.

At a time of 1500 yr, the first outflow cavity has reached a size of $\approx$ 15000 au and has expanded up to a radius of about 5000 au ($6''$ at the distance of Cep E-mm), and the head of the outflow has reached a distance of 2.8×10^4 au ($34''$), while a second outflow cavity is formed. As time increases, at $t = 2000$ yr, the second cavity expands to reach a similar radius of $\approx$ 5000 au. A complex network of relatively dense structures ($n \sim 10^5$–$10^6\,\mathrm{cm}^{-3}$) forms inside the outflow cavity very early. It is possible to note, in the first 1000 yr, the presence of a thin, yellow, wiggling structure parallel to the jet such as "filaments". In this panel, a filament has formed along the jet, located at R= 500au and it is detected up to $z = 2000$ au. We also note the presence of a bow or "shell" formed in the dense protostellar envelope and moves slowly ($\sim 20\,\mathrm{km\,s}^{-1}$) as it propagates over 8000au in 2000 yr, whereas the jet reached 40×10^3 au. This dense shell connects the jet envelope of entrained gas to the low-velocity outflow.

When looking at the density distribution at $t = 1500$ yr (Figure 5.1), a time similar to the dynamical age of the outflow/jet of Cep E, we find a very satisfying morphological agreement: both the size , the length, the radius of the outflow and the two cavities are produced.

In order to better understand the role of the core initial conditions in shaping the outflow morphology, we also carried out simulations without the inclusion of the high-density core of Crimier et al. (2010) nor the related gravitational term. It turned out that the low-velocity outflows which formed in the ambient medium of the jet propagation were actually far too collimated with respect to what is observed, in particular close to the protostar and the jet launch region. Therefore, it appears that the degree of opening of the low-velocity outflow cavity depends on the density of the inner envelope and the contribution of the latter to the gravitational field, two parameters which are related to the evolutionary stage of the system. These results are in agreement with theoretical works by Cabrit et al. (1997) who concluded that a steep radial density decrease would produce a wider opening angle for jet-driven outflows and MHD numerical simulation by Rabenanahary et al. (2022).

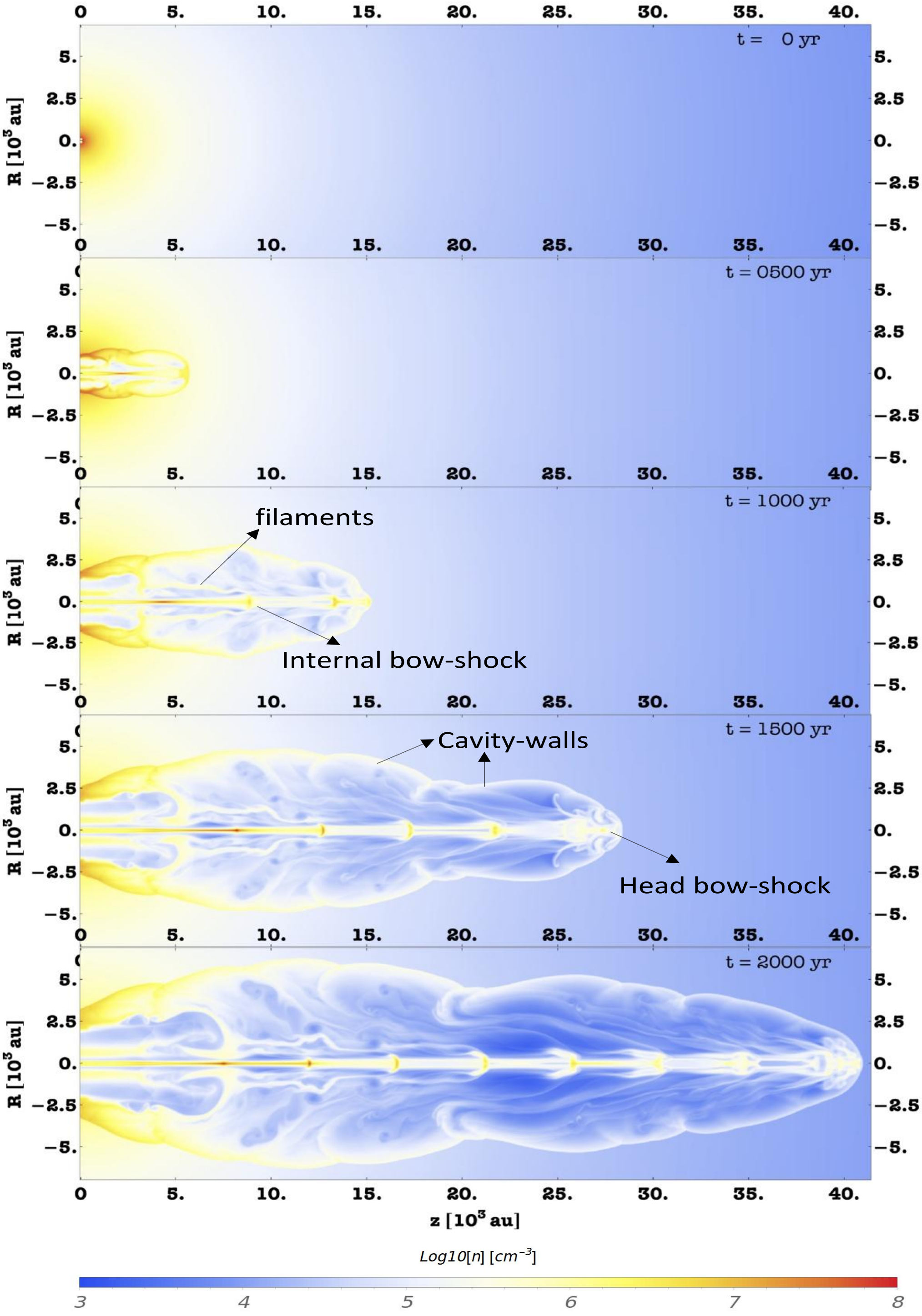

Figure 7.1: Outflow formation and impact of the jet on the gas density distribution as a function of time. snapshots for 0, 500, 1000, 1500, and 2000 yr. The injection velocity variability forms internal working surfaces, or knots, and a structured cavity. The leading bowshock accumulates the mass of several knots.

7.4 Gas acceleration

As we reported in Chapter 5, the Cep E jet displays evidence of gas acceleration over a distance of 5000 au away from the protostar. In order to compare with the Position-Velocity diagram of the CO data (see Figure 5.2), we computed a PV diagram along the main jet axis at a time $t = 1250$ yr (see Figure 7.2), close to the dynamical age of Cep E. Two kinematic components are clearly identified: i) a low velocity component, between +0 and +10 $\mathrm{km\,s^{-1}}$ up to 8000 au ($10''$) from the source, associated with the outflow cavity walls; ii) a high velocity component, that displays a periodical behavior, reflecting the mass injection variability and the internal shocks, where the fast material catches up with the slower material. The jet is detected at a velocity close to $V_j = 90\,\mathrm{km\,s^{-1}}$ at $d > 2000$ au from the source. Note that in this plot, velocities are corrected for the jet inclination with respect to plane of the sky.

Our simulations show that the effective velocity of the outflow is significantly lower than the injection jet velocity. This is the result of the jet interaction with the dense central envelope. In this case, the PV diagram in Fig. 7.2 shows that the CO gas emission accelerates from ambient velocity ($V = 0\,\mathrm{km\,s^{-1}}$) to the terminal jet velocity on a short scale < 5000 au. Close to the source, gas structures accelerated up to $V \sim 50\,\mathrm{km\,s^{-1}}$ are also detected along the jet axis up to 1000–2000 au (bottom panel of Fig. 7.2).

An observational signature of envelope gas can also be found in the Position-Velocity diagram of the CO J=2–1 emission across the jet main axis, as can be seen in Figure 5.2. The CO emission contours show how the ambient material initially at rest at $V_{lsr} = -11\,\mathrm{km\,s^{-1}}$ is gradually accelerated as one gets closer to the location of the protostar at $\alpha = 0''$. In addition to the jet mainly detected up to $V \sim 60\,\mathrm{km\,s^{-1}}$, signatures of high-velocity knots (up $+90\,\mathrm{km\,s^{-1}}$) are also identified close to the protostar (see Figure 5.3 at $\delta = 0''$ panel). It is worth remembering that the synthetic PV diagram (Figure 7.2) displays the total velocity variations whereas the Cep E observational plots (Figure 5.2) display the radial component of the jet velocity.

For the sake of comparison with the Cep E jet, we have checked whether the solution found by de A. Schutzer et al. (2022) $(V - V_{lsr})/V_j = exp(-\delta_0/\delta)$ could provide a reasonable fit to the synthetic jet velocity profile along the main axis. The yellow curve drawn in the bottom panel of Fig. 7.2 traces the best fitting solution obtained for a length scale $\delta_0 =$ 690 au, applied to the total jet velocity $V = 90\,\mathrm{km\,s^{-1}}$. Taking into account the inclination of the jet with respect to the line of sight, the agreement between numerical and observational jet velocity profiles is very satisfying both qualitatively and quantitatively. To summarize, our simulation successfully accounts for the observed acceleration of material from the protostellar envelope by the Cep E jet, from ambient velocity up to reaching the terminal jet velocity $V_j \sim 90\,\mathrm{km\,s^{-1}}$, this process occurs over a scale of 5000 au both in time and length scales.

7.5 Outflow mass evolution

7.5.1 The jet

The numerical simulation offer the unique opportunity of studying the evolution of outflowing material, its mass as a function of time, while measuring the mass of ejected material

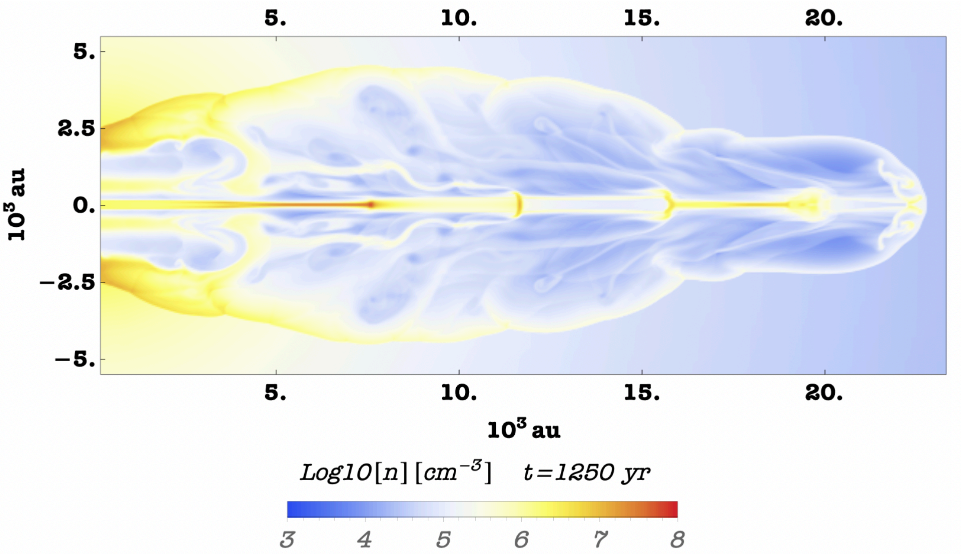

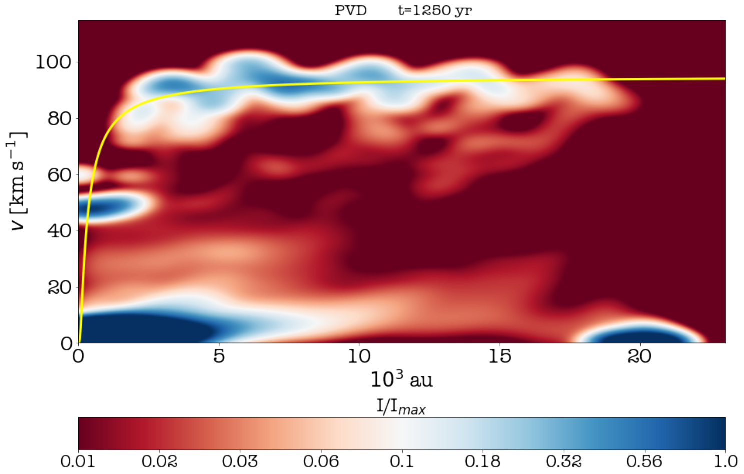

Figure 7.2: Best fitting model (M1) of the Cep E northern outflow at 1250 yr. (Top) Density distribution. The jet has propagated over a distance of 2.4×10^4 au and formed a low-velocity cavity of 3000 au radius. Five knots and their associated wings are detected along the jet. (Bottom) Position-Velocity diagram of the CO emission along the jet main axis. The fit to the observational data (see Fig. 5.2) and corrected for the jet inclination with respect to the plane of the sky is superimposed in yellow.

from the protostellar system. We show in Figure 7.3 the total mass of outflowing material, integrated over all velocities as a function of time. It comes out immediately that the outflow mass increases linearly with time at a rate of $1.6 \times 10^{-3}\, M_{\odot}\, \mathrm{yr}^{-1}$. At a time of 1400 yr in the simulation (similar to the dynamical age of Cep E) the mass of outflowing gas amounts to $2.2\, M_{\odot}$, a value in good agreement with the observational determination in the northern lobe (see Table 7.2).

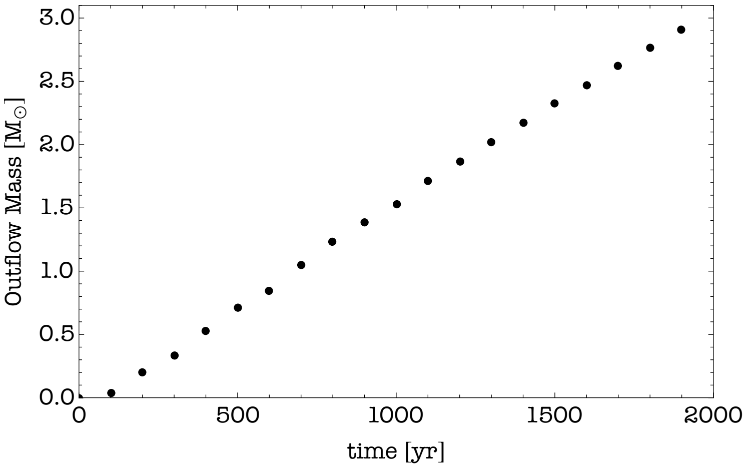

Figure 7.3: Model M1. Outflow mass evolution as a function of time.

In a second step, we have studied the variations of the jet mass as a function of time. We took into account all the gas at velocity $> 50\,\mathrm{km\,s^{-1}}$ to estimate the jet mass and follow its variations. The variations of the jet mass as a function of time are displayed in Figure. 7.4. After an initial delay of $\sim 200\,\mathrm{yr}$, which corresponds to the time needed for the knots to drill the envelope, the jet mass increases linearly with time, at a rate $\dot{M}= 2.3 \times 10^{-5}\, M_\odot\,\mathrm{yr}^{-1}$ in very good agreement with the observational determination of $2.7 \times 10^{-5}\, M_\odot\,\mathrm{yr}^{-1}$ (de A. Schutzer et al., 2022). It is important to note that one of the main results of CO kinematic analysis was that we could identify the entrainment process from the protostellar material by the high-velocity jet occurring at few arcsecond from the protostar (reported in Chapter 5 and 6).

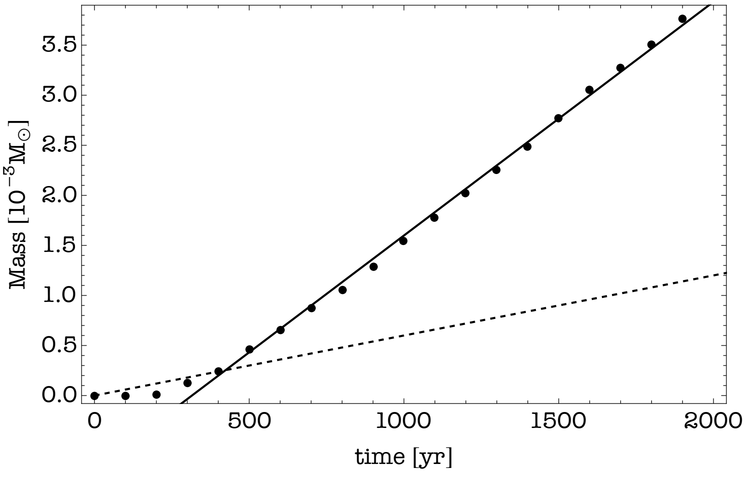

Figure 7.4: Model M1. Jet mass evolution as a function of time. The points are obtained from the simulation every 100 yr. The black continuous line is a linear fit of the points starting from 300 yr, with a slope of 2.3 $\times 10^{-5} M_\odot$ yr^{-1} and the dashed line corresponds to the material injection rate of $\dot{M} = 7.3 \times 10^{-6}$ used in the simulation.

In a third step, we estimated directly the importance of the material entrainment on the jet mass and mass flux determination. The jet mass flux (hence the jet mass) can be directly estimated from the amount of jet material injected at each timestep of the simulation. It can be also estimated theoretically, the jet mass injection rate per unit of time can be estimated as a function of the injected material density n_j, the jet velocity v_j and the jet injection radius r_j:

$$\left[\frac{\dot{M}}{\mathrm{M_\odot/yr}}\right] = 1.5\times10^{-6}\left[\frac{r_j}{50\mathrm{au}}\right]^2\left[\frac{n_j}{10^6\,\mathrm{cm^{-3}}}\right]\left[\frac{v_j}{165\,\mathrm{km\,s^{-1}}}\right], \tag{7.4}$$

In practice, we observed an excellent agreement between the numerical mass rate and the theoretical results from Equation 7.4: $\dot{M} = 7.3\times10^{-6}\,M_\odot\,\mathrm{yr}^{-1}$ (model M1). In both numerical and theoretical cases, the jet mass injection rate is lower than the jet mass rate $\dot{M}$ of the simulation by a factor of ≈ 3. We consider the difference between both values as very significant as it highlights the importance of the entrainment process of circumstellar material in the formation of molecular jets, at least in a certain range of physical parameter.

7.5.2 The knots

We have studied the gas density distribution along the jet as a function of time in the simulation up to 2000 yr. We found that the evolution is characterized by very short timescales of the order of 25 yr. In order to illustrate and better explain the process at work, we show in Fig. 7.5 a montage of the jet density profiles at intervals of 25 yr over a time of 125 yr, between 1450 yr and 1575 yr. The mean jet density distribution appears steady and constant at distances further than 10^4 au, while at shorter distances, there is a decreasing density profile, being a signature of the steep initial density profile of the envelope, since it is expected to be difficult to remove the dense envelope material close to the source, even when it has been processed by the continuous injection of the jet. Obviously, one may speculate that this discrepancy will tend to decrease as time evolves, with source evolutionary stage, when the envelope density gradually dissipates.

The peaks which appear on top of the mean density distribution, result from the ejection velocity variability in the jet which causes fast material to shock with lower velocity gas. Each of these peaks corresponds to a local overdensity structure in the jet. The peak properties were derived from a Gaussian profile fitting in the simulations: a size of 1000 au, a density of about $10^5\,\mathrm{cm}^{-3}$, and a typical mass of $10^{-3}\,M_\odot$. These physical properties are actually very similar to those of the CO knots reported in the Cep E jet like the knots N0, N1 and N2 (see Table 5.1), for instance.

By inspecting Figure 7.5, one can note that at distances larger than 10^4 au the density and the knot distributions are almost steady, which reflects the fact that the knots are travelling into the low-density material of the jet for about 525 au in a period of 25 yr or a velocity of $\sim 100\,\mathrm{km\,s^{-1}}$. The high-density in the inner 10^4 au makes the situation drastically different. Rivera-Ortiz et al. (2019) have shown that gas flowing into an environment of similar density can create reverse shocks that propagate at a significant fraction of the original velocity relatively to the shock velocity. This is precisely the present situation with a jet of density $10^6\,\mathrm{cm}^{-3}$ propagating into gas of density $2\text{–}4\times10^5\,\mathrm{cm}^{-3}$, beyond ~ 6000 au (based on Crimier et al., 2010). This means that such reverse shocks are likely to form in the inner protostellar envelope environment. This effect is seen in Figure 7.5, where the number of peaks varies in the inner 10^4au. First at $t = 1450$ yr, knot Kc is emerging from the inner protostellar region at ~ 2000 au ($3''$) from the protostar. Its size is quite extended along the jet axis, as measured by the density distribution. Whereas knots Kc and Kb are separated by ~ 2000 au at $t = 1450$ yr, they finally begin to merge at $t = 1500$ yr

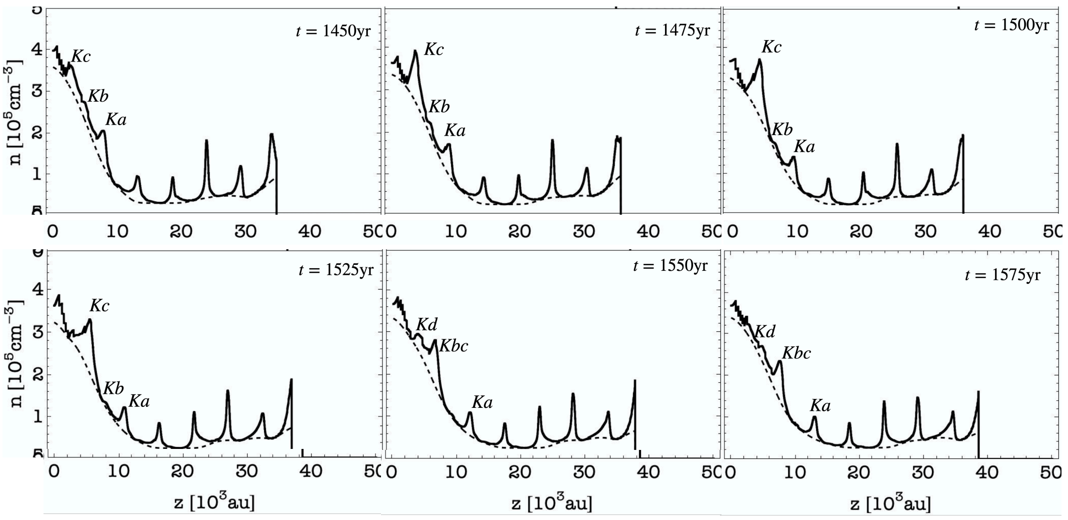

Figure 7.5: Gas density distribution along the jet main axis for different snapshots from 1450 to 1575 yr (dashed lines). Knots are identified as localised peaks in the density distribution (thick lines) with values of the order of 10^5 cm^{-3}.

and merge completely at $t = 1550$ yr. The two subsequent knots are no longer Ka and Kb, distant about 2000 au, but Ka and Kbc, which are separated by about 5000 au. The process appears to repeat itself at $t = 1575$ yr with the formation of Kd, a small knot behind Kbc, which moves forward at slightly lower velocity creating a similar density distribution to the one at $t = 1450$ yr. This interval of 125 yr is approximately the period of variability in the simulation. This process gets repeated several times, accelerating the fossil envelope material, and relates the process of gas acceleration with the formation of knots.

The mass of the knots as a function of their location along the jet at $t = 1500$ yr are displayed in Figure 7.6 (left panel). The knots tend to increase their mass by a factor of 2 as they move away from $z = 0$. The simulation shows that the mass increase occurs on a very short length scale as the second knot at $z \sim 3000$ au has already a mass of $1.7 \times 10^{-3}\ M_{\odot}$. Beyond 8000 au, all knots display similar masses $\sim 1.7 \times 10^{-3}\ M_{\odot}$. The terminal knot is an exception due to its higher mass ($> 3 \times 10^{-3}\ M_{\odot}$). This high value is consistent with the fact that several knots have already reached the tip of the jet and are accumulating there.

In the later times of the simulation, the spatial separation between the knots located close to the source is shorter by about a factor 0.5 than the separation between those located in the older region of the jet. Our simulations and the interaction of knots in the inner region appear to provide an explanation to the bimodal distribution of dynamical ages reported in Chapter 5 (see Figure 5.7).

We showed in Chapter 5 that the distribution of knot dynamical ages are bimodal, with the presence of two timescales: a short time interval of 50–80 yr close to the protostar (<8000 au) and a longer timescale (150–200 yr) at larger distances from the protostar. The numerical simulation reports the same trend, as shown in Figure 7.6 (right panel), the ages of all the knots identified along the jet have been reported. The first four younger knots are separated by a timescale of about 100 yr, whereas the following knots are separated by a timescale of about 200 yr, or twice the value measured close to the jet launch region. Our simulations show that a high-velocity knot can overcome the spatial separation to the previous one, which was slow down as a result of the interaction with the dense gas of the

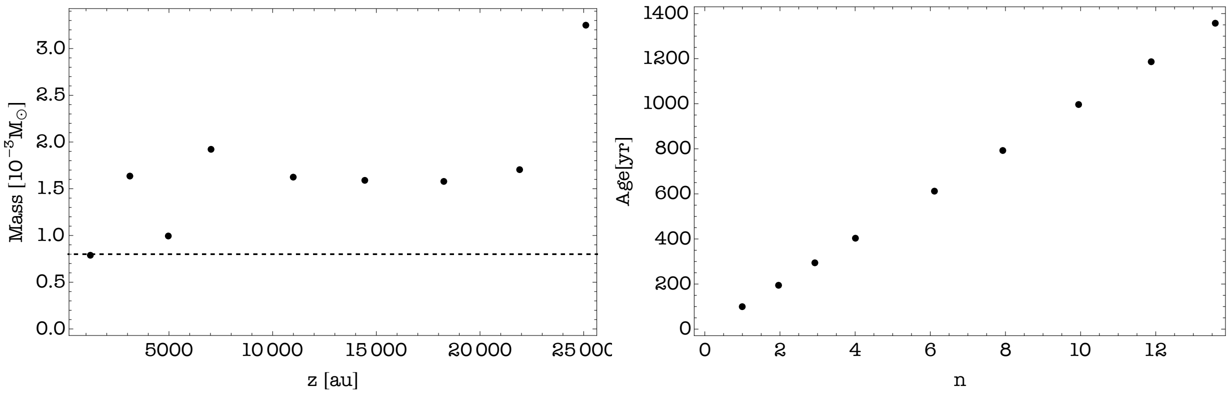

Figure 7.6: (Left) Mass of the knots measured at 1500 yr in Model M1 as a function of their position z along the jet, projected by 47°, which corresponds to the angle between the Cep E jet main axis and the plane of the sky. The dashed line corresponds to the mass injected to the simulation in a single period. (Right) The dynamical age of the knots identified in model M1 at t= 1500 yr in terms of a multiple number n_i of the shorter dynamical age.

protostellar envelope, and the typical timescale for the collision is 500 yr.

7.6 Studying the CO emission

We produced synthetic CO integrated emissivity maps of the outflow jet and cavity. The CO emissivity of the low-velocity outflow integrated between [3;7] km s^{-1}(in black contours) and the high-velocity jet between [50;150] km s^{-1}(blue). The CO synthetic map reveals a highly-collimated structure of the jet with a typical width of 1000 au, which slightly increases with distance from the source. As can be seen, the emission from the high-velocity jet and the low-velocity cavity decreases down to 2000 au before the terminal bowshock, whose location is marked by a red point in the image. The lack of low-velocity CO emission over a few 1000 au near the tip of the outflow cavity is explained by the fact that terminal bowshock is efficiently dissociating the CO molecular gas, as we will see bellow.

In order to understand how the CO abundance (relative to H_2) varies along the outflow, we computed this abundance distributions at 4 different times using the model M1: 0, 500 yr, 1000 yr, and 1500 yr. The distributions are reported in Figure 7.8. For the sake of simplicity, we have reported the ratio X_{CO} of the CO abundance to its initial value, taken the canonical value of 10^{-4}.

In the early stages of our simulation (t < 500 yr), when the jet has a length of a few thousand astronomical units, X_{CO} is well below its canonical value 1.0. At $t = 500$ yr, the abundance is $X_{CO} \approx 0.5$ at 5000 au from the protostar. When time evolves $t = 1000$ yr and $t = 1500$ yr, we can identify two regimes in the X_{CO} distribution observed along the jet: first, close to the jet launch region X_{CO}= 1 and the length of this region increases with time (2000 au at t=1000 yr and 12000 au at t=1500 yr) as the jet propagates with V_j= 140 km s^{-1}. Second, at larger distances, X_{CO} decreases from 1 to a few 10^{-1} when further away from the protostar. This decrease is smooth and does not display abrupt variations along the jet, the minimum value is reached at the terminal bowshock before X_{CO} jumps abruptly again to 1, the canonical value in the ambient quiescent gas where the jet propagates.

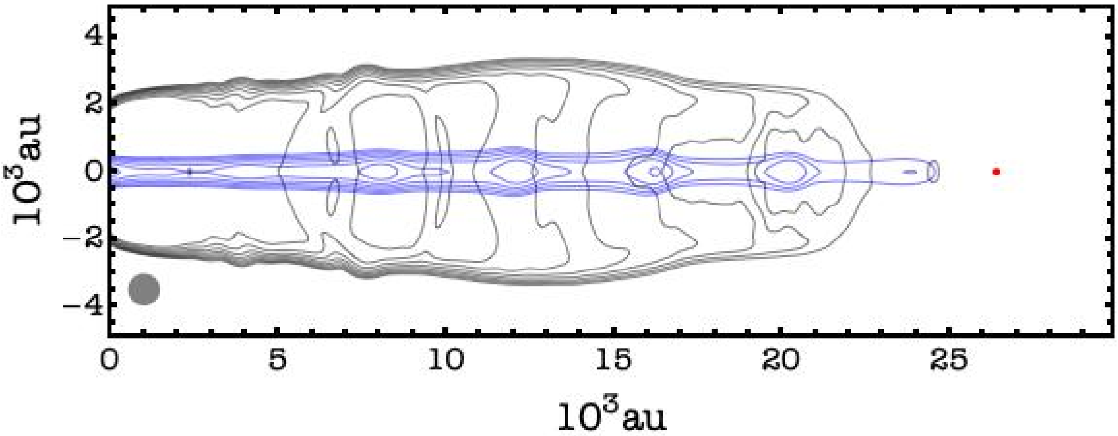

Figure 7.7: Synthetic map of Model M1 at t= 1500 yr. CO J= 2–1 integrated emissivity contour maps of the cavity (Black contours, 3 to 7 km s^{-1}) and the jet (Blue contours, 50 to 150 km s^{-1}) components. The scale is logarithmic with contours starting at 10% of maximum intensity. The response of the IRAM interferometer was modelled by a Gaussian of 830 au diameter (FWHM), corresponding to a beam size of 1$''$ (FWHP) at the distance of Cep E-mm, which is drawn with a gray disk (bottom left). The location of the frontal shock is marked with a red point.

To summarize, our simulation show that CO is partly destroyed in the early times of the jet launch, close to the protostar ($X_{CO} < 10^{-1}$). The destruction process appears to stop ≈ 900 yr after the beginning of the simulation and the CO abundance of the ejected material remains steady and equal to its initial value. We interpreted the CO dissociation as a consequence of the violent shocks caused by the first high-velocity knots (and the jet) when they are launched and impact the dense, protostellar envelope at the beginning of the simulation. It is only when the knots finally drill out the envelope and escape the inner protostellar region, entraining a fraction of the ambient protostellar envelope, that the local value of X_{CO} tends to return to its initial value. Additionally, this process can be influenced as well by the gas entrainment.

Inspecting Figure 7.8, we note that the slope of the X_{CO} distribution along the jet at t = 1000 yr and t = 1500 yr are similar, indicating that it is not varying with time. This indicates that X_{CO} is not affected by any dissociation process during the jet propagation and that the observed dissociation is an inheritage of the early ejection phase. The velocity variations between subsequent knots ($\sim$ 10 km s^{-1}) do not significantly affect the CO abundance. Therefore it seems that the jet somewhat kept memory of the initial launch process in the X_{CO} axial distribution.

Finally, our numerical result has several implications on the observational side. First, lower values of X_{CO} may actually reflect the conditions of the jet formation process. Of course, precession and/or knot interaction with the ambient gas (or the cavity) may alter this conclusion. We speculate that in the latter case, the X_{CO} variations occur on a much smaller length scale, corresponding to the knots size, i.e. 1000 au typically. Our model suggests that the distribution of X_{CO} along the jet could probably provide constraints robust enough to discriminate between the processes at work.

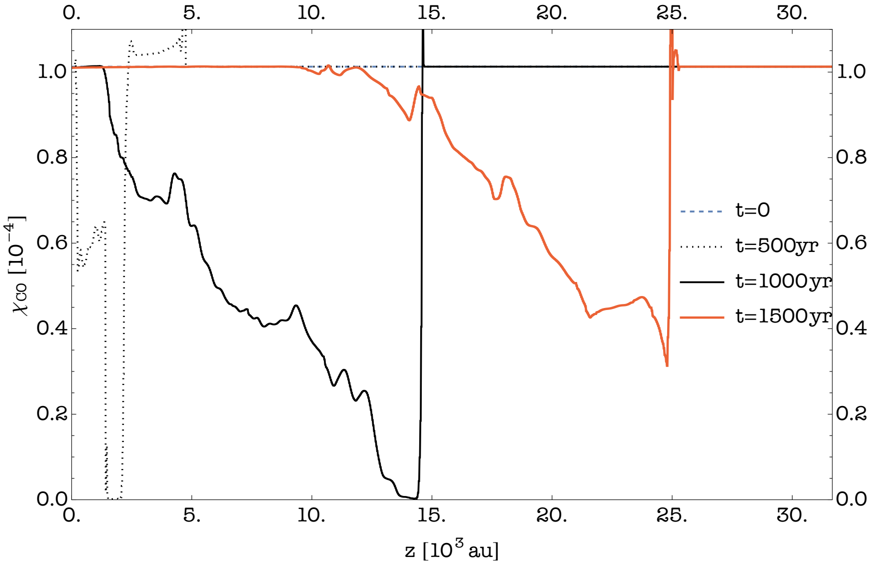

Figure 7.8: Variations of the CO/H_2 abundance relative to its initial value (10^{-4}) along the high-velocity jet at 4 different times of the simulation: 0, 500 (dotted), 1000 (solid black), 1500 yr (solid red).

7.7 Conclusions and remarks

Using the hydrodynamical code Walkimya-2D, we have carried out a set of simulations in order to reproduce the morphology and the physical properties of the molecular jet-driven outflow of the intermediate-mass protostellar source Cep E, as derived from previous observational studies (Lefloch et al., 2015; Ospina-Zamudio et al., 2019; de A. Schutzer et al., 2022). Although, outflow precession was not considered in this work, we have obtained a very satisfying agreement, both qualitatively and quantitatively, with the observations when modelling a time-variable jet with initial density $n(H)= 10^6\,\mathrm{cm}^{-3}$, radius $r_j= 100$ au, temperature $T_j= 300$ K, velocity $V_j= 200\,\mathrm{km\,s}^{-1}$ propagating into the density stratified protostellar envelope as modelled by Crimier et al. (2010). To summary, we obtained the following results:

- the jet and cavity morphologies (width and length) and the expected kinematics were satisfyingly reproduced by WALKYMIA-2D. The best fitting solution is obtained at a numerical dynamical age of $t_{dyn} \simeq 1250$ yr, consistent with the jet dynamical timescale estimated observationally ($\simeq 1400$ yr de A. Schutzer et al., 2022).

- the jet acceleration detected in molecular gas observations is reproduced in the simulations, and it appears to be the result of ambient material entrainment by the knots on a length scale of ~ 700 au, in agreement with the observational data.

- the properties of the knots along the jet are well accounted for periodic ejections. We found evidence for knot interactions in the dense inner protostellar region, where the densities of the local gas and the jet are comparable, which lead to the formation of secondary shocks in the close protostellar environment. At larger distances from the protostar, the lower ambient gas density allows the knots to propagate freely, without significant interaction. We propose that this process could account for the bimodal distribution of knots observed along the Cep E jet, the knots have a typical size of 1000-2000 au, with a mass of $\sim 1.5 \times 10^{-3}\, M_{\odot}$, and density of $10^5\,\mathrm{cm}^{-3}$. The mass carried away by the knots in the jet translates into a steady ejection mass rate of $2.3 \times 10^{-5}\, M_{\odot}\,\mathrm{yr}^{-1}$, a factor of 3 higher than the mass injection rate into the jet ($7.3 \times 10^{-6}\, M_{\odot}\,\mathrm{yr}^{-1}$). This difference is the signature of the entrainment and the subsequent acceleration of ambient material by the jet.

- the shock interaction of the jet knots with the protostellar envelope in the early times of the simulation lead to the dissociation of CO. The destruction process appears to stop after ≈ 900 yr, time from which the CO abundance of the ejected material remains steady and equal to its initial (canonical) value. As a consequence, the older part of the jet is characterized by a lower CO gas abundance, which gradually decreases as one moves closer to the jet head.

Our simulations underline the importance of mass ejection time variability in the molecular outflow formation process and its interaction with the protostellar envelope, as they confirm the importance of jet interaction with the protostellar envelope in the formation of molecular jet. Both observationally and numerically, more work needs to be done to investigate the role of knots and their importance in the dynamical evolution of other young protostellar systems.

Therefore, interferometric observations at subarcsec angular resolution of Cep E and other young protostellar jets should be undertaken as they would allow to make a significant step forward on bringing constraints on the knot internal structure and the dynamical processes at work in the jet. In parallel, the high spatial resolution accessible in the WALKIMYA-2D numerical simulations ($\sim$ 10 au) gives access to a novel view on the structure of protostellar jets and their dynamics, which will help interpret a new harvest of observations.

This work has been submitted in Astronomy and Astrophysics in 29 September 2022 and it is under peer-review process. Title: "Modelling the early mass-ejection in jet driven protostellar outflows. Lessons from Cep E." The submitted version is found bellow.

Modelling the early mass-ejection in jet driven protostellar outflows. Lessons from Cep E.

P. R. Rivera-Ortiz[1, 2], A. de A. Schutzer[2], B. Lefloch[2], and A. Gusdorf[3, 4]

[1] Instituto de Radioastronomía y Astrofísica, Universidad Nacional Autónoma de México, P.O. Box 3-72, 58090, Morelia, Michoacán, Mexico
e-mail: `privera@irya.unam.mx`
[2] Univ. Grenoble Alpes, CNRS, Institut de Planétologie et d'Astrophysique de Grenoble (IPAG), 38000 Grenoble, France
[3] Laboratoire de Physique de l'ENS, ENS, Université PSL, CNRS, Sorbonne Université, Université de Paris, 75005 Paris, France
[4] Observatoire de Paris, PSL University, Sorbonne Université, LERMA, 75014 Paris, France

Started June 10, 2021; June 10 version, 2021

ABSTRACT

Context. Protostellar jets and outflows are an important agent of star formation as they carry away a fraction of momentum and energy, needed for gravitational collapse and protostellar mass accretion to occur.
Aims. Our goal is to provide constraints on the dynamics of the inner protostellar environment from the study of the outflow/jet propagation away from the launch region.
Methods. We have used the 2D chemo-hydrodynamical code WALKIMYA-2D to numerically model and reproduce the physical and CO emission properties of the jet-driven outflow from the intermediate-mass protostar CepE-mm, which was observed at ∼ 800 au resolution in the CO J=2–1 line with the IRAM interferometer. Our simulations take into account the observational constraints available on the physical structure of the protostellar envelope.
Results. WALKIMYA-2D successfully reproduces the main qualitative and quantitative features of the Cep E outflow and the jet kinematics, naturally accounting for their time variability. Signatures of internal shocks are detected as knots along the jet. In the early times of the ejection process, the young emitted knots interact with the dense circumstellar envelope through high-velocity, dissociative shocks, which strongly decrease the CO gas abundance in the jet. As time proceeds, the knots propagate more smoothly through the envelope and dissociative shocks disappear after $\sim 10^3$ yr. The distribution of CO abundance along the jet shows that the latter bears memory of the early dissociative phase in the course of its propagation. Analysis of the velocity field shows that the jet material mainly consists of gas entrained from the circumstellar envelope and accelerated away from the protostar at 700 au scale. As a result, the overall jet mass loss rate appears higher than the actual mass ejection rate by a factor ∼ 3.
Conclusions. Numerical modelling of the Cep E jet-driven outflow and comparison with the CO observations have allowed us to peer into the outflow formation mechanism with unprecedented detail and to retrieve the history of the mass-loss events that have shaped the outflow.

Key words. stars: formation — ISM: jets and outflows — astrochemistry

1. Introduction

Protostellar jets and outflows are an ubiquitous phenomenon of the star formation process from the early Class 0 to the late Class I phase, when the parental envelope is dissipated. They are an important agent of star formation feedback, which affects the gas physical and chemical properties from cloud scale down to the central parental cocoon, where mass accretion is occuring. On the one hand, they act as a source of energy and momentum into the parental cloud, they disperse the material of the parental core, directly impacting the star formation efficiency and the final stellar mass (see Frank et al. (2014) for a review); on the other hand, they are thought to remove a significant fraction of the angular momentum from the star–disc system, enabling the gas in the accretion disc to reach the central protostar (Konigl & Pudritz 2000).

A natural consequence of the propagation of such high velocity outflows through the protostellar envelope and the ambient molecular medium are shock fronts (Reipurth & Raga 1999). These shocks both heat and compress the gas, which favors chemical reactions in the gas-phase while they modify the dust grain properties and release a fraction of their material in the gas phase through e.g. sputtering and shattering, thereby leading to a different chemical composition than observed in the ambient, pre-shock gas. Commonly, the high relative abundance of CO and its low energy J transitions makes it a good tracer for outflows in the conditions of cold molecular clouds. Evenmore, the morphology, velocity, and sizes of a molecular outflow depend on the observed tracer, the luminosity, mass and age of the outflow, which indicates its evolution and its inner structure (Bally 2016).

Over the years, there have been intense numerical efforts to simulate the chemical and dynamical structure of protostellar outflows and their evolution in the ambient interstellar gas. Smith (1994); Smith et al. (1997) carried out 3D numerical simulations of dense molecular jets drilling through a molecular environment. They succeeded in reproducing the morphology of the "classical" CO bipolar outflows, which image the accumulated and accelerated cool gas. They showed that the simulations predict infrared shock structures remarkably similar to those found in highly collimated Class 0 outflows. They proved that in spite of the limitations in their description of the physical conditions (dust, magnetic field), these hydrodynamical models could provide a meaningful description of the dynamics of bipolar outflows from young stars, accurate enough images for comparison with observations, and the outflow mass and energy contribution to the interstellar medium.

Raga et al. (1990) showed that simulations with an arbitrarily imposed ejection velocity variability lead to the formation of chains of internal working surfaces traveling down the jet flow. Such features strikingly resemble Herbig-Haro (HH) flows, with a chain of aligned knots close to the outflow source, and a large "head", resulting from the "turning on" of the jet flow, at larger distances. Later on, the authors showed that a two-mode ejection velocity variability leads to the formation of chains of "short period knots", which catch up with each other to form "long period knots". This class of models has successfully accounted for the properties of HH flows and they nowadays dominate the literature on the theory of astrophysical jets (Canto 1985; Raga et al. 1990, 2003; Noriega-Crespo et al. 2014; Frank et al. 2014; Rabenanahary et al. 2022).

On the other hand, most of the hydrodynamical codes developed so far do not include a chemical network and thereby do not address the molecular gas composition, in contradiction with the observational evidence that outflows from Class 0 protostars are often chemically active (e.g. Bachiller et al. 2001; Arce et al. 2007; Lefloch et al. 2017; Ospina-Zamudio et al. 2018; De Simone et al. 2020).

It is only with the advent of the first generation of chemo-hydrodynamical codes that it is now possible to accurately model the physical and chemical outflowing gas evolution and to build spectroscopic diagnostics which can be tested against the observational constraints provided by the large (sub)millimeter arrays such as NOEMA and ALMA, and to investigate in detail the processes that determine the jet/outflow properties in order to quantify the energetic and chemical feedback of newly born stars on their environment and eventually on galaxies.

In this work, we use WALKIMYA-2D, a new 2D hydrodynamical code coupled to a reduced gas phase chemical network allowing to follow the evolution of the CO chemistry in molecular outflows (Castellanos-Ramírez et al. 2018). The advantage of this code is that it computes the time evolution of chemical species in a full gas dynamic simulation. The new functionalities of WALKIMYA-2D allow us to investigate more thoroughly the dynamics and the physical structure of protostellar outflows.

We have selected the high-velocity outflow associated with the intermediate-mass Class 0 protostellar system Cep E-mm, located in the Cepheus OB3 association at a distance of 819 ± 16 pc (Karnath et al. 2019), whose CO emission observed at $1''$ with the IRAM interferometer is displayed in Fig. 1. This outflow has a luminosity of $\approx 100\, L_\odot$ (Lefloch, Eisloeffel & Lazareff 1996) and a core mass of $35\, M_\odot$ (Crimier et al. 2010). The source has been the subject of several detailed studies at arcsec angular resolution, in particular in the CO rotational transitions in the (sub)millimeter domain (Lefloch, Eisloeffel & Lazareff 1996; Lefloch et al. 2015; Ospina-Zamudio et al. 2019), which have constrained the jet and outflow dynamical parameters (mass, mass-loss rate, momentum, density, temperature). The recent study by Schutzer et al. (2022) has brought a detailed view of the jet structure and its time variability, showing a complex interaction with the ambient protostellar material. It is also one of the few protostellar jets for which a full 3D picture of the gas kinematics is available. Overall, this outflow appears as an excellent testbed for chemo-hydrodynamical codes, with the prospect of getting more insight into the jet and outflow formation process.

The goal of this study is to obtain an accurate numerical modelling of the Cep E molecular outflow in agreement with the constraints provided by the large (sub)millimeter observatories. In particular, we aim to understand the dynamics of the jet/envelope interaction near the source. The synergy between the WALKIMYA-2D numerical simulations and the observations with the IRAM interferometer has allowed us to peer into the outflow formation mechanism with unprecedented detail and to retrieve the history of the mass loss events that have shaped the outflow.

This paper is organized as follows: in Section 2, we describe the numerical setup and the boundary conditions, which were chosen in agreement with the observational constraints on Cep E and present the best fitting model. The following sections present our main results: the outflow formation in Section 3, the gas acceleration mechanism in Section 4, the mass-loss history in Section 5 and the CO emission in Section 6. Finally, we summarize our conclusions in Section 7.

2. Simulations

2.1. WALKIMYA-2D

In order to study the temporal evolution of the molecular composition of a gas, one needs to solve the rate of change of the abundances of the different species contained in it. It is required to construct a chemical network gathering the creation and destruction reactions for the different species. We have used the 2D chemo-hydrodynamical WALKIMYA-2D that solves the hydrodynamic equations and a chemical network, on an axisymmetric numerical adaptive mesh. A complete description of the code is presented in Castellanos-Ramírez et al. (2018). Initially, both the jet and the surrounding quiescent protostellar gas have a CO abundance of $1.6{\times}10^{-4}$ relative to H_2. The chemical network is designed mainly to follow the evolution of the CO chemistry, as induced by the heating/cooling processes in the jet propagation and the shock interaction(s) with the ambient gas. For computational reasons (to keep computational times within reach), the network is reduced to 14 chemical species, including C, O, H_2O, OH, and CO (Castellanos-Ramírez et al. 2018). The reaction rates were obtained from the UMIST database (McElroy et al. 2013). WALKIMYA-2D and its chemical network were successfully benchmarked against laboratory experiments to study the NO formation by electrical discharges using both a zero-dimensional and a gas dynamic model approach Castellanos-Ramírez et al. (2018). Also, in the astrochemical context, the code was successfully benchmarked against the model of dark molecular cloud presented in McElroy et al. (2013), and has been used to explain the CO emission produced by the Orion Fingers in the Orion KL region (Rodríguez-Gonález et al. 2022, in preparation).

The energy loss rate is calculated adopting the same prescription as in Rivera-Ortiz et al. (2019) (see references therein): for temperatures larger than 5800 K the cooling function considers the atomic contribution while in the lower temperature range, it uses a parametric molecular cooling function based on CO and H_2.

The adaptative mesh uses 7 levels of refinement, yielding 4096 × 1024 cells, in a computational domain $(5 \times 1.25) \times 10^4$ au, allowing a resolution as high as 12.2 au per cell side. We used a reflective boundary condition for the symmetry axis and a free outflow boundary condition for all the other borders. The size of the mesh is large enough that the outer boundaries do not affect the simulation. The jet is injected on the left side of the simulation box with the physical conditions indicated in Table 1.

2.2. Initial conditions : the protostellar core

In order to describe the protostellar core, we have adopted the physical conditions derived by Crimier et al. (2010) from a simple 1D modelling of the dust spectral energy distribution between $24\mu m$ and $1300\mu m$, using the radiative transfer code 1D DUSTY (Ivezic & Elitzur 1997). The temperature is fitted by a broken radial power law $T \propto r^{\beta}$ with $\beta = -0.8$ in the range 50–300 K and $\beta = -0.4$ in the range 7 K–50 K. In Crimier's model, the density profile is assumed to start at a radius $r_{in} = 70$ au and to follow a single radial power law distribution $n(r) = n_0 \times (r_0/r)^{\alpha}$.

In order to avoid density singularities in the limit $r \to 0$ in the numerical modelling, we have adopted the slightly modified density profile

$$n(r) = \frac{n_0}{1 + (r/r_0)^{\alpha}}, \tag{1}$$

where $n_0 = 10^9$ cm^{-3}, $r_0 = 100$ au and $\alpha = 1.9$. Note that this profile is very similar to the structure of an isothermal Bonnor-Ebert sphere (Zier et al. 2021).

The simulation takes into account the role of gravity, in agreement with the source density stratification evidenced from Crimier's analysis. Our model includes the resulting gravitational force as a source term, which reads :

$$g = -\frac{2\, c_0^2\, r}{r_0^2\,(1 + (r/r_0)^{\alpha})} \tag{2}$$

where c_0 is the local sound speed. The inclusion of this gravity term ensures hydrostatical equilibrium close to the source.

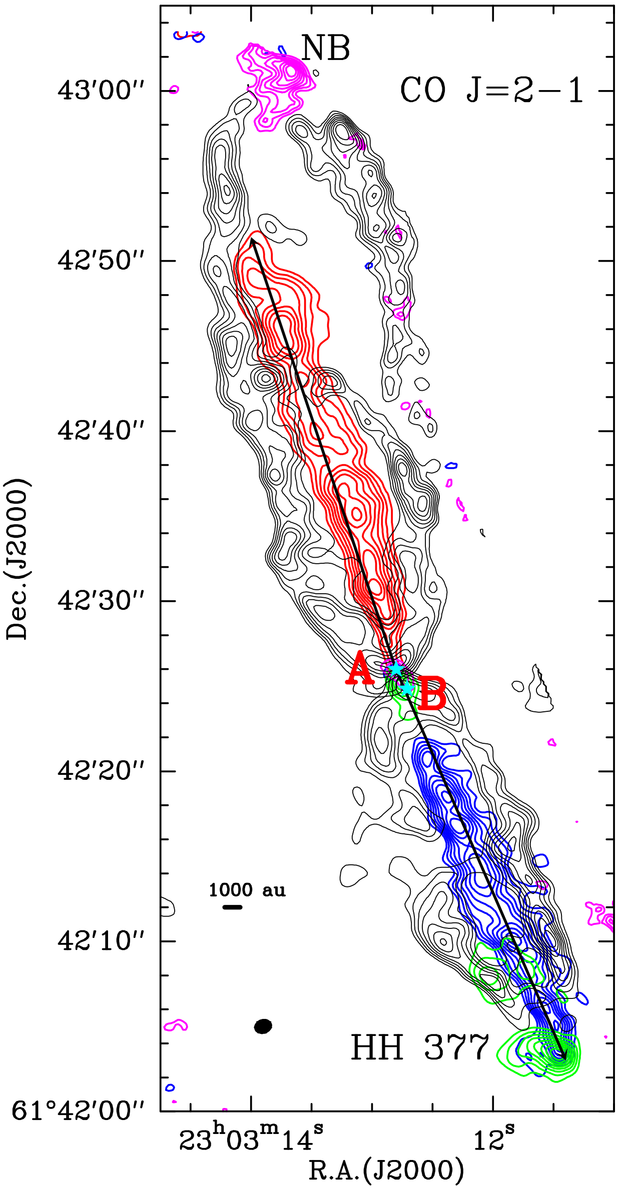

Fig. 1. CO 2–1 line emission in the Cep E-mm outflow as observed with the PdBI at 1″ resolution (Lefloch et al. 2015). Four main velocity components are detected: a) the outflow cavity walls (black) emitting at low velocities, in the range [−8;−3] km s^{-1} and [−19;−14] km s^{-1} in the northern and southern lobe, respectively; b) the jet, emitting at high velocities in the range [−135;−110] km s^{-1} in the southern lobe (blue) and in the range [+40;+80] km s^{-1} in the northern lobe (red); c) the southern terminal bow shock HH377, integrated in the range [−77,−64] km s^{-1} (green); d) the northern terminal bullet NB integrated in the velocity range [+84,+97] km s^{-1} (magenta). First contour and contour interval are 20% and 10% of the peak intensity in each component, respectively. The synthesized beam ($1\farcs07 \times 0\farcs87$, HPBW) is shown in the bottom left corner. The main axis of the northern and southern lobes of the jet are shown with black arrows. (Schutzer et al. 2022)

2.3. Initial conditions : the jet

The jet is bipolar and consists of a narrow (diameter < 400 au) central component surrounded by a collimated layer with a radial extent up to 1000 au, as shown by Schutzer et al. (2022). The jet appears young, with a dynamical age of 1400 yr, and compact, with a length of ∼ 0.1–0.14 pc (18000 − 29000 au) for the southern and northern lobes, respectively. The physical conditions (temperature, H_2 gas density) in the outflow were estimated by Lefloch et al. (2015) and Ospina-Zamudio et al. (2019) from a CO multi-rotational line study complemented with CO J=2–1 observations at 1″ angular resolution with the IRAM interferometer. In the southern lobe, the jet appears to consist of a warm (T=80–100 K) gas component of H_2 density $n(H_2)$= (0.5–1.0)×10^5 cm^{-3} component and a higher-excitation component of $n(H)$= (0.5–1.0)×10^6 cm^{-3} and temperature (T=400–750 K), which the authors associated with the high-velocity knots. Similar physical conditions are found in the northern lobe, with a kinetic temperature T=180–300 K and gas density $n(H_2)$= (0.6–2.0)×10^5 cm^{-3}. Therefore, the jet is rather massive, with a total mass of 0.03 $M_\odot$ (0.09 $M_\odot$) in the southern (northern) lobe, after taking into account the revised distance to the source (Karnath et al. 2019).

The jet asymptotic radial velocities were determined from the CO 2–1 line profiles as +65 km s^{-1} and −125 km s^{-1} in the northern and southern lobe, respectively (Lefloch et al. 2015). The jet proper motions in both lobes were measured by Noriega-Crespo et al. (2014) from combining multiple mid-infrared IRAC 4.5μm observations and H_2 2.12μm images at a difference of 16 years. We note that the revised distance of Cep E-mm (820 pc instead of 730 pc previously) does not significantly affect the tangential velocities, nor the inclination angle of the jet with respect to the plane of the sky derived by Lefloch et al. (2015), which is now 47° (40° previously estimated) and the estimated dynamical age of the jet (about 10^3 yr). Based on these observations, the molecular jet velocity is estimated ∼ 100 km s^{-1} (150 km s^{-1}) in the northern (southern) lobe, respectively. Kinematical analysis of the molecular gas knots in the jet shows evidence for time and velocity variability of the mass ejection process in Cep E (Schutzer et al. 2022).

In the simulation, the jet is launched at z=0, with a radius r_j, a gas density $n_j(H)$= 10^6 cm^{-3}, and a temperature T_j= 300 K. In order to account for knot formation inside the jet, we introduced variability in the gas injection, which we modeled following the equation

$$V_j = V_{j,0}\,[1 + \delta_v \cos(2\pi t/\tau)] \tag{3}$$

where $\tau = 130$ yr is the injection mass period and t is the evolutionary time. The jet injection velocity $V_{j,0}$ and the relative amplitude variability δ_v are free parameters of the simulation. We adopted δ_v= 0.05–0.08, which implies velocity variations of 10–15 km s^{-1}, consistent with the typical variations reported by Schutzer et al. (2022) in Cep E and in other outflows like e.g. IRAS04166+2706 (Santiago-García et al. 2009).

2.4. Comparison with observations

Parameter	M1	M2	M3	M4
r_j [au]	100	50	50	150
$v_{j,0}$ [km s^{-1}]	200	165	200	200
δ_v	0.08	0.08	0.05	0.08

Table 1. Initial parameters of the four models M1–M4 computed with WALKIMYA-2D: jet radius r_j, injection velocity $v_{j,0}$, relative velocity variability amplitude δ_v. M1 is the model which best fits the Cep E outflow.

We have run four models M1–M4, whose initial jet parameters are listed in Table 1. For the sake of simplicity, our WALKIMYA-2D simulations do not include the effect of jet precession. Comparison between numerical simulations and observations are made with the northern outflow lobe of Cep E, whose entrained gas dynamics is better revealed in CO interferometric observations (Schutzer et al. 2022): morphology, gas acceleration, time-variability and knot formation.

Parameter	M1	M2	M3	M4	Cep E North	 South
M_j [10^{-2}M$_\odot$]	2.7	0.75	1.5	5	3.6	2.6
M_o[M$_\odot$]	2.3	1.3	1.2	2.9	2.0	0.4
z_{bs}[10^3au]	28	23	29	31	28	21
r_{max}[10^3au]	4.8	1.5	3.6	5.3	5	4

Table 2. Outflow physical properties derived from CO emissivity maps at 1500 yr in the four numerical simulations (M1– M4) and comparison with the observational values of the Cep E outflow : jet mass M_j, outflow mass M_o, jet length z_{bs}, maximum outflow radius r_{max}. These values are taken from Lefloch et al. (2015) and Ospina-Zamudio et al. (2019) and have been corrected for the revised distance to the source.

The simulations give us access to the physical structure of the outflow and its chemical properties. Filtering the emission of the high- and low-velocity components allows direct comparison between the simulations and the observational signatures of the distinct outflow components and therefore it is possible to quantify the physical processes involved in the outflow formation. In order to compare our numerical simulations with the CO observations, the emissivity has been computed directly from the hydrodynamical simulations assuming LTE. We have constructed synthetic CO J= 2–1 maps of the outflow cavity and the jet, by integrating the emission in the velocity intervals [3;7 km s^{-1}] and [50;150 km s^{-1}], respectively. Those maps were subsequently convolved with a gaussian profile whose size (FWHM) corresponds to the synthetic beamsize of the interferometer (1″ or 820 au).

We first explored the parameter space and searched for the model which best reproduces the qualitative and quantitative properties of the Cep E northern outflow lobe. Overall, we found that all four models M1 − M4 show similar results. Therefore, in what follows we present the results of model M1, i.e. the simulation which best accounts for the molecular gas observations of Cep E, whose initial jet parameters are summarized in Table 1. The initial jet velocity is 200 km s^{-1}, with a velocity fluctuation amplitude of 0.08, and an ejection radius of 100 au.

We compare the numerical results to the main observational features of the northern outflow lobe, identified in the recent study by Schutzer et al. (2022) : morphology, gas acceleration, time-variability and knot formation.

3. Outflow formation

Figure 2 displays the molecular gas distribution at five timesteps of the outflow formation, from t=0 to t= 2000 yr by steps of 500 yr. (A video is available at Fig. 2).

The jet is launched at t=0 into gas of density 10^9 cm^{-3}. The density contrast between the jet (10^6 cm^{-3}) and the ambient gas (10^9 cm^{-3}) makes the shock propagate into the ambient gas at a velocity much lower than the injection velocity $v_{j,0}$, an effect that has been studied in detail already by Raga et al. (1990). Turning on the jet creates a high-velocity, collimated narrow component which propagates in the ejection direction. It is surrounded by a cocoon

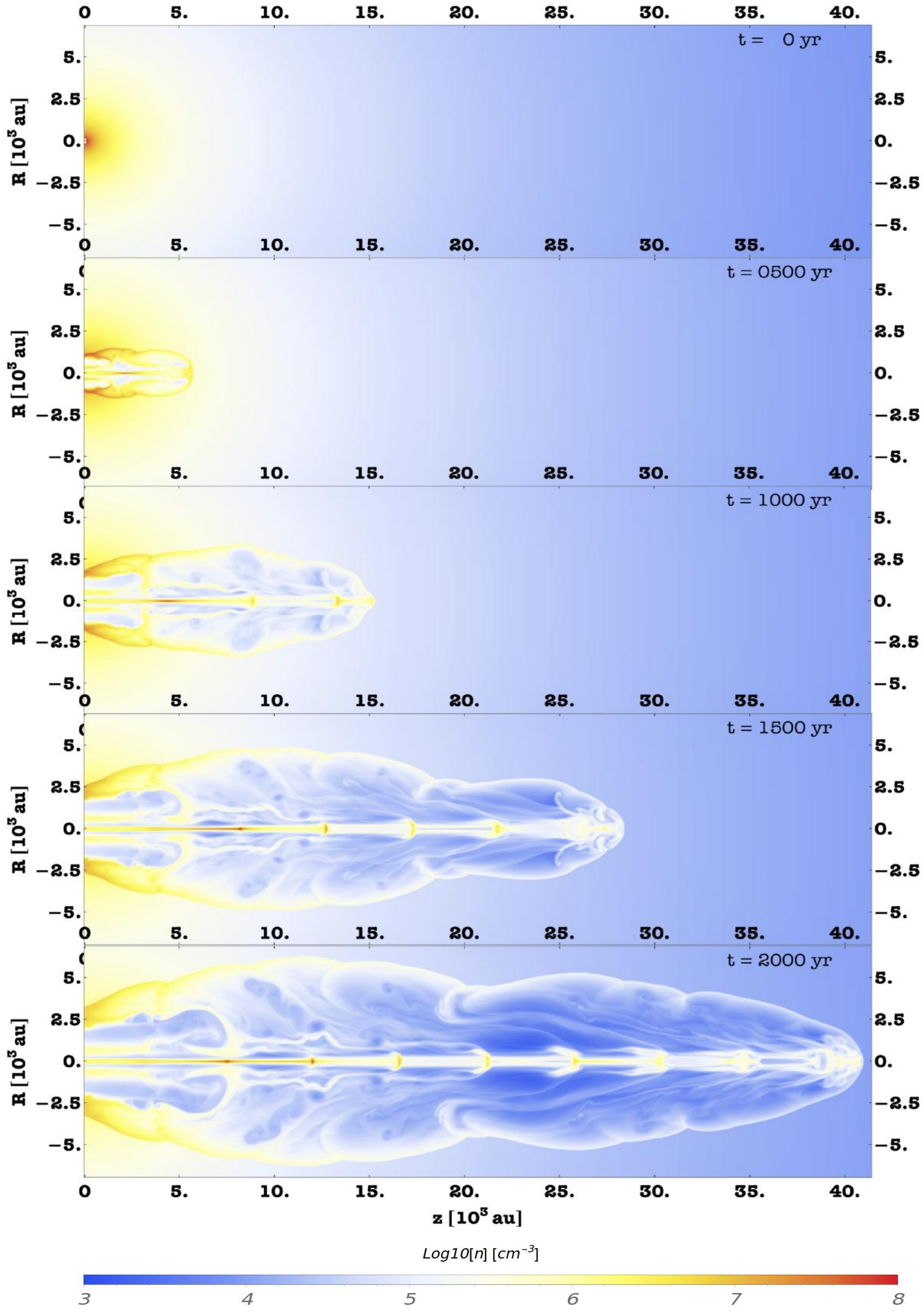

Fig. 2. Outflow formation and impact of the jet on the gas density distribution as a function of time. snapshots for 0, 500, 1000, 1500, and 2000 yr. The injection velocity variability forms internal working surfaces, or knots, and a structured cavity. The leading bowshock accumulates the mass of several knots.

of gas that expands laterally, creating a low-velocity (0–10 km s^{-1}) “cavity” component, with dense walls surrounding the jet. The first working surface interacts with the very dense gas close to the jet source, which makes it decelerate, causing the second ejected knot to catch up with the first bowshock. As shown in Fig. 2, this process repeats a few times until the bowshock leaves the inner envelope and propagates into the protostellar gas, reaching its terminal velocity. It is only after $\sim$ 200 yr and the launch of 3 knots that the jet manages to drill out the inner 1000 au of the protostellar envelope and to propagate into the surrounding gas (second panel from top). As a consequence the overpressure resulting from the accumulation of knots pushes the protostellar envelope laterally away from the jet, causing the formation of a wide-angle outflow cavity, and a density increase in the low-velocity cavity walls at the basis of the jet. This implies that a kinematic age computed from the bowshock position and velocity is actually a lower limit to the real age of the outflow.

As time proceeds, the model shows a leading jet head and a series of travelling "internal working surfaces" (IWS). These structures form as the result of the ejection time-variability and are observed as "knots", or overdensity regions with a small size of a few $\sim$ 100 au. At t= 1000 yr, 3 knots are easily detected along the jet, while at t= 2000 yr, 8 eight knots are easily identified. It is worth noticing they tend to expand radially as they propagate along the jet, tracing the wings of inner bowshocks, since the slower material interacts with the faster material ejected at later times. These wings appear to drive the formation of complex structures inside the outflow cavity as can be seen in the bottom panel of Fig. 2. Fast moving knots tend to accumulate at the head of the bow, increasing the density at the tip. After 1500 yr, the knots located at distance $>$ 15000 au display wings with a typical size of 1000 au.

One expects the gas density to decrease as a result of its radial expansion in the course of the jet propagation. However, looking in detail at the jet density field at e. g. t= 1000 yr (second panel in Fig. 2), it appears that the gas density does not decrease monotonically along the narrow jet. The density distribution of fast material along the propagation direction is analyzed in Section 5.2.

At t= 1500 yr, a second outflow cavity has now formed. The first outflow cavity has reached a size of $\approx$ 15000 au and expanded up to a radius of about 5000 au ($6''$ at the distance of Cep E-mm), and the head of the outflow has reached a distance of 2.8×10^4 au ($34''$). At later times, the second cavity expands to reach a similar radius of $\approx$ 5000 au.

Inspection of Figure 2 reveals that a complex network of relatively dense structures ($n \sim 10^5$–10^6 cm^{-3}) forms inside the outflow cavity very early. One can note the presence of "filaments" along the jet in the first 1000 yr. As can be seen in the panel at t= 1000 yr, a filament has formed along the jet. Located at R = 500 au, it is detected up to z = 2000 au and appears as a thin, yellow, wiggling structure parallel to the jet. We also note the presence of a "shell", or a bow, which formed in the dense protostellar envelope and moves slowly ($\sim$ 20 km s^{-1}) as it propagates over 8000au in 2000 yr, whereas the jet reached 40×10^3 au. This dense shell (or bow) connects the jet envelope of entrained gas to the cavity walls.

Our numerical results on the outflow morphology appear in good agreement with the NOEMA observations of the Cep E northern lobe (Fig. 1). As can be seen in Table 2, both the length and the radius of the outflow cavity are correctly reproduced; this good match between observations and simulations is obtained for a computational timescale of 1500 yr, similar to the estimated Cep E dynamical age (1400 yr). Even more, the jet momentum obtained from the simulation is 3.78 M$_\odot$ km s^{-1}, comparable to the momentum obtained by Lefloch et al. (2015) of 2.5 M$_\odot$ km s^{-1}, taking into account the inclination angle.

In order to better understand the role of the core initial conditions in shaping the outflow morphology, we also carried out simulations without the inclusion of the high-density core given by Crimier nor the related gravitational term. In these cases, it turned out that the low-velocity outflows formed in the ambient medium of the jet propagation were actually far too collimated with respect to what is observed, in particular close to the protostar and the jet launch region. Therefore, it appears that the wide opening of the low-velocity outflow cavity depends on the density of the dense inner region and the contribution of the latter to the gravitational field, two parameters that are related to the evolutionary stage of the system. The importance of including a density distribution and a gravitational term is in agreement with (Raga & Cabrit 1993) and (Cabrit et al. 1997) who proposed that a steep radial density decrease would produce a wider opening angle for jet-driven outflows.

4. Gas acceleration

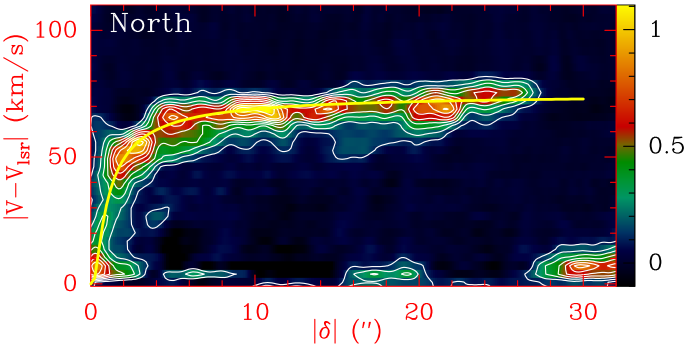

Fig. 3. Cep E northern outflow lobe. Position-Velocity diagram of the CO J= 2–1 line emission along the jet main axis. Positions are in arcsec offset relative to the location of the driving protostar Cep E-A. First contour and contour interval are 10% of the peak intensity. We have superimposed in yellow the best fitting solution $(V - V_{lsr})/V_0 = exp(-\delta_0/\delta)$ where δ_0= 690 au (Schutzer et al. 2022).

Cep E displays evidence of gas acceleration along the jet over a distance of 1000 au away from the protostar (Fig. 3). This effect was reported and observationally characterized by Schutzer et al. (2022). We show in the bottom panel of Fig. 4, the synthetic Position-Velocity diagram of the CO gas along the main axis of the jet. Two kinematical components are clearly identified : i) a low velocity component, between +0 and +10 km s^{-1} up to 8000 au ($10''$) from the source, associated with the outflow cavity walls; ii) a high velocity component, that displays a periodical behavior, reflecting the mass injection variability and the internal shocks, where the fast material catches up with the slower material. The jet is detected at a radial velocity close to V_j= 90 km s^{-1} at $z >$ 2000 au from the source.

Our simulations show that the effective velocity of the outflow is significantly lower than the injection jet velocity. This appears as a result of the jet interaction with the dense central envelope. In this case, the Position-Velocity

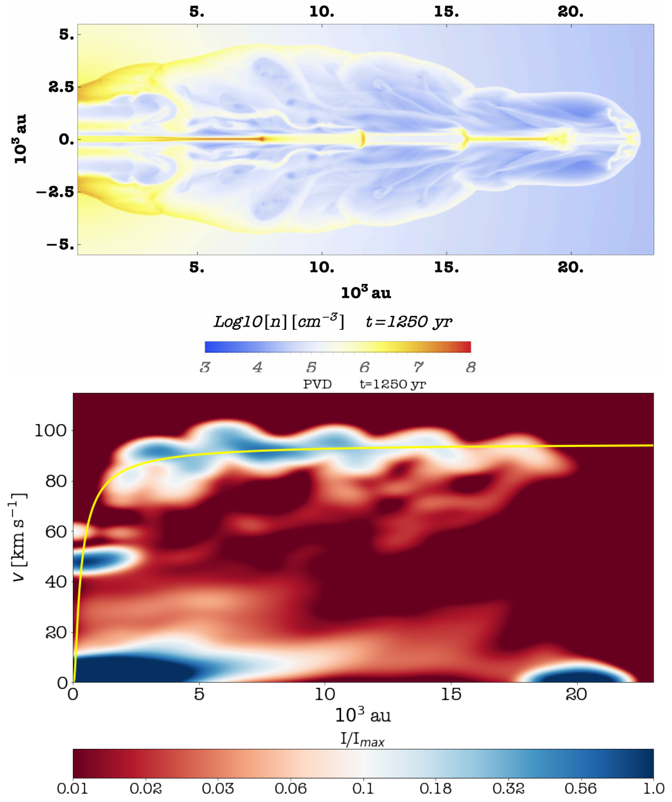

Fig. 4. Best fitting model (M1) to the Cep E northern outflow. (top) Density distribution at 1250 yr. The jet has propagated overa distance of 2.4×10^4 au and formed a low-velocity cavity of 3000 au radius. Five knots and their associated wings are detected along the jet.(bottom) Position-Velocity diagram of the CO emission along the jet main axis obtained using the outflow inclination angle with respect to the plane of the sky. The fit to the observational data (see Fig. 3) is superimposed in yellow.

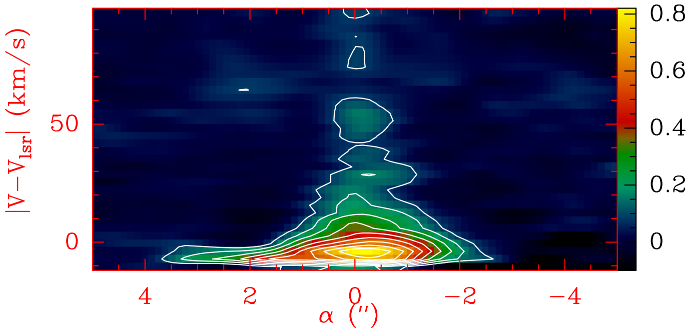

Fig. 5. Cep E northern outflow lobe. Position-Velocity diagram of the CO J= 2–1 line emission across the jet main axis at δ= 0″. Positions are in arcsec offset relative to the location of the driving protostar CepE-A. First contour and contour interval are 10% of the peak intensity (Schutzer et al. 2022).

diagram in Fig. 4 shows that the CO gas emission accelerates from ambient velocity (V= 0 km s^{-1}) to the terminal jet velocity on a short scale $< 5 \times 10^3$ au. Close to the source, gas structures accelerated up to $V \sim 50$ km s^{-1} are also detected along the jet axis up to 1000–2000 au (bottom panel of Fig. 4).

An observational signature of envelope gas can also be found in the Position-Velocity diagram of the CO J=2–1 emission across the jet main axis, as can be seen in Fig. 5. The CO emission contours show how the ambient material initially at rest at V_{lsr}= −11 km s^{-1} is gradually accelerated as one gets closer to the location of the protostar at α= 0.0″. In addition to the jet mainly detected up to $V \sim 60$ km s^{-1}, signatures of high-velocity knots (up +90 km s^{-1}) are also identified close to the protostar (Fig. 5).

It is worth remembering that the synthetic Position-Velocity diagrams display the total velocity variations whereas the Cep E observational plots (Fig. 3) display the radial component of the jet velocity. For the sake of comparison with the Cep E jet, we have checked whether the solution found by Schutzer et al. (2022) $(V - V_{lsr})/V_j = exp(-\delta_0/\delta)$ could provide a reasonable fit to the synthetic jet velocity profile along the main axis. The yellow curve drawn in the bottom panel of Fig. 4 traces the best fitting solution of Schutzer et al. obtained for a length scale δ_0= 690 au, applied to the radial jet velocity V_r=90 km s^{-1}. Taking into account the inclination of the jet with respect to the line of sight, the agreement between numerical and observational jet velocity profiles is very satisfying both qualitatively and quantitatively.

To conclude, our simulation satisfyingly accounts for the acceleration of material from the protostellar envelope by the Cep E jet, from ambient velocity up to reaching the radial terminal jet velocity $V_j \sim 90$ km s^{-1}. This process occurs over a scale of 5000 au.

5. Mass-loss history

5.1. The jet

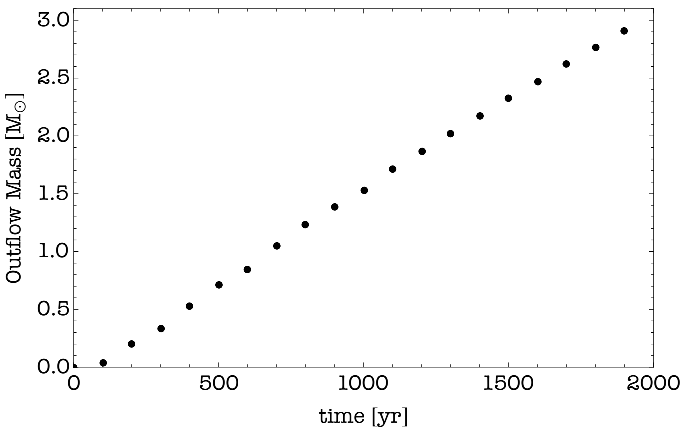

Fig. 6. Model M1. Outflow mass evolution as a function of time.

We first measured the mass of outflowing material as a function of time. The mass integration was performed over the whole velocity range. The result is displayed in Fig. 6 and shows that the outflow mass increases linearly with time at a rate of $1.6 \times 10^{-3}\, M_\odot$ yr^{-1}. At a time of 1500 yr in the simulation (similar to the dynamical age of Cep E) the mass of outflowing gas amounts to 2.3 $M_\odot$, a value in good agreement with the observational determination in the northern lobe (see Table 2).

In a second step, we have studied the variations of the jet mass as a function of time. We took into account all the gas at velocity $V > 50$ km s^{-1} to estimate the jet mass and follow its variations. The variations of the jet mass as a function of time are displayed in Fig. 7. After an initial delay of ∼ 200 yr, which corresponds to the time needed

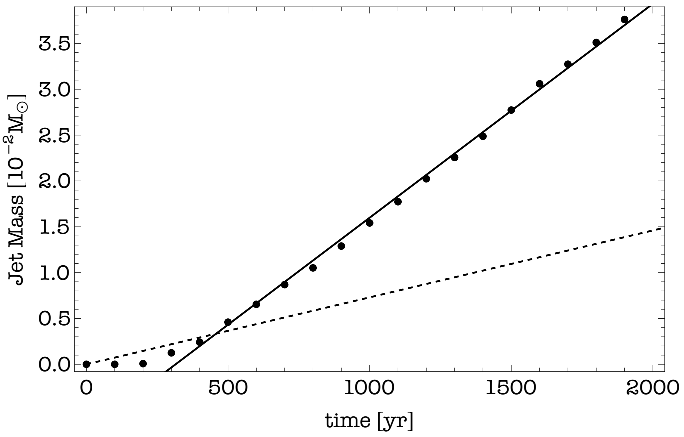

Fig. 7. Model M1. Jet mass evolution as a function of time. The points are obtained from the simulation every 100 yr. The black continous line is a linear fit of the points starting from 300 yr, with a slope of 2.3 $\times 10^{-5} M_\odot$ yr^{-1} and the dashed line corresponds to the material injection rate of $\dot{M} = 7.3 \times 10^{-6}$ used in the simulation.

for the knots to drill the envelope, the jet mass increases linearly with time, at a rate $\dot{M}$= 2.3 $\times$ 10^{-5} $M_\odot$ yr^{-1} in very good agreement with the observational determination by Schutzer et al. (2022) (2.7$\times 10^{-5}$ $M_\odot$ yr^{-1}). As discussed previously in Sect. 3.2, the protostellar material appears to feed the high-velocity jet through an entrainment process. An observational signature of this effect is found in the Position-Velocity diagram of the CO J=2–1 emission across the jet main axis, displayed in Fig. 5. The CO emission contours show how the ambient material initially at rest at V_{lsr}= −11 km s^{-1} is gradually accelerated as one gets closer to the location of the protostar at α= 0.0″. In addition to the jet mainly detected up to $V \sim 60$ km s^{-1}, signatures of higher-velocity knots (up +90 km s^{-1}) are also identified close to the protostar (Fig. 5).

Third, in order to quantify the magnitude of the entrainment effect to the jet mass, we have disentangled the contributions of the injected material from the entrained material. Theoretically, the jet mass injection rate per unit of time can be estimated as a function of the injected material density n_j, the jet velocity v_j and the jet injection radius r_j :

$$\left[\frac{\dot{M}}{\mathrm{M_\odot/yr}}\right] = 1.5\times10^{-6} \left[\frac{r_j}{50\mathrm{au}}\right]^2 \left[\frac{n_j}{10^6\,\mathrm{cm^{-3}}}\right] \left[\frac{v_j}{165\,\mathrm{km\,s^{-1}}}\right], \tag{4}$$

Numerically, the jet mass injection rate in the computational domain is in reasonable agreement with the simple, theoretical description from Eq. 4 ($\dot{M}$ = 7.3$\times 10^{-6}$ $M_\odot$ yr^{-1} with the conditions for model M1). In both numerical and theoretical cases, the jet mass injection rate is lower than the jet mass rate $\dot{M}$ of the simulation by a factor of $\approx$ 3. We consider the difference between both values as very significant as it highlights the importance of the entrainment process of circumstellar material in the formation of molecular jets.

5.2. The knots

We now examine the physical properties of the knots which form along the jet in the numerical simulation and their evolution with time. We then compare them with their observational counterparts in the Cep E jet.

5.2.1. Formation and evolution

We have studied the gas density distribution along the jet as a function of time in the simulation up to 2000 yr. We found that the evolution is characterized by very short timescales of the order of 25 yr. In order to illustrate and better explain the process at work, we present here in Fig. 8 a montage of the jet density profiles at intervals of 25 yr over a time of 125 yr, between 1450 yr and 1575 yr. The mean density distribution appears steady and constant at distances further than 10^4 au, while at shorter distances, there is a decreasing density profile. This is a fossil signature of the steep initial density profile of the envelope, since it is expected to be difficult to remove the dense envelope material close to the source, even when it has been processed by the countinuous injection of the jet. The peaks, which appear on top of the mean density distribution, result from the ejection velocity variability in the jet source (Sect. 2.3), which causes fast material to shock with lower velocity gas. Each of these peaks corresponds to a local overdensity structure in the jet, whose properties were derived from a gaussian profile fitting, leading to a typical size of 1000 au, a density of about 10^5 cm^{-3}, and a typical mass of 10^{-3} $M_\odot$. The physical properties of these peaks are actually very similar to those of the CO knots reported by Schutzer et al. (2022) in the Cep E jet, and, for that reason, they are probably their counterparts in the numerical simulation. Based on Fig. 8, it appears that at distances larger than 10^4 au the density and the knot distributions are almost steady, which reflects the fact that the knots are propagating into the low-density material of the jet at a speed of about 525 au in 25 yr. The high-density in the inner 10^4 au makes the situation drastically different. Rivera-Ortiz et al. (2019) have shown that gas flowing into an environment of similar density can create reverse shocks that propagates at a significant fraction of the original velocity relatively to the shock velocity. This is precisely the present situation with a jet of density 10^6 cm^{-3} propagating into gas of density 2–4 $\times$ 10^5 cm^{-3}. This effect is seen in Fig. 8, where the number of peaks varies in the inner 10^4au. As an example we follow the formation of the labeled as knot Kbc: at t = 1450 yr Kc looks as a short and wide peak, that gets taller and thiner up to 1500 yr, when it appears to have merged with Kc. Immediatly after this, a small peak Kd forms behind it at 1550 yr, which moves forward at a slightly lower velocity, creating a very wide peak and giving a similar density distribution at 1450 yr and 1575 yr, an interval of 125 yr, which is approximately the period of variability used in the simulation. This process gets repeated several times, accelerating the fossil envelope material, as described in Sec. 4, relating the process of gas acceleration with the formation of knots.

We have reported in Fig. 9 the mass of the knots as a function of their location along the jet at t= 1500 yr. It appears that the knots tend to increase their mass by a factor of 2 as they move away from the injection site. The simulation shows that the mass increase occurs on a very short length scale as the second knot at $z \sim 3000$ au has

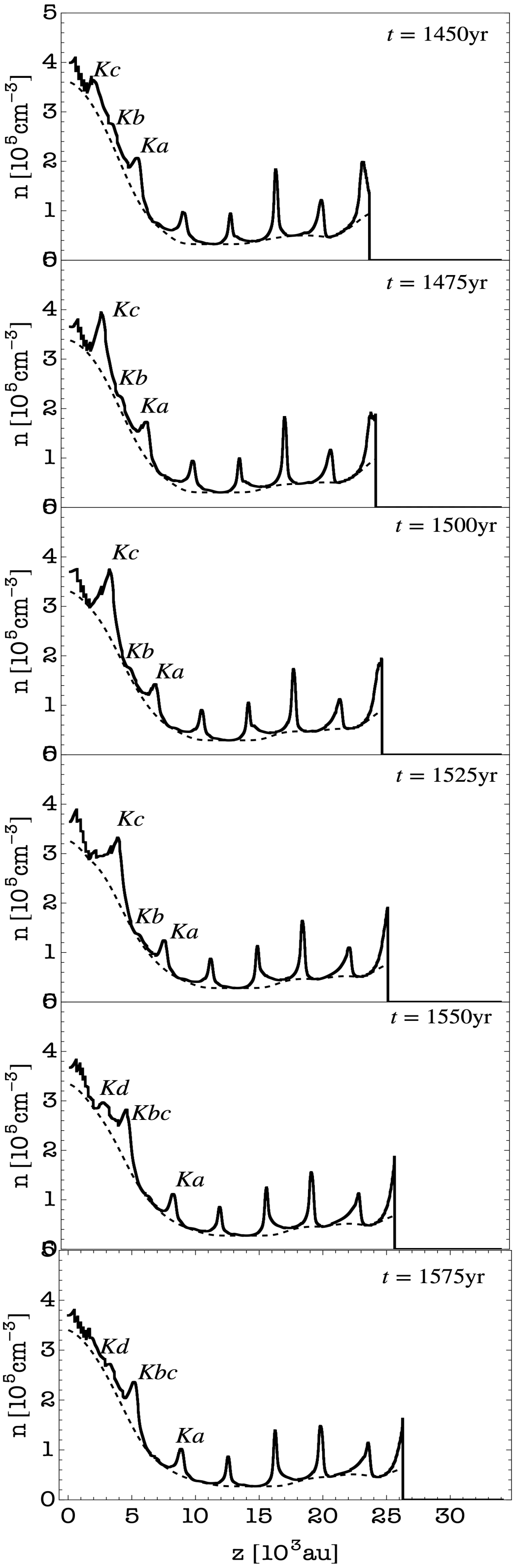

Fig. 8. Gas density distribution along the jet main axis for different snapshots from 1450 to 1575 yr (dashed lines). Knots can be identified as overdensities in the density distribution (thick lines) in the order of 10^5 cm^{-3}. To follow their behavior some knots have been labeled as Ka, Kb, Kc and Kd.

already a mass of 1.7×10^{-3} $M_\odot$. Beyond 8000 au, all knots display rather similar and steady masses, $\sim 1.7 \times 10^{-3}$ $M_\odot$. The terminal knot is an exception due to its higher mass ($> 3 \times 10^{-3}$ $M_\odot$). This high value is consistent with the fact that several knots have already reached the tip of the jet and are accumulating there, as can be seen in panels at t=1500 and 2000 yr in Fig. 2.

5.2.2. Observational comparison

In the later times of the simulation, it appears that the spatial separation between the knots located close to the source is actually shorter by about a factor 0.5 than the separation between those located in the older region of the jet. This is consistent with the bimodal distribution of dynamical ages reported by Schutzer et al. (2022).

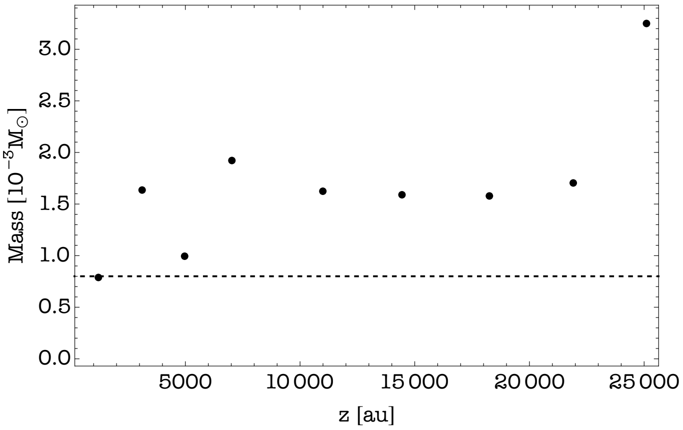

Fig. 9. Mass of the knots detected at 1500 yr in Model M1 as a function of their position z along the jet, projected by 47°, which corresponds to the angle between the Cep E jet main axis and the plane of the sky. The dashed line corresponds to the mass injected to the simulation in a single period.

The physical parameters of the knots (size, mass, density) such as derived from the numerical simulation, are therefore in good agreement with the observations. (Schutzer et al. 2022) noticed that the distribution of knot dynamical ages appeared to be bimodal, with the presence of two timescales : a short time interval of 50–80 yr close to the protostar (8000 au), corresponding to the first 4–5 knots, and a longer timescale (150—200 yr) at larger distances from the protostar.

Interestingly, the numerical simulation reports the same trend, as can be seen in Fig. 10, in which the ages of all the knots identified along the jet have been reported. The first four younger knots are separated by a timescale of about 100 yr, whereas the following knots are separated by a timescale of about 200 yr, or twice the value measured close to the jet launch region. Our simulations show that a high-velocity knot can overcome the spatial separation to the previous ejecta, which was slown down as a result of the interaction with the dense gas of the protostellar envelope. The typical timescale for the collision is 500 yr (Fig. 10).

We propose that the bimodal distribution is actually the signature of the interaction of the knots with the high-density gas inside the shell. As soon as the knots run out of the shell and propagate into lower density gas, they encounter free motion conditions.

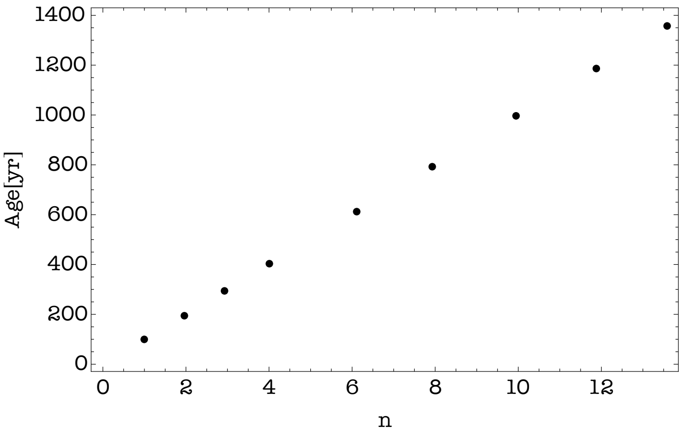

Fig. 10. The dynamical age of the knots identified in model M1 at $t=$ 1500 yr in terms of a multiple number n_i of the shorter dynamical age.

6. CO emission

Thanks to the detailed modelling of the CO chemistry by Walkimya-2D, we could produce synthetic CO integrated emissivity maps of the outflow jet and cavity, assuming LTE and optically thin emission. As an example, Fig. 11 displays the CO emissivity of the low-velocity outflow cavity integrated between 3 and 7 km s^{-1} (black contours) and of the high-velocity jet, integrated between 50 and 150 km s^{-1} (blue contours), as calculated by Model M1 at 1500 yr. The CO image reveals the previously identified highly-collimated structure of the jet with a typical width of $\sim$ 1000 au, which slightly increases with distance from the source. An important result is that the CO emission both from the high-velocity (50-150 km s^{-1}) jet (blue contours) and the low-velocity (3-7 km s^{-1}) cavity (black contours) drops $\sim$ 2000 au before the terminal bowshock, whose location is marked by a red spot in the plot. The lack of low-velocity CO emission over a few 1000 au near the apex of the outflow cavity is consistent with the terminal bowshock being very efficient at dissociating the ambient molecular gas.

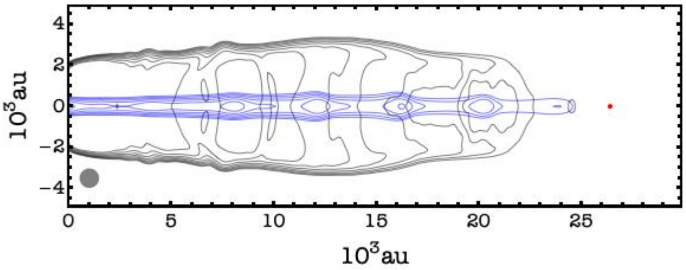

Fig. 11. Synthetic map of Model M1 at $t=$ 1500 yr. CO J= 2–1 integrated emissivity contour maps of the cavity (Black contours, 3 to 7 km s^{-1}) and the jet (Blue contours, 50 to 150 km s^{-1}) components. Scaling is logarithmic. The response of the IRAM interferometer was modeled by a gaussian of 830 au diameter (FWHM), corresponding to a beam size of 1″ (FWHP) at the distance of Cep E-mm, which is drawn with a gray disk (bottom left). The location of the frontal shock is marked with a red point.

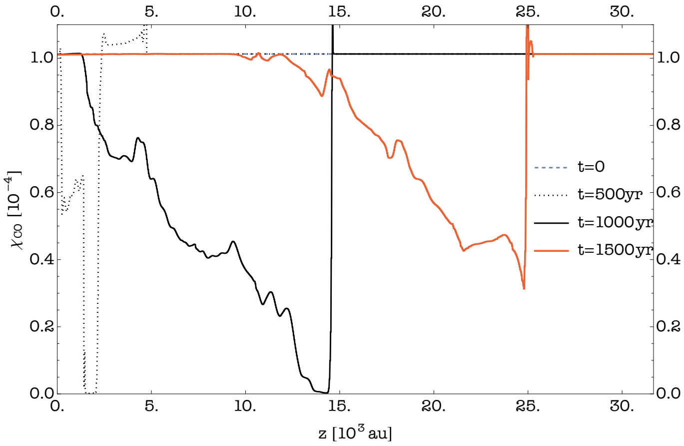

Fig. 12. Model M1. Variations of the CO/H_2 abundance relative to its initial value (10^{-4}) along the high-velocity jet at 4 different times of the simulation : 0, 500 (dotted), 1000 (solid black), 1500 yr (solid red).

In order to gain more insight into the time variations of the CO abundance (relative to H_2) in the outflow, we have computed the CO abundance distribution along the high-velocity jet at 4 different times of the simulation in model M1 : 0, 500 yr, 1000 yr, and 1500 yr. The distributions are shown in Fig. 12. For the sake of simplicity, we have reported the ratio X_{CO} of the CO abundance to its initial value, taken equal to 10^{-4}, a standard value in dense interstellar clouds (Lacy et al. 1994).

In the very early stages of the simulation (t < 500 yr), when the jet has run only a few 1000 au, X_{CO} is well below its canonical value of 1.0. For instance, we measure $X_{CO} \approx 0.5$ at 5000 au from the protostar at $t = 500$ yr. At later times in the simulation (1000 yr and 1500 yr in model M1, see Fig. 12), two regimes are identified in the X_{CO} distribution observed along the jet :

- close to the jet launch region X_{CO}= 1. The length of this region increases with time (2000 au at t=1000 yr, 10000 au at t=1500 yr) as the jet propagates at velocity V_j= 140 km s^{-1}.
- at larger distance, X_{CO} decreases from 1 to a few 10^{-1} with increasing distance to the protostar. The decrease is rather smooth and does not display abrupt variations along the jet. The minimum value is reached at the terminal bowshock before X_{CO} jumps abruptly again to 1, i.e. the canonical value in the ambient, quiescent gas in which the jet propagates.

To summarize, our simulation shows that CO is partly destroyed in the early times of the jet launch, close to the protostar ($X_{CO} < 10^{-1}$). The destruction process appears to stop ≈ 900 yr after the beginning of the simulation and the CO abundance of the ejected material remains steady, equal to its initial value. We propose that CO dissociation occurs as a consequence of the violent shocks caused by the first high-velocity knots (and the jet) when they are launched and impact the dense, protostellar envelope at the beginning of the simulation. It is only when the knots finally drill out the envelope and escape out of the inner protostellar region, entraining a fraction of the ambient protostellar envelope, that the local value of X_{CO} tends to return to its initial value. This process can also be influenced by the gas entrainment process.

Interestingly, we note that the slope of the X_{CO} distribution along the jet at $t=$ 1000 yr and $t=$ 1500 yr is similar, suggesting that it does not vary with time. Also, the velocity variations between subsequent knots ($\sim 10\,\mathrm{km\,s^{-1}}$) do not appear to significantly affect the $\mathrm{X_{CO}}$ distribution. Therefore it seems that the jet somewhat kept memory of the initial launch process in the $\mathrm{X_{CO}}$ axial distribution.

This numerical result has several implications on the observational side. First, lower values of $\mathrm{X_{CO}}$ may actually reflect the conditions of the jet formation process. Of course, precession and/or knot interaction with the ambient gas (or the cavity) may alter this conclusion. We speculate that in the latter case, the $\mathrm{X_{CO}}$ variations occur on a much smaller length scale, corresponding to the knots size, i.e. 1000 au typically. Our model suggests that the distribution of $\mathrm{X_{CO}}$ along the jet could probably provide constraints robust enough to discriminate between the processes at work.

On the observational side, Gusdorf et al. (2017) studied the emission of the OI $63\mu m$ line at $\sim 6''$ resolution with SOFIA and detected both the signature of the Cep E southern jet and the terminal bowshock HH377. A column density ratio N(OI)/N(CO)~ 2.7 was measured in the jet, indicating that that the jet is essentially atomic in the region of HH377. The authors proposed that the OI emission could arise from dissociative J-type shocks or with a radiative precursor, caused by the knots propagating at a different velocity in the jet (Lehmann et al. 2020). Interestingly, no signature of OI was detected in the jet towards shock position BI, located halfway between the protostar and HH377.

As discussed above, our numerical simulations propose an alternative explanation to the origin of OI in the Cep E jet. A detailed map of the OI emission along the southern jet with SOFIA, would help to confirm whether the CO dissociation is localized only towards HH377 or if it is also present along the jet, hence could trace the history of the early stages of the mass-ejection process.

7. Conclusions

Using the reactive hydrodynamical code Walkimya-2D, which includes a chemical network based on CO(Castellanos-Ramírez et al. 2018), we have carried out a set of simulations in order to reproduce the morphology and the physical properties of the molecular jet-driven outflow of the intermediate-mass protostellar source Cep E, as derived from previous observational studies (Lefloch et al. 2015; Gusdorf et al. 2017; Ospina-Zamudio et al. 2019; Schutzer et al. 2022). Outflow precession was not considered in this work. We have obtained a very satisfying agreement, both qualitatively and quantitatively, with the observations when modelling a time-variable jet with initial density $n(H)= 10^6\,\mathrm{cm^{-3}}$, radius $r_j= 100$ au, temperature $T_j= 300\,\mathrm{K}$, velocity $V_j= 200\,\mathrm{km\,s^{-1}}$ propagating into the density stratified protostellar envelope as modelled by Crimier et al. (2010). Our main results are as follows :

- The jet and cavity morphologies (width and length) are consistent with the observations and the expected kinematics using a variable jet ejection $\delta V/V_j= 0.08$. The best fitting solution is obtained at a numerical timescale $t_{dyn} \simeq 1500\,\mathrm{yr}$, consistent with the jet dynamical timescale estimated observationally (Schutzer et al. 2022, $\sim 1400\,\mathrm{yr}$).
- The jet terminal velocity ($\simeq 90\,\mathrm{km\,s^{-1}}$) is different from the injection velocity V_j ($200\,\mathrm{km\,s^{-1}}$), as a result of the first ejections being decelerated by the dense envelope and the entrainment of a layer of ambient protostellar material. It implies that the jet dynamical timescale is actually lower than the duration of the ejection phase.
- The jet acceleration reported observationally by Schutzer et al. (2022) is consistently reproduced in the simulations. It appears to be the result of ambient material entrainment by the knots on a length scale of ~ 700 au, in agreement with the observational data.
- We reproduce the properties of the knots along the jet assuming a periodic ejection. We found evidence for knot interactions in the dense inner protostellar region, where the densities of the local gas and the jet are comparable, which lead to the formation of secondary shocks in the close protostellar environment. At larger distances from the protostar, the lower ambient gas density allows the knots to propagate freely, without significant interaction. We propose that this process could account for the bimodal distribution of knots observed along the Cep E jet. Knots have a typical size of 1000-2000 au, with a mass of $\sim 1.5 \times 10^{-3}\,M_{\odot}$, and density of $10^5\,\mathrm{cm^{-3}}$. The mass carried away by the knots in the jet translates into a steady ejection mass rate of $2.3 \times 10^{-5}\,M_{\odot}\,\mathrm{yr^{-1}}$, a factor of 3 higher than the mass injection rate into the jet ($7.3 \times 10^{-6}\,M_{\odot}\,\mathrm{yr^{-1}}$). This difference is the signature of the entrainment and the subsequent acceleration of ambient material by the jet.
- The shock interaction of the jet knots with the protostellar envelope in the early times of the simulation lead to the dissociation of CO. The destruction process appears to stop after $\approx 900\,\mathrm{yr}$, time from which the CO abundance of the ejected material remains steady and equal to its initial (canonical) value. As a consequence, the older part of the jet is characterized by a lower CO gas abundance, which gradually decreases as one moves closer to the jet head.

Our simulations underline the importance of mass ejection time variability in the molecular outflow formation process and its interaction with the protostellar envelope. More work should be done, both observationally and numerically, in order to investigate the role of knots and their importance in the dynamical evolution of other young protostellar systems. Interferometric observations at subarcsec angular resolution of Cep E and other young protostellar jets should be undertaken as they would allow to make a significant step forward by bringing extremely useful constraints on the knot internal structure and the dynamical processes at work in the jet. In parallel, the high spatial resolution accessible in the Walkimya-2D numerical simulations ($\sim$ 10au) gives access to a novel view on the structure of protostellar jets and their dynamics, which will help interpret a new harvest of observations.

Acknowledgments

PR-RO, AS, BL acknowledge support from a) the European Union's Horizon 2020 research and innovation program under the Marie Skłodowska-Curie grant agreement No 811312 for the project "Astro-Chemical Origins" (ACO); b) the European Research Council (ERC) under the European Union's Horizon 2020 research and innovation program for the Project "The Dawn of Organic Chemistry" (DOC) grant agreement No 741002; c) the UNAMPAPIIT grant IN110722. Some of the computations presented in this paper were performed using the GRICAD infrastructure (https://gricad.univ-grenoble-alpes.fr), which is partly supported by the Equip@Meso project (reference ANR-10-EQPX-29-01) of the programme Investissements d'Avenir supervised by the Agence Nationale de la Recherche and the Miztli-UNAM supercomputer, project LANCADUNAM-DGTIC-123 2022-1.

References

Arce, H. G., Shepherd, D., Gueth, F., et al. Protostars and Planets V, B. Reipurth, D. Jewitt, and K. Keil (eds.), University of Arizona Press, Tucson, 2007, p.245-260
Bachiller, R., & Pérez-Gutiérrez, M. 1997, ApJ, 487, L93
Bachiller, R., Pérez-Gutiérrez, M., Kumar, M. S. N., et al. 2001, A&A, 372, 899
Bachiller, R., 1996, ARA&A, 34, 111
Bally J., Reipurth B., Davis C. J., 2007, prpl.conf, 215
Bally J., 2016, ARA&A, 54, 491
Cabrit, S., Raga, A., Gueth, F., in Herbig-Haro Flows and the Birth of Stars; IAU Symposium No. 182, Eds. Bo Reipurth and Claude Bertout. Kluwer Academic Publishers, 1997, p. 163-180
Canto, J. 1985, Cosmical Gas Dynamics, 267
Castellanos-Ramírez, A., Rodríguez-González, A., Rivera-Ortíz, P. R., et al., 2018, RMxAA, 54, 409.
Crimier, N., Ceccarelli, C., Alonso-Albi, T., et al., 2010, A&A, 516, 102
De Simone, M., Codella, C., Ceccarelli, C., et al., 2020, A&A, 640, 75
Eisloeffel, J., Smith, M. D., Davis, C. J., et al., 1996, AJ, 112, 2086.
Frank, A., Ray, T., Cabrit, S., et al., 2014, Protostars and Planets VI, eds H. Beuther, R.S. Klessen, C.P. Dullemond & T. Henning Tucson, AZ: University of Arizona Press, 451
Gusdorf A., Anderl S., Lefloch B., et al., 2017, A&A, 602, 8
Hughes, V. A. 1997, Herbig-Haro Flows and the Birth of Stars, 182, 141
Ivezić, Z., Elitzur, M., 1997, MNRAS, 287, 799
Jin, M., Lee, J.-E.E, Kim, K.-T., 2015, ApJS, 219, 2
Karnath N., Prchlik J. J., Gutermuth R. A., et al., 2019, ApJ, 871, 46.
Konigl, A. & Pudritz, R. E. 2000, Protostars and Planets IV, 759
Lacy, J. H., Knacke, R., Geballe, T. R., et al., 1994, ApJ, 428, L69
Lefloch B., Eisloeffel J., Lazareff B., 1996, A&A, 313, L17
Lefloch, B., Gusdorf, A., Codella, C., et al. 2015, A&A, 581, A4
Lefloch, B., Ceccarelli, C., Codella, C., et al., 2017, MNRAS, 469, L73
Lehmann, A., Godard, B., Pineau des Forêts, G., et al. 2020, Uncovering Early Galaxy Evolution in the ALMA and JWST Era, 352, 73. doi:10.1017/S1743921320000654
Masciadri, E., Raga, A. C., 2002, ApJ, 568, 733
McElroy, D., Walsh, C., Markwick, A.J., et al., 2013, A&A, 550, 36
Milam, S. N., Savage, C., Brewster, M. A., et al., 2005 ApJ, 634, 1126
Nony, T., Motte, F., Louvet, F., et al., 2020, 636, A&A, 38
Noriega-Crespo, A., Raga, A. C., Moro-Martín, A., et al., 2014, New Journal of Physics, 16, 10
Ospina-Zamudio, J., Lefloch, B., Ceccarelli, C., et al., 2019, A&A, 618, 145
Ospina-Zamudio, J., Lefloch, B., Favre, C., et al., 2019, MNRAS, 490, 2679
Plunkett A. L., Arce H. G., Mardones D., et al., 2015, Nature, 527, 70
Rabenanahary, M., Cabrit, S., Meliani, Z., et al., 2022, A&A, arXiv:2204.05850
Raga, A.C., Cantó, J., Binette, Calvet, N., 1990, ApJ, 364, 601
Raga A., Cabrit S., 1993, A&A, 278, 267
Raga, A.C., Cantó, J., 2003, A&A, 412, 745
Reipurth, B. & Raga, A. C. 1999, The Origin of Stars and Planetary Systems, 540, 267
Rodríguez-González, A., Rivera-Ortiz, P.R., A. Castellanos-Ramírez, Raga A.C. et al., in preparation
Rivera-Ortiz, P. R., Rodríguez-González, A., Hernández-Martínez, L., et al., 2019, ApJ, 874, 38
Santiago-García, J., Tafalla, M., Johnstone, D., et al. 2009, A&A, 495, 169
Schutzer, A. de A., Rivera-Ortiz, P. R., Lefloch, B., et al. 2022, A&A, 662, 104
Smith, M. D., 1994, A&A, 289, 256
Smith, M. D., Suttner, G., & Yorke, H. W. 1997, A&A, 323, 223
Zier, O., Burkert, A., Alig, C., 2021, ApJ, 915, 7
Zucker, C., Speagle, J. S., Schlafly, E. F. et al. 2019, ApJ, 879, 125

Chapter 8

Conclusions and perspectives

8.1 Conclusions

During my thesis, I got particularly interested in determining the physical and chemical conditions in the jet/outflow of Cep E-mm, this isolated intermediate-mass protostellar system with such a spectacular protostellar jet. Intermediate-mass protostars play an important role in understanding the difference and similarities between the formation of solar-type and high-mass stars. These two types have been extensively studied in the past, works which have revealed significant differences in physical and chemical structures, as discussed in Chapter 1. Although intermediate-mass stars play a critical role, the early stages of their formation have not been as extensively studied up to now.

The protostellar source I have studied, Cep E-mm, has a luminosity of $100\,L_{\odot}$, which places it between solar-type and massive objects, it has a bright bipolar outflow with a known 3D geometry. The object is isolated in the parent cloud and appears to be protected from external disturbances, such as the radiation field of neighboring stars. Hence, Cep E is a privileged object to study to understand the physical and chemical evolution of its jet-outflow. From previous works, it was known that Cep E jet shows a gradient of temperature within the jet and a complex knotty structure, as well an unusual chemical composition and chemical differentiation between outflow lobes (see Chapter 2).

The main questions I addressed during my thesis deal with the structure and the dynamics of the Cep E-mm jet, and its chemical composition, in particular the spatial distribution of molecular species and their origin inside the jet. Considering the molecular richness detected in chemically active outflows, I wanted to investigate whether the richness of the Cep E outflow is indeed produced inside the outflowing (low-/high-velocity) gas, despite the short timescale linked with the jet ($\sim 1000\,\mathrm{yr}$) or if the chemistry is simply carried away by the protostellar jet and the initial chemical composition of the protostellar gas is essentially preserved.

My overall motivation for these 3 years of work on Cep E could be resumed by the question "are chemically rich outflows an illusion?"

I made use of the spectroscopic maps of the molecular emission between 86–90 GHz and 216–220 GHz obtained with the NOEMA interferometer, as part of the W14AF project, at $2''$ angular resolution. I also analysed NOEMA data within the framework of the Large SOLIS program (Ceccarelli et al., 2017), between $1.5''$ and $0.4''$, in the 85–93 GHz, 95–103 GHz and 200–208 GHz bands. Additionally, I worked with CO interferometric data at 1″ obtained with PdBI (Lefloch et al., 2015). All these data were described in detail in Chapter 4.

These data were all analyzed in an in-depth and systematic manner. They are probably quite unique for an intermediate-mass protostar and have led to amazing, unexpected results, and to several articles in the main journals of the discipline, already published, in press, or in preparation. More importantly, the results obtained on the structure of the jet, and the formation of the high-velocity *molecular* jet raise many questions, which will require new observations, some with higher sensitivity, others with higher angular resolution, some in other complementary spectral windows. My NOEMA colleagues will certainly have exciting nights of unexpected results waiting for them.

The results regarding the dynamics of the Cep E jet were presented in de A. Schutzer et al. (2022) and to some extent in Rivera-Ortiz et al. (2022, *submitted*). The results concerning the chemical composition of the high-velocity jet are the subject of an article in preparation (Schutzer et al.,*in prep.*), presented in Chapter 6 of this thesis. Finally, the numerical simulations of the outflow/jet system carried out with the 2D-chemo hydrodynamical code WALKYMIA, have led to an article in collaboration with Dr. Rivera-Ortiz, currently in the reviewing process of the Astronomy & Astrophysics Journal (Rivera-Ortiz, P.R., Schutzer, A. et al.,*submitted*) in order to explore the evolution of the jet/outflow of Cep E, it is also discussed in Chapter 7.

As mentioned in the Introduction, a lot has been learned in the decades 1990-2000 thanks to near- and mid-infrared space observations (ISO, Spitzer, Herschel) of the intermediate-mass protostellar phase. Thanks to the progress made both in angular resolution and spectral sensitivity, a lot of surprises, exciting, unexpected results could now come from the new generation infrared space observatory JWST in the near- and mid-IR. In particular, observations of the pure H_2 rotational lines v=0–0 S(J), and ionic lines such as Ne^+, Ne^{2+} will certainly bring interesting constraints on the nature of the protostellar shocks associated with jets, the thermal structure of shocks. Based on the preliminary (partly published) infrared spectroscopic Herschel data (Lefloch et al., 2015), there is no doubt that observations of Cep E with the JWST will bring a novel view as well accurate constraints on the thermal structure and nature of shocks (C, J, CJ) in Cep E: jet, outflow cavities, terminal bowshocks.

Meanwhile, it is very unfortunate that the far-IR observatory SOFIA is now being decommissioned. This airborne telescope was our last possibility of getting access to the far-infrared lines OI (145μm, 63μm) and C^+ (158μm) with excellent spectral resolution. I remain still optimistic as a full OI map of the Cep E outflow has been obtained (and completed) with SOFIA a few months before the decommissioning of the telescope. We now count our collaborator in the team (A. Gusdorf, LERMA) to obtain and calibrate the full map, the relative calibration of various datasets being not an easy exercise, nor evaluating the pointing accuracy and its impact on the data calibration. As discussed in Chapter 7, the results may impact our understanding of the composition of the Cep E jet, and its CO abundance. Indeed, it would be extremely to detect extended OI emission, and to confirm that the most remote regions of the jet in the southern lobe (between S1 and HH 377) still bear memory of the early phases of the ejection process, when the knots (the mass ejecta) were finding their way out of the dense protostellar envelope.

8.1.1 Jet kinematics

My first work was dedicated to study the kinematics of the molecular jet of Cep E. Analysis of the molecular tracers, including CO, identified two components in the jet: a) a central, narrow, highly collimated, extremely high-velocity ($V > 55\,\mathrm{km\,s^{-1}}$) jet, detected mainly in CO and SO; b) an external, radially more extended, and *slightly* lower velocity ($45 < V < 55\,\mathrm{km\,s^{-1}}$) component surrounding the firs component. This component may contain gas from the inner protostellar envelope entrained and accelerated by the jet; another possibility, as suggested by our numerical simulations, is that the lower-velocity component could be also made of gas from the (not so empty) outflow "cavity", and accelerated in the jet interaction in particular the lower velocity wings of the bows associated with the knots (or internal shocks) propagating along the jet. Clearly, higher angular resolution in CO and SiO are needed to answer this question, and discriminate on the origin of the secondary component. The detection of species such as CS, HCO^+, HCN in this second component says that part of the material is probably protostellar gas entrained by the central jet but the interaction with the outflow cavity gas cannot be discarded at this stage. Only higher sensitivity and higher angular resolution observations of the same tracers can discriminate and bring a reliable answer to this question.

The jet shows evidence for mass-ejection variability, as traced by the many internal shocks detected (18) along the high-velocity jet. Part of the material from the envelope is being entrained by the high velocity jet and dragged away, an acceleration process which occurs up to several 1000 au from the protostar. We computed the mass-loss rate through a cumulative mass function for both lobes of the jet and obtained $\dot{M}= 8.9 \times 10^{-6}\,M_{\odot}\,\mathrm{yr}^{-1}$ in the southern and $\dot{M}= 2.7 \times 10^{-5}\,M_{\odot}\,\mathrm{yr}^{-1}$ in the northern lobe, therefore, twice higher in the northern. In this lobe, we also reported two knots (N3 and N6) which presented larger sizes and higher masses than others, with values several times (2–3) higher, that could indicate an interaction with ambient gas at these locations. We note that both knots coincide with the emission of peaks of organic species along the jet: CH_3OH, H_2CO. Analysis of the gas kinematics also suggest direct interaction between the high-velocity the jet and the ambient gas at these specific positions. Such an interaction would result into shocks strong enough to provide an efficient sputtering of the dust grains, hence an efficient enrichment of the gas phase in organics such as CH_3OH, H2CO provide a natural explanation to the bright emission. Again, such a scenario could be checked (and validated) by observations of the CH_3OH (and H_2CO) from higher-excitation transitions, like the E-/A-CH_3OH 5_k-4_k lines in the 1.3mm band with an angular resolution allowing to resolve the structure of the wings associated with the internal knots (and their bows) along the jet, typically $0.5''$. This project could be ideally led by NOEMA. Finally, we investigated the wiggling measured by the knots spatial distribution along the jet main axis, and we propose that jet precession originates from the orbit around a binary companion.

The results presented throughout Chapter 5 are key to understand the processes taking place at small and large scale in the jet of Cep E, as well as the interaction between the jet and the low velocity material such as ambient gas entraining and interaction with the low-velocity outflow.

8.1.2 Molecular emission: unveiling the spatial distribution

We have carried out a systematic search for molecular species in the high-velocity jet. We have identified and mapped the spatial distribution of 7 species, including one new detection with respect to previous studies: SiO, HCN, HCO^+, CS, H_2CO, SO and CH_3OH (for the first time). It is clear from the intensity maps obtained that a chemical differentiation is present between both lobes of the jet, especially apparent in CS, H_2CO and CH_3OH (undetected in the Southern lobe). The emission in the Northern lobe is knotty and dominated by the emission from the internal shocks N3 and N6. In the Southern lobe, only HCO^+ is detected along the jet, while the other species SiO, SO and HCN are detected from the protostar up to S1 and in the terminal bow shock HH 377.

Analysis of gas kinematics along the jet shows clear evidence for gas acceleration in the northern and southern lobes. Many of the species detected are actually entrained from the protostellar envelope: CS, HCO^+, HCN and SO. Some species (CH_3OH, H_2CO) are detected only in the protostellar envelope around the protostar, which is however not contradictory with the fact that the dust grains on which they are frozen are entrained too by the jet. Infrared images actually show evidence for the presence of small dust grains inside the Northern outflow cavity (Lefloch et al., 1996). As for the southern lobe, the jet shows weak entrainment in the close environment of the protostar and gas acceleration is seen close to the protostar but the molecular emission of several tracers (except CO and HCO^+) seems to suddenly stop after knot S1, $10''$ away from the protostar.

We found hints that the jet powered by protostar Cep E-B could be impacting the cavity walls of the outflow of Cep E-A in the Southern lobe. The question is whether the weak molecular entrainment observed in this lobe, could be the consequence of this jet interaction, possibly in relation with the structure of the protostellar envelope, which appears clearly different in the Northern and Southern lobes. In order to make progress on this question, numerical simulations and detailed modelling of the molecular emission (line profiles) of other species than CO are required. Complementary interferometric observations of additional transitions from the molecular species detected in the jet, allowing to derive with a higher and more reliable accuracy the conditions of temperature and density inside the low-velocity outflow, are definitely required to get a more detailed picture of the situation and possibly answer this question.

We analysed in more detail the shocks N6, N3, S1 and HH 377. We found evidence of interaction between the high-velocity jet and low-velocity outflow at positions N3 and N6, suggesting that the jet is actually hitting the cavity walls. The large linewidths of the molecular lines measured towards S1 ($20\,\mathrm{km\,s^{-1}}$) indicate that this knot is somewhat different from the N6 and N3. The much lower brightness of the shock, its size, and the velocity field tend to exclude an origin similar to that of N3 and N6 (shock impact against the cavity walls /and or the ambient gas). Then, the unusually large linewdith could trace the signature of knot collisions with the presence of a reverse shock. Higher angular resolution observations (at subarsec scale) are clearly required to disentangle the emission in S1 and confirm (or not) the presence of two components with different velocity fields. The terminal bow shock HH 377 is denser and hotter when compared to the internal knots and it is transversally extended.

Finally, given all this complexity phenomena taking place in the jet and the interaction with the cavity walls, it is possible to say that, in the case of Cep E, the chemically richness in the jet seems to be an illusion. This chemical richness appears to be the result of a strong interaction with the ambient gas of the protostellar envelope, part of which is entrained and accelerated by the high-velocity jet itself. This interaction leads to the formation of a molecular gas layer around the central jet. Chemo-Hydrodynamical simulations indicate that the jet structure appears to be perturbed by the interaction with the gas of the outflow cavity, resulting into the formation of wings, filamentary structures associated internal bowshocks propagating along the jet.

8.1.3 Outflow formation: numerical modelling

Using the chemi-hydrodynamical code WALKYMIA-2D, we have carried out a set of simulations in order to understand and reproduce as well as possible the morphology and the physical properties of the molecular jet-driven outflow of the Cep E, such as derived from our observational dataset (Lefloch et al., 2015; Ospina-Zamudio et al., 2019; de A. Schutzer et al., 2022).

The jet and cavity morphologies (width, length) and the expected kinematics were reproduced in excellent agreement with the observations by WALKYMIA-2D. The best fitting solution was obtained at a numerical dynamical age of $t_{dyn} \simeq 1250\,\mathrm{yr}$, in agreement with the jet dynamical timescale estimated observationally ($\sim 1400\,\mathrm{yr}$ de A. Schutzer et al., 2022). The jet acceleration detected in the molecular gas observations is also reproduced in the simulations, and it appears to be the result of ambient material entrainment by the knots on a length scale of $\sim$ 700 au, again in good agreement with the observations. The properties of the knots along the jet are well accounted for by a periodic ejection process with a timescale of 140 yr. We found evidence for knot interactions in the dense inner protostellar region, where the densities of the local gas and the jet are comparable, which lead to the formation of secondary shocks in the jet. At larger distances from the protostar, the lower ambient gas density allows the knots to propagate freely, without significant interaction. The mass carried away by the knots in the jet translates into a steady ejection mass rate of $2.3 \times 10^{-5}\,M_{\odot}\,\mathrm{yr}^{-1}$, a factor of 3 higher than the mass injection rate into the jet ($7.3 \times 10^{-6}\,M_{\odot}\,\mathrm{yr}^{-1}$). This difference is the signature of the entrainment of ambient material and its subsequent acceleration by the jet.

The numerical simulations underline the importance of the mass ejection time variability in the outflow formation process and its interaction with the protostellar envelope. They confirm the importance of the jet-envelope interaction in the formation of the "molecular jet", such as observed at large scale. The importance of an accurate modelling of the circumstellar envelope taking into account its self-gravity, appeared very clearly in the simulations as a necessary, critical condition to reproduce the opening of the low-velocity cavity walls and the jet acceleration. The next step is definitely to investigate at smaller scale, both on the observational and the numerical sides, the dynamics of knots and their interaction with the inner protostellar envelope, where the ambient gas density is high enough that it interacts with the jet and influence the propagation of the mass ejecta.

These are ambitious projects, which clearly require interferometric observations at high spatial resolution (ideally a few 10 au) together with multi-molecular chemo-hydrodynamical simulations in order to make a significant step forward in the understanding of the dynamical processes at work in the jet and the inner protostellar envelope.

8.2 Perspectives

- **Unveiling the inner shock structure**. Following our analysis particularly on the shocks N3, N6 and S1, where N3 and N6 in northern lobe of the jet have proved to be different from the normal internal shocks in the jet. We proposed that these knots are likely to be hitting the cavity walls. The knot S1, on the other hand, seems to be an internal shock in the jet, given it is less chemically rich. We also noticed that S1 presents significantly broader linewidths (x2) when compared to the other knots N3 and N6; such unusually broad line profiles could be the signature of a collision between two knots. The complexity of such an interaction, in particular the possibility of a reverse shock, again requires higher angular and spectral resolution observations at a fraction of arcsec, in order to disentangle the contributions of both components. Thanks to the recent upgrades in NOEMA, it is now possible to observe at angular resolutions $\sim 0.4''$ at 230 GHz, which might be enough to disentangle the different components (knots?).

- **Low-velocity outflow chemistry**. While performing a systematic search for molecules in the high-velocity jet in Cep E, I also searched for molecules in the low-velocity outflow (outflow cavities). Immediately it came out that these cavities are quite chemically rich in organics and COMs, as also reported by the single-dish observations of Ospina-Zamudio et al. (2018). All the molecules detected in the jet are detected as well in the low-velocity outflow plus COMs and related species such as HNCO, CH_3CHO and H_2CCO. I detected and mapped during my search for molecules in the jet. Surprisingly, the southern lobe of the cavity-walls are chemically richer than the northern, opposite to the high-velocity jet where the northern is richer. Since they come from the same protostellar envelope i.e., from *a priori* the same initial pre-shock, dust and gas conditions, it is expected this differentiation means that shocks could be impacting the chemical composition of the cavity-walls and it is definitely a worth subject to investigate in the future. This hypothesis must be taken with caution as the size, the morphology of the outflow cavities and the jet lobes are different in the Northern and Southern lobes. This appears clearly when looking at the CO morphology of the low-velocity cavity walls. Hence, it might well be that the gas density (and the temperature ?) is significantly different between both lobes, and/or the protostellar envelope connects in a different manner to the ambient cloud. This would certainly have consequences on the shock dynamical properties (shock velocity, expansion of the cavity walls), hence the sputtering efficiency, the maximum temperature reached in the shocks, which could have a marked impact on the final composition of the shocked gas. Much more detailed work, both observationally and in terms of modelling, is required to make progress. But the ultimate goal is definitely worthwhile, as it would provide a clear picture of the reasons why outflows can be chemically active and so diverse in this activity. Very exciting and demanding tasks are waiting ahead.

- **Sulfur chemistry in Cep E-A**. The abundance of gaseous S-bearing species drastically increases in the regions where the species frozen out onto the dust mantles are injected into the gas-phase either due to thermal evaporation in the heated central zone of protostars (e.g. hot corinos) or because of gas-grain sputtering and grain-grain shattering in shocked regions (see Bachiller et al., 2001; Podio et al., 2014; Taquet

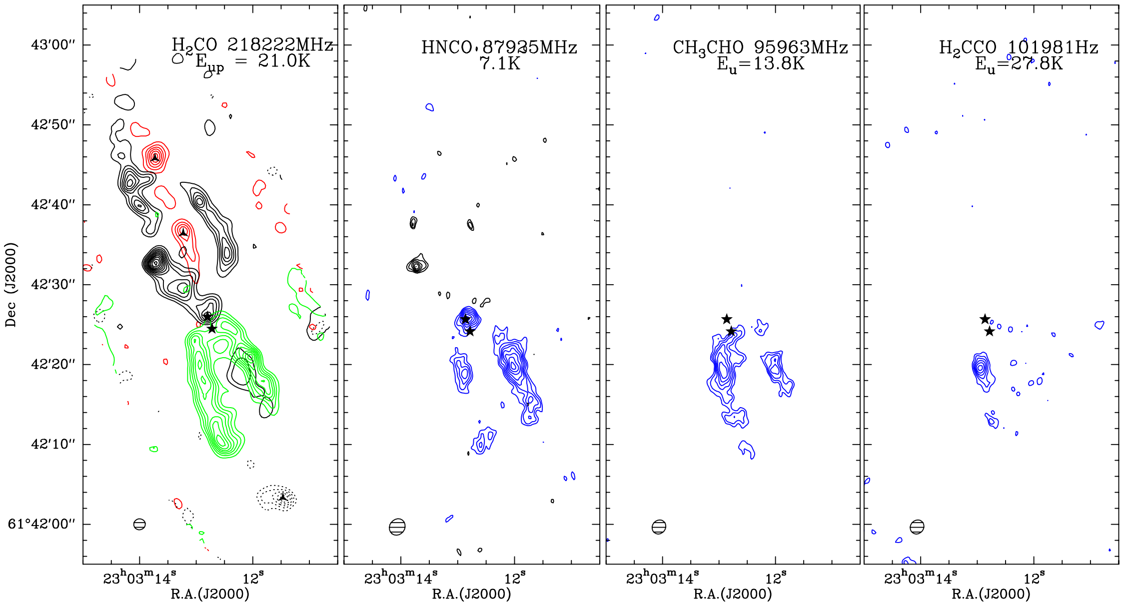

Figure 8.1: Montage of moment 0 maps of transitions of the different molecular species detected in the Cep E cavity-walls: H_2CO, HCNO, CH_3CHO and H_2CCO. The emission intervals were integrated in the same velocities ranges as in figure 6.3. Here, the first contour is at the 3σ level and contour interval is 3σ for each component.

et al., 2020, among others). In both cases, S-bearing species have proved to be extremely useful to reconstruct both the chemical history and dynamics of objects. In addition, these species have been recently imaged in relatively older protoplanetary disks (e.g. Le Gal et al., 2019; Garufi et al., 2020; Codella et al., 2021). Therefore, these studies have shown that S-bearing species are a powerful tool to follow the evolution of the chemistry until the latest stages of star formation.

During my thesis, in the work led by myself and my collaborator Ross O'Donoghue, we performed a sulfur molecular survey toward the Cep E hot corino by means of the interferometric data presented in Chapter 4. We detected 22 transitions among the molecular species: SO, SO_2, NS, CS, OCS, CCS, H_2S and H_2CS. Even with our highest angular resolution data: 1 mm band from SOLIS (0.5″) and W14AF (1.4″) we are barely able to resolve the emission. Therefore, in order to compute emission sizes and to account for the outflow contribution of some species, we proposed and tried an approach, different from the one often used (fitting two gaussian in the spectra). Our methodology was based on removing the outflow contribution as a baseline in the spectra and then reconstruct the image to compute the emitting region size. Hence, we extracted the spectra toward the hot corino and obtained the parameters (intensity, line width and peak velocity). We started the radiative transfer by means of the codes Radex and MadeX in to compute the column densities, density and kinetic temperatures in the hot corino. Finally, the next step is to perform a chemical modelling with UCLCHEM (Holdship et al., 2019) in order to constrain the evolution of the source given the S-bearing species have high reactivity.

Finally, the systematic work performed throughout this thesis allowed us to unveil the inner jet structure in Cep E-mm and its interaction with protostellar material and the low-velocity outflow. These works brought a new degree of complexity and understanding on protostellar jets by studying particularly the kinematics and the formation of the jet/outflow. More dedicated studies of shock regions and protostellar jets are required to better understand the origin of these phenomena and the impact they caused on the chemical and physical conditions of its surroundings. As part of this material that it is altered by the outflow and shocks may eventually fall onto the proto-planetary disk and can possible explain the presence of COMs and organics during the early stages of Solar System formation.

Bibliography

Alonso-Albi, T., Fuente, A., Crimier, N., Caselli, P., Ceccarelli, C., Johnstone, D., Planesas, P., Rizzo, J. R., Wyrowski, F., Tafalla, M., Lefloch, B., Maret, S., & Dominik, C. (2010). Chemical study of intermediate-mass (IM) Class 0 protostars. CO depletion and N_2H^+ deuteration. , *518*, A52.

Altwegg, K., Balsiger, H., Bar-Nun, A., Berthelier, J. J., Bieler, A., Bochsler, P., Briois, C., Calmonte, U., Combi, M. R., Cottin, H., De Keyser, J., Dhooghe, F., Fiethe, B., Fuselier, S. A., Gasc, S., Gombosi, T. I., Hansen, K. C., Haessig, M., Ja ckel, A., Kopp, E., Korth, A., Le Roy, L., Mall, U., Marty, B., Mousis, O., Owen, T., Reme, H., Rubin, M., Semon, T., Tzou, C. Y., Waite, J. H., & Wurz, P. (2016). Prebiotic chemicals–amino acid and phosphorus–in the coma of comet 67P/Churyumov-Gerasimenko. *Science Advances*, *2*(5), e1600285–e1600285.

André, P. (2002). The Initial Conditions for Protostellar Collapse: Observational Constraints. In J. Bouvier, & J.-P. Zahn (Eds.) *EAS Publications Series*, vol. 3 of *EAS Publications Series*, (pp. 1–38).

Andre, P., Ward-Thompson, D., & Barsony, M. (1993). Submillimeter Continuum Observations of rho Ophiuchi A: The Candidate Protostar VLA 1623 and Prestellar Clumps. , *406*, 122.

Arce, H. G., & Goodman, A. A. (2001a). The Episodic, Precessing Giant Molecular Outflow from IRAS 04239+2436 (HH 300). , *554*(1), 132–151.

Arce, H. G., & Goodman, A. A. (2001b). The Mass-Velocity and Position-Velocity Relations in Episodic Outflows. , *551*(2), L171–L174.

Arce, H. G., Santiago-García, J., Jørgensen, J. K., Tafalla, M., & Bachiller, R. (2008). Complex Molecules in the L1157 Molecular Outflow. , *681*(1), L21.

Arce, H. G., & Sargent, A. I. (2006). The Evolution of Outflow-Envelope Interactions in Low-Mass Protostars. , *646*(2), 1070–1085.

Arce, H. G., Shepherd, D., Gueth, F., Lee, C. F., Bachiller, R., Rosen, A., & Beuther, H. (2007). Molecular Outflows in Low- and High-Mass Star-forming Regions. In B. Reipurth, D. Jewitt, & K. Keil (Eds.) *Protostars and Planets V*, (p. 245).

Audard, M., Ábrahám, P., Dunham, M. M., Green, J. D., Grosso, N., Hamaguchi, K., Kastner, J. H., Kóspál, Á., Lodato, G., Romanova, M. M., Skinner, S. L., Vorobyov, E. I., & Zhu, Z. (2014). Episodic Accretion in Young Stars. In H. Beuther, R. S. Klessen, C. P. Dullemond, & T. Henning (Eds.) *Protostars and Planets VI*, (p. 387).

Ayala, S., Noriega-Crespo, A., Garnavich, P. M., Curiel, S., Raga, A. C., Böhm, K. H., & Raymond, J. (2000). Optical and Near-Infrared Study of the Cepheus E Outflow, A Very Low-Excitation Object. , *120*(2), 909–919.

Bachiller, R. (1996). Bipolar Molecular Outflows from Young Stars and Protostars. , *34*, 111–154.

Bachiller, R., Guilloteau, S., Gueth, F., Tafalla, M., Dutrey, A., Codella, C., & Castets, A. (1998). A molecular jet from SVS 13B near HH 7-11. , *339*, L49–L52.

Bachiller, R., & Pérez Gutiérrez, M. (1997). Shock Chemistry in the Young Bipolar Outflow L1157. , *487*(1), L93–L96.

Bachiller, R., Pérez Gutiérrez, M., Kumar, M. S. N., & Tafalla, M. (2001). Chemically active outflow L 1157. , *372*, 899–912.

Bacmann, A., Lefloch, B., Ceccarelli, C., Castets, A., Steinacker, J., & Loinard, L. (2002). The degree of CO depletion in pre-stellar cores. , *389*, L6–L10.

Bacmann, A., Lefloch, B., Ceccarelli, C., Steinacker, J., Castets, A., & Loinard, L. (2003). CO Depletion and Deuterium Fractionation in Prestellar Cores. , *585*(1), L55–L58.

Bacmann, A., Taquet, V., Faure, A., Kahane, C., & Ceccarelli, C. (2012). Detection of complex organic molecules in a prestellar core: a new challenge for astrochemical models. , *541*, L12.

Bally, J. (2016). Protostellar Outflows. , *54*, 491–528.

Bally, J., & Lada, C. J. (1983). The high-velocity molecular flows near young stellar objects. , *265*, 824–847.

Bally, J., Reipurth, B., & Davis, C. J. (2007). Observations of Jets and Outflows from Young Stars. In B. Reipurth, D. Jewitt, & K. Keil (Eds.) *Protostars and Planets V*, (p. 215).

Beichman, C. A., Becklin, E. E., & Wynn-Williams, C. G. (1979). New multiple systems in molecular clouds. , *232*, L47–L51.

Beichman, C. A., Myers, P. C., Emerson, J. P., Harris, S., Mathieu, R., Benson, P. J., & Jennings, R. E. (1986). Candidate Solar-Type Protostars in Nearby Molecular Cloud Cores. , *307*, 337.

Benedettini, M., Busquet, G., Lefloch, B., Codella, C., Cabrit, S., Ceccarelli, C., Giannini, T., Nisini, B., Vasta, M., Cernicharo, J., Lorenzani, A., & di Giorgio, A. M. (2012). The CHESS survey of the L1157-B1 shock: the dissociative jet shock as revealed by Herschel-PACS. , *539*, L3.

Bergin, E. A., Alves, J., Huard, T., & Lada, C. J. (2002). N_2H^+ and $C^{18}O$ Depletion in a Cold Dark Cloud. , *570*(2), L101–L104.

Bergin, E. A., Ciardi, D. R., Lada, C. J., Alves, J., & Lada, E. A. (2001). Molecular Excitation and Differential Gas-Phase Depletions in the IC 5146 Dark Cloud. , *557*(1), 209–225.

Bergin, E. A., & Tafalla, M. (2007). Cold Dark Clouds: The Initial Conditions for Star Formation. , *45*(1), 339–396.

Bergner, J. B., Shirley, Y. L., Jørgensen, J. K., McGuire, B., Aalto, S., Anderson, C. M., Chin, G., Gerin, M., Hartogh, P., Kim, D., Leisawitz, D., Najita, J., Schwarz, K. R., Tielens, A. G. G. M., Walker, C. K., Wilner, D. J., & Wollack, E. J. (2022). Astrochemistry with the Orbiting Astronomical Satellite for Investigating Stellar Systems (OASIS). *Frontiers in Astronomy and Space Sciences*, *8*, 246.

Beuther, H., & Shepherd, D. (2005). Precursors of UchII Regions and the Evolution of Massive Outflows. In M. S. N. Kumar, M. Tafalla, & P. Caselli (Eds.) *Astrophysics and Space Science Library*, vol. 324 of *Astrophysics and Space Science Library*, (p. 105).

Bianchi, E., Codella, C., Ceccarelli, C., Fontani, F., Testi, L., Bachiller, R., Lefloch, B., Podio, L., & Taquet, V. (2017). Decrease of the organic deuteration during the evolution of Sun-like protostars: the case of SVS13-A. , *467*(3), 3011–3023.

Blaauw, A., Hiltner, W. A., & Johnson, H. L. (1959). Photoelectric Photometry of the Association III Cephei. , *130*, 69.

Blitz, L., & Lada, C. J. (1979). H_2O masers near OB associations. , *227*, 152–158.

Bonnell, I. A., Bate, M. R., Clarke, C. J., & Pringle, J. E. (2001). Competitive accretion in embedded stellar clusters. , *323*(4), 785–794.

Bonnell, I. A., Bate, M. R., & Zinnecker, H. (1998). On the formation of massive stars. , *298*(1), 93–102.

Bontemps, S., Andre, P., Terebey, S., & Cabrit, S. (1996). Evolution of outflow activity around low-mass embedded young stellar objects. , *311*, 858–872.

Boogert, A. C. A., Gerakines, P. A., & Whittet, D. C. B. (2015). Observations of the icy universe. , *53*, 541–581.

Cabrit, S., Raga, A., & Gueth, F. (1997). Models of Bipolar Molecular Outflows. In B. Reipurth, & C. Bertout (Eds.) *Herbig-Haro Flows and the Birth of Stars*, vol. 182, (pp. 163–180).

Canto, J., & Raga, A. C. (1991). Mixing Layers in Stellar Outflows. , *372*, 646.

Cantó, J., Raga, A. C., & Riera, A. (2003). A Model for the Cross Section of a Turbulent, Radiative Jet or Wake. , *39*, 207–212.

Caselli, P., Walmsley, C. M., Tafalla, M., Dore, L., & Myers, P. C. (1999). CO Depletion in the Starless Cloud Core L1544. , *523*(2), L165–L169.

Castellanos-Ramírez, A., Rodríguez-González, A., Rivera-Ortíz, P. R., Raga, A. C., Navarro-González, R., & Esquivel, A. (2018). KIMYA, a Code for Solving Chemical Reaction Networks in Astrophysics. , *54*, 409–422.

Cazaux, S., Tielens, A. G. G. M., Ceccarelli, C., Castets, A., Wakelam, V., Caux, E., Parise, B., & Teyssier, D. (2003). The Hot Core around the Low-mass Protostar IRAS 16293-2422: Scoundrels Rule! , *593*(1), L51–L55.

Ceccarelli, C., Bacmann, A., Boogert, A., Caux, E., Dominik, C., Lefloch, B., Lis, D., Schilke, P., van der Tak, F., Caselli, P., Cernicharo, J., Codella, C., Comito, C., Fuente, A., Baudry, A., Bell, T., Benedettini, M., & Bergin, e. a. (2010). Herschel spectral surveys of star-forming regions. Overview of the 555-636 GHz range. , *521*, L22.

Ceccarelli, C., Caselli, P., Bockelée-Morvan, D., Mousis, O., Pizzarello, S., Robert, F., & Semenov, D. (2014). Deuterium Fractionation: The Ariadne's Thread from the Precollapse Phase to Meteorites and Comets Today. In H. Beuther, R. S. Klessen, C. P. Dullemond, & T. Henning (Eds.) *Protostars and Planets VI*, (p. 859).

Ceccarelli, C., Caselli, P., Fontani, F., Neri, R., López-Sepulcre, A., Codella, C., Feng, S., Jiménez-Serra, I., Lefloch, B., Pineda, J. E., Vastel, C., Alves, F., Bachiller, R., Balucani, N., Bianchi, E., & Bizzocchi, e. a. (2017). Seeds Of Life In Space (SOLIS): The Organic Composition Diversity at 300-1000 au Scale in Solar-type Star-forming Regions. , *850*(2), 176.

Ceccarelli, C., Caselli, P., Herbst, E., Tielens, A. G. G. M., & Caux, E. (2007). Extreme Deuteration and Hot Corinos: The Earliest Chemical Signatures of Low-Mass Star Formation. In B. Reipurth, D. Jewitt, & K. Keil (Eds.) *Protostars and Planets V*, (p. 47).

Ceccarelli, C., Castets, A., Caux, E., Hollenbach, D., Loinard, L., Molinari, S., & Tielens, A. G. G. M. (2000). The structure of the collapsing envelope around the low-mass protostar IRAS 16293-2422. , *355*, 1129–1137.

Cernicharo, J. (2012). Laboratory astrophysics and astrochemistry in the Herschel/ALMA era. In C. Stehlé, C. Joblin, & L. d'Hendecourt (Eds.) *EAS Publications Series*, vol. 58 of *EAS Publications Series*, (pp. 251–261).

Cernicharo, J., Agúndez, M., Cabezas, C., Tercero, B., Marcelino, N., Pardo, J. R., & de Vicente, P. (2021). Pure hydrocarbon cycles in TMC-1: Discovery of ethynyl cyclopropenylidene, cyclopentadiene, and indene. , *649*, L15.

Cernicharo, J., Heras, A. M., Tielens, A. G. G. M., Pardo, J. R., Herpin, F., Guélin, M., & Waters, L. B. F. M. (2001). Infrared Space Observatory's Discovery of C_4H_2, C_6H_2, and Benzene in CRL 618. , *546*(2), L123–L126.

Cernicharo, J., & Reipurth, B. (1996). Herbig-Haro Jets, CO Flows, and CO Bullets: The Case of HH 111. , *460*, L57.

Cerqueira, A. H., Lefloch, B., Esquivel, A., Rivera-Ortiz, P. R., Codella, C., Ceccarelli, C., & Podio, L. (2021). H_2 mass-velocity relationship from 3D numerical simulations of jet-driven molecular outflows. , *645*, A135.

Chini, R., Ward-Thompson, D., Kirk, J. M., Nielbock, M., Reipurth, B., & Sievers, A. (2001). Mm/Submm images of Herbig-Haro energy sources and candidate protostars. , *369*, 155–169.

Clark, B. G. (1980). An efficient implementation of the algorithm 'CLEAN'. , *89*(3), 377.

Codella, C., Benedettini, M., Beltrán, M. T., Gueth, F., Viti, S., Bachiller, R., Tafalla, M., Cabrit, S., Fuente, A., & Lefloch, B. (2009). Methyl cyanide as tracer of bow shocks in L1157-B1. , *507*(2), L25–L28.

Codella, C., Bianchi, E., Podio, L., Mercimek, S., Ceccarelli, C., López-Sepulcre, A., Bachiller, R., Caselli, P., Sakai, N., Neri, R., Fontani, F., Favre, C., Balucani, N., Lefloch, B., Viti, S., & Yamamoto, S. (2021). SOLIS. XII. SVS13-A Class I chemical complexity as revealed by S-bearing species. , *654*, A52.

Codella, C., Cabrit, S., Gueth, F., Cesaroni, R., Bacciotti, F., Lefloch, B., & McCaughrean, M. J. (2007). A highly-collimated SiO jet in the HH212 protostellar outflow. , *462*(3), L53–L56.

Codella, C., Ceccarelli, C., Bianchi, E., Balucani, N., Podio, L., Caselli, P., Feng, S., Lefloch, B., López-Sepulcre, A., Neri, R., Spezzano, S., & De Simone, M. (2020). Seeds of Life in Space (SOLIS). V. Methanol and acetaldehyde in the protostellar jet-driven shocks L1157-B0 and B1. , *635*, A17.

Codella, C., Ceccarelli, C., Caselli, P., Balucani, N., Barone, V., Fontani, F., Lefloch, B., Podio, L., Viti, S., Feng, S., Bachiller, R., Bianchi, E., Dulieu, F., Jiménez-Serra, I., Holdship, J., Neri, R., & Pineda, e. a. (2017). Seeds of Life in Space (SOLIS). II. Formamide in protostellar shocks: Evidence for gas-phase formation. , *605*, L3.

Codella, C., Maury, A. J., Gueth, F., Maret, S., Belloche, A., Cabrit, S., & André, P. (2014). First results from the CALYPSO IRAM-PdBI survey. III. Monopolar jets driven by a proto-binary system in NGC 1333-IRAS2A. , *563*, L3.

Cohen, R. J., Rowland, P. R., & Blair, M. M. (1984). The source of the bipolar outflow in Cepheus A. , *210*, 425–438.

Cotton, W. D., & Schwab, F. R. (1983). Global Fringe Fitting in VLBI. In *In: Joint Topical Meeting on Information Processing in Astronomy and Optics (OSA): FA5/1-FA5/4*, (p. 5).

Crawford, D. L., & Barnes, J. V. (1970). Four-color and Hbeta photometry for open clusters. VI. The association III Cephei. , *75*, 952–956.

Crimier, N., Ceccarelli, C., Alonso-Albi, T., Fuente, A., Caselli, P., Johnstone, D., Kahane, C., Lefloch, B., Maret, S., Plume, R., Rizzo, J. R., Tafalla, M., van Dishoeck, E., & Wyrowski, F. (2010). Physical structure of the envelopes of intermediate-mass protostars. , *516*, A102.

Crockett, N. R., Bergin, E. A., Neill, J. L., Favre, C., Schilke, P., Lis, D. C., Bell, T. A., Blake, G., Cernicharo, J., Emprechtinger, M., Esplugues, G. B., Gupta, H., Kleshcheva, M., Lord, S., Marcelino, N., McGuire, B. A., Pearson, J., Phillips, T. G., Plume, R., van der Tak, F., Tercero, B., & Yu, S. (2014). Herschel Observations of Extraordinary Sources: Analysis of the HIFI 1.2 THz Wide Spectral Survey toward Orion KL. I. Methods. , *787*(2), 112.

Cudworth, K. M., & Herbig, G. (1979). Two large-proper-motion Herbig-Haro objects. , *84*, 548–551.

Dayou, F., & Balança, C. (2006). Rotational excitation of SiO by collisions with helium. , *459*(1), 297–305.

de A. Schutzer, A., Rivera-Ortiz, P. R., Lefloch, B., Gusdorf, A., Favre, C., Segura-Cox, D., López-Sepulcre, A., Neri, R., Ospina-Zamudio, J., De Simone, M., Codella, C., Viti, S., Podio, L., Pineda, J., O'Donoghue, R., Ceccarelli, C., & et al., C. (2022). SOLIS. XVI. Mass ejection and time variability in protostellar outflows: Cep E. , *662*, A104.

de Jong, T., Chu, S., & Dalgarno, A. (1975). Carbon monoxide in collapsing interstellar clouds. , *199*, 69–78.

De Simone, M., Ceccarelli, C., Codella, C., Svoboda, B. E., Chandler, C., Bouvier, M., Yamamoto, S., Sakai, N., Caselli, P., Favre, C., Loinard, L., Lefloch, B., Liu, H. B., López-Sepulcre, A., Pineda, J. E., Taquet, V., & Testi, L. (2020). Hot Corinos Chemical Diversity: Myth or Reality? , *896*(1), L3.

di Francesco, J. (1997). *High-Resolution Studies of Circumstellar Material around Intermediate-Mass Young Stellar Objects at Far-Infrared and Millimeter Wavelengths*. Ph.D. thesis, University of Texas, Austin.

Draine, B. T. (2011). *Physics of the Interstellar and Intergalactic Medium*.

Dutrey, A., Guilloteau, S., & Guelin, M. (1997). Chemistry of protosolar-like nebulae: The molecular content of the DM Tau and GG Tau disks. , *317*, L55–L58.

Eisloffel, J., Smith, M. D., Davis, C. J., & Ray, T. P. (1996). Molecular Hydrogen in the Outflow From CEP E. , *112*, 2086.

Elitzur, M. (1992). *Astronomical masers*, vol. 170.

Ellerbroek, L. E., Podio, L., Kaper, L., Sana, H., Huppenkothen, D., de Koter, A., & Monaco, L. (2013). The outflow history of two Herbig-Haro jets in RCW 36: HH 1042 and HH 1043. , *551*, A5.

Elmegreen, B. G., & Lada, C. J. (1977). Sequential formation of subgroups in OB associations. , *214*, 725–741.

Endres, C. P., Schlemmer, S., Schilke, P., Stutzki, J., & Müller, H. S. P. (2016). The Cologne Database for Molecular Spectroscopy, CDMS, in the Virtual Atomic and Molecular Data Centre, VAMDC. *Journal of Molecular Spectroscopy*, *327*, 95–104.

Evans, I., N. J., Becklin, E. E., Beichman, C., Gatley, I., Hildebrand, R. H., Keene, J., Slovak, M. H., Werner, M. W., & Whitcomb, S. E. (1981). Far-infrared observations of the Cepheus OB3 molecular cloud. , *244*, 115–123.

Ewen, H. I., & Purcell, E. M. (1951). Observation of a Line in the Galactic Radio Spectrum: Radiation from Galactic Hydrogen at 1,420 Mc./sec. , *168*(4270), 356.

Favre, C., Despois, D., Brouillet, N., Baudry, A., Combes, F., Guélin, M., Wootten, A., & Wlodarczak, G. (2011). HCOOCH$_3$ as a probe of temperature and structure in Orion-KL. , *532*, A32.

Favre, C., Fedele, D., Semenov, D., Parfenov, S., Codella, C., Ceccarelli, C., Bergin, E. A., Chapillon, E., Testi, L., Hersant, F., Lefloch, B., Fontani, F., Blake, G. A., Cleeves, L. I., Qi, C., Schwarz, K. R., & Taquet, V. (2018). First Detection of the Simplest Organic Acid in a Protoplanetary Disk. , *862*(1), L2.

Favre, C., Pagani, L., Goldsmith, P. F., Bergin, E. A., Carvajal, M., Kleiner, I., Melnick, G., & Snell, R. (2017). The complexity of Orion: an ALMA view. II. gGg'-ethylene glycol and acetic acid. , *604*, L2.

Felli, M., Tofani, G., Harten, R. H., & Panagia, N. (1978). The thermal radio emission from the S 155 nebula and the Cepheus OB 3 association. , *69*, 199–211.

Ferreira, J., Dougados, C., & Cabrit, S. (2006). Which jet launching mechanism(s) in T Tauri stars? , *453*(3), 785–796.

Few, R. W., & Cohen, R. J. (1983). A survey of formaldehyde in the Cepheus OB3 molecular cloud. , *203*, 853–859.

Fiege, J. D., & Henriksen, R. N. (1996). A global model of protostellar bipolar outflow - I. , *281*(3), 1038–1054.

Flower, D. R. (1999). Rotational excitation of HCO$\hat{+}$ by H_2. , *305*(3), 651–653.

Flower, D. R., & Pineau des Forets, G. (1994). Grain / Mantle Erosion in Magnetohydrodynamic Shocks. , *268*, 724.

Frank, A., Ray, T. P., Cabrit, S., Hartigan, P., Arce, H. G., Bacciotti, F., Bally, J., Benisty, M., Eislöffel, J., Güdel, M., Lebedev, S., Nisini, B., & Raga, A. (2014). Jets and Outflows from Star to Cloud: Observations Confront Theory. In H. Beuther, R. S. Klessen, C. P. Dullemond, & T. Henning (Eds.) *Protostars and Planets VI*, (p. 451).

Fuente, A., Ceccarelli, C., Neri, R., Alonso-Albi, T., Caselli, P., Johnstone, D., van Dishoeck, E. F., & Wyrowski, F. (2007). Protostellar clusters in intermediate mass (IM) star forming regions. , *468*(3), L37–L40.

Fuente, A., Cernicharo, J., Caselli, P., McCoey, C., Johnstone, D., Fich, M., van Kempen, T., Palau, A., Yıldız, U. A., Tercero, B., & López, A. (2014). The hot core towards the intermediate-mass protostar NGC 7129 FIRS 2. Chemical similarities with Orion KL. , *568*, A65.

Fuente, A., Rizzo, J. R., Caselli, P., Bachiller, R., & Henkel, C. (2005). Chemical evolution in the environment of intermediate mass young stellar objects. , *433*(2), 535–552.

Fukui, Y., Iwata, T., Mizuno, A., Bally, J., & Lane, A. P. (1993). Molecular Outflows. In E. H. Levy, & J. I. Lunine (Eds.) *Protostars and Planets III*, (p. 603).

Fukui, Y., Iwata, T., Takaba, H., Mizuno, A., Ogawa, H., Kawabata, K., & Sugitani, K. (1989). Molecular outflows in protostellar evolution. , *342*(6246), 161–163.

Garrod, R. T., & Herbst, E. (2006). Formation of methyl formate and other organic species in the warm-up phase of hot molecular cores. , *457*(3), 927–936.

Garufi, A., Podio, L., Codella, C., Rygl, K., Bacciotti, F., Facchini, S., Fedele, D., Miotello, A., Teague, R., & Testi, L. (2020). ALMA chemical survey of disk-outflow sources in Taurus (ALMA-DOT). I. CO, CS, CN, and H_2CO around DG Tau B. , *636*, A65.

Giannini, T., Nisini, B., & Lorenzetti, D. (2001). Far-Infrared Investigation of Class 0 Sources: Line Cooling. , *555*(1), 40–57.

Goldsmith, P. F., & Langer, W. D. (1999). Population Diagram Analysis of Molecular Line Emission. , *517*(1), 209–225.

Gómez-Ruiz, A. I., Codella, C., Lefloch, B., Benedettini, M., Busquet, G., Ceccarelli, C., Nisini, B., Podio, L., & Viti, S. (2015). The density structure of the L1157 molecular outflow. , *446*(4), 3346–3355.

Gómez-Ruiz, A. I., Gusdorf, A., Leurini, S., Codella, C., Güsten, R., Wyrowski, F., Requena-Torres, M. A., Risacher, C., & Wampfler, S. F. (2012). High-J CO emission in the Cepheus E protostellar outflow observed with SOFIA/GREAT. , *542*, L9.

Green, S. (1991). Collisional Excitation of Formaldehyde in "Hot" Interstellar Molecular Regions. , *76*, 979.

Guélin, M., & Cernicharo, J. (2022). Organic Molecules in Interstellar Space: Latest Advances. *Frontiers in Astronomy and Space Sciences*, *9*, 787567.

Gueth, F., & Guilloteau, S. (1999). The jet-driven molecular outflow of HH 211. , *343*, 571–584.

Gueth, F., Guilloteau, S., & Bachiller, R. (1996). A precessing jet in the L1157 molecular outflow. , *307*, 891–897.

Gueth, F., Guilloteau, S., & Bachiller, R. (1998). SiO shocks in the L1157 molecular outflow. , *333*, 287–297.

Gusdorf, A., Anderl, S., Lefloch, B., Leurini, S., Wiesemeyer, H., Güsten, R., Benedettini, M., Codella, C., Godard, B., Gómez-Ruiz, A. I., Jacobs, K., Kristensen, L. E., Lesaffre, P., Pineau des Forêts, G., & Lis, D. C. (2017). Nature of shocks revealed by SOFIA OI observations in the Cepheus E protostellar outflow. , *602*, A8.

Gusdorf, A., Cabrit, S., Flower, D. R., & Pineau Des Forêts, G. (2008a). SiO line emission from C-type shock waves: interstellar jets and outflows. , *482*(3), 809–829.

Gusdorf, A., Pineau Des Forêts, G., Cabrit, S., & Flower, D. R. (2008b). SiO line emission from interstellar jets and outflows: silicon-containing mantles and non-stationary shock waves. , *490*(2), 695–706.

Hara, C., Kawabe, R., Nakamura, F., Hirano, N., Takakuwa, S., Shimajiri, Y., Kamazaki, T., Di Francesco, J., Machida, M. N., Tamura, M., Saigo, K., Matsumoto, T., & Tomida, K. (2021). Misaligned Twin Molecular Outflows from the Class 0 Protostellar Binary System VLA 1623A Unveiled by ALMA. , *912*(1), 34.

Haro, G. (1952). Herbig's Nebulous Objects Near NGC 1999. , *115*, 572.

Hatchell, J., Fuller, G. A., & Ladd, E. F. (1999). Hot molecular bullets in HH 111 and CEP E. , *346*, 278–284.

Heiles, C., & Troland, T. H. (2003). The Millennium Arecibo 21 Centimeter Absorption-Line Survey. II. Properties of the Warm and Cold Neutral Media. , *586*(2), 1067–1093.

Herbig, G. H. (1951). The Spectra of Two Nebulous Objects Near NGC 1999. , *113*, 697–699.

Herbst, E., & van Dishoeck, E. F. (2009). Complex Organic Interstellar Molecules. , *47*(1), 427–480.

Hewish, A., Bell, S. J., Pilkington, J. D. H., Scott, P. F., & Collins, R. A. (1968). Observation of a Rapidly Pulsating Radio Source. , *217*(5130), 709–713.

Heyer, M. H., & Ladd, E. F. (1995). A Multitransitional CO Study of the Cepheus C Cloud Core. , *439*, 269.

Higuchi, A. E., Sakai, N., Watanabe, Y., López-Sepulcre, A., Yoshida, K., Oya, Y., Imai, M., Zhang, Y., Ceccarelli, C., Lefloch, B., Codella, C., Bachiller, R., Hirota, T., Sakai, T., & Yamamoto, S. (2018). Chemical Survey toward Young Stellar Objects in the Perseus Molecular Cloud Complex. , *236*(2), 52.

Hillenbrand, L. A., & Hartmann, L. W. (1998). A Preliminary Study of the Orion Nebula Cluster Structure and Dynamics. , *492*(2), 540–553.

Hirano, N., Liu, S.-Y., Shang, H., Ho, P. T. P., Huang, H.-C., Kuan, Y.-J., McCaughrean, M. J., & Zhang, Q. (2006). SiO J = 5-4 in the HH 211 Protostellar Jet Imaged with the Submillimeter Array. , *636*(2), L141–L144.

Hirth, G. A., Mundt, R., Solf, J., & Ray, T. P. (1994). Asymmetries in Bipolar Jets from Young Stars. , *427*, L99.

Högbom, J. A. (1974). Aperture Synthesis with a Non-Regular Distribution of Interferometer Baselines. , *15*, 417.

Holdship, J., Viti, S., Codella, C., Rawlings, J., Jimenez-Serra, I., Ayalew, Y., Curtis, J., Habib, A., Lawrence, J., Warsame, S., & Horn, S. (2019). Observations of CH_3OH and CH_3CHO in a Sample of Protostellar Outflow Sources. , *880*(2), 138.

Ivezic, Z., & Elitzur, M. (1997). Self-similarity and scaling behaviour of infrared emission from radiatively heated dust - I. Theory. , (4), 799–811.

Jacobsen, S. K., Jørgensen, J. K., Di Francesco, J., Evans, N. J., Choi, M., & Lee, J.-E. (2019). Organic chemistry in the innermost, infalling envelope of the Class 0 protostar L483. , *629*, A29.

Johansson, L. E. B., Andersson, C., Ellder, J., Friberg, P., Hjalmarson, A., Hoglund, B., Irvine, W. M., Olofsson, H., & Rydbeck, G. (1984). Spectral scan of Orion A and IRC +10216 from 72 to 91 GHz. , *130*, 227–256.

Jordi, C., Trullols, E., & Galadi-Enriquez, D. (1996). Cepheus OB3 association: faint members. , *312*, 499–507.

Jørgensen, J. K., Hogerheijde, M. R., Blake, G. A., van Dishoeck, E. F., Mundy, L. G., & Schöier, F. L. (2004). The impact of shocks on the chemistry of molecular clouds. High resolution images of chemical differentiation along the NGC 1333-IRAS 2A outflow. , *415*, 1021–1037.

Jørgensen, J. K., Lahuis, F., Schöier, F. L., van Dishoeck, E. F., Blake, G. A., Boogert, A. C. A., Dullemond, C. P., Evans, I., Neal J., Kessler-Silacci, J. E., & Pontoppidan, K. M. (2005). Protostellar Holes: Spitzer Space Telescope Observations of the Protostellar Binary IRAS 16293-2422. , *631*(1), L77–L80.

Kahane, C., Ceccarelli, C., Faure, A., & Caux, E. (2013). Detection of Formamide, the Simplest but Crucial Amide, in a Solar-type Protostar. , *763*(2), L38.

Karnath, N., Prchlik, J. J., Gutermuth, R. A., Allen, T. S., Megeath, S. T., Pipher, J. L., Wolk, S., & Jeffries, R. D. (2019). The Dynamics, Structure, and Fate of a Young Cluster during Gas Dispersal: Hectoschelle, Chandra, Spitzer, and Gaia Observations of Cep OB3b. , *871*(1), 46.

Koppenaal, K., Sargent, A. I., Nordh, L., van Duinen, R. J., & Aalders, J. W. G. (1979). Observations of new far infrared sources in the Cepheus OB3 molecular cloud. , *75*(1-2), L1–L3.

Kwan, A. S. H., & Ko, N. W. M. (1976). Coherent structures in subsonic coaxial jets. *Journal of Sound Vibration*, *48*(2), 203–219.

Lada, C. J. (1987). Star formation: from OB associations to protostars. In M. Peimbert, & J. Jugaku (Eds.) *Star Forming Regions*, vol. 115, (p. 1).

Lada, C. J., Blitz, L., Reid, M. J., & Moran, J. M. (1981). VLBI observations of the water vapor masers in Cepheus A, S 252 a, Gl2789, GL 2139, CO 59.79+0.04, W 33 b, and U Orionis. , *243*, 769–777.

Lada, C. J., & Fich, M. (1996). The Structure and Energetics of a Highly Collimated Bipolar Outflow: NGC 2264G. , *459*, 638.

Ladd, E. F., & Hodapp, K. W. (1997). A Double Outflow from a Deeply Embedded Source in Cepheus. , *474*(2), 749–759.

Lai, S.-P., Velusamy, T., Langer, W. D., & Kuiper, T. B. H. (2003). The Physical and Chemical Status of Pre-Protostellar Core B68. , *126*(1), 311–318.

Le Gal, R., Öberg, K. I., Loomis, R. A., Pegues, J., & Bergner, J. B. (2019). Sulfur Chemistry in Protoplanetary Disks: CS and H_2CS. , *876*(1), 72.

Lee, C.-F. (2020). Molecular jets from low-mass young protostellar objects. , *28*(1), 1.

Lee, C.-F., Ho, P. T., Hirano, N., Bourke, T. L., Beuther, B., Shang, H., & Zhang, Q. (2007). SMA Observations Of A Remarkable Protostellar Jet HH 212. In *American Astronomical Society Meeting Abstracts #210*, vol. 210 of *American Astronomical Society Meeting Abstracts*, (p. 123.03).

Lee, C.-F., Mundy, L. G., Reipurth, B., Ostriker, E. C., & Stone, J. M. (2000). CO Outflows from Young Stars: Confronting the Jet and Wind Models. , *542*(2), 925–945.

Lee, C.-F., Rao, R., Ching, T.-C., Lai, S.-P., Hirano, N., Ho, P. T. P., & Hwang, H.-C. (2014). Magnetic Field Structure in the Flattened Envelope and Jet in the Young Protostellar System HH 211. , *797*(1), L9.

Lee, C.-F., Stone, J. M., Ostriker, E. C., & Mundy, L. G. (2001). Hydrodynamic Simulations of Jet- and Wind-driven Protostellar Outflows. , *557*(1), 429–442.

Lefloch, B., Bachiller, R., Ceccarelli, C., Cernicharo, J., Codella, C., Fuente, A., Kahane, C., López-Sepulcre, A., Tafalla, M., Vastel, C., Caux, E., González-García, M., Bianchi, E., Gómez-Ruiz, A., Holdship, J., Mendoza, E., Ospina-Zamudio, J., Podio, L., Quénard, D., Roueff, E., Sakai, N., Viti, S., Yamamoto, S., Yoshida, K., Favre, C., Monfredini, T., Quitián-Lara, H. M., Marcelino, N., Boechat-Roberty, H. M., & Cabrit, S. (2018). Astrochemical evolution along star formation: overview of the IRAM Large Program ASAI. , *477*(4), 4792–4809.

Lefloch, B., Busquet, G., Viti, S., Vastel, C., Mendoza, E., Benedettini, M., Codella, C., Podio, L., Schutzer, A., Rivera-Ortiz, P. R., Lépine, J. R. D., & Bachiller, R. (2021). HCN/HNC chemistry in shocks: a study of L1157-B1 with ASAI. , *507*(1), 1034–1046.

Lefloch, B., Cabrit, S., Busquet, G., Codella, C., Ceccarelli, C., Cernicharo, J., Pardo, J. R., Benedettini, M., Lis, D. C., & Nisini, B. (2012). The CHESS Survey of the L1157-B1 Shock Region: CO Spectral Signatures of Jet-driven Bow Shocks. , *757*(2), L25.

Lefloch, B., Castets, A., Cernicharo, J., & Loinard, L. (1998). Widespread SiO Emission in NGC 1333. , *504*(2), L109–L112.

Lefloch, B., Ceccarelli, C., Codella, C., Favre, C., Podio, L., Vastel, C., Viti, S., & Bachiller, R. (2017). L1157-B1, a factory of complex organic molecules in a solar-type star-forming region. , *469*(1), L73–L77.

Lefloch, B., Cernicharo, J., Cabrit, S., Noriega-Crespo, A., Moro-Martín, A., & Cesarsky, D. (2003). Warm Molecular Hydrogen and Ionized Neon in the HH 2 Outflow. , *590*(1), L41–L44.

Lefloch, B., Cernicharo, J., Pacheco, S., & Ceccarelli, C. (2011). Shocked water in the Cepheus E protostellar outflow. , *527*, L3.

Lefloch, B., Cernicharo, J., Reipurth, B., Pardo, J. R., & Neri, R. (2007). Anatomy of HH 111 from CO Observations: A Bow-Shock-driven Molecular Outflow. , *658*(1), 498–508.

Lefloch, B., Eisloeffel, J., & Lazareff, B. (1996). The remarkable Class 0 source CEP E. , *313*, L17–L20.

Lefloch, B., Gusdorf, A., Codella, C., Eislöffel, J., Neri, R., Gómez-Ruiz, A. I., Güsten, R., Leurini, S., Risacher, C., & Benedettini, M. (2015). The structure of the Cepheus E protostellar outflow: The jet, the bowshock, and the cavity. , *581*, A4.

Lefloch, B., Vastel, C., Viti, S., Jimenez-Serra, I., Codella, C., Podio, L., Ceccarelli, C., Mendoza, E., Lepine, J. R. D., & Bachiller, R. (2016). Phosphorus-bearing molecules in solar-type star-forming regions: first PO detection. , *462*(4), 3937–3944.

Lery, T., Henriksen, R. N., Fiege, J. D., Ray, T. P., Frank, A., & Bacciotti, F. (2002). A global jet/circulation model for young stars. , *387*, 187–200.

Li, Z.-Y., & Shu, F. H. (1996). Magnetized Singular Isothermal Toroids. , *472*, 211.

Lique, F., & Spielfiedel, A. (2007). Ro-vibrational excitation of CS by He. , *462*(3), 1179–1185.

Lique, F., Spielfiedel, A., Dubernet, M. L., Feautrier, N., & Cernicharo, J. (2006). Rotational excitation of sulfur monoxide by collisions with Helium at low temperature. In D. Barret, F. Casoli, G. Lagache, A. Lecavelier, & L. Pagani (Eds.) *SF2A-2006: Semaine de l'Astrophysique Francaise*, (p. 243).

Lis, D. C., Roueff, E., Gerin, M., Phillips, T. G., Coudert, L. H., van der Tak, F. F. S., & Schilke, P. (2002). Detection of Triply Deuterated Ammonia in the Barnard 1 Cloud. , *571*(1), L55–L58.

Longmore, S. N., Burton, M. G., Keto, E., Kurtz, S., & Walsh, A. J. (2009). Too large and overlooked? Extended free-free emission towards massive star formation regions. , *399*(2), 861–877.

López-Sepulcre, A., Jaber, A. A., Mendoza, E., Lefloch, B., Ceccarelli, C., Vastel, C., Bachiller, R., Cernicharo, J., Codella, C., Kahane, C., Kama, M., & Tafalla, M. (2015). Shedding light on the formation of the pre-biotic molecule formamide with ASAI. , *449*(3), 2438–2458.

López-Sepulcre, A., Sakai, N., Neri, R., Imai, M., Oya, Y., Ceccarelli, C., Higuchi, A. E., Aikawa, Y., Bottinelli, S., Caux, E., Hirota, T., Kahane, C., Lefloch, B., Vastel, C., Watanabe, Y., & Yamamoto, S. (2017). Complex organics in IRAS 4A revisited with ALMA and PdBI: Striking contrast between two neighbouring protostellar cores. , *606*, A121.

Louvet, F., Dougados, C., Cabrit, S., Mardones, D., Ménard, F., Tabone, B., Pinte, C., & Dent, W. R. F. (2018). The HH30 edge-on T Tauri star. A rotating and precessing monopolar outflow scrutinized by ALMA. , *618*, A120.

Manigand, S., Jørgensen, J. K., Calcutt, H., Müller, H. S. P., Ligterink, N. F. W., Coutens, A., Drozdovskaya, M. N., van Dishoeck, E. F., & Wampfler, S. F. (2020). The ALMA-PILS survey: inventory of complex organic molecules towards IRAS 16293-2422 A. , *635*, A48.

Mannings, V., & Sargent, A. I. (1997). A High-Resolution Study of Gas and Dust around Young Intermediate-Mass Stars: Evidence for Circumstellar Disks in Herbig Ae Systems. , *490*(2), 792–802.

Mannings, V., & Sargent, A. I. (2000). High-Resolution Studies of Gas and Dust around Young Intermediate-Mass Stars. II. Observations of an Additional Sample of Herbig AE Systems. , *529*(1), 391–401.

Maret, S., Bergin, E. A., Neufeld, D. A., Green, J. D., Watson, D. M., Harwit, M. O., Kristensen, L. E., Melnick, G. J., Sonnentrucker, P., Tolls, V., Werner, M. W., Willacy, K., & Yuan, Y. (2009). Spitzer Mapping of Molecular Hydrogen Pure Rotational Lines in NGC 1333: A Detailed Study of Feedback in Star Formation. , *698*(2), 1244–1260.

Maret, S., Ceccarelli, C., Caux, E., Tielens, A. G. G. M., Jørgensen, J. K., van Dishoeck, E., Bacmann, A., Castets, A., Lefloch, B., Loinard, L., Parise, B., & Schöier, F. L. (2004). The H_2CO abundance in the inner warm regions of low mass protostellar envelopes. , *416*, 577–594.

Masciadri, E., & Raga, A. C. (2002). Herbig-Haro Jets from Orbiting Sources. , *568*(2), 733–742.

Matzner, C. D., & McKee, C. F. (1999). Bipolar Molecular Outflows Driven by Hydromagnetic Protostellar Winds. , *526*(2), L109–L112.

McCaughrean, M. J., Rayner, J. T., & Zinnecker, H. (1994). Discovery of a Molecular Hydrogen Jet near IC 348. , *436*, L189.

McElroy, D., Walsh, C., Markwick, A. J., Cordiner, M. A., Smith, K., & Millar, T. J. (2013). The UMIST database for astrochemistry 2012. , *550*, A36.

McGuire, B. A., Loomis, R. A., Burkhardt, A. M., Lee, K. L. K., Shingledecker, C. N., Charnley, S. B., Cooke, I. R., Cordiner, M. A., Herbst, E., Kalenskii, S., Siebert, M. A., Willis, E. R., Xue, C., Remijan, A. J., & McCarthy, M. C. (2021). Detection of two interstellar polycyclic aromatic hydrocarbons via spectral matched filtering. *Science*, *371*(6535), 1265–1269.

McKee, C. F., & Tan, J. C. (2003). The Formation of Massive Stars from Turbulent Cores. , *585*(2), 850–871.

Megeath, S. T., Flaherty, K. M., Hora, J., Allen, L. E., Fazio, G. G., Hartmann, L., Myers, P. C., Muzerolle, J., Pipher, J. L., Siegler, N., Stauffer, J. R., & Young, E.

(2005). A Spitzer/IRAC survey of the Orion Molecular Clouds. In R. Cesaroni, M. Felli, E. Churchwell, & M. Walmsley (Eds.) *Massive Star Birth: A Crossroads of Astrophysics*, vol. 227, (pp. 383–388).

Mehringer, D. M., Zhou, S., & Dickel, H. R. (1997). BIMA Array Observations of the 107 GHz Methanol Masers in Cepheus A. , *475*(1), L57–L60.

Mendoza, E., Lefloch, B., Ceccarelli, C., Kahane, C., Jaber, A. A., Podio, L., Benedettini, M., Codella, C., Viti, S., Jimenez-Serra, I., Lepine, J. R. D., Boechat-Roberty, H. M., & Bachiller, R. (2018). A search for cyanopolyynes in L1157-B1. , *475*(4), 5501–5512.

Mendoza, E., Lefloch, B., López-Sepulcre, A., Ceccarelli, C., Codella, C., Boechat-Roberty, H. M., & Bachiller, R. (2014). Molecules with a peptide link in protostellar shocks: a comprehensive study of L1157. , *445*(1), 151–161.

Michelson, A. A., & Pease, F. G. (1921). Measurement of the Diameter of α Orionis with the Interferometer. , *53*, 249–259.

Moro-Martín, A., Noriega-Crespo, A., Molinari, S., Testi, L., Cernicharo, J., & Sargent, A. (2001). Infrared and Millimetric Study of the Young Outflow Cepheus E. , *555*(1), 146–159.

Motte, F., Bontemps, S., & Louvet, F. (2018). High-Mass Star and Massive Cluster Formation in the Milky Way. , *56*, 41–82.

Muller, C. A., & Oort, J. H. (1951). Observation of a Line in the Galactic Radio Spectrum: The Interstellar Hydrogen Line at 1,420 Mc./sec., and an Estimate of Galactic Rotation. , *168*(4270), 357–358.

Mundt, R., & Fried, J. W. (1983). Jets from young stars. , *274*, L83–L86.

Myers, P. C., & Benson, P. J. (1983). Dense cores in dark clouds. II. NH3 observations and star formation. , *266*, 309–320.

Neri, R., Fuente, A., Ceccarelli, C., Caselli, P., Johnstone, D., van Dishoeck, E. F., Wyrowski, F., Tafalla, M., Lefloch, B., & Plume, R. (2007). The IC1396N proto-cluster at a scale of ~250 AU. , *468*(3), L33–L36.

Nisini, B., Codella, C., Giannini, T., Santiago Garcia, J., Richer, J. S., Bachiller, R., & Tafalla, M. (2007). Warm SiO gas in molecular bullets associated with protostellar outflows. , *462*(1), 163–172.

Nony, T., Motte, F., Louvet, F., Plunkett, A., Gusdorf, A., Fechtenbaum, S., Pouteau, Y., Lefloch, B., Bontemps, S., Molet, J., & Robitaille, J. F. (2020). Episodic accretion constrained by a rich cluster of outflows. , *636*, A38.

Noriega-Crespo, A., Garnavich, P. M., & Molinari, S. (1998). ISOCAM Molecular Hydrogen Images of the Cepheus E Outflow. , *116*(3), 1388–1395.

Noriega-Crespo, A., Moro-Martin, A., Carey, S., Morris, P. W., Padgett, D. L., Latter, W. B., & Muzerolle, J. (2004). Is the Cepheus E Outflow Driven by a Class 0 Protostar? , *154*(1), 402–407.

Noriega-Crespo, A., Raga, A. C., Lora, V., Stapelfeldt, K. R., & Carey, S. J. (2011). The Precession of the Herbig-Haro 111 Flow in the Infrared. , *732*(1), L16.

Noriega-Crespo, A., Raga, A. C., Moro-Martín, A., Flagey, N., & Carey, S. J. (2014). Proper motions of young stellar outflows in the mid-infrared with Spitzer II HH 377/Cep E. *New Journal of Physics*, *16*(10), 105008.

Öberg, K. I., Guzmán, V. V., Furuya, K., Qi, C., Aikawa, Y., Andrews, S. M., Loomis, R., & Wilner, D. J. (2015). The comet-like composition of a protoplanetary disk as revealed by complex cyanides. , *520*(7546), 198–201.

Öberg, K. I., van der Marel, N., Kristensen, L. E., & van Dishoeck, E. F. (2011). Complex Molecules toward Low-mass Protostars: The Serpens Core. , *740*(1), 14.

Ohishi, M., & Kaifu, N. (1998). Chemical and physical evolution of dark clouds. Molecular spectral line survey toward TMC-1. *Faraday Discussions*, *109*, 205.

Olofsson, H., Ellder, J., Hjalmarson, A., & Rydbeck, G. (1982). Extended and anisotropic high-velocity gas flows in the Orion-KL region. , *113*, L18–L21.

Ospina-Zamudio, J., Lefloch, B., Ceccarelli, C., Kahane, C., Favre, C., López-Sepulcre, A., & Montarges, M. (2018). First hot corino detected around an isolated intermediate-mass protostar: Cep E-mm. , *618*, A145.

Ospina-Zamudio, J., Lefloch, B., Favre, C., López-Sepulcre, A., Bianchi, E., Ceccarelli, C., De Simone, M., Bouvier, M., & Kahane, C. (2019). Molecules in the Cep E-mm jet: evidence for shock-driven photochemistry? , *490*(2), 2679–2691.

Ospina-Zamudio, J. D. (2019). *Complexité chimique des protoétoiles de masse intermédiaire : une étude de Cep E-mm*. Ph.D. thesis, Astrophysique [astro-ph].

Ossenkopf, V., & Henning, T. (1994). Dust opacities for protostellar cores. , *291*, 943–959.

Osterbrock, D. E. (1974). *Astrophysics of gaseous nebulae*.

Oya, Y., Sakai, N., Watanabe, Y., Higuchi, A. E., Hirota, T., López-Sepulcre, A., Sakai, T., Aikawa, Y., Ceccarelli, C., Lefloch, B., Caux, E., Vastel, C., Kahane, C., & Yamamoto, S. (2017). L483: Warm Carbon-chain Chemistry Source Harboring Hot Corino Activity. , *837*(2), 174.

Palau, A., Ho, P. T. P., Zhang, Q., Estalella, R., Hirano, N., Shang, H., Lee, C. F., Bourke, T. L., Beuther, H., & Kuan, Y. J. (2006). Submillimeter Emission from the Hot Molecular Jet HH 211. , *636*(2), L137–L140.

Palla, F., Cesaroni, R., Brand, J., Caselli, P., Comoretto, G., & Felli, M. (1993). H2O masers associated with dense molecular clouds and ultracompact HII regions. II. The extended sample. , *280*, 599–608.

Panagia, N., & Thum, C. (1981). A study of the S 155A - CEP B cloud and its relation to Cepheus OB3 association. , *98*(2), 295–299.

Pantaleone, S., Enrique-Romero, J., Ceccarelli, C., Ferrero, S., Balucani, N., Rimola, A., & Ugliengo, P. (2021). H_2 Formation on Interstellar Grains and the Fate of Reaction Energy. , *917*(1), 49.

Pardo, J. R., Cernicharo, J., & Serabyn, E. (2001). Atmospheric transmission at microwaves (ATM): an improved model for millimeter/submillimeter applications. *IEEE Transactions on Antennas and Propagation*, *49*(12), 1683–1694.

Parise, B., Castets, A., Herbst, E., Caux, E., Ceccarelli, C., Mukhopadhyay, I., & Tielens, A. G. G. M. (2004). First detection of triply-deuterated methanol. , *416*, 159–163.

Patel, N. A., Curiel, S., Zhang, Q., Sridharan, T. K., Ho, P. T. P., & Torrelles, J. M. (2007). Submillimeter Array Observations of 321 GHz Water Maser Emission in Cepheus A. , *658*(1), L55–L58.

Penzias, A. A., & Wilson, R. W. (1965). A Measurement of Excess Antenna Temperature at 4080 Mc/s. , *142*, 419–421.

Pety, J., Gueth, F., Guilloteau, S., & Dutrey, A. (2006). Plateau de Bure interferometer observations of the disk and outflow of HH 30. , *458*(3), 841–854.

Pickett, H. M., Poynter, R. L., Cohen, E. A., Delitsky, M. L., Pearson, J. C., & Müller, H. S. P. (1998). Submillimeter, millimeter and microwave spectral line catalog. , *60*(5), 883–890.

Pilbratt, G. L., Riedinger, J. R., Passvogel, T., Crone, G., Doyle, D., Gageur, U., Heras, A. M., Jewell, C., Metcalfe, L., Ott, S., & Schmidt, M. (2010). Herschel Space Observatory. An ESA facility for far-infrared and submillimetre astronomy. , *518*, L1.

Plunkett, A. L., Arce, H. G., Mardones, D., van Dokkum, P., Dunham, M. M., Fernández-López, M., Gallardo, J., & Corder, S. A. (2015). Episodic molecular outflow in the very young protostellar cluster Serpens South. , *527*(7576), 70–73.

Podio, L., Codella, C., Gueth, F., Cabrit, S., Maury, A., Tabone, B., Lefèvre, C., Anderl, S., André, P., Belloche, A., Bontemps, S., Hennebelle, P., Lefloch, B., Maret, S., & Testi, L. (2016). First image of the L1157 molecular jet by the CALYPSO IRAM-PdBI survey. , *593*, L4.

Podio, L., Lefloch, B., Ceccarelli, C., Codella, C., & Bachiller, R. (2014). Molecular ions in the protostellar shock L1157-B1. , *565*, A64.

Podio, L., Tabone, B., Codella, C., Gueth, F., Maury, A., Cabrit, S., Lefloch, B., Maret, S., Belloche, A., André, P., Anderl, S., Gaudel, M., & Testi, L. (2021). The CALYPSO IRAM-PdBI survey of jets from Class 0 protostars. Exploring whether jets are ubiquitous in young stars. , *648*, A45.

Porras, A. J., Federman, S. R., Welty, D. E., & Ritchey, A. M. (2014). OH^+ in Diffuse Molecular Clouds. , *781*(1), L8.

Pottage, J. T., Flower, D. R., & Davis, S. L. (2001). The rotational excitation of methanol by helium at low temperatures. *Journal of Physics B Atomic Molecular Physics*, *34*(16), 3313–3330.

Rabenanahary, M., Cabrit, S., Meliani, Z., & Pineau des Forêts, G. (2022). Wide-angle protostellar outflows driven by narrow jets in stratified cores. , *664*, A118.

Raga, A., & Cabrit, S. (1993). Molecular outflows entrained by jet bowshocks. , *278*, 267–278.

Raga, A. C., Canto, J., & Biro, S. (1993). Ballistic stellar jets from sources with a time-dependent ejection direction. , *260*, 163–170.

Reipurth, B., & Bally, J. (2001). Herbig-Haro Flows: Probes of Early Stellar Evolution. , *39*, 403–455.

Rivera-Ortiz, P. R., Rodríguez-González, A., Hernández-Martínez, L., & Cantó, J. (2019). The Motion of a Losing Mass Plasmon. , *874*(1), 38.

Rivilla, V. M., Jiménez-Serra, I., Martín-Pintado, J., Briones, C., Rodríguez-Almeida, L. F., Rico-Villas, F., Tercero, B., Zeng, S., Colzi, L., de Vicente, P., Martín, S., & Requena-Torres, M. A. (2021). Discovery in space of ethanolamine, the simplest phospholipid head group. *Proceedings of the National Academy of Science*, *118*(22), e2101314118.

Rodriguez, L. F., Ho, P. T. P., & Moran, J. M. (1980). Anisotropic mass outflow in Cepheus A. , *240*, L149–L152.

Roueff, E., Lis, D. C., van der Tak, F. F. S., Gerin, M., & Goldsmith, P. F. (2005). Interstellar deuterated ammonia: from NH_3 to ND_3. , *438*(2), 585–598.

Rybicki, G. B., & Lightman, A. P. (1986). *Radiative Processes in Astrophysics*.

Sakai, N., Sakai, T., Hirota, T., & Yamamoto, S. (2008). Abundant Carbon-Chain Molecules toward the Low-Mass Protostar IRAS 04368+2557 in L1527. , *672*(1), 371–381.

Sakai, N., Sakai, T., Hirota, T., & Yamamoto, S. (2009). Deuterated Molecules in Warm Carbon Chain Chemistry: The L1527 Case. , *702*(2), 1025–1035.

Santiago-García, J., Tafalla, M., Johnstone, D., & Bachiller, R. (2009). Shells, jets, and internal working surfaces in the molecular outflow from IRAS 04166+2706. , *495*(1), 169–181.

Sargent, A. I. (1977). Molecular clouds and star formation. I. Observations of the Cepheus OB3 molecular cloud. , *218*, 736–748.

Sargent, A. I. (1979). Molecular clouds and star formation. II. Star formation in the Cepheus OB3 and Perseus OB2 molecular clouds. , *233*, 163–181.

Schilke, P., Walmsley, C. M., Pineau des Forets, G., & Flower, D. R. (1997). SiO production in interstellar shocks. , *321*, 293–304.

Schuster, K. F., Lefloch, B., Ungerechts, H., Thum, C., Gueth, F., Sterzik, M., & Wiesemeyer, H. (2004). A Square Degree Survey for Molecular Flows in TMC1. In S. Pfalzner, C. Kramer, C. Staubmeier, & A. Heithausen (Eds.) *The Dense Interstellar Medium in Galaxies*, vol. 91, (p. 611).

Schwartz, R. D. (1975). T Tauri nebulae and Herbig-Haro nebulae: evidence for excitation by a strong stellar wind. , *195*, 631–642.

Shu, F. H., & Adams, F. C. (1987). Star formation and the circumstellar matter of young stellar objects. In I. Appenzeller, & C. Jordan (Eds.) *Circumstellar Matter*, vol. 122, (p. 7).

Shu, F. H., Najita, J., Ostriker, E. C., & Shang, H. (1995). Magnetocentrifugally Driven Flows from Young Stars and Disks. V. Asymptotic Collimation into Jets. , *455*, L155.

Shu, F. H., Ruden, S. P., Lada, C. J., & Lizano, S. (1991). Star Formation and the Nature of Bipolar Outflows. , *370*, L31.

Smith, M. D., Suttner, G., & Yorke, H. W. (1997). Numerical hydrodynamic simulations of jet-driven bipolar outflows. , *323*, 223–230.

Snell, R. L., Loren, R. B., & Plambeck, R. L. (1980). Observations of CO in L 1551 : evidence for stellar wind driven shocks. , *239*, L17–L22.

Sobolev, V. V. (1960). *Moving envelopes of stars*.

Tafalla, M., Bachiller, R., Lefloch, B., Rodríguez-Fernández, N., Codella, C., López-Sepulcre, A., & Podio, L. (2015). Fast molecular jet from L1157-mm. , *573*, L2.

Tafalla, M., Santiago-García, J., Hacar, A., & Bachiller, R. (2010). A molecular survey of outflow gas: velocity-dependent shock chemistry and the peculiar composition of the EHV gas. , *522*, A91.

Tan, J. C., & McKee, C. F. (2003). Outflow-Confined HII Regions and the Formation of Massive Stars by Accretion. *arXiv e-prints*, (pp. astro–ph/0309139).

Taquet, V., Codella, C., De Simone, M., López-Sepulcre, A., Pineda, J. E., Segura-Cox, D., Ceccarelli, C., Caselli, P., Gusdorf, A., Persson, M. V., Alves, F., Caux, E., Favre, C., Fontani, F., Neri, R., Oya, Y., Sakai, N., Vastel, C., Yamamoto, S., & Bachiller, e. a. (2020). Seeds of Life in Space (SOLIS). VI. Chemical evolution of sulfuretted species along the outflows driven by the low-mass protostellar binary NGC 1333-IRAS4A. , *637*, A63.

Tercero, B., Vincent, L., Cernicharo, J., Viti, S., & Marcelino, N. (2011). A line-confusion limited millimeter survey of Orion KL. II. Silicon-bearing species. , *528*, A26.

Terquem, C., Eislöffel, J., Papaloizou, J. C. B., & Nelson, R. P. (1999). Precession of Collimated Outflows from Young Stellar Objects. , *512*(2), L131–L134.

Testi, L., Palla, F., & Natta, A. (1999). The onset of cluster formation around Herbig Ae/Be stars. , *342*, 515–523.

Testi, L., & Sargent, A. I. (1998). Star Formation in Clusters: A Survey of Compact Millimeter-Wave Sources in the Serpens Core. , *508*(1), L91–L94.

Thompson, A. R. (1989). The Interferometer in Practice. In R. A. Perley, F. R. Schwab, & A. H. Bridle (Eds.) *Synthesis Imaging in Radio Astronomy*, vol. 6 of *Astronomical Society of the Pacific Conference Series*, (p. 11).

Thompson, A. R., Moran, J. M., & Swenson, G. W. (1986). *Interferometry and synthesis in radio astronomy*.

Tielens, A. G. G. M. (2005). *The Physics and Chemistry of the Interstellar Medium*.

Turner, B. E. (1989). A Molecular Line Survey of Sagittarius B2 and Orion-KL from 70 to 115 GHz. I. The Observational Data. , *70*, 539.

Tychoniec, Ł., Hull, C. L. H., Kristensen, L. E., Tobin, J. J., Le Gouellec, V. J. M., & van Dishoeck, E. F. (2019). Chemical and kinematic structure of extremely high-velocity molecular jets in the Serpens Main star-forming region. , *632*, A101.

Tychoniec, Ł., van Dishoeck, E. F., van't Hoff, M. L. R., van Gelder, M. L., Tabone, B., Chen, Y., Harsono, D., Hull, C. L. H., Hogerheijde, M. R., Murillo, N. M., & Tobin, J. J. (2021). Which molecule traces what: Chemical diagnostics of protostellar sources. , *655*, A65.

Urquhart, J. S., Figura, C. C., Moore, T. J. T., Hoare, M. G., Lumsden, S. L., Mottram, J. C., Thompson, M. A., & Oudmaijer, R. D. (2014). The RMS survey: galactic distribution of massive star formation. , *437*(2), 1791–1807.

van Dishoeck, E. F., Kristensen, L. E., Benz, A. O., Bergin, E. A., Caselli, P., Cernicharo, J., Herpin, F., Hogerheijde, M. R., Johnstone, D., Liseau, R., Nisini, B., Shipman, R., Tafalla, M., van der Tak, F., Wyrowski, F., Aikawa, Y., Bachiller, R., Baudry, A., & Benedettini, e. a. (2011). Water in Star-forming Regions with the Herschel Space Observatory (WISH). I. Overview of Key Program and First Results. , *123*(900), 138.

Vastel, C., Bottinelli, S., Caux, E., Glorian, J. M., & Boiziot, M. (2015). CASSIS: a tool to visualize and analyse instrumental and synthetic spectra. In *SF2A-2015: Proceedings of the Annual meeting of the French Society of Astronomy and Astrophysics*, (pp. 313–316).

Vastel, C., Ceccarelli, C., Lefloch, B., & Bachiller, R. (2014). The Origin of Complex Organic Molecules in Prestellar Cores. , *795*(1), L2.

Vazart, F., Ceccarelli, C., Balucani, N., Bianchi, E., & Skouteris, D. (2020). Gas-phase formation of acetaldehyde: review and new theoretical computations. , *499*(4), 5547–5561.

Vázquez-Semadeni, E., Gómez, G. C., Jappsen, A. K., Ballesteros-Paredes, J., & Klessen, R. S. (2009). High- and Low-Mass Star-Forming Regions from Hierarchical Gravitational Fragmentation. High Local Star Formation Rates with Low Global Efficiencies. , *707*(2), 1023–1033.

Velázquez, P. F., Raga, A. C., Cantó, J., Schneiter, E. M., & Riera, A. (2013). A ballistic model for a precessing and orbiting jet with a time-dependent ejection velocity. , *428*(2), 1587–1593.

Velázquez, P. F., Riera, A., Raga, A. C., & Toledo-Roy, J. C. (2014). An Asymmetric Jet-launching Model for the Protoplanetary Nebula CRL 618. , *794*(2), 128.

Viti, S., Natarajan, S., & Williams, D. A. (2002). Enhanced molecular abundances in low-mass star-forming cores. , *336*(3), 797–802.

Wakelam, V., Herbst, E., Loison, J. C., Smith, I. W. M., Chandrasekaran, V., Pavone, B., Adams, N. G., Bacchus-Montabonel, M. C., Bergeat, A., Béroff, K., Bierbaum, V. M., Chabot, M., Dalgarno, A., van Dishoeck, E. F., Faure, A., Geppert, W. D., Gerlich, D., Galli, D., Hébrard, E., Hersant, F., Hickson, K. M., Honvault, P., Klippenstein, S. J., Le Picard, S., Nyman, G., Pernot, P., Schlemmer, S., Selsis, F., Sims, I. R., Talbi, D., Tennyson, J., Troe, J., Wester, R., & Wiesenfeld, L. (2012). A KInetic Database for Astrochemistry (KIDA). , *199*(1), 21.

Walmsley, C. (1989). Dust and the Gas Phase Composition of Dense Clouds. In L. J. Allamandola, & A. G. G. M. Tielens (Eds.) *Interstellar Dust*, vol. 135, (p. 263).

Walsh, C., Loomis, R. A., Öberg, K. I., Kama, M., van 't Hoff, M. L. R., Millar, T. J., Aikawa, Y., Herbst, E., Widicus Weaver, S. L., & Nomura, H. (2016). First Detection of Gas-phase Methanol in a Protoplanetary Disk. , *823*(1), L10.

Ward-Thompson, D., Scott, P. F., Hills, R. E., & Andre, P. (1994). A Submillimetre Continuum Survey of Pre Protostellar Cores. , *268*, 276.

Watanabe, N., & Kouchi, A. (2002). Efficient Formation of Formaldehyde and Methanol by the Addition of Hydrogen Atoms to CO in H_2O-CO Ice at 10 K. , *571*(2), L173–L176.

Watanabe, N., Shiraki, T., & Kouchi, A. (2004). Formation mechanism of formaldehyde and methanol by the addition of hydrogen atoms to CO on amorphous icy grains. *Astronomical Herald*, *97*(2), 101–106.

Wilkin, F. P. (1996). Exact Analytic Solutions for Stellar Wind Bow Shocks. , *459*, L31.

Wilson, R. W., Jefferts, K. B., & Penzias, A. A. (1970). Carbon Monoxide in the Orion Nebula. , *161*, L43.

Wilson, T. L., Rohlfs, K., & Hüttemeister, S. (2009). *Tools of Radio Astronomy*.

Winnewisser, G., & Kramer, C. (1999). Spectroscopy Between the Stars. , *90*, 181–202.

Wouterloot, J. G. A., & Walmsley, C. M. (1986). H_2O masers associated with IRAS sources in regions of star formation. , *168*, 237–247.

Yang, B., Stancil, P. C., Balakrishnan, N., & Forrey, R. C. (2010). Rotational Quenching of CO due to H_2 Collisions. , *718*(2), 1062–1069.

Young, K. E., Lee, J.-E., Evans, I., Neal J., Goldsmith, P. F., & Doty, S. D. (2004). Probing Pre-Protostellar Cores with Formaldehyde. , *614*(1), 252–266.

Yu, Z.-Y., Nagahama, T., & Fukui, Y. (1996). The New Observation of C 18O(J=1–0) Molecular Emission in the Cepheus OB3 Molecular Cloud. , *471*, 867.

Zinnecker, H., & Yorke, H. W. (2007). Toward Understanding Massive Star Formation. , *45*(1), 481–563.

Zuckerman, B., Kuiper, T. B. H., & Rodriguez Kuiper, E. N. (1976). High-velocity gas in the Orion infrared nebula. , *209*, L137–L142.

Appendix A

Beam dilution factor

In order to estimate the physical conditions and abundances of molecular species, it is necessary to retrieve the intrinsic brightness distribution of an astrophysical source $T_B(\Omega)$ from the intensity distribution observed by the telescope $T_A(\Omega)$, corrected for atmospheric extinction. The distributions of $T_B(\Omega)$ and $T_A(\Omega)$ are linked by the relation bellow which expresses that the first is the convolution product of the astrophysical brightness distribution $T_B(\Omega)$ with the response of the antenna B:

$$T_A(\Omega_0) = \frac{1}{\int_{4\pi} B(\Omega)d\Omega} \int B(\Omega_0 - \Omega) \cdot T_B(\Omega)d\Omega = \frac{1}{\Omega_A} \int B(\Omega_0 - \Omega) \cdot T_B(\Omega)d\Omega \tag{A.1}$$

with Ω_A the response of the telescope within 4π sr.

When the size of the astrophysical source is small, in practice, up to a few times the size of the main lobe of the telescope, it is possible to consider that the flux collected by the antenna comes from mainly from the main lobe. The Main-Beam temperature T_{MB} is thus defined by the relation:

$$T_{MB} = \frac{\Omega_A}{\Omega_{MB}} T_A, \tag{A.2}$$

which can be rewritten using the definition of main beam efficiency $\eta_{MB} = \Omega_{MB}/\Omega_A$, being Ω_{MB} defined by:

$$\Omega_{MB} = \int_{MainLobe} B()d\Omega. \tag{A.3}$$

Therefore, substituting the equations above in equation A.2, one obtains:

$$T_{MB} = \frac{1}{\Omega_{MB}} \int B(\Omega_0 - \Omega)T_B(\Omega)d\Omega. \tag{A.4}$$

The main lobe profile is described through a Gaussian (see Chapter 3) through the relation:

$$B(\theta) = e^{-\frac{\theta^2}{\sigma_b}}, \tag{A.5}$$

while the *Half Power Beam Width* (HPBW, see Chapter 3):

$$\text{HPBW} = 2\sigma_b\sqrt{\ln(2)}, \tag{A.6}$$

related to the main-beam solid angle by:

$$\Omega_{MB} = \int B(\Omega)d\Omega = \pi\sigma_b^2. \tag{A.7}$$

Finally, it is possible to obtain the relation between the main-beam solid angle and the HPBW:

$$\Omega_{MB} = \frac{\pi}{4\ln(2)}\mathrm{HPBW}^2 \tag{A.8}$$

A.1 Gaussian source

Considering an antenna pointing in the direction Ω_0 towards a source of brightness distribution that follows a Gaussian profile:

$$S(x,y) = T_{Peak}\cdot e^{-(x^2+y^2/\sigma_s)}, \tag{A.9}$$

with a *Full Width at Half Maximum* (FWHM, see chapter 3) defined by:

$$\mathrm{FWHM} = 2\sigma_s\sqrt{\ln(2)}. \tag{A.10}$$

Therefore, the intensity received in the antenna is:

$$T_{MB} = \frac{1}{\Omega_{MB}}\int S(\Omega)(\Omega_0-\Omega)d\Omega. \tag{A.11}$$

The main-beam temperature can be expressed in Cartesian coordinates on the sky (x_0,y_0) as:

$$T_{MB}(x_0,y_0) = \frac{T_s}{\Omega_{MB}}\int_{-\infty}^{\infty} exp\left[-\left(\frac{x^2}{\sigma_b^2}+\frac{(x-x_0)^2}{\sigma_s^2}\right)\right]dx\int_{-\infty}^{\infty} exp\left[-\left(\frac{y^2}{\sigma_b^2}+\frac{(y-y_0)^2}{\sigma_s^2}\right)\right]dy \tag{A.12}$$

The integrals can be solved individually so let's focus in the first one, starting by expanding the equation:

$$\begin{aligned}\int_{\infty}^{\infty} exp\left[-\left(\frac{x^2}{\sigma_b^2}+\frac{(x-x_0)^2}{\sigma_s^2}\right)\right]dx &= \int_{-\infty}^{\infty} exp\left[-\left(\frac{x^2}{\sigma_b^2}+\frac{x^2+x_0^2-2xx_0}{\sigma_s^2}\right)\right]dx\\ &= \int_{-\infty}^{\infty} exp\left[-x^2\left(\frac{1}{\sigma_b^2}+\frac{1}{\sigma_s^2}\right)-\frac{2xx_0}{\sigma_s^2}+\frac{x_0^2}{\sigma_s^2}\right]dx, \end{aligned}\tag{A.13}$$

the trick here is the relation $\alpha^2 = \frac{\sigma_b^2\cdot\sigma_s^2}{\sigma_s^2+\sigma_b^2}$. Substituting α in the equation above:

$$\int_{-\infty}^{\infty} exp\left[-\frac{1}{\alpha^2}\left(x^2-2\alpha^2\frac{xx_0}{\sigma_s^2}\right)-\frac{x_0^2}{\sigma_s^2}\right]dx = e^{-\frac{x_0^2}{\sigma_s^2}}\int_{-\infty}^{\infty} exp\left[-\frac{1}{\alpha^2}\left(x^2-2\alpha^2\frac{xx_0}{\sigma_s^2}\right)\right]dx \tag{A.14}$$

To integrate this equation, first let's apply the following relation:

$$\left(x^2-2\alpha^2\frac{xx_0}{\sigma_s^2}\right)+\left(\frac{\alpha^2x_0}{\sigma_s^2}\right)^2 = \left(x-\frac{\alpha^2x_0}{\sigma_s^2}\right)^2 \tag{A.15}$$

substituting this relation:

$$
\begin{aligned}
& e^{-\frac{x_0^2}{\sigma_s^2}} \int_{-\infty}^{\infty} exp\left[-\frac{1}{\alpha^2}\left(x - \frac{\alpha^2 x_0}{\sigma_s} \right)^2 - \frac{\alpha^4 x_0^2}{\sigma_s^4} \right] dx \\
&= e^{-\frac{x_0^2+\alpha^4 x_0^2}{\sigma_s^4}} \int_{-\infty}^{\infty} exp\left[-\frac{1}{\alpha^2}\left(x - \frac{\alpha^2 x_0}{\sigma_s} \right)^2 \right] dx \\
&= exp\left[\frac{x_0^2}{\sigma_s^2}\left(\frac{\alpha^2}{\sigma_s^2} - 1 \right) \right] \int_{-\infty}^{\infty} e^{-u/\alpha^2} du \qquad \text{(A.16)}
\end{aligned}
$$

where $u = (x - \frac{\alpha^2 x_0}{\sigma_s})$ and $du = dx$. Therefore, the integral is:

$$
exp\left[\frac{x_0^2}{\sigma_s^2}\left(\frac{\alpha^2}{\sigma_s^2} - 1 \right) \right] \int_{-\infty}^{\infty} e^{-u/\alpha^2} du = \alpha\sqrt{\pi} \cdot exp\left[\frac{-x_0^2}{\sigma_s^2} + \sigma_b^2 \right] \qquad \text{(A.17)}
$$

The solution for x in equation A.12 was achieved and for y is exactly the same including the change in variables. It is therefore possible to rewrite equation A.12:

$$
T_{MB} = \alpha^2 \pi \frac{T_s}{\Omega_{MB}} exp\left[-\frac{(x_0^2 + y_0^2)}{\sigma_s^2 + \sigma_b^2} \right]. \qquad \text{(A.18)}
$$

Applying the definition of FWHM (equation A.2) and HPBW and its relation with Ω_{MB}:

$$
\begin{aligned}
\mathrm{HPBW} &= 2\sigma_b \sqrt{\ln(2)} \qquad \text{(A.19)} \\
\Omega_{MB} &= \frac{\pi}{4\ln(2)} \mathrm{HPBW}^2, \qquad \text{(A.20)}
\end{aligned}
$$

substituting these equations above in equation A.18:

$$
T_{MB} = \frac{T_s \pi}{\frac{\pi \mathrm{HPBW}}{4\ln(2)}} \frac{\sigma_s^2 \sigma_b^2}{(\sigma_s^2 + \sigma_b^2)} exp\left[-\frac{(x_0^2 + y_0^2)}{(\sigma_s^2 + \sigma_b^2)} \right], \qquad \text{(A.21)}
$$

and then,

$$
\boxed{T_{MB} = T_s \frac{\mathrm{FWHM}^2}{\mathrm{FWHM}^2 + \mathrm{HPBW}^2} exp\left[-\frac{(x_0^2 + y_0^2)}{(\sigma_s^2 + \sigma_b^2)} \right],} \qquad \text{(A.22)}
$$

where $\frac{\mathrm{FWHM}^2}{\mathrm{FWHM}^2 + \mathrm{HPBW}^2}$ is the so called filling factor. The Gaussian brightness distribution is the one of the few analytic solutions for the beam dilution. Therefore, we have decided to apply this factor for the beam dilution of the interferometer throughout this thesis work, the results are presented in chapters 5 and 6.

Appendix B

Article as a co-author

B.1 Contributions: HCN/HNC chemistry in L1157-B1

MNRAS **000**, 1–?? (2021) Preprint 23 July 2021 Compiled using MNRAS LaTeX style file v3.0

HCN/HNC chemistry in shocks: a study of L1157-B1 with ASAI

B. Lefloch[1], G. Busquet[1,2,3], S. Viti[4,5], C. Vastel[6], E. Mendoza[7], M. Benedettini[8], C. Codella[9,1], L. Podio [9], A. Schutzer[1], P.R. Rivera-Ortiz[1], J.R.D. Lépine[7], R. Bachiller[10]

[1] *Univ. Grenoble Alpes, CNRS, IPAG, F-38000 Grenoble, France*
[2] *Institut de Ciències de l'Espai (ICE, CSIC), Can Magrans, s/n, 08193 Cerdanyola del Vallès, Catalonia, Spain*
[3] *Institut d'Estudis Espacials de Catalunya (IEEC), 08034 Barcelona, Catalonia, Spain*
[4] *Leiden Observatory, Leiden University, PO Box 9513, NL-2300 RA Leiden, the Netherlands*
[5] *Department of Physics and Astronomy, University College London, Gower Street, London, WC1E 6BT, England*
[6] *IRAP, Université de Toulouse, CNRS, UPS, CNES, 31400 Toulouse, France*
[7] *Instituto de Astronomia, Geofísica e Ciências Atmosféricas, Universidade de São Paulo, São Paulo 05508-090, SP, Brazil*
[8] *INAF, Istituto di Astrofisica e Planetologia Spaziali, via Fosso del Cavaliere 100, 00133 Roma, Italy*
[9] *INAF, Osservatorio Astrofisico di Arcetri, Largo Enrico Fermi 5, I-50125 Firenze, Italy*
[10] *IGN, Observatorio Astronómico Nacional, Calle Alfonso XII, 3 E-28004 Madrid, Spain*

Accepted 2021 July 13. Received 2021 June 14; in original form 2021 April 14.

ABSTRACT

HCN and its isomer HNC play an important role in molecular cloud chemistry and the formation of more complex molecules. We investigate here the impact of protostellar shocks on the HCN and HNC abundances from high-sensitivity IRAM 30m observations of the prototypical shock region L1157-B1 and the envelope of the associated Class 0 protostar, as a proxy for the pre-shock gas. The isotopologues $H^{12}CN$, $HN^{12}C$, $H^{13}CN$, $HN^{13}C$, $HC^{15}N$, $H^{15}NC$, DCN and DNC were all detected towards both regions. Abundances and excitation conditions were obtained from radiative transfer analysis of molecular line emission under the assumption of Local Thermodynamical Equilibrium. In the pre-shock gas, the abundances of the HCN and HNC isotopologues are similar to those encountered in dark clouds, with a HCN/HNC abundance ratio ≈ 1 for all isotopologues. A strong D-enrichment (D/H≈ 0.06) is measured in the pre-shock gas. There is no evidence of ^{15}N fractionation neither in the quiescent nor in the shocked gas. At the passage of the shock, the HCN and HNC abundances increase in the gas phase in different manners so that the HCN/HNC relative abundance ratio increases by a factor 20. The gas-grain chemical and shock model UCLCHEM allows us to reproduce the observed trends for a C-type shock with pre-shock density $n(\mathrm{H}) = 10^5\,\mathrm{cm}^{-3}$ and shock velocity $V_s = 40\,\mathrm{km\,s^{-1}}$. We conclude that the HCN/HNC variations across the shock are mainly caused by the sputtering of the grain mantle material in relation with the history of the grain ices.

Key words: astrochemistry – methods: observational – ISM: jets and outflow – ISM: molecules – ISM: abundances

1 INTRODUCTION

Hydrogen cyanide (HCN) is one of the most simple interstellar molecules. Thanks to its large dipole moment (2.99 Debye; Bhattacharya & Gordy 1960), its rotation transitions are good probe of dense molecular gas in Galactic and extragalactic environments. HCN and its isomer hydrogen isocyanide HNC are thought to play an important role in the formation of more complex molecules, like cyanopolyynes $HC_{2n+1}N$, either in dark cloud cores (Suzuki et al. 1992) or in more energetic regions, like protostellar shocks (Mendoza et al. 2018). Since HCN and HNC have similar energy spectra and dipole moments, their differences in spatial distribution is mainly related to the gas chemical conditions. For this reason, they have often been used as probes of gas chemical evolution in both dense cores and star-forming regions (Schilke et al. 1992; Ungerechts et al. 1997; Daniel et al. 2013).

Many systematic studies of dark clouds and low-mass protostellar cores have shown the HNC/HCN ratio to be close to unity (see e.g., Irvine & Schloerb 1984; Hirota et al. 1998; Hily-Blant et al. 2010). No difference is observed between the values measured in prestellar and protostellar cores, implying that the evaporation of HCN and HNC from dust grains does not contribute significantly to the observed emission in the cold envelope. On the contrary, towards the high-mass star forming region OMC-1 in Orion, the HNC/HCN ratio displays strong variations with especially low values ≈ 0.01 towards the hot core regions while it is of the order of 0.2 in adjacent ridge positions. While the abundance of HCN is similar to that of dark cloud cores, the HNC abundance is 2 orders of magnitude lower in the high-temperature gas of the hot core (Schilke et al. 1992). A somewhat similar behaviour is observed towards IRAS16293−2422 when looking at the high-excitation lines of HCN and HNC (van Dishoeck et al. 1995). Recently, Hacar et al. (2020) demonstrated the high sensitivity of the HCN/HNC J=1–0 line intensity ratio to the gas kinetic temperature.

In his pioneering work on outflow shock chemistry Bachiller & Pérez-Gutiérrez (1997) brought the first hints of HCN abundance enhancement in protostellar shock region. At that time, only a low number of molecular transitions was observed with the IRAM 30m telescope, hence preventing an accurate determination of the excitation conditions and molecular abundances. From a theoretical point of view, both the dependence of the HCN/HNC ratio to the temperature and the sputtering of dust grains are two processes which could *a priori* alter molecular gas abundances of HCN and HNC across a shock.

Many subsequent observational studies on the physical and chemical characterization of L1157-B1 have been carried out both with (sub)millimeter single-dish and interferometers, which led to a rather detailed, consistent picture of the outflow shock while unveiling its chemical richness (see e.g. Codella et al. (2010, 2017); Viti et al. (2011); Lefloch et al. (2012, 2016, 2017); Busquet et al. (2014); Mendoza et al. (2014, 2018); Podio et al. (2014, 2016, 2017); Gómez-Ruiz et al. (2015)). The spatial distribution of the HCN emission in the L1157 southern outflow lobe was obtained at ≈ 5″ scale for the first time by Benedettini et al. (2007) with the IRAM Plateau de Bure interferometer. The emission of the rare ^{13}C, D and ^{15}N isotopologues was investigated a few years later at a few arcsec resolution with the IRAM NOEMA interferometer (Busquet et al. 2017; Benedettini et al. 2021). In particular, the distribution of DCN was shown to result from a combination of gas-phase chemistry that produces the widespread DCN emission, dominating especially in the head of the bow-shock, and sputtering from grain mantles toward the jet impact region.

These results incited us to revisit the emission of the HCN and HNC isotopologues in L1157-B1 in a more comprehensive and accurate way than was possible before. This study benefits from the unbiased and high-sensitivity millimeter spectral line survey of the shock region carried out as part of the IRAM 30m Large Program ASAI ("Astrochemical Surveys At IRAM", Lefloch et al. (2018)). In order to better understand and constrain more precisely the impact of the shock on the chemistry of HCN and HNC, we have also investigated the properties of their isotopologue emission in the envelope of the Class 0 protostar L1157-mm, at about 1 arcmin away, which we took as a proxy of the initial gas composition before the arrival of the shock. The origin of the molecular emission was then derived from comparison of our observational results with the predictions of the time-dependent gas-grain chemical and shock model UCLCHEM (Holdship et al. 2017).

The paper has been organized as follows. In Sect. 2, we summarize the main observational properties of the shock region L1157-B1. The observations are described in Sect. 3. In Sect. 4, we present our results on the HCN spatial distribution in the region and the gas properties (excitation temperature, column density, abundance) obtained for the HCN and HNC isotopologues based on a simple radiative transfer analysis of the line emission. We discuss in Section 5 the behaviour of HCN and HNC across the shock and we analyse the origin of the molecular emission from comparison with the results of our modelling. Finally, we present our conclusions in Sect. 6.

2 THE SOURCE

The GAIA mission has led to a revision of the distance to L1157 by several groups Dzib et al. (2018) and **?**, who found (360 ± 32) pc and (340 ± 21) pc, respectively. In this work, we will adopt the value of (352 ± 19) pc derived by Zucker et al. (2019), in agreement with Benedettini et al. (2021). Gueth, Guilloteau, & Bachiller (1996, 1998) have studied at high-angular resolution (≈ 3″) the structure and dynamics of the southern lobe of the outflow driven by the protostar L1157-mm from the emission of the CO J=1–0 and SiO J=2–1 lines observed with the IRAM Plateau de Bure interferometer. These authors showed that the southern lobe of this molecular outflow consists of two cavities, likely created by the propagation of large bow shocks due to episodic events in a precessing, highly collimated, high-velocity jet. This jet was detected by Tafalla et al. (2015) and imaged by Podio et al. (2016). Based on higher-angular and high-sensitivity CO observations with NOEMA at 0.3″, Podio et al. (2016) refined the jet precession modelling by Gueth, Guilloteau, & Bachiller (1996) and estimated an age of ≈ 1500 yr for B1 (and 2500 yr for B2), adopting the new distance of 352 pc. Located at the apex of the more recent cavity, the bright bow shock region B1 displays a peculiar molecular complexity (e.g., Codella et al. 2010; Benedettini et al. 2012), which makes it a benchmark for magnetized shock models (e.g., Gusdorf et al. 2008a,b; Viti et al. 2011). Multi-transition analysis of the emission of tracers such as CO (Lefloch et al. 2010, 2012), H_2O (Busquet et al. 2014) and CS (Gómez-Ruiz et al. 2015) has allowed to elucidate a coherent scenario where the molecular emission appears to arise from four physically distinct components, with specific excitation conditions:

- Component g_1: Lefloch et al. (2012) and Benedettini et al. (2012) evidenced a region of high excitation of ≈ 10″ size, with a kinetic temperature $T_{\rm kin} \approx 200$ K and gas density $n(\rm H_2) \simeq 10^6$ cm^{-3}. This region is associated with the impact of the jet against the L1157-B1 bow shock.
- Component g_2 is tracing the outflow cavity associated with L1157-B1, for which a kinetic temperature $T_{\rm kin} \approx 60$ K and a gas density $n(\rm H_2) \simeq (1\text{–}10)\times10^5$ cm^{-3} were estimated.
- Component g_3 is tracing the late outflow cavity associated with L1157-B2, for which have been estimated $T_{\rm kin} \approx$ 20 K and $n(\rm H_2) \simeq 10^5$ cm^{-3}
- A hot ($T_{\rm kin} \simeq 1000$ K) and tenuous gas component ($n(\rm H_2) \simeq 10^3 - 10^4$ cm^{-3}) with a size of 2″ -

3 OBSERVATIONS

3.1 ASAI

Observations of L1157-B1 and L1157-mm were carried out during several runs between September 2012 and March 2015 as part of the Large Program ASAI (Lefloch et al. 2018). The source nominal positions are $\alpha_{J2000} = 20^{\rm h}\ 39^{\rm m}\ 10.^{\rm s}2$ $\delta_{J2000} = +68^\circ\ 01'\ 10''$ for L1157-B1 and $\alpha_{J2000} = 20^{\rm h}\ 39^{\rm m}\ 06.^{\rm s}3$ $\delta_{J2000} = +68^\circ\ 02'\ 15.8''$ for L1157-mm. We made use of the broad-band EMIR receivers connected to Fast Fourier Transform Spectrometers in the 200 kHz spectral resolution mode.

Detailed information on the observation and the data reduction procedures can be found in Lefloch et al. (2018).

The ASAI observations were carried out using the "Wobbler Switching" (WSW) mode with a throw of 3′.

3.2 On-The-Fly mapping

The ASAI dataset was complemented with a fully sampled map of the HCN $J=$ 3–2 transition in the southern lobe of the L1157 outflow with the IRAM 30m telescope in December 2013. The size of the map, $2' \times 2.5'$, is large enough to encompass the whole southern lobe. Observations were carried out with the receiver E230 and the FTS spectrometer in its 192 kHz resolution mode, using the On-The-Fly mode. We chose a reference position offset by 10′ in right ascension from L1157-B1, and checked to be free of emission in the HCN J=3–2 line. Atmospheric calibrations were performed every 15 min and showed the weather to be stable, with 2.5 – 3.0 mm of precipitable water vapour, and system temperatures in the range 450 – 550 K. Pointing was monitored every hour and corrections were always found lower than 3″.

3.3 Data reduction

The data reduction was performed using the GILDAS/CLASS software[1]. We have detected several transitions of HCN, HNC, and their rare ^{13}C-, D- , ^{15}N-isotopologues, between 72 and 272 GHz, towards the shock region L1157-B1 and the protostar L1157-mm. The line spectra are presented in Figs. 2–5. The resolution of the spectrometer allowed us to resolve the hyperfine structure of the rotational transitions of HCN, H^{13}CN and DCN. The location of the hyperfine components are indicated by red arrows in the spectra. The line intensities are expressed in units of antenna temperature corrected for atmospheric attenuation and rearward losses (T_A^*).

For subsequent analysis and radiative transfer modelling, fluxes were expressed in main beam temperature units ($T_{\rm mb}$). The telescope and receiver parameters (beam efficiency, $B_{\rm eff}$; forward efficiency, $F_{\rm eff}$; Half Power beam Width, HPBW) were taken from the IRAM webpage[2]. The calibration uncertainties are typically 10, 15, 20% at 3 mm, 2 mm, 1.3 mm, respectively.

The spectroscopic properties and the observational parameters of all the detected transitions are summarized in Tables 1–2, for L1157-B1 and L1157-mm, respectively. We extracted the observational properties of the line profiles (velocity-integrated flux, Full Width at Half Maximum, emission peak velocity) performing a simple gaussian fitting using CLASS whenever possible. The only exceptions concern HCN and H^{13}CN in L1157-B1, where the presence of several components prevents from disentangling the emission of the hyperfine satellites. In that case, the total flux (in T_A^* km s^{-1}) was obtained from integrating over the whole velocity range of emission.

4 RESULTS

4.1 Spatial distribution

In Fig. 1, we show in white contours the spatial distribution of the HCN J=3–2 velocity-integrated emission between −20 and +5 km s^{-1} over the southern outflow lobe. The emission draws two extended features of different Parallatic Angles, which coincide with the two CO outflow cavities identified by Gueth, Guilloteau, & Bachiller (1996). The emission peaks at the nominal position of the outflow shock position B1. Secondary emission peaks are found towards the shock positions B0 and B2, at about 30″ north and south of B1, respectively (Bachiller et al. 2001). Hardly any emission is detected along the outflow between B0 and the protostar (located North, red cross in Fig. 1). The systemic velocity of L1157 is +2.7 km s^{-1} (Bachiller & Pérez-Gutiérrez 1997). We show in color scale in Fig. 1 the HCN J=3–2 emission integrated over the three velocity intervals (in km s^{-1}): [−10.2; −2.7], [−2.7; +4.3] and [+4.3; +6.3], from left to right. We find that the low-velocity emission (middle panel in Fig. 1) is associated with the bright shocked regions B0, B1, and B2, as well as faint and extended emission tracing the whole outflow lobe. As shown by Podio et al. (2016), the outflow is oriented almost in the plane of the sky (inclination $i \sim 73°$). We propose that the HCN emission between −2.7 and +4.3 km s^{-1} could arise from low-velocity shocks associated with the cavity walls of the outflow, which would explain the extended emission at blue- and red-shifted velocities. This is consistent with the distribution of the HCN J=1–0 emission line as mapped by Benedettini et al. (2007) at ≈ 5″ with the Plateau de Bure Interferometer. The high-velocity blueshifted gas traces the young shocks B0 and B1 (left panel in Fig. 1), while the redshifted emission is only detected toward the oldest B2 shock (right panel). These maps indicate that the shocked gas in B0 and B1 emit at a velocity distinct from that of B2. Interestingly, the brightest HCN J=3–2 emission coincides with the apex of the outflow cavities, consistent with the high angular resolution NOEMA images of H^{13}CN and HC^{15}N (Busquet et al. 2017; Benedettini et al. 2021).

To summarize, HCN emission is detected throughout most of the southern outflow lobe, from B0 to the tip of the outflow at position B2, and the brightest emission regions are associated with outflow shocks. This is consistent with the distribution of the HCN J=1–0 emission line as mapped by Benedettini et al. (2007) at ≈ 5″ with the Plateau de Bure Interferometer.

4.2 L1157-B1

All the transitions of the HCN isotopologues and most of the transitions of the HNC isotopologues present in the spectral range of ASAI, between 72 and 272 GHz, were detected towards the shock region (see Table 1). Due to instrumental (spectral bandwidth) and observational (rms noise) limitations, only the ground state transitions of HN^{13}C and H^{15}NC were detected with a SNR > 3. The profiles of the transitions display broad linewidths (up to ≈ 10 km s^{-1}). All the line profiles peak at $V_{lsr} \approx 0$ km s^{-1} and trace blueshifted gas, in agreement with the other molecular tracers reported in previous works (Lefloch et al. 2012; Codella et al. 2012; Gómez-Ruiz et al. 2015).

---

[1] https://www.iram.fr/IRAMFR/GILDAS/

[2] http://publicwiki.iram.es/Iram30mEfficiencies/

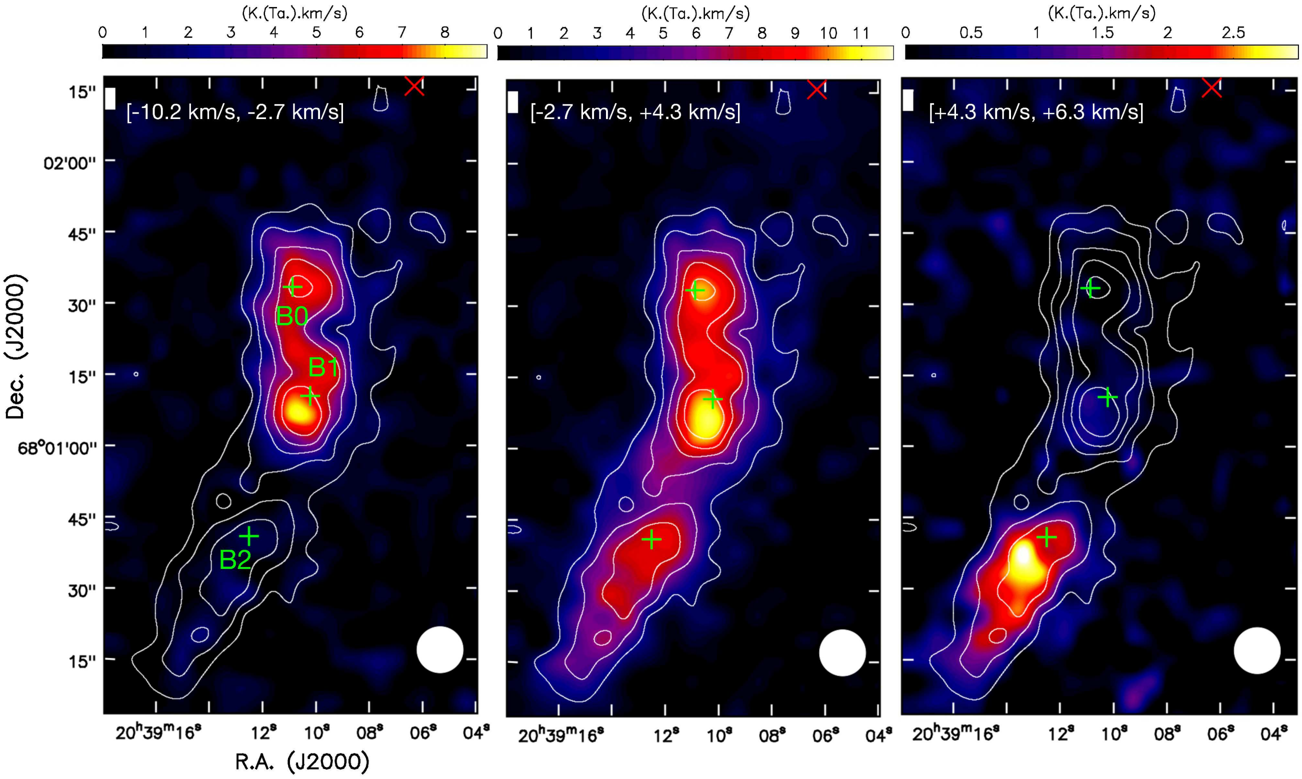

Figure 1. HCN J=3–2 velocity-integrated emission in the southern lobe of the L1157 outflow. The emission is integrated over the velocity range indicated in each panel (colour scale) to illustrate the separation of the emitting gas into the B0 and B1 shocks and the B2 shock. The emission in the central panel between -2.7 and $+4.3\,\mathrm{km\,s^{-1}}$ encompasses the emission from the ambient gas at $V_{lsr}= +2.7\,\mathrm{km\,s^{-1}}$. White contours represent the total velocity-integrated emission of the HCN J=3–2 line. Contour levels range from 3σ to 15σ in steps of of 3σ, where $\sigma = 1.07$ K km s^{-1} is the rms noise of the map. In each panel, green crosses mark the nominal position of shocks B0, B1, and B2; a red cross marks the nominal position of protostar L1157-mm (Gueth et al. 1997). The size (HPBW) of the telescope main beam is draw by the white circle in the bottom right corner of each panel.

Table 1. Spectroscopic and observational parameters of the transitions of the HCN and HNC and their rare D, ^{13}C and ^{15}N isotopologues detected towards the protostellar shock L1157-B1. Note that the flux uncertainties reported here contain only the statistical rms noise. TAG is a 5-digit code which indicates the spectroscopic database used for CASSIS line identification and modelling.

Species	TAG	Transition	Frequency MHz	E_u K	A_{ul} 10^{-5} s^{-1}	HPBW ″	η_{mb}	$\int T_A^* dv$ K km s^{-1}	FWHM km s^{-1}	V_{lsr} km s^{-1}
HCN	27501	1 – 0	88631.602	4.3	2.4	27.8	0.85	31.2(1.5)	4 .7(1)	-0.2(1.0)
		3 – 2	265886.434	25.5	83.6	9.3	0.59	29.9(1.0)	9.5(2)	-1.3(.7)
DCN	28509	1 – 0	72414.905	3.5	1.33	34.0	0.86	0.12(.03)	7.9(.5)	-0.2 (.1)
		2 – 1	144828.001	10.4	12.7	17.0	0.79	0.19(.01)	7.0(.3)	-0.3(.2)
		3 – 2	217238.538	20.9	46.0	11.3	0.65	0.10(.01)	6.5(.6)	-0.1(.3)
H^{13}CN	28501	1 – 0	86340.184	4.1	2.23	28.5	0.85	1.76(.03)	4.8(1)	-0.4(.2)
		2 – 1	172677.851	12.4	21.4	14.3	0.75	1.20(.01)	7.2(4)	-0.3 (1)
		3 – 2	259011.798	24.9	77.3	9.5	0.60	0.73(.02)	6.2(1)	-0.34(.3)
HC^{15}N	28506	1 – 0	86054.961	4.1	2.2	28.6	0.86	0.35(.01)	6.1(.1)	-1.0(.1)
		2 – 1	172107.956	12.4	21.1	14.3	0.75	0.27(.01)	5.6(.6)	-0.3(.3)
		3 – 2	258157.100	24.8	76.5	9.5	0.60	0.13(.01)	6.2(.7)	-0.1(.3)
HNC	27502	1 – 0	90663.568	4.4	2.69	27.1	0.85	4.26(.02)	4.5 (1)	0.3(.1)
		3 – 2	271981.142	26.1	93.4	9.0	0.58	2.36(.04)	3.7(1)	1.5(.3)
DNC	28508	1 – 0	76305.701	3.7	1.60	32.2	0.86	0.010(.004)	1.4(.6)	0.3(.3)
		2 – 1	152609.746	11.0	15.4	16.1	0.77	0.04(.02)	1.7(.6)	0.6(.4)
		3 – 2	228910.481	22.0	55.7	10.7	0.64	0.012(.003)	2.7(.7)	2.1(.3)
HN^{13}C	28515	1 – 0	87090.825	4.2	2.38	28.3	0.85	0.093(.005)	5.2(.3)	0.8(1)
H^{15}NC	28006	1 – 0	88865.715	4.3	2.53	27.8	0.85	0.025(.008)	3.4(.3)	1.8(.1)

Table 2. Spectroscopic properties and observational parameters of the transitions of the HCN and HNC and their rare D, ^{13}C and ^{15}N isotopologues detected towards the protostar L1157-mm. Note that the flux uncertainties reported here contain only the statistical rms noise. TAG is a 5-digit code which indicates the spectroscopic database used for CASSIS line identification and modelling.

Species	TAG	Transition	Frequency MHz	E_u K	A_{ul} 10^{-5} s^{-1}	HPBW ″	η_{mb}	$\int T_A^* dv$ K km s^{-1}	FWHM km s^{-1}	V_{lsr} km s^{-1}
HCN	27501	1 – 0	88631.602	4.3	2.4	27.8	0.85	3.40(.01)	1.4(.1)	2.2 (.1)
		3 – 2	265886.434	25.5	83.6	9.3	0.59	1.86(.20)	0.8(.1)	2.2 (.1)
DCN	28509	1 – 0	72414.905	3.5	1.3	34.0	0.86	0.49(.02)	1.5(.2)	2.4(.1)
		2 – 1	144828.001	10.4	12.7	17.0	0.79	0.32(.01)	1.0(.1)	2.5(.1)
		3 – 2	217238.538	20.9	46.0	11.3	0.65	0.10(.01)	0.96(.04)	2.8(.1)
H^{13}CN	28501	1 – 0	86340.184	4.1	2.2	28.5	0.85	0.27 (.02)	1.3(.1)	2.7(.1)
		2 – 1	172677.851	12.4	21.4	14.3	0.75	0.10(.02)	1.4(.3)	2.4(.1)
		3 – 2	259011.798	24.9	77.3	9.5	0.60	0.08(.01)	1.3(.1)	2.7(.1)
HC^{15}N	28506	1 – 0	86054.961	4.1	2.2	28.6	0.86	0.09(.02)	1.5(.2)	2.6(.1)
		2 – 1	172107.956	12.4	21.1	14.3	0.75	0.06(.01)	1.8(.4)	2.0(.2)
		3 – 2	258157.100	24.8	76.5	9.5	0.60	0.04(.01)	1.5(.2)	2.6(.1)
HNC	27502	1 – 0	90663.568	4.4	2.7	27.1	0.85	3.1(.1)	1.8(.1)	2.4(.1)
		3 – 2	271981.142	26.1	93.4	9.0	0.58	1.3(.1)	0.99(.1)	2.5(.1)
DNC	28508	1 – 0	76305.701	3.7	1.60	32.2	0.86	0.90(.01)	1.7(.1)	2.7(.1)
		2 – 1	152609.746	11.0	15.4	16.1	0.77	0.69(.01)	1.0(.1)	2.6(.1)
		3 – 2	228910.489	22.0	55.7	10.7	0.64	0.26(.01)	0.8(.1)	2.7(.1)
HN^{13}C	28515	1 – 0	87090.825	4.2	2.4	28.3	0.85	0.29(.01)	1.4(.1)	2.4 (.1)
		3 – 2	261263.310	25.1	82.8	9.4	0.60	0.079(.004)	0.8(.1)	2.3(.1)
H^{15}NC	28006	1 – 0	88865.715	4.3	2.5	27.8	0.85	0.063(.004)	1.4(.1)	2.7(.1)
		3 – 2	266587.800	25.6	87.9	9.2	0.59	0.026(.005)	1.5(.4)	2.9(.2)

The excellent rms of the data permits detection of emission up to $V_{\rm LSR} \approx -20$ km s^{-1} in the different transitions of HCN. Several transitions of DCN, H^{13}CN and HC^{15}N were also detected towards L1157-B1 and their profiles display similar broad linewidths, confirming the shock association (Fig. 2). The detection of bright deuterated emission suggests that despite shock processing, the gas has preserved part of the initial chemical conditions, an effect already pointed out by Codella et al. (2012) and Fontani et al. (2014), who reported the detection of singly deuterated isotopologues of H$_2$CO, CH$_3$OH, NH$_3$. A small systematic velocity shift (less than 0.5 km s^{-1}) is measured between the emission peaks of the HCN and HNC line profiles, suggesting they are tracing different regions inside the shock.

We note that the HNC isotopologues (HN^{12}C, HN^{13}C, H^{15}NC) display much weaker lines intensities than the HCN isotopologues. Line intensities and fluxes of the ground state transitions are weaker by one order of magnitude. There is however one exception, which is the case of deuterated isotopologues DNC and DCN, whose peak intensities are similar within a factor of 2.

Following the approach presented in Lefloch et al. (2012), we have fitted the line profiles by an exponential law of the type $\exp(-V/V_0)$, a procedure which is obviously limited by the SNR of the data. In practice, we considered the lower-J transitions of HCN, H^{13}CN and HNC. The results are displayed in Fig. 6, where the spectra are displayed in a linear-logarithmic scale. The spectral slope of the HCN (H^{13}CN) line profiles considered can be fitted by an exponential law of the type $\exp(-V/V_0)$, with V_0= 3.8 km s^{-1} (V_0= 4.5 km s^{-1}; Fig 6). The similar values obtained for V_0 indicate that we are indeed probing the same gas in the different transitions of the same molecular species. A small deviation with respect to the fit is observed at $V < -10$ km s^{-1} in the HCN J=1–0 line profile. This is probably due to the overlap between the contributions of the different hyperfine satellites. Another possibility would be the presence of spatial gradients of emission across the telescope beam (Benedettini et al. 2013).

The spectral slope V_0 of the HCN line profiles is very similar to that found for the CO emission from the L1157-B1 outflow cavity (component g_2) by (Lefloch et al. 2012), as indicated by the similarity of the fits and the derived exponent values (V_0 = 4.4 km s^{-1}). This implies that in the velocity range between -20 and -5 km s^{-1}, both species are probing the same gas component. This is consistent with the analysis of the HCN J=3–2 spatial distribution obtained with the IRAM 30m telescope at 9.3″ (Sect. 4.1) and the HCN J=1–0 and H^{13}CN J=2–1 with the IRAM interferometer at a few arcsec resolution (Benedettini et al. 2007; Busquet et al. 2017). As can be seen in Fig. 6, the HNC line profiles look very different from those of HCN in a linear-logarithmic scale. The velocity range of the emission is narrower and stops at -10 km s^{-1}, whereas the emission of HCN extends up to -30 km s^{-1}. Quantitatively, the HNC line profiles are well fitted by an exponential function $\exp(-V/V_0)$ with V_0= 2.1 km s^{-1}, i.e. a value of V_0 half the value obtained for HCN. This supports the idea that HNC and HCN are tracing different regions. We note that the V_0 value obtained for HNC is actually similar to that found for the CO component g_3 (V_0 = 2.5 km s^{-1}), which Lefloch et al. (2012) showed to be associated with the L1157-B2 outflow cavity.

In L1157-B1, the HCN line profiles follow an exponential signature $\exp(-V/V_0)$, with the same V_0 value for the rotational transitions J= 1–0 and J= 3–2, so that the HCN line intensity ratio J= 3–2/J=1–0 is almost constant for velocities beyond -6 km s^{-1} (see Fig. 6). Hence, the HCN excitation conditions are essentially independent of velocity, at least in this velocity range. Similar results were previously reported

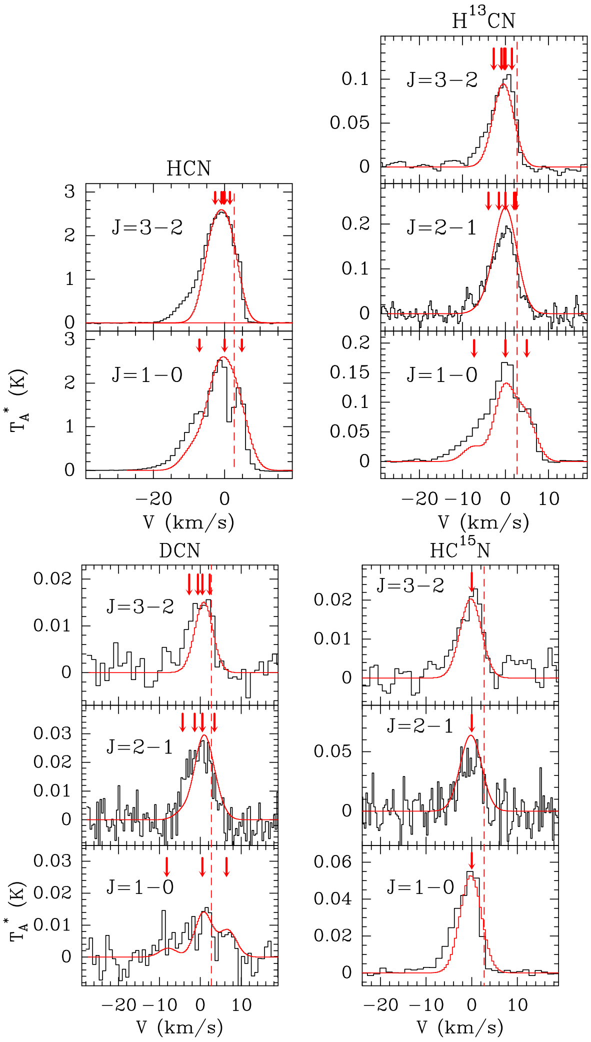

Figure 2. Montage of line profiles of HCN and its rare isotopologues (H^{13}CN, DCN, HC^{15}N), as observed with ASAI towards L1157-B1. Dashed-dotted lines indicate the baseline and rest velocity, V_{lsr}= +2.7 km s^{-1}. All the spectra are smoothed to a resolution of 1 km s^{-1}. The best fits obtained from the LTE analysis with CASSIS are displayed in red. The velocity axis is associated to the reference frequency given in Table 2. Red arrows mark the location of the hyperfine satellites on the velocity axis, based on the frequencies given in the CASSIS database.

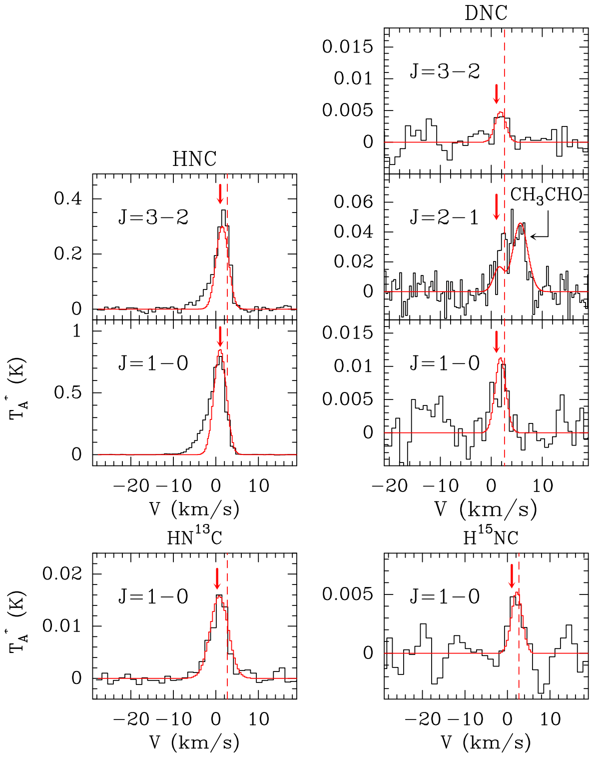

Figure 3. Montage of line profiles of HNC and its rare isotopologues (HN^{13}C, DNC, H^{15}NC), as observed with ASAI towards L1157-B1. Dashed-dotted lines indicate the baseline and rest velocity, V_{lsr}= +2.7 km s^{-1}. All the spectra are smoothed to a resolution of 1 km s^{-1}. The best fits obtained from the LTE analysis with CASSIS are displayed in red. The velocity axis is associated to the reference frequency given in Table 2. Red arrows mark the location of the hyperfine satellites on the velocity axis, based on the frequencies given in the CASSIS database.

for CO (Lefloch et al. 2012). The similarity of the spectral slopes of HCN and CO between −20 and −5 km s^{-1} implies that the HCN/CO line flux ratio is constant, and since the excitation conditions of both species are independent of velocity in this interval, it means that the relative abundance ratio is also independent of velocity in this velocity range.

The HCN/H^{13}CN total line flux ratio is ≈ 19 and 42 for the J=1–0 and J=3–2 transitions, respectively. Assuming similar excitation conditions for both isotopologues and an elemental abundance ratio ^{12}C/^{13}C equal to 66 (see below), close to the local ISM value (Milam et al. 2005), we then derive line opacities $\tau_{10} \simeq 3$ and $\tau_{32} \simeq 0.8$ for the J=1–0 and J=3–2, respectively, i.e. the gas is moderately optically thick. The HNC/HN^{13}C takes lower values, ≈ 11 and 16 for the J=1–0 and J=3–2 transitions, respectively, which implies opacities of about 5 and 4 for the main isotopologue, respectively, still under the assumption of a standard elemental abundance ratio.

4.3 L1157-mm

Emission from the HCN and HNC isotopologues was detected towards the protostellar envelope of L1157-mm. All the detected molecular transitions display narrow linewidths between 0.8 and 1.8 km s^{-1}, as expected for cold and quiescent protostellar gas (Figs. 4–5). This permits identification of the hyperfine satellites, whose emission was hidden otherwise in the outflowing gas at position B1. The signature of the protostellar outflow is detected in the HCN and HNC J=1–0 lines, as a broad, low intensity component with a typical linewidth of 5 km s^{-1}.

Overall, comparison of the HCN and HNC isotopologues emission shows that the transitions from same rotational levels display similar similar intensities for each pair of isomers, as can be seen in Figs. 4-5 (see also Table 4). Since the corresponding line intensity ratios are only weakly dependent on the excitation temperature, this suggests that both isomers and their rare isotopologues should have similar abundances. Note that the situation differs very much from L1157-B1, where much brighter emission is detected in the HCN isotopologues.

The HCN/H^{13}CN (HNC/HN^{13}C) line flux ratio is 11

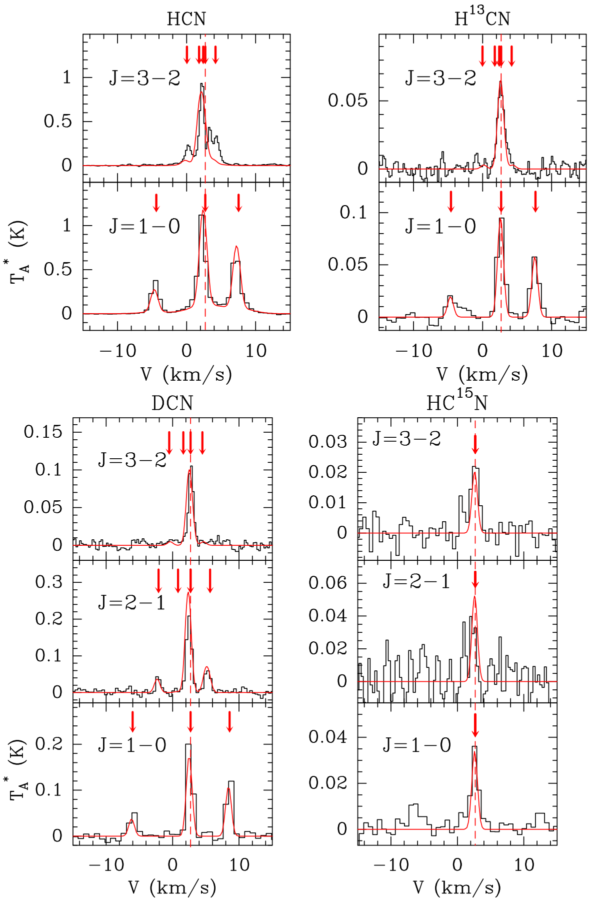

Figure 4. Montage of line profiles of HCN and its rare isotopologues ($H^{13}CN$, DCN, $HC^{15}N$), as observed with ASAI towards L1157-mm. Dashed-dotted lines indicate the baseline and rest velocity, V_{lsr}= +2.7 km s^{-1}. The best fits obtained from the LTE analysis with CASSIS are displayed in red. The velocity axis is associated to the reference frequency given in Table 2. Red arrows mark the location of the hyperfine satellites on the velocity axis, based on the frequencies given in the CASSIS database.

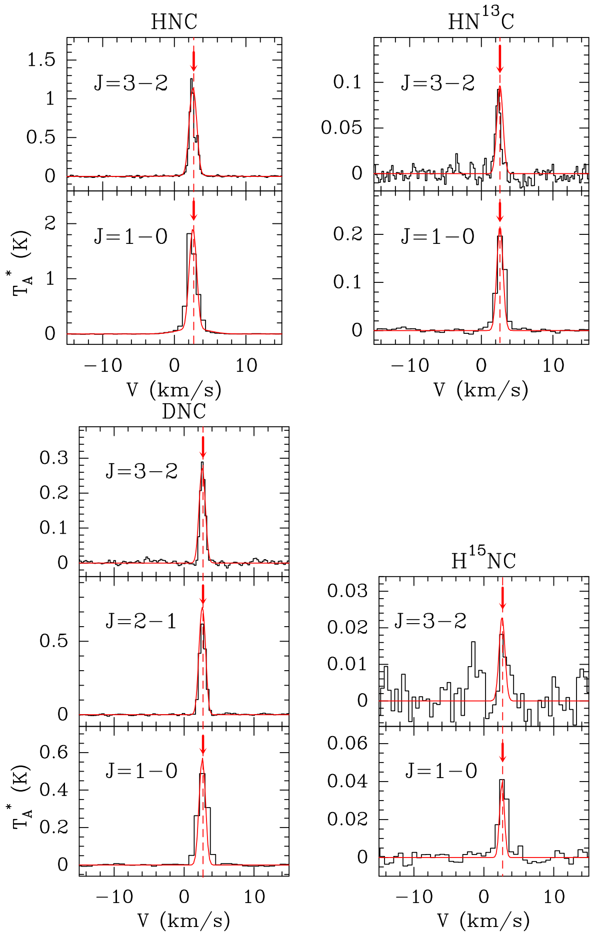

Figure 5. Montage of line profiles of HNC and its rare isotopologues ($HN^{13}C$, DNC, $H^{15}NC$), as observed with ASAI towards L1157-mm. Dashed-dotted lines indicate the baseline and rest velocity, V_{lsr} = +2.7 km s^{-1}. The best fit obtained from the LTE analysis with CASSIS are displayed in red. The velocity axis is associated to the reference frequency given in Table 2. Red arrows mark the location of the hyperfine satellites on the velocity axis, based on the frequencies given in the CASSIS database.

and 16 (12 and 23) for the J=1–0 and 3–2 transitions, respectively. Adopting a standard elemental abundance ratio $^{12}C/^{13}C = 66$, we then derive HCN line optical depths $\tau_{10} \simeq 5.5$ and $\tau_{32} \simeq 2.3$, for the J=1–0 and J=3–2 transitions, respectively. Similar results are obtained for HNC. Hence, both the HCN and HNC emissions are optically thick. Therefore, we have used the ^{13}C isotopologues to determine the total gas column density of HCN and HNC.

To summarize, a simple comparison of the line intensities of the HCN and HNC isotopologues measured towards L1157-mm suggests that both isomers are present in the pre-shock phase with similar abundances. The pre-shock gas displays hints of isotopic fractionation enrichment, in particular deuteration, which is partially preserved through the shock. A strong differentiation is observed in the shock between HCN and HNC with the emission of the former strongly enhanced over the latter. Analysis of the spectral signature suggests that both isomers are tracing different regions in the shock region.

4.4 Line excitation

The above analysis of the line profiles shows hints of chemical evolution in the passage of the shock. In order to gain more insight on the shock impact on nitrile chemistry, we have first determined the excitation conditions of the different molecular species (excitation temperature, column density). The detection of the rare isotopologues offers an opportunity to constrain directly the evolution of isotopic fractionation through the passage of a protostellar shock. In the case of L1157-mm, rather than a detailed physical and chemical description of the structure of the envelope, our goal here is to determine the relative abundances of these various species, which we take as representative of the chemical composition of the pre-shock gas in the L1157-B1 region.

In order to follow a systematic approach in the molecular abundance determination, we decided to model the line profiles in the approximation of Local Thermodynamical Equi-

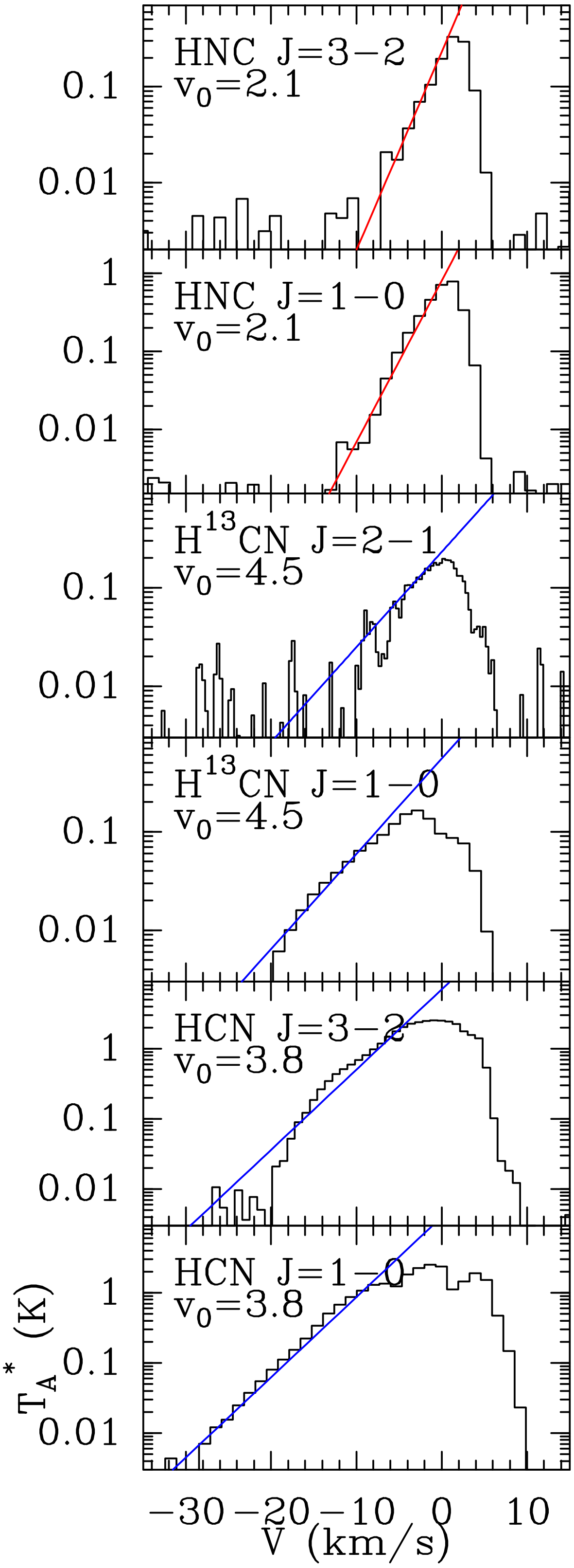

Figure 6. Montage of emission line profiles observed towards L1157-B1 displayed in linear-logarithmic scale, from top to bottom: HNC $J = 3-2$, $J = 1-0$, H^{13}CN $J = 2-1$, $J = 1-0$, HCN $J = 3-2$, $J = 1-0$. In each panel, we have superposed in red (blue) a fit to the spectral slope of the type $T(v) \propto \exp(-V/V_0)$ with $V_0 \simeq 2.0$ (4.0) km s^{-1}, associated with the component g_3 (g_2) of the outflow. The exponent v_0 is given for each transitions in the corresponding panel.

librium (LTE) using CASSIS[3] (Vastel et al. 2015). In the case only one transition was detected (HC^{15}N, HN^{13}C in L1157-B1), an excitation temperature of 7 K was adopted, in good agreement with the other rare isotopologues. Line profiles towards L1157-B1 could usually be reproduced with one single Gaussian component, of Full Width at Half Power (FWHP) consistent with our determination of the line parameters (see Table 1). In order to reproduce as accurately as possible the observed line profiles, we made use of the CASSIS private database which takes into account the hyperfine spectroscopic properties of HCN isotopologues. Towards L1157-mm, it was necessary to introduce a second component of broad linewidth (5 km s^{-1}) and low intensity in order to reproduce the outflow signature (see Sect. 4.3).

We have adopted a size of 60″ for the envelope of L1157-mm, a value in good agreement with the size of the envelope observed in N$_2$H$^+$ (Tobin et al. 2013). In practice, this value allowed us to best simultaneously reproduce the emission of the various transitions of a given molecular species under the assumption of one single excitation temperature. We have adopted a total gas column density of 2×10^{22} cm^{-2}, based on the H$_2$ column density maps of the region obtained in the Herschel Gould Belt Survey (HGBS) of nearby star-forming molecular clouds (Di Francesco et al. 2020). We note that this H$_2$ column density is about a factor of 3 higher than the determination obtained by Mendoza et al. (2018). The latter value (6×10^{21} cm^{-2}) was derived from the ^{13}CO J=1–0 line in the ASAI spectrum of the protostar, adopting a canonical abundance of 1.6×10^{-6}. As a matter of fact, the low gas kinetic temperature (∼ 10 K) and the relatively high gas density (∼ a few 10^4 cm^{-3}) of the envelope are such that CO is most likely depleted at large scale in the envelope by a factor of a few, as is commonly measured in cold cores (see e.g., Bacmann et al. 2002). Both column density values can be reconciled if CO is moderately depleted by a factor of about 3–4 over the envelope. We have adopted a linewidth of ∼ 1 km s^{-1} for the line profile modelling in L1157-mm, in agreement with the results of our gaussian fits to the line spectra (see Figs. 4–5 and Table 2).

In the case of L1157-B1, previous observational work showed that the molecular gas emission arises from a region with a typical gaussian size (FWHM) in the range 20″ – 25″ (Gueth, Guilloteau, & Bachiller 1996; Lefloch et al. 2012; Benedettini et al. 2013). This is consistent with the distribution of the HCN J=3–2 emission (Fig. 1), which appears extended between the protostar and the B1 shock position. The high-J transitions of the HCN and HNC isotopologues lie in a frequency range for which the main-beam of the telescope is comparable to or smaller than the size of the shock region, as estimated from interferometric observations (see Tables 1–2). For these transitions, the emission can be considered as extended and the main-beam temperature becomes a satisfying approximation to the molecular line brightness temperature. The case of the ground state transitions of the HCN and HNC isotopologues is more complicated for two reasons: first, the telescope beamwidth (HPBW) is comparable to the molecular emission size; second, the typical physical conditions ($n(\mathrm{H_2})$ ∼ 10^5 cm^{-3}; T_{kin}= 60 K–90 K) are such than the rotational transitions present in the millimeter bands are

---

[3] http://cassis.irap.omp.eu/

subthermally excited. The J=1–0 excitation temperature is higher than that of the J=3–2 line, as can be checked by a simple calculation using a radiative transfer code in the Large Velocity Gradient approximation, like Madex (Cernicharo et al. 2012). In the LTE approximation, the T_{ex} of the J=1–0 line is underestimated by the fitting procedure, and the approximation is no longer very satisfying. However, the approximation of extended, or main-beam averaged, emission compensates for the previous effect, which mainly affects the ground state transitions, as explained above. We found that this approximation yields much better quality LTE fits. The source-averaged column density is then obtained by correcting the fitted (main-beam averaged) column density for the main-beam filling factor.

The results of our LTE analysis (source-averaged column density N, excitation temperature T_{ex}) and the corresponding molecular abundances are summarised in Table 3. Due to the uncertainties in the derivation of the HCN column densities from the ^{12}C isotopologue, we have reported for HCN and HNC the values obtained from the rare ^{13}C isotopologues, adopting an elemental abundance ratio $^{12}C/^{13}C = 66$ (see below Sect. 5.1). They are indicated with a (*) in Table 3.

The best fits to the individual line profiles obtained with CASSIS are superimposed in red on the spectra in Figs. 2–5. The error bars on $T_{\rm rot}$ and N were estimated from LTE fits to the line profiles taking into account the absolute flux calibration uncertainties (see Sect. 3.3) and the statistical rms noise. Our column density determinations for HCN and HNC towards L1157-mm and L1157-B1 are in good agreement with those of Bachiller & Pérez-Gutiérrez (1997). Recently, Benedettini et al. (2021) observed the H^{13}CN and HC^{15}N J=1–0 line emission at 4$''$ resolution toward L1157-B1 using NOEMA, as part of the Large Program SOLIS. Their radiative transfer modelling of both lines yielded $N(H^{13}CN) \sim 7 \times 10^{12}$ cm^{-2} and $N(HC^{15}N) \sim 2 \times 10^{12}$ cm^{-2}. Our observational determinations are in satisfying agreement with these values (see Table 3).

5 DISCUSSION

In this section, we discuss the properties of the HCN and HNC isotopologues in the pre-shock gas, based on the L1157-mm envelope properties, and their evolution across the shock in L1157-B1. The molecular abundances and line ratios of interest derived towards L1157-B1 and L1157-mm are presented in Table 4. Using the time dependent gas-grain chemical and parametrised shock model UCLCHEM (Holdship et al. 2017) we simulate the pre-shock abundances for the gas and the solid phase, before the arrival of the shock, as well as during and after the shock has passed. We discuss the modelling findings with an emphasis of the behaviour of HCN and HNC.

5.1 $^{12}C/^{13}C$ elemental abundance ratio

We have used the detected transitions of HC$_3$N and its rare ^{13}C isotopologues observed towards L1157-B1 to estimate the elemental abundance ratio $^{12}C/^{13}C$ in the L1157 star-forming region. The transitions of the rare isotopologues J=10–9, J=11–10, J=12–11 of H^{13}CCCN, HC^{13}CCN and HCC^{13}CN were presented in Mendoza et al. (2018). The transitions of same quantum numbers of the different ^{13}C isotopologues are very close in frequency, separated by a few GHz at most. These different transitions were observed simultaneously in the ASAI survey, with the advantage of minimizing the calibration uncertainty, which is then dominated by the rms noise of the spectrum. Mendoza et al. (2018) showed that the emission of all the HC$_3$N isotopologues detected in the millimeter range is optically thin. Hence, the line flux ratio of the ^{12}C to the sum of the ^{13}C isotopologues is equal to three times the elemental abundance ratio $^{12}C/^{13}C$. For the J=10–9 and J=12–11 transitions, we found $^{12}C/^{13}C = 66\pm6$. For the J=11-10, we discarded the H^{13}CCCN line whose intensity is almost twice as bright as the lines of HC^{13}CCN and HCC^{13}CN, a dissymmetry which is observed only in this transition and not in the J=10–9 and J=12–11. It then comes $^{12}C/^{13}C = 70\pm10$, in agreement with the determinations from the J=10–9 and J=12–11. This direct observational determination of the $^{12}C/^{13}C$ ratio in the L1157 star forming region is actually very close to the elemental abundance ratio in the local ISM, equal to 68, (Lucas & Liszt 1998; Milam et al. 2005) and the value assumed in our previous works (see Sect. 2).

Both the HCN/H^{13}CN and HNC/HN^{13}C column density ratios display values well below the canonical $^{12}C/^{13}C$ elemental abundance ratio in the ISM, equal to 68 (Lucas & Liszt 1998; Milam et al. 2005). In particular, a low $^{12}C/^{13}C$ ratio of $\approx 11 \pm 4$ is measured towards towards the cold protostellar core L1157-mm. We first note that models of ^{13}C isotopic fractionation in cold cores lead to an opposite effect, i.e. a H^{12}CN/H^{13}CN (HN^{12}C/HN^{13}C) ratio higher than the $^{12}C/^{13}C$ elemental abundance ratio (Langer et al. 1984; Roueff et al. 2015). A similar effect was reported by citetDaniel2013 in their detailed study of nitrogen hydrides and nitriles in the Class 0 protostellar core Barnard 1. The authors concluded that the apparently low H^{12}CN/H^{13}CN ratio was most likely a bias caused by the simple hypothesis made in the radiative transfer modelling of the line excitation and the geometry of the astrophysical source. In particular, the excitation of the HCN and HNC ground-state transitions also depends on the extended, low-density gas surrounding the dense core, so that a detailed multi-dimensional radiative transfer model of the source taking into account the full density and velocity fields is needed in order to properly reproduce the line profiles .

From what precedes, we conclude that there is no convincing evidence for $^{12}C/^{13}C$ fractionation of HCN/HNC in the star-forming region. Because of the high optical depth of the HCN and HNC lines, which cast some uncertainties on the determation of the HCN and HNC total column densities, these were obtained from the column densities of their optically thin ^{13}C isotopologues and taking into account our estimate of the elemental abundance $^{12}C/^{13}C = 66 \pm 6$.

5.2 Isomers

In the pre-shock gas, we find similar molecular abundances of HCN and HNC, close to 2×10^{-9}, and a a relative abundance ratio HCN/HNC= H^{13}CN/HN^{13}C= 1.1 ± 0.4. These values were derived from a direct to the L1157-mm line profiles with CASSIS, taking into account the line optical depths. Similar results were obtained when considering the rare isotopologues ratios DCN/DNC ($= 1.1 \pm 0.4$) and HC^{15}N/H^{15}NC

Table 3. Excitation conditions (source-averaged column density N, rotational temperature $T_{\rm rot}$, abundance X) of the HCN and HNC isotopologues detected towards L1157-B1 and L1157-mm. Emission sizes of 60″ and 20″ were adopted for L1157-mm and L1157-B1, respectively. A total H_2 column density of 2×10^{22} cm^{-2} and 2×10^{21} cm^{-2} was adopted for L1157-mm and L1157-B1, respectively (Lefloch et al. 2012; Di Francesco et al. 2020), in order to compute the molecular abundances. We follow the convention $a(b) = a \times 10^b$. The HCN and HNC parameters are marked with a * to indicate that they were obtained from the ^{13}C isotopologue, adopting an abundance ratio ^{12}C/^{13}C= 66 (see Sect. 5.1).

	L1157-mm			L1157-B1		
Species	$T_{\rm rot}$ (K)	N (cm^{-2})	X	$T_{\rm rot}$ (K)	N (cm^{-2})	X
Main Body						
HCN(*)	$6.7^{+0.7}_{-0.5}$	$4.6^{+0.6}_{-0.6}$(13)	$2.3^{+0.3}_{-0.3}$(-9)	$7.2^{+0.6}_{-1.0}$	$6.6^{+1.1}_{-0.6}$(14)	$3.3^{+0.6}_{-0.3}$(-7)
$H^{13}CN$	$6.7^{+0.7}_{-0.5}$	$7.0^{+1.0}_{-1.0}$(11)	$3.5^{+0.5}_{-0.5}$(-11)	$7.2^{+0.6}_{-1.0}$	$1.0^{+0.4}_{-0.1}$(13)	$5.0^{+2.0}_{-1.0}$(-9)
DCN	$4.9^{+0.2}_{-0.2}$	$2.8^{+0.5}_{-0.3}$(12)	$1.4^{+0.3}_{-0.2}$(-10)	$6.5^{+0.5}_{-0.5}$	$2.1^{+0.5}_{-0.5}$(12)	$1.1^{+0.2}_{-0.3}$(-9)
$HC^{15}N$	$7.7^{+0.5}_{-0.4}$	$1.2^{+0.3}_{-0.2}$(11)	$0.7^{+0.1}_{-0.1}$(-11)	$6.8^{+0.4}_{-0.5}$	$2.0^{+0.5}_{-0.3}$(12)	$1.0^{+0.3}_{-0.2}$(-9)
HNC(*)	$6.8^{+0.3}_{-0.3}$	$4.2^{+0.8}_{-0.5}$(13)	$2.1^{+0.4}_{-0.3}$(-9)	$7.0^{+1.3}_{-1.5}$	$3.5^{+0.3}_{-0.6}$(13)	$1.7^{+0.2}_{-0.2}$(-8)
$HN^{13}C$	$6.8^{+0.3}_{-0.3}$	$6.3^{+1.2}_{-0.7}$(11)	$3.2^{+0.6}_{-0.4}$(-11)	$7.0^{+3.0}_{-1.7}$	$5.3^{+0.6}_{-0.6}$(11)	$2.6^{+0.3}_{-0.2}$(-10)
DNC	$5.7^{+0.3}_{-0.2}$	$2.5^{+0.5}_{-0.3}$(12)	$1.3^{+0.2}_{-0.2}$(-10)	$6.0^{+2.0}_{-2.0}$	$3.2^{+1.8}_{-1.4}$(11)	$1.6^{+0.9}_{-0.7}$(-10)
$H^{15}NC$	$7.7^{+0.5}_{-0.6}$	$1.3^{+0.3}_{-0.4}$(11)	$0.7^{+0.1}_{-0.3}$(-11)	$7.0^{+3.0}_{-1.5}$	$1.8^{+0.7}_{-0.6}$(11)	$8.5^{+3.5}_{-2.5}$(-11)
Outflow component						
HCN	5.0	4.0(12)	2.4(-8)	-	-	-
HNC	5.0	1.5(12)	0.9(-8)	-	-	-

Table 4. Isomer and isotopic abundance ratios of HCN and HNC in L1157-mm and L1157-B1. For each source, the ratios are computed adopting a canonical elemental ^{12}C/^{13}C abundance ratio of 66 (see also Sect. 5.1).

	L1157-mm	L1157-B1
HCN/H	$1.2^{+0.2}_{-0.2}$(-9)	$1.7^{+0.4}_{-0.2}$(-7)
HCN/$H^{13}CN$	66	66
HCN/$HC^{15}N$	383 ± 145	330 ± 110
HCN/DCN	16 ± 5	314 ± 110
$H^{13}CN/HC^{15}N$	5.8 ± 2.2	5.0 ± 2.5
HNC/$HN^{13}C$	66	66
HNC/$H^{15}NC$	323 ± 160	194 ± 100
HNC/DNC	17 ± 7	109 ± 70
$HN^{13}C/H^{15}NC$	4.8 ± 2.4	3.0 ± 1.5
HCN/HNC	1.1 ± 0.4	19 ± 6
$H^{13}CN/HN^{13}C$	1.1 ± 0.4	19 ± 8
$HC^{15}N/H^{15}NC$	0.9 ± 0.5	11 ± 6
DCN/DNC	1.1 ± 0.4	6 ± 5

($= 0.9 \pm 0.5$). The consistency between these values determined independently, makes us confident about the reliability of our method. The molecular abundances of HCN and HNC are similar to those reported in previous surveys of dark cloud cores and low-mass star forming cores (e.g., Hirota et al. 1998; Hily-Blant et al. 2010; Daniel et al. 2013), suggesting that the envelope of L1157-mm has kept memory of the prestellar phase. Hirota et al. (1998) pointed out that since no difference is observed between the values measured in prestellar and protostellar cores, the evaporation of HCN and HNC from dust grains does not contribute significantly to the observed emission in the cold gas.

Comparison of the molecular abundances of L1157-mm (pre-shock gas) and the shocked region L1157-B1 (see Table 3) shows that the HCN and HNC isomers behave differently across the shock. First, we observe an increase in the abundance of all the HCN isotopologues. The rare $H^{13}CN$ and $HC^{15}N$ (and HCN) abundances increase by a similar factor of 140 while the DCN abundance increases much less, by a factor ≈ 8. Unlike HCN, the abundances of all the HNC isotopologues vary by a much smaller factor of a few (≈ 8–12). The abundance DNC remains almost unchanged. Overall, the abundances of the HNC isotopologues seem barely affected by the passage of the shock. From a ratio HCN/HNC with an initial value of 1 in the quiescent gas, it is now 19 ± 6 in the post-shocked gas. The isomer ratio displays values in the range 11–19 which are consistent, within the uncertainties, for $H^{13}CN/HN^{13}C$ and $HC^{15}N/H^{15}NC$. The deuterated isomers seem to behave differently with a much lower increase of the DCN/DNC ratio.

In the protostellar outflow near L1157-mm, the high sensitivity of the ASAI data has permitted detection of the emission of the ground state transition of HCN and HNC. This emission can be modelled as a broad component of ≈ 5 km s^{-1} and low excitation (Table 3). Interestingly, the HCN/HNC abundance (column density) ratio is close to 3, suggesting that the relative abundance of HCN with respect to HNC is enhanced in the formation of the outflow.

5.3 Isotopic fractionation

5.3.1 Deuterium

It is well established that strong Deuterium enrichment takes place in molecular material of cold, dark and prestellar cores (Caselli & Ceccarelli 2012). The first evidence of molecular deuteration in L1157-mm were brought by Bachiller & Pérez-Gutiérrez (1997), with the detection of the deuterated forms of HCN and HCO^+, and a molecular D/H ratio of 0.018 in the cold envelope. Our own determinations, which are based on the modelling of a larger number of rotational transitions, yield a somewhat higher D/H ratio 0.06 ± 0.02 for both HCN and HNC, in rough agreement with Bachiller & Pérez-Gutiérrez (1997).

At the passage of the shock, the DCN abundance increases by a factor 7 whereas DNC remains unchanged. Overall, the magnitude of these variations remain small in front of those affecting the main isotopologues and indicate that, at first order, the abundances of these deuterated species are only moderately affected by the passage of the shock, with a different behaviour for DCN and DNC. As for L1157-B1, previous estimates of the DCN/HCN ratio were obtained by Codella et al. (2012), based on a reduced number of transitions of $H^{13}CN$ and DCN. Our present determination of $(3.1 \pm 1.0) \times 10^{-3}$ is consistent with their previous estimate $D/H = (0.5\text{–}3) \times 10^{-3}$. More recently, Busquet et al. (2017) reported similar deuterium fractionation ratios ($\approx 4.0 \times 10^{-3}$) in the small-scale structures detected in the bow-shock, with no significant spatial variation. Our unbiased analysis of the deuterated isomers confirms that the molecular D/H ratio decreases across the shock and it allows us to quantify the magnitude of the effect: a factor 26 and 8 for HCN and HNC, respectively.

The behaviour of DCN/HCN in the B1 shock position has already been studied in detail by Busquet et al. (2017) based on high-angular resolution observations of $H^{13}CN$ J=2–1 and DCN J=2–1 combined with the UCLCHEM code and adopting the deuterated network of Esplugues et al. (2013). The results from the model show that the DCN/HCN abundance ratio varies with the passage of the shock. The observed DCN/HCN ratio is well reproduced by the model in the post-shock gas material, around $t \sim 1000$ yr, when the gas has cooled down to ~ 80 K. The morphology of DCN together with the shock model suggests that gas-phase chemistry is the dominant mechanism producing the widespread DCN emission, which dominates in the head of the bow-shock.

5.3.2 Nitrogen

We do not find any evidence of ^{15}N isotopic fractionation. Towards L1157-mm, we obtain $^{13}C/^{15}N$ ratios of 5.8 ± 2.2 and 4.8 ± 2.4 for HCN and HNC, respectively. Both values agree within the uncertainties, and they are also consistent with the canonical elemental abundance ratio of 6.5 in the local ISM (Milam et al. 2005; Marty et al. 2011). This translates into elemental abundance ratios $HC^{14}N/HC^{15}N$ of 380 ± 145 and $H^{14}NC/H^{15}NC \approx 320 \pm 160$ towards L1157-mm. Both values are consistent with the solar value in the local ISM (440; Marty et al. 2011). Towards L1157-B1, the $H^{13}CN/HC^{15}N$ is almost unchanged (5.0 ± 2.5) whereas the $HN^{13}C/H^{15}NC$ takes a lower value (3.0 ± 1.5), but still in rough agreement with the canonical value.

At the passage of the shock, the rare ^{15}N isotopologues display the same behaviour as HCN and HNC, as can be seen in Table 3. The $H^{13}CN$ and $HC^{15}N$ abundances in L1157-B1 increase by a factor of 140 with respect to the values measured towards L1157-mm. By comparison, $HN^{13}C$ and $H^{15}NC$ increase by a factor (~ 8). Overall, these variations remain very modest. Therefore, our analysis brings *direct* observational evidence that the $^{14}N/^{15}N$ elemental abundance ratio is not affected by the passage of the shock.

Recently, Benedettini et al. (2021) have investigated the $^{14}N/^{15}N$ fractionation of HCN in the two shocked clumps, B1 and B0, of the L1157 outflow using the NOEMA interferometer at $\sim 3''$ resolution, and obtained $^{14}N/^{15}N = 340 \pm 70$, in good agreement with our determination (see Table 4). Based on the chemical shock modelling, Benedettini et al. (2021) conclude that the rich gas chemistry activated by the passage of the shock does not affect the $^{14}N/^{15}N$ ratio with respect to the local ISM value. This conclusion is observationally confirmed by our results.

5.4 Chemical modelling

As discussed in the previous section, a simple qualitative analysis of the spectral line signature shows evidence for the shock impact on Nitrile gas composition. The HCN isotopologue abundances have been deeply affected in the shock, increasing by more than one order of magnitude, whereas the HNC isotopologues seem to have barely noticed its presence.

Our goal is to identify the chemical processes responsible for the HCN and HNC gas phase abundances in L1157-B1, before and during the passage of the shock. The different studies of H_2O, NH_3, CH_3OH, H_2CO, HC_3N, H_2S, NO, PN, PO by our group (Viti et al. 2011; Lefloch et al. 2016; Holdship et al. 2017; Benedettini et al. 2013; Mendoza et al. 2018; Benedettini et al. 2013; Busquet et al. 2017; Codella et al. 2018; Benedettini et al. 2021) have led to a coherent picture of L1157-B1, in which the detected molecular emission is accounted for by a C-type shock propagating into a pre-shock medium of density $n(H_2) \simeq 5 \times 10^4\ \mathrm{cm^{-3}}$ and shock velocity V_s in the range $20 - 40\ \mathrm{km\,s^{-1}}$. We have adopted the same methodological approach as in our previous studies, and have used the public time dependent gas-grain chemical and parametrised shock model UCLCHEM code (Holdship et al. 2017) to follow the evolution of the gas phase composition across a protostellar shock, adopting a cosmic ray ionization rate of $\zeta = 1.3 \times 10^{-16}\ \mathrm{s^{-1}}$, in agreement with Podio et al. (2014). We refer the reader to the release paper of UCLCHEM for a detailed description of this public code (Holdship et al. 2017). Briefly, the code is run in two phases, where Phase I forms a dense core out of a diffuse, essentially atomic medium. An initial density of $100\ \mathrm{cm^{-3}}$ is adopted here, for the diffuse medium. During this phase, gas-phase chemistry, freezing on to dust particles and subsequent surface processing, occurs.

We have considered two cases, depending on the duration on the pre-shock phase. In the first case ("short" duration), one considers the extreme case where the jet impacts the cloud as soon as the latter is formed; in the second case

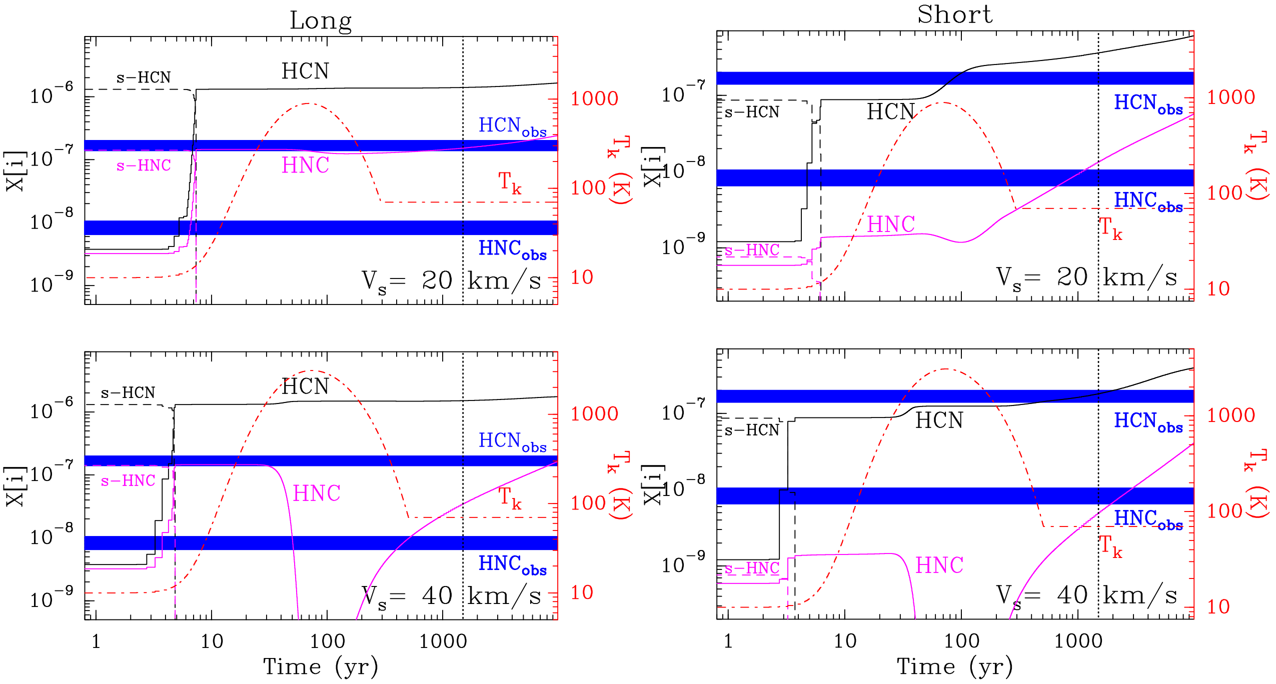

Figure 7. Time-dependent fractional abundances (with respect to the number of hydrogen nuclei) of HCN and HNC across a protostellar shock propagating at $V = 20\,\mathrm{km\,s^{-1}}$ (top) and $V = 40\,\mathrm{km\,s^{-1}}$ (bottom), respectively. *(left)*"Long" pre-shock phase. *(right)* "Short" pre-shock phase. The abundances of HCN (black) and HNC (magenta) in the gas phase and on the dust grains are indicated by the solid and the dashed curve, respectively. The temperature profile across the shock is drawn with the red dash-dot curve. The fractional abundances measured towards L1157-B1 and their uncertainties are indicated by the blue rectangles. The vertical dotted line at $t = 1500$ yr indicates the estimated age of the shock by Podio et al. (2016).

(long" duration), one begins with a situation where 5 million years pass after the cloud is formed and before the shock arrives. The density at the end of Phase I is a free parameter, called from now on the pre-shock density. The second phase computes the time-dependent chemical evolution of the gas and dust during the passage of a magnetized (C-type) shock whose structure is at steady-state.

Figure 7 presents the variations of the HCN and HNC molecular abundances *relative to the number of H nuclei* as a function of time through the shock, as predicted by our model for the shock velocities $V_s = 20\,\mathrm{km\,s^{-1}}$ (top) and $V_s = 40\,\mathrm{km\,s^{-1}}$ (bottom) and for the durations of the pre-shock phase, long (left) and short (right). The HCN (HNC) abundance in the gas and the solid phase are drawn in solid and dotted black (magenta), respectively. In this figure, the shock is propagating to the left. Since the shock is propagating at steady state, the time variations of the different physical or chemical parameters (temperature, density, abundances) can simply be converted into space variations, via the relation $z = V_s \times t$, hence giving access to the shock structure itself. The observational determinations of the gas phase abundances of HCN and HNC and their uncertainties are indicated by the dark blue rectangles.

5.4.1 *Pre-shock phase*

Our modelling of the pre-shock phase is consistent with the physical and chemical conditions in the envelope of L1157-mm, i.e., cold gas at 10 K of moderate density ($n(\mathrm{H_2}) = 10^5\,\mathrm{cm^{-3}}$), for which we determined an abundance of 1.2×10^{-9} and 1.1×10^{-9} for HCN and HNC, respectively, relative to H. The key observational constraint here is that the abundances of HCN and HNC in the gas phase are similar. As can be seen in Fig. 7, our chemical modelling succeeds in reproducing similar gas phase abundances for HCN and HNC in the pre-shock phase. The HCN/HNC ratio barely varies between the long duration (~ 1) and the short duration scenario (~ 2). Both scenarios also predict correct gas phase abundances relative to H, of the order of 10^{-9} (Table 3). The short duration scenario predicts gas phase abundances in slightly better agreement with our observational determinations, within the observational uncertainties. The "long" duration scenario predicts abundances higher by a factor of 3. The gas phase abundances of the rare isotopologues are also in good agreement with our observational determinations and with the absence of ^{13}C and ^{15}N fractionation, as discussed above in Sect. 5.3.

In the gas phase, HNC and HCN are efficiently produced by the dissociative recombination (DR) of HCNH$^+$ with a branching ratio ≈ 1 (Herbst et al. 2000; Mendes et al. 2012):

$$\mathrm{HCNH^+ + e^- \rightarrow HNC + H, HNC + H}.$$

Several other routes involving neutral-neutral reactions can substantially contribute to the formation of HCN, especially at higher densities (and hence at later times). The dominant route of "destruction" for both species is freeze-out on the dust grains.

We show in Fig. 7 (in magenta dashed) the abundances of HCN and HNC on the dust grains (respectively s-HCN and s-HNC). The main difference between the short and the long duration Phase 1 models lies in fact in the solid HCN/HNC ratio, whereby the latter model predicts a ratio of ∼ 10 while the former a ratio of more than 100. This is probably due to the very efficient formation route for HNC in the gas phase, which then readily freezes out. On the surface of grains, HCN can also continue to form via the efficient hydrogenation of CN, while HNC is not produced nor efficiently destroyed on the grains. This explains the larger ratio of solid HCN/HNC compared to the gas phase HCN/HNC. Therefore, the duration of the pre-shock phase has a marked impact on the HCN and HNC abundance in the solid phase.

5.4.2 Shock impact

In the models with V_s= 20 km s^{-1} (top right and left panels in Fig. 7), the shock impact on the HCN and HNC abundances is essentially the same. In the magnetic precursor region, where ions and neutrals are kinematically decoupled, all the material stored at the surface of the dust grains is sputtered and released into the gas phase. This leads to a quick increase of both the HCN and HNC abundances in the gas phase in a few years. Therefore, in the early years, the gas phase abundance of HCN and HNC is mainly determined by the abundance of both species on the dust grains and, at later times, by the different pre-shock gas composition between the long and short Phase I models, as well as by temperature-dependent gas-phase chemistry. The main differences between the long-duration and the short-duration scenarii are the late time behaviours of HCN and HNC, where both increase, in the latter case, much more sharply. The reactions that seem to contribute to these increases are the two neutral-neutral reactions of molecular H_2 with CN (for HCN) and of atomic N with CH_2 (for HNC). A full chemical analysis of this behaviour is beyond the scope of this work, especially as the age of L1157-B1 is estimated to be ∼ 1500 yr (Podio et al. 2016) but the shorter Phase I duration certainly implies a richer gas phase at the beginning of Phase 2, and hence more abundant nitrogen and CN. This is because of a less effective freeze out during Phase I which would have not only depleted these two species but also hydrogenated them into NH_3 and HCN respectively.

The models with higher shock velocities (V_s= 40 km s^{-1}) and hence higher maximum temperatures (see bottom panels in Fig. 7), display qualitatively similar evolution for HCN among the two models. Quantitatively, the "short" duration scenario predicts HCN and HNC abundances both in agreement with our observational determinations for time $t \simeq 2000$ yr, which is also consistent with the estimated age of B1 (∼ 1500 yr; Podio et al. (2016)). On the contrary, the "long" duration scenario results into an overabundance of HCN (HNC) in the shocked gas by a factor of 10 (5) with respect to our estimates, so that the HCN abundance remains essentially constant with time. In both the "long" and the "short" duration scenarii, the HNC abundance suddenly drops to values of a few 10^{-11} when the temperature rises above a threshold value of ≈ 2000 K. This is probably due to the endothermic reaction C^+ + HNC which only becomes efficient at a temperature above 2000 K.

Therefore, our modelling favors a scenario with a "short" duration pre-shock phase and a shock propagating at V_s = 40 km s^{-1} into pre-density gas $n(H_2) = 5 \times 10^4$ cm^{-3}. It successfully accounts quantitatively for the dramatic increase of HCN abundance with respect to HNC on timescales consistent with the age of the shock. The dramatic increase of HCN/HNC mainly appears as an effect of grain sputtering, which is already efficient in low velocity shocks (V_s = 20 km s^{-1}). This could explain why the HCN and HNC emission is so extended along the outflow, while other species, like e.g. NH_2CHO, require more stringent shock conditions to be formed (Codella et al. 2017). We note that these results are fully consistent with our previous studies of L1157-B1.

6 CONCLUSIONS

Using the IRAM 30m telescope in the framework of ASAI, we have carried out a comprehensive observational study of the HCN/HNC isotopologues in the protostellar shock region L1157-B1.

Based on the observations of the envelope of the protostar L1157-mm, we find that the abundances of the rare HCN/HNC isotopologues in the pre-shock gas are similar to those found in cold dark and prestellar cores. We find a ratio HCN/HNC close to unity for all rare isotopologues and we derive an elemental abundance ratio ^{14}N/^{15}N close to its elemental value in the ISM. There is no evidence of elemental fractionation, except for Deuterium.

The impact of the shock is characterized by a strong increase of the HCN/HNC abundance ratio and of the HCN abundance relative to H_2. The ^{13}C and ^{15}N isotopologues display the same qualitative and quantitative behaviour as the main isopologues, i.e. the elemental abundance ratios remain unchanged in the passage of the shock.

A chemical modelling using UCLCHEM successfully accounts for the properties of HCN/HNC in the gas phase and their evolution in the shock. A very good agreement with the observations is obtained for a steady-state C-shock propagating with velocity V_s = 40 km s^{-1} into a pre-shock medium of density n(H) = 10^5 cm^{-3} at a time (∼ 2000 yr) reasonably consistent with the age of the shock as estimated by Podio et al. (2016). These results agree with our previous UCLCHEM studies on the chemical composition of L1157-B1 (Viti et al. 2011; Lefloch et al. 2016; Holdship et al. 2017; Benedettini et al. 2013; Mendoza et al. 2018; Benedettini et al. 2013; Busquet et al. 2017; Codella et al. 2018; Benedettini et al. 2021).

The HCN/HNC chemical evolution appears to be tighly connected to the history and the composition of the pre-shock phase. In the case of L1157-B1, it is mainly driven by grain sputtering, a process also efficient in lower velocity shocks (20 km s^{-1}). We propose this could explain the wide spatial extent of the HCN and HNC emissions in the L1157-B1 outflow, while other species (e.g. NH_2CHO) require more stringent shock conditions to be formed.

DATA AVAILABILITY

The ASAI data are publicly available under the IRAM Data Archive webpage at https://www.iram.fr/ILPA/LP007/. The other, complementary data underlying this article will be shared on reasonable request to the corresponding author.

ACKNOWLEDGEMENTS

Based on observations carried out as part of the Large Program ASAI (project number 012-12) with the IRAM 30m telescope. IRAM is supported by INSU/CNRS (France), MPG (Germany) and IGN (Spain). This work was supported by : (i) a grant from LabeX Osug@2020 (Investissements d'avenir - ANR10LABX56), by the French National Research Agency in the framework of the Investissements d'Avenir program (ANR-15-IDEX-02), through the funding of the "Origin of Life" project of the Univ. Grenoble-Alpes; (ii) the ERC Horizon 2020 research and innovation programme "The Dawn of Organic Chemistry" (DOC), grant agreement No 741002; (iii) the ERC Horizon 2020 ITN Project "Astro-Chemistry Origins" (ACO), grant agreement No 811312. SV acknowledges the European Research Council (ERC) Advanced Grant MOPPEX 833460 E.M. and JL acknowledge support from the Brazilian agency FAPESP (grant 2014/22095-6 and 2015/22254-0). G.B. is supported by the State Agency for Research (AEI) of the Spanish MCIU through the AYA2017-84390-C2-2-R grant.

REFERENCES

Bachiller, R., & Pérez-Gutiérrez, M. 1997, ApJ, 487, L93
Bachiller, R., Pérez-Gutiérrez, M., Kumar, M. S. N., et al. 2001, A&A, 372, 899
Bacmann, A., Lefloch, B., Ceccarelli, C., et al. 2002, A&A, 389, L6
Benedettini, M., Viti, S., Codella, C., et al. 2007, MNRAS, 381, 1127
Benedettini, M., Busquet, G., Lefloch, B., et al. 2012, A&A, 539, L3
Benedettini, M., Viti, S., Codella, C., et al. 2013, MNRAS, 436, 179
Benedettini, M., Viti, S., Codella, C., et al. 2021, A&A, 645, 91
Bhattacharya, B. N. & Gordy, W. 1960, PhRv, 119, 144
Busquet, G., Lefloch, B., Benedettini, M., et al., 2014, A&A, 561, A120
Busquet, G., Fontani, F., Viti, S., et al., 2017, A&A, 604, A20
Caselli, P., & Ceccarelli, C. 2012, A&ARv, 20, 56
Codella, C., Lefloch, B., Ceccarelli, C., et al. 2010, A&A, 518, L112
Codella, C., Ceccarelli, C., Lefloch, B. et al. 2012, ApJ, 757, L9
Codella, C., Ceccarelli, C., Caselli, P. et al. 2017, A&A, 605, L3
Codella, C., Viti, S., Lefloch, B., et al. 2018, MNRAS, 474, 5694
Daniel, F., Gérin, M., Roueff, E. et al. 2013, A&A, 560, 3
Di Francesco, J., Keown, J., Fallscheer, C. et al. 2020, ApJ, 904, 172
Dzib, S. A., Loinard, L., Ortiz-León, G. N. et al. 2018, ApJ, 867, 151
Esplugues, G.B., Cernicharo, J., Viti, S., et al. 2013, A&A, 559, 51
Fontani, F., Codella, C., Ceccarelli, C., et al., 2014, ApJ, 788, L43
Gómez-Ruiz, A. I., Codella, C., Lefloch, B., et al., 2015, MNRAS, 446, 3346
Gueth, F., Guilloteau, S., & Bachiller, R. 1996, A&A, 307, 891
Gueth, F., Guilloteau, S., Dutrey, A., & Bachiller, R. 1997, A&A, 323, 943
Gueth, F., Guilloteau, S., Bachiller, R. 1998, A&A, 333, 287
Gusdorf, A., Cabrit, S., Flower, D. R., Pineau Des Forêts, G. 2008a, A&A, 482, 809
Gusdorf, A., Pineau Des Forêts, G., Cabrit, S., Flower, D. R. 2008b, A&A, 490, 695
Hacar, A., Bosman, A.D., van Dishoeck, E.F., 2020, A&A, 635, 4
Herbst, E., Terzieva, R., & Talbi, D., 2000, MNRAS, 311, 869
Hily-Blant, P., Walmsley, M., Pineau des Forets, G, Flower, D., 2010, A&A 513, 41
Hirota, T., Yamamoto, S., Mikami, H., Ohishi, M. 1998, ApJ, 503, 717
Holdship, J., Viti, S., Jiménez-Serra, I., et al., 2017, AJ, 154, 38
Irvine, W. M. & Schloerb, F. P. 1984, ApJ, 282, 516
Langer, W.D., Graedel, T.E., Freerking, M.A., Armentrout, P.B., 1984, ApJ, 277, 581
Lefloch, B., Cabrit, S., Codella, C., et al. 2010, A&A, 518, L113
Lefloch, B., Cabrit, S., Busquet, G., et al. 2012, ApJL, 757, L25
Lefloch, B., Gusdorf, A., Codella, C., et al. 2015, A&A, 581, A4
Lefloch, B., Vastel, C., Viti, S., et al. 2016, MNRAS, 462, 3937
Lefloch, B., Ceccarelli, C., Codella, C., et al., 2017, MNRAS, 469, L73
Lefloch, B., Bachiller, R., Ceccarelli, C. et al. 2018, MNRAS, 477, 4792
Lucas, R., Liszt, H., 1998, A&A, 337, 246
Marty, B., Chaussidon, M., Wiens, R. C., et al., 2011, Science, 332, 6037
Mendes, M.B., Buhr, H., Berg, M.H., et al., 2012, ApJ, 746, L8
Mendoza, E., Lefloch, B., López-Sepulcre, A., et al. 2014, MNRAS, 445, 151
Mendoza, E., Lefloch, B., Ceccarelli, C. et al. 2018, MNRAS, 475, 5501
Milam, S. N., Savage, C., Brewster, M. A., et al., 2005 ApJ, 634, 1126
Podio, L., Lefloch, B., Ceccarelli, C., et al. 2014, A&A, 565, A64
Podio, L., Codella, C., Gueth, F., et al. 2016, A&A, 593, L4
Podio, L., Codella, C., Lefloch,B., et al., 2017, MNRAS, 470, L16
Roueff, E., Loison, J.C., & Hickson, K.M., 2015, A&A, 576, 99
Schilke, P., Walmsley, C. M., Pineau Des Forets, G. et al. 1992, A&A, 256, 595
Suzuki, H., Yamamoto, S., Ohishi, M. et al. 1992, ApJ, 392, 551
Tafalla, M., Bachiller, R., Lefloch, B., et al. 2015, A&A, 573, L2
Tobin, J. J., Bergin, E. A., Hartmann, L. et al. 2013, ApJ, 765, 18
Turner, B. E. 1971, ApJ, 163, L35
Ungerechts, H., Bergin, E. A., Goldsmith, P. F. et al. 1997, ApJ, 482, 245
van Dishoeck, E. F., Blake, G. A., Jansen, D. J., Groesbeck, T. D. 1995, ApJ, 447, 760
Vastel, C., Bottinelli, S., Caux, E., et al., 2015, SF2A-2015: Proceedings of the Annual meeting of the French Society of Astronomy and Astrophysics. Eds.: F. Martins, S. Boissier, V. Buat, L. Cambrésy, P. Petit, pp.313-316
Viti, S., Jimenez-Serra, I., Yates, J. A. et al. 2011, ApJ, 740, L3
Zucker, C., Speagle, J. S., Schlafly, E. F. et al. 2019, ApJ, 879, 125